SISSA
Scuola
Internazionale
Superiore di
Studi Avanzati

Physics Area - PhD course in
Theory and numerical simulation of Condensed Matter Physics

Novel quantum states in multicomponent fermionic systems

Candidate:
Matteo Ferraretto

Advisor:
Massimo Capone

Co-advisor:
Andrea Richaud

Academic Year 2022-2023

Contents

List of publications

This is the list of works where I have given my contribution and that have been published during my Ph.D. activity, organized in chronological order:

- Andrea Richaud, Matteo Ferraretto and Massimo Capone. *Interaction-resistant metals in multicomponent Fermi systems*. Physical Review B 103 (20), 205132 [1].
- Andrea Richaud, Matteo Ferraretto and Massimo Capone. *Mimicking Multiorbital Systems with SU(N) Atoms: Hund's Physics and Beyond*. Condensed Matter 7 (1), 18. [2].
- Matteo Ferraretto, Andrea Richaud, Lorenzo Del Re, Leonardo Fallani and Massimo Capone. *Enhancement of chiral edge currents in* $(d+1)$*-dimensional atomic Mott-band hybrid insulators*. SciPost Physics 14 (3), 048. [3].

The DMFT code is available at my GitHub page

https://github.com/matteoferraretto/DMFT_Hub

The code is written with the Wolfram language and requires the installation of Wolfram Mathematica. Instructions for installation and usage can be found in the GitHub page. Since the code is constantly updated, in this thesis we do not explain any function in detail, but we only discuss the general ideas and algorithms. However, a basic documentation is already built in the code and we plan to improve it in the future.

Introduction

The general framework of this thesis is the study of multicomponent strongly interacting fermions moving on a lattice. These are defined as systems of many particles obeying the Fermi-Dirac statistics, having more degrees of freedom than the usual particle spin (or at least more than two spin states) and being subject to non-negligible two-body interaction potentials. This broad definition covers a variety of topics that are nowadays the subject of a great research effort, such as the study of exotic quantum phases of electrons in solids (including high-temperature superconductivity, excitonic condensates, magnetism, topological states etc.) and the study of the low temperature behavior of atomic gases trapped in optical lattices. Among the latter, fermionic isotopes of alkaline-earth-like atoms have drawn attention in the last decade, as their electronic and nuclear properties, along with the possibility to experimentally control their interaction strength and kinetic energy, are particularly suitable to realize tunable multicomponent systems. In particular, the vanishing angular momentum of the two low-lying electronic states ${}^1S_0$ and ${}^3P_0$ induces a nearly perfect decoupling between electronic and nuclear degrees of freedom, which eventually results in a SU(N) symmetric interaction scheme, where N is the number of nuclear angular momentum states. The nuclear state can thus be regarded as an internal "flavor" index (which reduces to a pseudospin index if $N = 2$) with up to N possible values; while the electronic state provides an extra "orbital" component. In the present work, we mostly focus on implementations of multicomponent systems that can be realized in experiments with alkaline-earth-like atoms trapped in optical lattices and we investigate several phenomena where the strong interactions play a crucial role.

We investigate the equilibrium properties of multicomponent fermionic systems by using an hybrid approach, combining numerical methods and analytic (or semi-analytic) results. Among the numerical methods, we mention the exact diagonalization of systems on a lattice with a small number of sites, and the dynamical mean field theory (DMFT). In chapter [1] we give a practical introduction to DMFT, adopting a slightly different approach with respect to the usual way of presenting the topic. There are two reasons behind this choice: first of all, the presentation is adapted to the models that we have studied throughout the thesis and it is meant to explain how our code is built; the second is a pedagogical motivation, since our purpose is to provide a total beginner with the main instruments to quickly get involved in the topic, sacrificing a little bit the more general theoretical framework. Among the analytic or semi-analytic methods, we mention the Hartree-Fock mean-field approximation and the Schrieffer-Wolff transformation; we don't devote a specific chapter to these methods, instead we introduce them progressively, before discussing the corresponding results.

We can schematically divide our study in two main directions. First of all, in chapters [2] and [3] we investigate the low-temperature equilibrium states of systems where the SU(N) symmetry is explicitly broken by coupling the atoms with an external pair of laser beams, which induce optical Raman transitions with a space-dependent phase. In this context, a laser-induced Raman transition is the excitation and

subsequent disexcitation of the electronic state to an excited state characterized by significant hyperfine coupling to the nucleus (typically the $^3P_1$ state): if the photon fields are suitably polarized, the atom exchanges quanta of angular momentum with light in the process and the final result is a nuclear spin flip. The equilibrium states of the system display a *chiral* behavior: they are characterized by persistent flavor-dependent currents flowing in opposite directions, that can be experimentally detected via time-of-flight measurements on the momentum distribution of each fermionic component.

We begin by considering a single "orbital" in the remarkable cases $N = 2, 3$ and, after introducing the theoretical and experimental framework, we analyze the non-interacting limit, where many analytic results can be found, particularly for the flavor currents. After that, we consider the interacting case (both in one and two spatial dimensions), where we first derive semi-analytic results within the Hartree-Fock approximation and then we include dynamical quantum correlations by means of DMFT. Specifically, we investigate how the flavor currents are affected by the Hubbard repulsion between particles, spanning the whole range of parameters, from the weak to the strong coupling regimes. We observe that the flavor currents have a sharp increase at the phase transition, and in the "insulating" phase are much larger than in the "metallic" state. We then support our results with more analytic calculations performed in the limit of very strong coupling, where – at integer filling factors and low temperatures – the charge fluctuations are completely quenched, and the only relevant degree of freedom is the flavor state. This provides an intuitive picture to understand the smooth hyperbolic decrease of the flavor currents at increasing values of the interaction.

Finally we consider systems with two orbitals, which are physically realized preparing an admixture of particles in the two low-lying electronic states. The extra component enriches the interaction scheme introducing new interorbital couplings, in particular the spin exchange, a process that swaps the flavor of two particles localized at the same lattice site with opposite orbital indexes. In absence of interorbital coupling, Raman transitions generated by a single pair of laser beams induces a chiral behavior in only one of the two orbitals, leaving the other unaffected. The reason is that, in order to effectively induce nuclear spin flips, the frequencies of the two Raman beams should be nearly resonant to the natural frequency of an electronic transition involving $^3P_1$ (in fact slightly detuned), hence they can't be at the same time resonant to both $^3P_1 \leftrightarrow {}^1S_0$ and $^3P_1 \leftrightarrow {}^3P_0$. This scenario is completely modified by the presence of spin-exchange dynamics, as the latter can induce effective nuclear spin flips also in the orbital that is not interacting with the external photon fields, therefore providing that orbital with a chiral behavior. We apply both the Hartree-Fock method and DMFT to investigate how the spin exchange affects the flavor currents in the two orbitals, also taking into account the possible presence of antiferromagnetic order. Our result is that the flavor currents, in the orbital that does not interact with photons, are sharply enhanced at the critical value of the spin exchange which marks the transition between antiferromagnetic and normal phase. Moreover, we find that these currents are slightly larger than the currents in the other orbital and they both decrease smoothly at large values of the spin exchange.

The second direction that we investigate is within the framework of the quantum simulation of electronic properties in solids by means of ultracold fermionic atoms. In chapter [4] we begin by considering the physics of Hund's metals, i.e. materials (such as transition metal oxides) where the metallic character survives at large values of the Hubbard interaction, as a consequence of the presence of a Hund's coupling, which tends to maximize the local spin and angular momentum. We overview the physics of transition metal oxides, showing how the atomic d orbitals of the metal are modified by the environment of ligands, as described by the *crystal field theory*, which leads to the formulation of the Hund's model. We solve this model by means of an exact numerical diagonalization on a minimal lattice of three sites that includes nearest-neighbors spatial correlations, and draw a phase diagram based on the Drude weight (the DC

component of optical conductivity), which is the most natural candidate to probe the metallic character of a state. We observe the presence of a metallic phase which is resilient to the Hubbard interaction and which results from the competition of two insulating phases with different character: the Hund's metal. We complement previous results obtained with DMFT, where spatial fluctuations were not captured and the quasiparticle weight was used as an indicator of metallicity, finding a very good agreement and thus showing that the DMFT result is robust against the presence of nearest-neighbors quantum correlations.

The quantum simulation of a Hund's metal with ultracold fermions is extremely challenging, due to the difficulty of coherently manipulating atoms in a mixture of three different electronic states, which are necessary to mimic the three t_{2g} orbitals. Nevertheless, the theoretical mechanism underlying the formation of an interaction-resilient metal is quite general: it stems from the energetic competition of two distinct insulating solutions, characterized by Fock states which are connected to each other by hopping processes. We thus propose a model where the ground state is governed by the exact same mechanism, but which is at reach for modern experiments with ultracold alkaline-earth-like fermions. The model describes atoms with $N = 3$ flavors trapped in an optical lattice with an extra superlattice potential that lifts the on-site energy of one lattice site out of three. Again, we numerically solve the model on a minimal cluster of three sites, and we draw the phase diagram based on the Drude weight, discussing similarities and differences with respect to the Hund's physics.

Finally, in chapter [5] we consider the problem of superconductivity in multiorbital systems, which is particularly relevant to provide simple guidelines to understand the high-temperature superconductors (such as the cuprates and the iron-based compounds). These materials are all characterized by multiple degenerate bands around the Fermi level, hence a thorough mathematical description should account for all of them and for all the possible interactions between electrons in different bands. The interplay between so many degrees of freedom is non trivial and, as a matter of fact, a completely satisfactory description of high-temperature superconductors is still lacking. A possible strategy to investigate such a problem is to disentangle the role of the different contributions, considering them one by one. Here we make a little step forward in this direction, considering a system with two superconducting bands described by an attractive Hubbard model and coupled by a *Josephson coupling*, i.e. a local interband hopping of fermionic pairs. We compare a solution obtained within the Hartree-Fock approximation to the numerical solution provided by DMFT, which is exact when the system is on an inifnite-dimensional Bethe lattice. Spanning the whole BCS-BEC crossover, we find that the presence of a Josephson coupling has two distinct effects on the superfluid behavior of the system: in the BCS regime, it enhances the order parameters of both channels; while in the BEC limit it hinders superconductivity, favoring an insulating solution with spatially localized pairs that are delocalized between the bands. While the former effect is predicted within the Hartree-Fock approximation, the latter is not, since it is induced by dynamical quantum correlations.

The recent experimental realizations of the *orbital Feshbach resonance* with alkaline-earth-like atoms opens the door to the possibility of simulating a two-channel BCS-BEC crossover, as the typical energy shift between open and closed channels is much smaller than in typical magnetic Feshbach resonances. Moreover, the spin-exchange dynamics provides a coupling between the two channels and, under a suitable unitary transformation, it becomes a Josephson coupling. Yet, in order to fully describe an orbital Feshbach resonance, we should generalize our model to include other non-negligible interorbital interactions, as well as a "crystal field splitting" between the two bands. We devote the last section to discuss this problem and to set up the correct model and the reasonable approximations, but we leave the numerical investigation as a purpose for future work.

As a final remark, before moving to the first chapter, we briefly explain the style that we use throughout the thesis, which is essentially pedagogical. In contrast with what we usually do in research papers, where

we direct our message to a public of peer experts of the field, here we deliberately try to speak to younger students who are approaching the field with an important preliminary knowledge, but don't necessarily know the specific topics discussed here. On the one hand, this implies that sometimes we go straight to the point, especially when discussing the methods, cutting off an important part of the theoretical background (that the interested reader can always find in the appropriate references), while giving all the relevant information to reproduce the analysis. On the other hand, mostly when we discuss the physical background of the systems under investigation, we provide as many details as possible, at the cost of specifying things that to the expert reader might appear trivial and/or boring. This approach will hopefully help a student avoid wasting precious time desperately browsing papers with a non-entry-level language in order to find relevant pieces of information to fully understand our results.

Chapter 1

Introduction to multicomponent Fermi systems

A multicomponent fermionic system is, in general, a system of interacting particles obeying the Fermi-Dirac statistics, which have several internal degrees of freedom, typically spanning more than the two values associated to the spin $\frac{1}{2}$ that usually characterizes fermionic elementary particles. These internal degrees of freedom can originate from different physical scenarios, for example in solid state systems with multiple degenerate electronic energy bands around the Fermi level, besides the spin states, the electrons have another degree of freedom labeled by the band index. Other remarkable examples are fermionic isotopes of atomic species, which feature a large value of the total angular momentum F (sum of nuclear and electronic angular momenta): in this case the particles have $2F+1$ internal states labeled by the projection of such angular momentum along a given axis. This chapter is mainly devoted to provide an overview of these two specific examples, along with the general description of dynamical mean field theory (DMFT), a theoretical and computational method which has proved successful in dealing with such systems. The chapter is organized as follows: in sec. [1.1] we introduce the most general version of the multiorbital Hubbard model which stems from writing the screened Coulomb interaction in the second quantized form; in sec. [1.2] we introduce the model that describes a mixture of alkaline-earth-like atoms in the two low-lying electronic states and trapped in an optical lattice, along with the resulting SU(N) symmetric local interaction. Finally, sec. [1.3] is devoted to provide a practical guide to dynamical mean field theory.

1.1 Multiorbital Hubbard model in solid state physics

The theoretical description of experimentally observed properties of solids, such as resistivity, specific heat, thermal conductivity etc., within the Born-Oppenheimer approximation, reduces to two problems: the study of interacting electrons moving on a regular lattice of positively charged ions and the study of the dynamics of ions induced by the interaction with electrons. The former problem has been extensively investigated within the framework of quantum mechanics over the past decades, and many important results have been established; however an exhaustive comprehension of the behavior of electrons in solids is still missing, especially when the electrons have multiple components, such as a band index.

For systems of electrons where the states close to the Fermi level originate from the same band, i.e. when all these states stem from the spectral broadening of the same atomic orbital, a qualitatively simple – yet very rich – description of the low temperature physics is provided by the well-known Hubbard

Hamiltonian:

$$H = -t \sum_{\langle ij \rangle, \sigma} \left(c^\dagger_{i\sigma} c_{j\sigma} + \text{h.c.} \right) + U \sum_j n_{j\uparrow} n_{j\downarrow} - \mu \sum_{j,\sigma} n_{j\sigma}. \tag{1.1}$$

This model describes electrons moving on a periodic potential provided by the crystal structure of the atomic nuclei and subject to a screened Coulomb interaction. The second quantized operators $c^\dagger_{i\sigma}$ ($c_{i\sigma}$) create (annihilate) a particle on the i-th lattice site in the spin state σ, and they satisfy the usual fermionic anticommutation rules $\{c_{i\sigma}, c^\dagger_{j\rho}\} = \delta_{ij}\delta_{\sigma\rho}$ and $\{c_{i\sigma}, c_{j\rho}\} = \{c^\dagger_{i\sigma}, c^\dagger_{j\rho}\} = 0$; while the number operators are defined as $n_{j\sigma} = c^\dagger_{j\sigma} c_{j\sigma}$. The first term in eq. [1.1] describes tunneling events of electrons between nearest neighbor sites of the lattice, it stems from the tight binding model and represents the contributions of the kinetic energy and the potential energy of the background. The second term represents the repulsive Coulomb interaction between electrons, and it penalizes the double occupation of any site by an energy amount $U > 0$. The Coulomb interaction, which is a long range interaction in vacuum, is here considered extremely short-ranged (actually purely local) to account for the screening effect due to the presence of other filled bands. Finally, in the last term, μ is the chemical potential used to describe the system within the grand canonical ensemble and it determines the average density of the system. The half filling condition, i.e. the situation where the system contains on average one particle per lattice site, is realized at $\mu = \frac{U}{2}$, for which Hamiltonian [1.1] becomes particle-hole symmetric.

The success of the Hubbard model is mostly due to the possibility to explain the existence of Mott insulators, i.e. materials that should be metals according to standard band theory [4, 5] (which fully neglects the electronic repulsion), but are instead insulators. Remarkable examples of Mott insulators are some transition metal oxides such as MnO [6], VO_2 [7, 8], Cr-doped V_2O_3 [9], etc. Moreover, the Hubbard model is able to describe the *Mott transition*, a phase transition from a metallic to an insulating state which is typically driven by a linear strain of the sample (resulting in a variation of the ratio U/t). Finally, the Hubbard model can be solved exactly in some specific cases, for example via Bethe ansatz when the lattice is a one-dimensional chain [10, 11], or by means of *dynamical mean field theory* (DMFT) in the limit of infinite-dimensional lattices [12] (as we will discuss in sec. [1.3]).

Despite the great success obtained by the Hubbard model, many materials have, according to band theory, electronic states with different band indexes around the Fermi level. Such states arise by the spectral broadening of different degenerate atomic orbitals. For instance, in coordination complexes of transition metals, according to *crystal field theory*, the degeneracy of the five valence d-orbitals of the metal ion can be split in several ways, depending on the geometry of ligands. This mechanism generates a plethora of possible band structures, where the number of degenerate bands at the Fermi level goes from one to five. An accurate mathematical description of such systems should clearly consider all the N_{orb} degenerate bands on equal grounds by including the band index $a = 1, \dots, N_{\text{orb}}$ as an internal electronic degree of freedom. The screened Coulomb interaction now leads to a variety of terms, coupling electrons on the same site with all the possible combinations of band and spin indexes. A generalized version of the Hubbard model to the multiorbital case, known as Hubbard-Kanamori model [13], is described by the Hamiltonian:

$$\begin{aligned} H = &\sum_{\langle ij \rangle, ab, \sigma} t^{ab}_{ij} \left(c^\dagger_{ia\sigma} c_{jb\sigma} + \text{h.c.} \right) - \mu \sum_{ja\sigma} n_{ja\sigma} + \sum_{j,a} U_a n_{ja\uparrow} n_{ja\downarrow} + U' \sum_{j, a\neq b} n_{ja\uparrow} n_{jb\downarrow} \\ &+ U'' \sum_{j, a<b, \sigma} n_{ja\sigma} n_{jb\sigma} + J_{\text{ph}} \sum_{j, a\neq b} c^\dagger_{ja\uparrow} c^\dagger_{ja\downarrow} c_{jb\downarrow} c_{jb\uparrow} + J_{\text{se}} \sum_{j, a\neq b} c^\dagger_{ja\uparrow} c_{ja\downarrow} c^\dagger_{jb\downarrow} c_{jb\uparrow}. \end{aligned} \tag{1.2}$$

In this model, the hopping term is generalized to include the possibility that electrons with different orbital states have different tunneling amplitudes t^{aa}_{ij} and to include orbital hybridization via the off-diagonal

hopping term t_{ij}^{ab} ($a \neq b$). The local interaction contains several terms: an orbital dependent intraorbital density-density interaction of amplitude U_a, an interorbital density-density interaction of amplitude U' for electrons with opposite spins and U'' for electrons with the same spins, a *pair-hopping* interaction of amplitude J_{ph} describing tunneling of electronic pairs from one orbital to another, and finally a *spin-exchange* interaction of amplitude J_{se} describing a simultaneous spin flip of two electrons with opposite spins in different orbitals.

The interplay of so many parameters leads to a rich physics which has not yet been fully explored; however some important results have been established. For example, this model accounts for the existence of the so called *Hund's metals* [14, 15], metallic states that survive at large values of the intraorbital electronic repulsion (we will discuss more extensively this topic in sec. [4.1]), as well as for the orbital selective Mott transition [16]. Moreover, the Hubbard-Kanamori model provides a suitable description of the parent compounds of recently discovered high temperature superconductors, such as the iron-based superconductors, which are characterized by up to five degenerate active bands [17, 18].

1.2 SU(N) symmetric multiorbital Hubbard model in ultracold fermionic atoms

The theoretical importance of the Hubbard-Kanamori model has paved the way to the quantum simulation of similar systems with platforms of ultracold fermionic atoms trapped in optical lattices. The promising perspective provided by ultracold atoms is the flexibility to tune several physical parameters of the system, such as dimensionality, hopping amplitudes, interaction parameters, particle density etc. by exploiting the magneto-optical properties of the atomic species. Although a quantum simulation that perfectly matches the Hamiltonian of a realistic material is extremely challenging, due to many technical difficulties, it is still possible to realize simplified versions of eq. [1.2]. On the one hand, studying a simplified model is still useful to disentangle the effects of all the processes on the equilibrium states of the system; while on the other hand, it opens the possibility to investigate novel quantum states that are not realized in solid state systems.

1.2.1 Atomic properties of alkaline-earth atoms

In this respect, growing attention has been devoted to fermionic isotopes of atoms having the electronic configuration of alkaline-earth elements (with two electrons in the s valence shell), such as ^{87}Sr and ^{173}Yb. The former is an alkaline-earth metal, located in the second group of the periodic table, with an electronic configuration of the ground state given by [Kr]5s^2. The latter is in fact a heavy lanthanide, but the electronic configuration of its ground state, which is [Xe]4f^{14}6s^2, closely resembles that of alkaline-earth elements, featuring two electrons in the valence s shell. In spectroscopic notation, the electronic ground state is $^1S_0 \equiv |g\rangle$, with the two valence electrons in a singlet spin state, vanishing orbital angular momentum and consequently vanishing total angular momentum $J = 0$. The first excited state is $^3P_0 \equiv |e\rangle$, with the electrons forming a triplet state ($S = 1$) and acquiring orbital angular momentum ($L = 1$), while maintaining a vanishing total angular momentum ($J = 0$). The atomic transition $^3P_0 \leftrightarrow {}^1S_0$ doesn't change the total electronic spin, hence it is forbidden by the selection rule $\Delta S \neq 0$. However, $|e\rangle$ is not stable, but rather a long-lived metastable state and it is typically associated to a very narrow spectral line (clock transition). For example, in ^{173}Yb, the lifetime of $|e\rangle$ is ≈ 20 s and the width of the spectral line is 38.5 mHz, which is extremely small compared to typical linewidths of non-clock transitions (hundreds of kHz to few MHz) [19, 20].

The reason behind the finite lifetime of $|e\rangle$ is the presence of a small but significant hyperfine coupling to the nuclear degrees of freedom. This stems from the interaction of electrons with the magnetic field produced by the nucleus, and it is present whenever electrons have non-vanishing spin or orbital angular momentum. This implies that L, S and J are not good quantum numbers or, equivalently, that the state ${}^3P_0$ is no longer an eigenstate of the atomic Hamiltonian when a hyperfine coupling is taken into account. Treating the hyperfine Hamiltonian as a small perturbation and applying perturbation theory at first order, a better approximation of the first excited state is obtained as a superposition of several unperturbed states: $|e\rangle = \alpha|^3P_0\rangle + \beta|^3P_1\rangle + \gamma|^1P_1\rangle$, where $\alpha \gg \beta, \gamma$. Consequently, the presence of an overlap with the electronic state ${}^1P_1$, which is a spin-singlet state, ensures that the selection rule $\Delta S = 0$ can be respected and makes the transition possible. In spite of the finite lifetime, the state $|e\rangle$ remains stable for a sufficiently long time to perform measurements of the equilibrium properties. Therefore, it is possible to prepare a stable mixture of atoms in the two states $|g\rangle$ and $|e\rangle$, identifying these states as orbital degrees of freedom of the particles.

On the other hand, the "spin" degrees of freedom are provided by the internal states of the nucleus, which are labeled by the projection along the z axis of the total nuclear angular momentum I_z. The important difference with respect to electrons on a solid is that the nuclear angular momentum is typically very large, for example $I = \frac{5}{2}$ for ^{173}Yb and $I = \frac{9}{2}$ for ^{87}Sr, so there are in principle $2I + 1 = 6$ nuclear states in the former case and $2I + 1 = 10$ in the latter. These numbers are clearly much larger than the 2 spin states of electrons; however it is possible to prepare the system in a mixture of nuclear states which are a subset of the whole manifold and, as we will discuss below, the number of particles in each state will not change upon interactions. Therefore it is possible to restrict the dynamics to an arbitrary subset of nuclear states and in particular to only 2 nuclear states, thus mimicking the electron spin. However, the large nuclear angular momentum provides a way to explore multiorbital fermionic systems with more than 2 internal states, opening interesting scenarios for the quantum simulation of more exotic quantum states.

In order to describe the interaction between particles, we consider only two-body collisions and neglect collisions involving a larger number of particles, which typically occur with lower probability. The two-particle wave function is a tensor product of a spatial part, an orbital part (describing the electronic state) and a "spin" part (describing the nuclear state) and because the atoms are fermions, it is overall anti-symmetric with respect to particle exchange. We consider two arbitrary nuclear states and label them with $|\uparrow\rangle$ and $|\downarrow\rangle$; moreover we observe that the probability of a contact collision is significantly enhanced when the spatial part of the wave function $\psi(\mathbf{r}_1 - \mathbf{r}_2)$ is symmetric, as there is a non vanishing probability to observe the two particles in the same position. This limits the relevant scattering channels to those with an orbital triplet and a spin singlet (first row), or with an orbital singlet and a spin triplet (second row) [21]:

$$|gg\rangle \otimes \frac{|\uparrow\downarrow\rangle - |\downarrow\uparrow\rangle}{\sqrt{2}} \otimes \psi(\mathbf{r}_1 - \mathbf{r}_2); \qquad |ee\rangle \otimes \frac{|\uparrow\downarrow\rangle - |\downarrow\uparrow\rangle}{\sqrt{2}} \otimes \psi(\mathbf{r}_1 - \mathbf{r}_2); \qquad \frac{|ge\rangle + |eg\rangle}{\sqrt{2}} \otimes \frac{|\uparrow\downarrow\rangle - |\downarrow\uparrow\rangle}{\sqrt{2}} \otimes \psi(\mathbf{r}_1 - \mathbf{r}_2);$$
$$\frac{|ge\rangle - |eg\rangle}{\sqrt{2}} \otimes |\uparrow\uparrow\rangle \otimes \psi(\mathbf{r}_1 - \mathbf{r}_2); \qquad \frac{|ge\rangle - |eg\rangle}{\sqrt{2}} \otimes |\downarrow\downarrow\rangle \otimes \psi(\mathbf{r}_1 - \mathbf{r}_2); \qquad \frac{|ge\rangle - |eg\rangle}{\sqrt{2}} \otimes \frac{|\uparrow\downarrow\rangle + |\downarrow\uparrow\rangle}{\sqrt{2}} \otimes \psi(\mathbf{r}_1 - \mathbf{r}_2). \tag{1.3}$$

Two-body collisions between neutral atoms at low energy are described by scattering theory [22], and are characterized by the s-wave scattering length, which depends on the "collisional channel", i.e. on the specific two-body state of the colliding particles. More precisely, in alkaline-earth like atoms, the scattering length only depends on the electronic component of the state, but it is (almost) perfectly independent on the nuclear component. This is a consequence of the nearly vanishing hyperfine interaction, which ensures an almost perfect decoupling between electronic and nuclear degrees of freedom: since only the electronic

cloud is involved in a collision, the nuclear state of the two colliding particles does not affect the scattering length. In conclusion, there are only four independent scattering lengths: a_{gg}, a_{ee}, a_{eg^+}, a_{eg^-}, associated respectively to the orbital states $|gg\rangle$, $|ee\rangle$, $(|ge\rangle + |eg\rangle)/\sqrt{2}$ and $(|ge\rangle - |eg\rangle)/\sqrt{2}$. As we will discuss below, this property is the physical origin of the SU(N) symmetry (where $N \leq 2I+1$) of the resulting interaction Hamiltonian and, remarkably, it is specific of alkaline-earth like atoms. The differential scattering lengths δa, obtained when the particles are prepared in all the possible combinations of nuclear states, have been estimated for ^{87}Sr in [23]. The result is a nearly perfect independence when the two colliding particles are in the electronic ground state with no hyperfine interaction: $\delta a_{gg} \approx 10^{-9} a_{gg}$; while the independence is less robust when at least one of the particles is in the electronic excited state and there is indeed a weak hyperfine interaction: $\delta a_{ee} \approx 10^{-3} a_{ee}$ and $\delta a_{ge^\pm} \approx 10^{-3} a_{ge^\pm}$.

An important issue related to the scattering properties of alkaline-earth atoms which is worth mentioning is the problem of losses. When both colliding particles populate the excited electronic state, there is a significant probability of inelastic scattering, i.e. that they decay in the ground state, converting their potential energy into kinetic energy and escaping from the magneto-optical trap. Mathematically, this reflects in a relatively large imaginary part of the scattering length a_{ee}, which can be of the same order of magnitude as the real part. This mechanism drives the system out of thermal equilibrium, resulting in a more challenging theoretical description and in a defective quantum simulation of solid state systems. The problem of losses can be diminished by reducing the density of particles populating the $|e\rangle$ state, in order to reduce the average number of collisions resulting in a loss. Alternatively, a better solution would be to use a mixture of two different atomic species, both of them in their electronic ground state, rather than using a single species in a mixture of ground and metastable electronic states. On the one hand, this would completely avoid particle losses and would strengthen the SU(N) symmetry, as no hyperfine coupling would be present whatsoever; but on the other hand it would be experimentally more challenging to deal with the simultaneous cooling and optical confinement of two different species having different atomic properties (such as mass, polarizability, natural frequencies of optical transitions etc.). Furthermore, the fact that two particles are now distinguishable, reduces the number of independent scattering lengths to three (for the three channels $|gg\rangle$, $|ee\rangle$ and $|ge\rangle$) and results in $a_{ge^+} = a_{ge^-}$. As we will discuss below, this results in the absence of a spin exchange coupling, enhancing the symmetry of the resulting Hamiltonian, but excluding the possibility to observe interesting phenomena such as the orbital Feshbach resonance [24, 25] that we briefly introduce in sec. [5.3], and the multiorbital chirality discussed in sec. [3.5].

1.2.2 SU(N) symmetric multiorbital Hubbard model and its symmetries

In this section, we introduce an Hamiltonian model to describe a mixture of $|g\rangle$ and $|e\rangle$ alkaline-earth like atoms on an optical lattice with two-body interactions determined by the four scattering lengths introduced above. The two-body interaction potential is a function of the relative atomic coordinate $\mathbf{r} = \mathbf{r}_1 - \mathbf{r}_2$ and typically it has a spherical symmetry. The specific functional form $V(r)$ is well approximated by the Lennard-Jones function: it is weakly attractive at long distances, and strongly repulsive at short distances, comparable to the atomic radius r_0. However, the asymptotic two-body wave function at $r \gg r_0$ is only determined by the s-wave scattering length in that specific two-body interaction channel $|X\rangle$, and it does not depend on the specific functional form of the interaction potential, as long as it provides the correct scattering length. Therefore, a typical choice to simplify the calculations is to assume a zero-range contact interaction potential proportional to the Dirac delta function $\delta(\mathbf{r})$ with a suitable prefactor:

$$V(r) = \sum_{X=gg,\, ee,\, eg^+,\, eg^-} \frac{4\pi\hbar^2 a_X}{m} \delta(\mathbf{r}) \, |X\rangle \langle X| \,, \tag{1.4}$$

where m is the atomic mass and $|X\rangle\langle X|$ is the projector onto the state with orbital part labeled by X. The presence of a Dirac delta function can lead to a singular behavior of the wave function, hence we stress that this is not the only possible choice and in some cases it is useful to use a regular potential, for instance a finite potential well. Another common way to regularize eq. [1.4] is to multiply the delta function by $\frac{\partial}{\partial r}(r\cdot)$ when the potential operator is applied to a state: this is known as Lee-Huang-Yang pseudopotential. We will make use of this regularization in sec. [5.3].

From eq. [1.4], after observing that the labels $\uparrow, \downarrow$ can be extended to any pair of nuclear states, we can readily obtain the second-quantized version of the Hamiltonian following standard prescriptions [23, 26]:

$$H = -\sum_{\langle ij\rangle,\, a,\, \sigma} t_{ij}^{aa}\left(c_{ia\sigma}^\dagger c_{ja\sigma} + \text{h.c.}\right) - \mu\sum_{j,a,\sigma} n_{ja\sigma} + \sum_{j,\,a}\frac{U_a}{2} n_{ja}(n_{ja}-1) + V\sum_{j,\,a\neq b,\,\sigma>\rho} n_{ja\sigma}n_{jb\rho} + (V - V_{\text{ex}})\sum_{j,\,a<b,\,\sigma} n_{ja\sigma}n_{jb\sigma} - V_{\text{ex}}\sum_{j,\,a\neq b,\,\sigma>\rho} c_{ja\sigma}^\dagger c_{ja\rho}\, c_{jb\rho}^\dagger c_{jb\sigma}. \tag{1.5}$$

Considering only two nuclear states, this is a specific version of the Hubbard-Kanamori model [1.2] for a system with two orbitals, where the interorbital interaction is described by only two parameters (V and V_{ex}) instead of four; in particular we have the identification $U' = V$, $U'' = V - V_{\text{ex}}$, $J_{\text{ph}} = 0$ and $J_{\text{se}} = -V_{\text{ex}}$. Moreover, the hopping matrix t_{ij}^{ab} is diagonal in the orbital index, as there is no hybridization between the band structures of $|g\rangle$ and $|e\rangle$. All the parameters in eq. [1.5] can be written in terms of the four scattering lengths and of Wannier functions $w_a(\mathbf{r})$ associated to the orbital-dependent potential $V_a(\mathbf{r})$ of the optical lattice:

$$t_{ij}^{aa} = \int d^3r\, w_a(\mathbf{r})\left[-\frac{\hbar^2}{2m}\nabla_{\mathbf{r}}^2 + V_a(\mathbf{r})\right] w_a(\mathbf{r}-\mathbf{R}_{ij}),$$

$$U_{gg} = \frac{4\pi\hbar^2 a_{gg}}{m}\int d^3r\,|w_g(\mathbf{r})|^4, \qquad U_{ee} = \frac{4\pi\hbar^2 a_{ee}}{m}\int d^3r\,|w_e(\mathbf{r})|^4, \tag{1.6}$$

$$V = \frac{4\pi\hbar^2}{m}\frac{a_{eg^+} + a_{eg^-}}{2}\int d^3r\,|w_g(\mathbf{r})|^2|w_e(\mathbf{r})|^2, \qquad V_{\text{ex}} = \frac{4\pi\hbar^2}{m}\frac{a_{eg^+} - a_{eg^-}}{2}\int d^3r\,|w_g(\mathbf{r})|^2|w_e(\mathbf{r})|^2,$$

where $\mathbf{R}_{ij}$ is the lattice vector connecting site i and site j.

The peculiar feature of this model is that the number of fermionic "spin" states N is not limited to 2, but it can be as large as $2I+1$. Moreover, the SU(2) spin symmetry of the Hubbard-Kanamori model is enhanced to a SU(N) "flavor" symmetry, which can be formally proved by introducing a set of generators

$$S_{\sigma\rho} = \sum_{j,a} c_{ja\sigma}^\dagger c_{ja\rho} \tag{1.7}$$

and showing that the Hamiltonian [1.5] commutes with all of them: $[S_{\sigma\rho},\, H] = 0$. More precisely, the operators $S_{\sigma\rho}$ are a set of N^2 operators, while the generators of SU(N) are only N^2-1. The reason is that these are in fact the generators of U(1)×SU(N), where the U(1) symmetry stems from the conservation of the total number of particles. This can be easily seen by observing that $\sum_\sigma S_{\sigma\sigma}$, which, being a linear combination of the generators, is an element of the corresponding Lie algebra, is the total number operator. The structure constants of the Lie algebra $\mathfrak{u}(1)\oplus\mathfrak{su}(N)$ can be extracted from the commutation relations of $S_{\sigma\rho}$:

$$[S_{\alpha\beta},\, S_{\gamma\delta}] = \delta_{\beta\gamma}S_{\alpha\delta} - \delta_{\alpha\delta}S_{\gamma\beta}. \tag{1.8}$$

We observe that the operators $S_{\sigma\sigma} \equiv N_\sigma$ represent the total number of particles with a given flavor σ, which are conserved quantities as a result of the symmetry. In particular, if the system is prepared in a

state with $N_\sigma = 0$ for a specific σ, then the state σ will never be populated by atomic collisions. Therefore, at least in principle, the number of active flavors N can be tuned arbitrarily by depleting the population of the remaining nuclear states, the upper bound being the number of nuclear states $2I + 1$.

Remarkably, the Hamiltonian [1.5] has a more structured symmetry U(1)×U(1)×SU(N), as it commutes with the total number of particles populating the state $|g\rangle$ (N_g) and the state $|e\rangle$ (N_e), so the total number of particles per orbital is a conserved quantity: $[N_g,\, H] = [N_e, H] = 0$. However we emphasize that this is true only as long as losses in the $|e\rangle$ channel can be neglected. This symmetry is particularly useful in practice as it can be exploited to greatly simplify the computational cost of several numerical methods, such as exact diagonalization and dynamical mean field theory (see sec. [1.3.2]).

1.3 Dynamical mean field theory: an overview

One of the most successful and well established methods to study quantum interacting systems on a lattice is the *dynamical mean field theory* (DMFT) [27]. The great success of DMFT has several motivations. First of all, it is an unbiased method to investigate interacting systems, namely it is not based on perturbation theory, so it does not imply any assumption on the values of the interaction parameters; in fact it is exact in two opposite regimes of parameters: the non-interacting limit ($U = U' = U'' = J_{\text{p.h.}} = J_{\text{s.e.}} = 0$) and the atomic limit ($t_{ij}^{ab} = 0$). Secondly, DMFT provides exact equations when the lattice geometry of the system is infinite dimensional: this situation, which at first glance could appear unphysical, turns out sufficient to reasonably describe three-dimensional systems, avoiding complications due to the details of the lattice. Moreover, it is a very flexible tool that can be generalized to investigate different physical scenarios, including states with spontaneously broken symmetries (such as superconductors, magnetic systems and excitonic insulators [28]), interacting bosons (also out of equilibrium [29]), fermions coupled to bosonic modes (also with multiple orbitals [30]), systems in mesoscopic non-periodic structures such as "carbon nanoflakes" [31] and many more. Finally, over the last two decades, several limitations of the "standard" formulation of DMFT have been overcome by suitable extensions of the method, including real space DMFT (see sec. 1.3.4), dynamical cluster approximation (DCA+DMFT) [32], cluster DMFT [33, 34, 35, 36], out of equilibrium DMFT [37, 38, 39].

The purpose of this section is not to give an exhaustive review of the theoretical framework behind DMFT, that the interested reader can find in ref. [27], but rather to give a practical guide to the implementation of the method and to discuss its strengths and limitations. In this spirit, here we follow a different path with respect to the classical way of presenting the topic: since the heart of DMFT is a mapping of the original lattice problem onto a suitably generalized Anderson impurity problem, whose parameters should be determined self-consistently, we begin by discussing the generalized Anderson impurity model and showing numerical methods to solve it, and we explain the self-consistent relation to the original lattice problem afterwards. After that, we introduce real-space DMFT, a generalized version of the method which accounts for the lack of translation invariance in the system and that we will use in sec. [3.5]. Finally, we discuss some tricks on how to compute some of the most relevant observables for the present work.

1.3.1 The Anderson impurity model

The Anderson impurity model describes a magnetic impurity hybridized with a Fermi sea, and it has been originally proposed by Philip Warren Anderson to explain the Kondo effect [40]. The model describes a single site $\ell = 0$ (impurity) with on-site energy ε_0 embedded in a bath of states labeled by $\ell = 1, \dots, N_{\text{bath}}$

with energy ε_ℓ. When two fermions with opposite spins are in the impurity site, they experience a Hubbard repulsive interaction of strength U, while they do not interact in the bath. The impurity and the bath are hybridized, in the sense that fermions can hop from the impurity to any state of the bath with hopping amplitude V_ℓ. Remarkably, there is no underlying geometrical structure. The Anderson impurity model is thus described by the following Hamiltonian:

$$H_{\text{AIM}} = \sum_{\ell=1}^{N_{\text{bath}}} \sum_{\sigma=\uparrow\downarrow} \varepsilon_k c^\dagger_{\ell\sigma} c_{\ell\sigma} + \sum_{k=1}^{N_{\text{bath}}} \sum_{\sigma=\uparrow\downarrow} \left(V_\ell c^\dagger_{\ell\sigma} c_{0\sigma} + \text{h.c.} \right) + U n_{0\uparrow} n_{0\downarrow} + (\varepsilon_0 - \mu) n_0. \tag{1.9}$$

Although this model contains a very rich physics, we will limit the discussion to the features which are more relevant for DMFT, in particular we want to compute the impurity component of the Green function. In the non-interacting case ($U = 0$), we can easily find an analytic expression for the latter quantity: organizing the fermionic operators on the spinor $\Psi^\dagger_\sigma = (c^\dagger_{0\sigma}, c^\dagger_{1\sigma}, \dots, c^\dagger_{N_{\text{bath}}\sigma})$, the non-interacting part of [1.9] can be recast in the matrix notation

$$H_{\text{AIM}} = \sum_\sigma \Psi^\dagger_\sigma \hat{H} \Psi_\sigma, \qquad \hat{H} = \begin{pmatrix} \varepsilon_0 - \mu & V_1 & V_2 & \dots \\ V_1^* & \varepsilon_1 & 0 & \dots \\ V_2^* & 0 & \varepsilon_2 & \dots \\ \vdots & \vdots & \vdots & \ddots \end{pmatrix} \qquad (U = 0). \tag{1.10}$$

The full Green function is given by the resolvent operator $\hat{\mathcal{G}}(z) = (z - \hat{H})^{-1}$, which has $(N_{\text{bath}} + 1)^2$ components $\mathcal{G}_{\ell,p}(z)$ organized in the matrix structure

$$\hat{\mathcal{G}}(z) = \begin{pmatrix} \mathcal{G}_{0,0}(z) & \mathcal{G}_{0,1}(z) & \mathcal{G}_{0,2}(z) & \dots \\ \mathcal{G}_{1,0}(z) & \mathcal{G}_{1,1}(z) & \mathcal{G}_{1,2}(z) & \dots \\ \mathcal{G}_{2,0}(z) & \mathcal{G}_{2,1}(z) & \mathcal{G}_{2,2}(z) & \dots \\ \vdots & \vdots & \vdots & \ddots \end{pmatrix}. \tag{1.11}$$

To compute the impurity Green function $\mathcal{G}_{0,0}(z)$ we can explicitly write some components of the defining equation $(z - \hat{H})\hat{\mathcal{G}} = \mathbb{1}$:

$$\begin{aligned} &(z - \varepsilon_0 + \mu)\mathcal{G}_{0,0} + \sum_\ell V_\ell \mathcal{G}_{\ell,0} = 1 \qquad && \text{component } (0,0) \\ &V_\ell^* \mathcal{G}_{0,0} + (z - \varepsilon_\ell)\mathcal{G}_{\ell,0} = 0 && \text{component } (\ell > 0,\, 0) \end{aligned} \tag{1.12}$$

and solve the set of coupled equations for $\mathcal{G}_{0,0}$:

$$\mathcal{G}^{-1}_{0,0}(z) = z - \varepsilon_0 + \mu - \sum_{\ell=1}^{N_{\text{bath}}} \frac{|V_\ell|^2}{z - \varepsilon_\ell}. \tag{1.13}$$

So far we have discussed the conventional version of the Anderson impurity model, with SU(2) spin symmetry and no orbital degrees of freedom; however, to implement DMFT in the context of multicomponent Fermi systems such as [1.2] and [1.5], we need a generalized version of the model. We will keep the discussion as general as possible, to include effects due to explicit breaking of the SU(N) symmetry (chapter [3]) or superconducting order (chapter [5]). A multicomponent Anderson impurity model can be simply written by introducing a set of impurity and bath spinors Ψ_ℓ that include the flavor

and orbital degrees of freedom. The structure of Ψ_ℓ in terms of fermionic operators depends on the specific physical problem under investigation (e.g. it depends on the number of flavors and orbitals, on the presence of superconducting order etc.). For example, the suitable spinor for a system with two flavor states $\sigma = \uparrow, \downarrow$, two orbitals g, e and no superconducting order could be $\Psi_k^\dagger = (c_{\ell g\uparrow}^\dagger,\, c_{\ell g\downarrow}^\dagger,\, c_{\ell e\uparrow}^\dagger,\, c_{\ell e\downarrow}^\dagger)$. The general structure of the multi-component Anderson impurity model reads:

$$H_{\text{AIM}} = \sum_{\ell=1}^{N_{\text{bath}}} \Psi_\ell^\dagger \hat{\varepsilon}_\ell \Psi_\ell + \sum_{\ell=1}^{N_{\text{bath}}} \left(\Psi_\ell^\dagger \hat{V}_\ell \Psi_0 + \text{h.c.} \right) + \Psi_0^\dagger \hat{\varepsilon}_0 \Psi_0 + H_{\text{int}}, \tag{1.14}$$

where now $\hat{\varepsilon}_\ell$ and $\hat{V}_\ell$ are square matrices of dimension $N \cdot N_{\text{orb}}$, the chemical potential is absorbed in the definition of $\hat{\varepsilon}_0$ and H_{int} is the interaction Hamiltonian on the impurity site, which coincides with the local interaction Hamiltonian of the original lattice problem.

The impurity Green function can be readily computed in the non-interacting case $H_{\text{int}} = 0$ by introducing the spinor $\Psi^\dagger = (\Psi_0^\dagger,\, \Psi_1^\dagger,\, \Psi_2^\dagger,\, \dots)$ and recasting the problem in matrix notation

$$H_{\text{AIM}} = \Psi^\dagger \hat{H} \Psi, \qquad \hat{H} = \begin{pmatrix} \hat{\varepsilon}_0 & \hat{V}_1 & \hat{V}_2 & \dots \\ \hat{V}_1^\dagger & \hat{\varepsilon}_1 & 0 & \dots \\ \hat{V}_2^\dagger & 0 & \hat{\varepsilon}_2 & \dots \\ \vdots & \vdots & \vdots & \ddots \end{pmatrix} \qquad (H_{\text{int}} = 0). \tag{1.15}$$

The resolvent operator $\hat{\mathcal{G}}(z)$ now has a block structure, with $(N_{\text{bath}}+1)^2$ blocks $\hat{\mathcal{G}}_{\ell,p}(z)$, each of them having dimension $N \cdot N_{\text{orb}}$, and the impurity part can be obtained by solving the defining equation $(z\mathbb{1} - \hat{H})\hat{\mathcal{G}} = \mathbb{1}$, which now leads the coupled matrix equations:

$$\begin{aligned} (z - \hat{\varepsilon}_0)\hat{\mathcal{G}}_{0,0} + \sum_\ell \hat{V}_\ell \hat{\mathcal{G}}_{\ell,0} &= 1 \\ \hat{V}_\ell^\dagger \hat{\mathcal{G}}_{0,0} + (z - \hat{\varepsilon}_\ell)\hat{\mathcal{G}}_{\ell,0} &= 0. \end{aligned} \tag{1.16}$$

The solution for the inverse impurity Green function reads

$$\hat{\mathcal{G}}_{0,0}(z)^{-1} = z - \hat{\varepsilon}_0 - \sum_{\ell=1}^{N_{\text{bath}}} \hat{V}_\ell^\dagger \left(z - \hat{\varepsilon}_\ell\right)^{-1} \hat{V}_\ell. \tag{1.17}$$

In the following, we will mostly need the impurity Green function (instead of the full Green function), so for the sake of simplicity we will drop the subscripts and adopt a slight abuse of notation, referring to it with $\hat{\mathcal{G}}$ instead of $\hat{\mathcal{G}}_{0,0}$.

1.3.2 Exact diagonalization and the Lanczos method

The problem of computing the impurity Green function becomes dramatically more complicated in the presence of interactions. In this case, we could either apply analytic methods introducing some approximations (e.g. the Hartree-Fock mean field approximation [41]), or switch to numerical methods. Among the latter, a good candidate is the exact numerical diagonalization (ED), which amounts to write the Hamiltonian matrix in the basis of Fock states and find out the whole spectrum of eigenvalues E_n

and corresponding eigenvectors $|n\rangle$, from which any observable can be computed. In particular, we can compute the impurity Green function via the Lehmann representation [42]:

$$G_{\alpha\beta}(z) = \frac{1}{\mathcal{Z}} \sum_{m,n} \frac{\langle n|\Psi_{0\alpha}|m\rangle\langle m|\Psi_{0\beta}^\dagger|n\rangle}{z - E_m + E_n} \left(e^{-\beta E_m} + e^{-\beta E_n}\right), \tag{1.18}$$

where $\beta = 1/T$ is the inverse temperature[1] and $\mathcal{Z} = \sum_n e^{-\beta E_n}$ is the partition function. However, the dimension of the Hilbert space is $2^{N\cdot N_{\text{orb}}\cdot(1+N_{\text{bath}})}$, which is exponentially increasing with the number of fermionic components and bath sites. This is a significant drawback of the method, as the computational cost is huge even with a relatively small number of components.

A first improvement can be obtained by exploiting the symmetries of the Hamiltonian: if $\mathcal{Q}_i$ is a set of symmetry operators such that $[\mathcal{Q}_i,\, H_{\text{AIM}}] = 0$ and $[\mathcal{Q}_i,\, \mathcal{Q}_j] = 0\ \forall ij$, then every $\mathcal{Q}_i$ and H_{AIM} have the same eigenstates. This means that, if we write the Hamiltonian matrix in a basis that diagonalizes the set $\mathcal{Q}_i$, then it will be block-diagonal, and each block will be labeled by specific eigenvalues of the symmetry operators $\{q_1,\, q_2,\, \dots\}$. Every Hilbert subspace spanned by the eigenstates of the symmetry operators with a given list of eigenvalues is called a *sector*; the "sectorization" process is sketched in fig. [1.1]. Remarkably, we only expect the Hamiltonian matrix to be block-diagonal (not fully diagonal) because every sector has in general a large dimension: on the one hand this simplifies the choice of a basis set; on the other hand it is very unlikely that the chosen basis diagonalizes the Hamiltonian. For example, if the Hamiltonian commutes with the total number of particles, then we can group the Fock states in sectors with 0 particles, 1 particle, 2 particles, etc. The sector with 0 particles contains just the completely empty state; while for example the sector with 1 particle contains all the possible Fock states where the particle is accommodated in any of the bath states or in the impurity site. The problem of diagonalizing a very large matrix is thus reduced to the problem of diagonalizing a set of matrices with smaller sizes, with significant improvements in the computational cost; however the blocks can still be very large (even for small systems), and the full diagonalization is still numerically challenging.

A massive improvement of the computational cost is possible if we work at a very low temperature, where we can only compute a few eigenstates of the Hamiltonian instead of the full spectrum, since there are several numerical methods that allow to compute very efficiently a small set of the largest/smallest eigenvalues of a given hermitian matrix.[2] A remarkable example is the Lanczos method [43, 44, 45]. The idea behind this method is to minimize the energy functional $E[\Phi] = \langle\Phi|H|\Phi\rangle/\langle\Phi|\Phi\rangle$ over the space of states $|\Phi\rangle$. Starting from a random point Φ_0 in the space of states, we need to find the direction Φ_1 where the functional decreases most rapidly, which is given by the negative gradient evaluated at $|\Phi_0\rangle$:

$$|\Phi_1\rangle = -\frac{\partial E[\Phi]}{\partial\langle\Phi|}\bigg|_{\Phi_0} = \frac{E[\Phi_0]|\Phi_0\rangle - H|\Phi_0\rangle}{\langle\Phi_0|\Phi_0\rangle}.$$

The functional will thus decrease along the line $\Phi_0 + \alpha\Phi_1$, at least for small values of the free parameter α, so we can now minimize $E[\Phi_0 + \alpha\Phi_1]$ with respect to α. This problem boils down to find a normalized vector $|v\rangle$ in the *Krylov* subspace $\text{span}(|\Phi_0\rangle,\, |\Phi_1\rangle) \equiv \text{span}(|\Phi_0\rangle, H|\Phi_0\rangle)$ that minimizes $\langle v|H|v\rangle$. If now we find an orthornormal basis $\{|v_0\rangle,\, |v_1\rangle\}$ of the Krylov subspace via a Gram-Schmidt procedure (where $|v_0\rangle$ is just the normalized version of $|\Phi_0\rangle$), the Hamiltonian projected in the Krylov subspace and written in this

[1] Here we are following the most widespread convention of working in natural units $k_B = \hbar = 1$. Units of the international system can be reintroduced by mapping $T \to k_B T$ and (later) $\omega_n \to \hbar\omega_n$.

[2] We can only evaluate many-body eigenstates having a Boltzmann weight $e^{-\beta(E_n - E_0)}$ larger than an arbitrary threshold: as the temperature approaches $T = 0$, the number of eigenvalues to be computed decreases significantly.

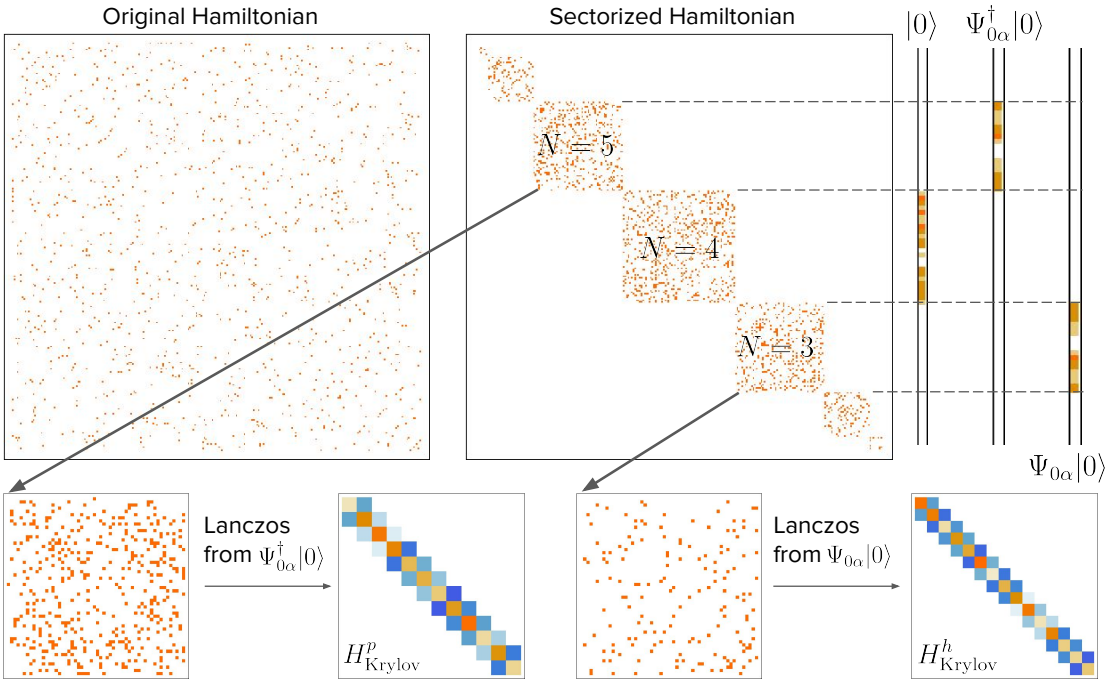

Figure 1.1: The top row shows a matrix plot of the "sectorization" process. The Hamiltonian matrix written in the original randomly chosen basis does not have any particular structure, but when written in terms of eigenstates of a symmetry operator (in this case the total number of particles N), it is block-diagonal, and each block is labeled by a specific eigenvalue of N. The ground state $|0\rangle$ has non-zero components only on a specific sector ($N = 4$ in this example). The bottom row sketches the Lanczos procedure to compute the Green function: $\Psi^\dagger_{0\alpha}|0\rangle$ and $\Psi_{0\alpha}|0\rangle$ are vectors with components in the sectors with one more and one less particle respectively and are used as starting vectors for the Lanczos method to obtain the corresponding Krylov Hamiltonians.

basis will take the form

$$H_{\text{Krylov}} = \begin{pmatrix} a_0 & b_1 \\ b_1 & a_1 \end{pmatrix}, \qquad a_0 = \langle v_0|H|v_0\rangle, \qquad a_1 = \langle v_1|H|v_1\rangle, \qquad b_1 = \langle v_1|H|v_0\rangle. \tag{1.19}$$

The smallest eigenvalue of H_{Krylov} represents the value of the energy functional at the new point (i.e. an estimate of the ground state energy), and the associated eigenvector (α_0, α_1) multiplied by the orthonormal basis $\alpha_0|v_0\rangle+\alpha_1|v_1\rangle$ gives the searched vector $|v\rangle$ (i.e. an estimate of the ground state of H). This procedure can now be iterated starting from $|v\rangle$ and repeated several times until convergence. Alternatively, observing that at the n-th iteration the "optimal" vector lies in the Krylov subspace span$(|v_0\rangle, H|v_0\rangle, \ldots, H^n|v_0\rangle)$, we can apply the Gram-Schmidt procedure to this space, finding an orthonormal basis $\{|v_0\rangle, |v_1\rangle, \ldots, |v_n\rangle\}$ and the projected Hamiltonian in this basis takes the $n \times n$ dimensional tridiagonal form

$$H_{\text{Krylov}} = \begin{pmatrix} a_0 & b_1 & 0 & 0 & \ldots \\ b_1 & a_1 & b_2 & 0 & \ldots \\ 0 & b_2 & a_2 & b_3 & \ldots \\ 0 & 0 & b_3 & a_3 & \ldots \\ \vdots & \vdots & \vdots & \vdots & \ddots \end{pmatrix}, \qquad a_k = \langle v_k|H|v_k\rangle, \qquad b_k = \langle v_k|H|v_{k-1}\rangle. \tag{1.20}$$

Once again, the smallest eigenvalue of H_{Krylov} is the estimate of the ground state energy, and the corresponding eigenvector $(\alpha_0, \alpha_1, \ldots, \alpha_n)$ provides the list of coefficients for the estimated ground state vector $\sum_{k=0}^{n} \alpha_k |v_k\rangle$. The procedure should again be repeated increasing n until convergence; however the convergence is typically obtained for n much smaller than the size of H [44].

When the system is at zero temperature ($T = 0$), the calculation of static observables only requires the ground state of H (including possible degeneracies) that we can obtain via the Lanczos algorithm, considerably speeding up the exact diagonalization. However, computing dynamical response functions such as the Green function, still requires in principle the whole spectrum: when $T = 0$, the Lehmann representation in eq. [1.18] reduces to

$$G_{\alpha\beta}(z) = \sum_n \frac{\langle 0|\Psi_{0\beta}^\dagger|n\rangle\langle n|\Psi_{0\alpha}|0\rangle}{z + E_n - E_0} + \sum_n \frac{\langle 0|\Psi_{0\alpha}|n\rangle\langle n|\Psi_{0\beta}^\dagger|0\rangle}{z - E_n + E_0}, \tag{1.21}$$

which still contains the full spectrum E_n and $|n\rangle$. However, it is still possible to avoid the full diagonalization while getting a convergent Green function by using two more runs of the Lanczos method [44, 46]. Considering at first the diagonal components $G_{\alpha\alpha}(z)$, we can recast eq. [1.21] as

$$G_{\alpha\alpha}(z) = \langle 0|\Psi_{0\alpha}^\dagger \frac{1}{z + H - E_0} \Psi_{0\alpha}|0\rangle + \langle 0|\Psi_{0\alpha} \frac{1}{z - H + E_0} \Psi_{0\alpha}^\dagger|0\rangle. \tag{1.22}$$

As illustrated in fig. [1.1], the two terms in eq. [1.22] can be computed starting two Lanczos runs from the vectors $\Psi_{0\alpha}|0\rangle$ and $\Psi_{0\alpha}^\dagger|0\rangle$ respectively, obtaining the Krylov Hamiltonian blocks H^h_{Krylov} and H^p_{Krylov} of the corresponding sectors. We can now approximate eq. [1.22] using the Krylov matrices instead of the Hamiltonian blocks:

$$\begin{aligned} G_{\alpha\alpha}(z) &\approx \langle 0|\Psi_{0\alpha}^\dagger \frac{1}{z + H^h_{\text{Krylov}} - E_0} \Psi_{0\alpha}|0\rangle + \langle 0|\Psi_{0\alpha} \frac{1}{z - H^p_{\text{Krylov}} + E_0} \Psi_{0\alpha}^\dagger|0\rangle \\ &= \langle 0|\Psi_{0\alpha}^\dagger \Psi_{0\alpha}|0\rangle \left[z + H^h_{\text{Krylov}} - E_0\right]^{-1}\Big|_{(1,1)} + \langle 0|\Psi_{0\alpha} \Psi_{0\alpha}^\dagger|0\rangle \left[z - H^p_{\text{Krylov}} + E_0\right]^{-1}\Big|_{(1,1)} \end{aligned} \tag{1.23}$$

where we take the top-left $(1,1)$ components of the inverse matrices because, by construction, upon normalization $\Psi_{0\alpha}|0\rangle$ and $\Psi_{0\alpha}^\dagger|0\rangle$ are the first vectors of the basis of the respective Krylov subspaces.

This method is not suitable to compute off-diagonal components of $G_{\alpha\beta}(z)$, as the vector $\Psi_{0\beta}|0\rangle$ is not necessarily an element of the basis of the Krylov subspace constructed from $\Psi_{0\alpha}|0\rangle$, which implies that e.g. $\langle 0|\Psi_{0\beta}^\dagger[z + H^h_{\text{Krylov}} - E_0]^{-1}\Psi_{0\alpha}|0\rangle$ does not correspond to a specific element of the inverse. In turn, this means that we need to evaluate the full inverse matrix, instead of a single element, with a considerable increase in computational cost. A smart method to avoid the full evaluation of the inverse is to compute the purely diagonal Green functions $G_{\mathcal{O}}(z)$ and $G_{\mathcal{P}}(z)$ associated to the linear combinations of operators $\mathcal{O} = \Psi_{0\alpha} + \Psi_{0\beta}$ and $\mathcal{P} = \Psi_{0\alpha} - i\Psi_{0\beta}$ ($\alpha \neq \beta$) with the method outlined above, and then to use the algebraic relations

$$\begin{aligned} G_{\alpha\beta}(z) &= \frac{1}{2}\left[G_{\mathcal{O}}(z) - iG_{\mathcal{P}}(z) - (1-i)\left(G_{\alpha\alpha}(z) + G_{\beta\beta}(z)\right)\right] \\ G_{\beta\alpha}(z) &= \frac{1}{2}\left[G_{\mathcal{O}}(z) + iG_{\mathcal{P}}(z) - (1+i)\left(G_{\alpha\alpha}(z) + G_{\beta\beta}(z)\right)\right]. \end{aligned} \tag{1.24}$$

If the ground state is degenerate, the Green function can be computed repeating this procedure for all the degenerate states and then averaging over all the resulting functions. The reason why replacing the

Hamiltonian block with the Krylov matrix captures so well the spectral properties is that the Lanczos method reproduces exactly the first n moments of the spectral function [44, 47, 48].

Although sectorizing the Hamiltonian and using Lanczos to determine the ground state and the Green function considerably speeds up the exact diagonalization, the number of bath sites that we can include is still relatively small (roughly $N_{\text{bath}} \lesssim 10$, but it depends on the physical problem and on the available computer memory), as a consequence of the exponential increase of the Hilbert space as a function of N_{bath}. However, as we discuss in the next section, in the context of DMFT this is generally enough to get reliable results, because the bath is merely used as a fitting tool for the Weiss field.

1.3.3 The self-consistency equation

Now that we have seen how to compute the impurity Green function of a multi-component Anderson impurity model, we discuss how DMFT relates the original problem on the lattice to an auxiliary impurity problem. The following procedure originates from the *cavity method* in quantum field theory [27], but here we just give a brief outline of the algorithm.

First of all, let's consider the non-interacting lattice problem: if the system is translation invariant, we can Fourier transform the lattice fermionic operators in momentum space ($c_{i\alpha\sigma} \to c_{\mathbf{k}\alpha\sigma}$) and, after organizing these operators in a suitable spinor $\Psi_{\mathbf{k}}$, the non-interacting Hamiltonian assumes the general form

$$\sum_{\mathbf{k}\in \text{BZ}} \Psi^{\dagger}_{\mathbf{k}} \hat{H}_{\mathbf{k}} \Psi_{\mathbf{k}},$$

where the sum runs over the first Brillouin zone of the specific lattice (BZ). If the system is not translation invariant, the single site DMFT outlined in this section is not adequate and more sophisticated extensions of DMFT should be implemented. Among these we mention real-space DMFT, which is discussed in sec. [1.3.4], and cluster-DMFT [33].

Now we determine the general structure of the auxiliary impurity problem. The interaction Hamiltonian H_{int} in eq. [1.14] must be exactly equivalent to the local interaction Hamiltonian on the lattice. We assume throughout this work that the interaction is purely local, with the general Hubbard-Kanamori structure presented in sec. [1.1]. The general structure of the bath, i.e. possible symmetries in $\hat{\varepsilon}_k$ and $\hat{V}_k$, should be decided *a priori* with an educated guess based on the physical intuition. Specific numerical values of the independent components of $\hat{\varepsilon}_k$ and $\hat{V}_k$ instead should be determined self-consistently with a suitable iterative procedure. The self-consistency is met when the impurity Green function matches the local lattice Green function on a discrete set of Matsubara frequencies $\omega_n = (2n-1)\pi T$ labeled by an integer n:

$$\boxed{\hat{G}(i\omega_n) = \hat{G}_{\text{loc}}(i\omega_n).} \tag{1.25}$$

Remarkably, in the limit of zero temperature $T \to 0$, the Matsubara frequencies are not discrete, but rather form a continuum, which means that for any numerical purpose we need to introduce a fictitious temperature T_{Mats} to discretize the frequencies as $\omega_n = (2n-1)\pi T_{\text{Mats}}$. This numerical parameter can be adjusted to achieve the desired resolution for the correlation functions. The local lattice Green function is given by the Dyson equation as

$$\hat{G}_{\text{loc}}(i\omega_n) = \frac{1}{N_{\text{sites}}} \sum_{\mathbf{k}\in \text{BZ}} \frac{1}{i\omega_n - \hat{H}_{\mathbf{k}} - \hat{\Sigma}(\mathbf{k}, i\omega_n)}, \tag{1.26}$$

where N_{sites} is the number of lattice sites (or, equivalently, the number of points in the Brillouin zone) and $\hat{\Sigma}(\mathbf{k}, i\omega_n)$ is the self-energy, which encodes the information about interactions.

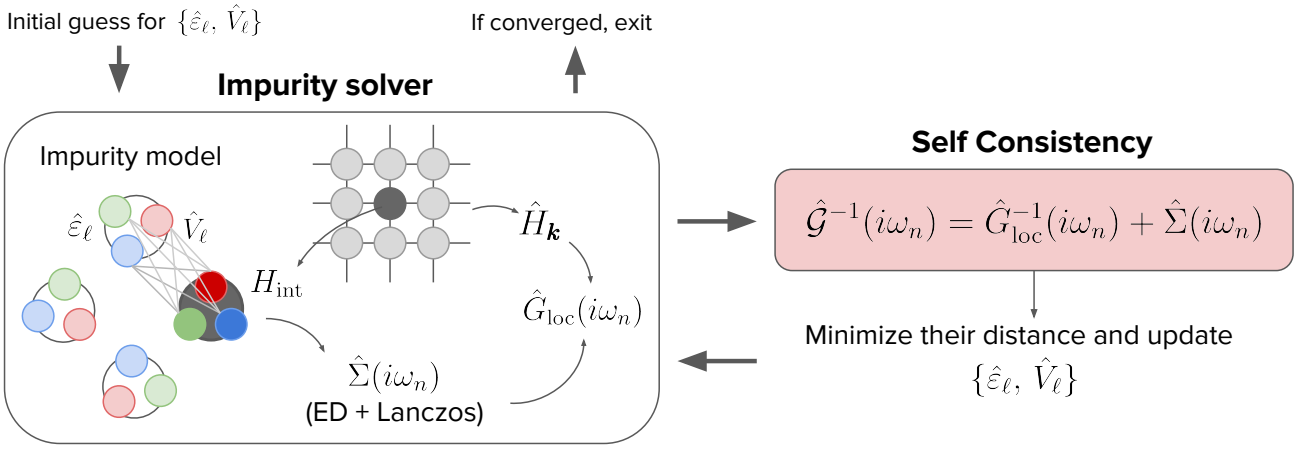

Figure 1.2: Schematic illustration of the DMFT recursion. The impurity problem sketched here has three fermionic components illustrated with different colors. The impurity site is shown with darker colors, while the three bath sites coupled to the impurity are shown with lighter colors.

A key assumption of DMFT is that the self-energy does not depend on momentum: $\hat{\Sigma}(\mathbf{k}, i\omega_n) \approx \hat{\Sigma}(i\omega_n)$, which amounts to neglect the spatial quantum fluctuations induced by the interaction, while fully retaining the dynamical quantum fluctuations. An immediate consequence of this assumption is that the self-energy of the lattice problem is the same as the self-energy of the impurity problem, as both systems have the same interaction Hamiltonian. Interestingly, if the lattice is infinite-dimensional, one can prove that the self-energy does not depend on $\mathbf{k}$ [27] and this is no longer an approximation, hence the solution of the self-consistency equation of DMFT [1.25] is in principle the exact Green function. In particular, a lattice that simplifies several calculations is the Bethe lattice in the limit of infinite coordination $z \to +\infty$ (z being the number of nearest neighbors of any given site). On a Bethe lattice, the concept of space translational symmetry and consequently the crystal momentum can't be properly defined; however one can still compute the density of states. If the hopping occurs only between nearest neighbors, and if we simultaneously consider $z \to +\infty$ and $t \to 0$ in such a way that the quantity $t\sqrt{z} = D/2$ remains finite, the density of states has a semicircular shape of radius D [49, 50]:

$$D(\varepsilon) = \frac{2}{\pi D^2}\sqrt{D^2 - \varepsilon^2}. \tag{1.27}$$

Remarkably, $D(\varepsilon)$ can be regarded as an approximated spectral function of an energy band, where the detailed spiky structure typical of real materials is smoothed out. Therefore, since the lattice enters in our equations only through the density of states, working on an infinitely coordinated Bethe lattice is in many cases a reasonable approximation, despite the exotic geometrical structure. This becomes questionable when the real band structure significantly differs from a semicircle, or when the problem cannot be recast on a Bethe lattice, for example when a gauge field is minimally coupled to the crystal momentum.

The self-consistency procedure starts by an educated initial guess on the specific values of the bath parameters $\{\hat{\varepsilon}_\ell, \hat{V}_\ell\}$, from which one can compute the impurity Green function both in the interacting case $\hat{G}(i\omega_n)$, via ED and the Lanczos method, and in the non-interacting case $\hat{\mathcal{G}}(i\omega_n)$ using eq. [1.17]. One can now use these functions to compute the self-energy $\hat{\Sigma}(i\omega_n) = \hat{\mathcal{G}}^{-1}(i\omega_n) - \hat{G}^{-1}(i\omega_n)$, which in turn can be used to compute the local Green function via eq. [1.26]. The bath parameters should now be updated self-consistently, i.e. in such a way to satisfy eq. [1.25]. This can be done as follows: let's first rewrite the

latter equation as

$$\boxed{\hat{\mathcal{G}}^{-1}(i\omega_n) = \hat{G}^{-1}_{\text{loc}}(i\omega_n) + \hat{\Sigma}(i\omega_n),} \tag{1.28}$$

where the quantity $\hat{G}^{-1}_{\text{loc}}(i\omega_n) + \hat{\Sigma}(i\omega_n) \equiv \hat{W}(i\omega_n)$ is called *Weiss field*, and observe that $\hat{\mathcal{G}}^{-1}(i\omega_n)$ has a functional dependence on the bath parameters $\{\hat{\varepsilon}_\ell,\, \hat{V}_\ell\}$, which is formally expressed in eq. [1.17]. We can thus recast this into an optimization problem, where we need to find the specific values of $\{\hat{\varepsilon}_\ell,\, \hat{V}_\ell\}$ that minimize a suitably defined "distance" between the numerically computed Weiss field and the functional expression [1.17]. A natural choice for the definition of a "distance" function is

$$\chi(\{\hat{\varepsilon}_\ell, \hat{V}_\ell\}) = \sum_{n=1}^{N_{\text{Mats}}} \sum_{\alpha\beta} w_n \left| \mathcal{G}^{-1}_{\alpha\beta}(i\omega_n) - W_{\alpha\beta}(i\omega_n) \right|^2, \tag{1.29}$$

where N_{Mats} is the number of Matsubara frequencies that we use to sample the correlation functions and w_n represents a list of frequency dependent weights that can be chosen in order to give more or less importance to low-frequency features of the Weiss field. Typical choices include $w_n = 1/N_{\text{Mats}}$ for all n; or $w_n = 1/N_{\text{Cutoff}}$ for $n \leq N_{\text{Cutoff}}$ and $w_n = 0$ for $n > N_{\text{Cutoff}}$. The sum over spinor indexes α, β can be restricted to some specific values of the indexes depending on the physical symmetries of the problem, in order to avoid a bias towards fitting diagonal or off-diagonal components. The optimal parameters are chosen as the input for starting the loop over, while the minimum value of the distance function is the fit residue and it gives a numerical estimate of how good the chosen N_{bath} is to capture the features of the Weiss field. This recursive procedure is repeated until some convergence criterion is met, for example until the distance between the self-energy at the current iteration and at the previous iteration is below an arbitrary threshold. A schematic illustration of the DMFT loop described so far is shown in fig. [1.2].

As a final remark, we emphasize that the number of bath sites of the impurity problem (N_{bath}) is not related to the number of lattice points (N_{sites}). While the latter is the number of crystal momenta that we use to compute the local Green function, the former determines the number of parameters that we use to perform the fitting procedure of the Weiss field. This observation has two consequences: first of all, in the framework of DMFT we can treat very large lattices with a computational cost that scales linearly with the number of sites; and secondly it is generally fine to use a relatively small number of bath sites as long as the self-consistent procedure converges.

1.3.4 Real-space DMFT

In this section we give an introductory overview on how to go beyond the assumption of spatial translation invariance in DMFT. If the system is subject to processes that break the translational symmetry, we cannot Fourier transform the spinor to a momentum space representation, hence we have to use the real space representation Ψ_j, where j labels a lattice site. In this case, the non-interacting Hamiltonian takes the form

$$H = \Psi^\dagger \hat{H} \Psi = \sum_{ij} \Psi^\dagger_i \hat{H}_{ij} \Psi_j \qquad \text{(non-interacting)},$$

where $i, j = 1, \ldots, N_{\text{sites}}$, $\Psi^\dagger = (\Psi^\dagger_1, \ldots, \Psi^\dagger_{N_{\text{sites}}})$ and $\hat{H}_{ij}$ is a block of the full Hamiltonian $\hat{H}$. Consistently, the self-energy has the same structure: $\hat{\Sigma}_{ij}(i\omega_n)$; however we still neglect non-local spatial fluctuations of the self-energy, which implies that it is diagonal in the lattice indexes: $\hat{\Sigma}_{ij}(i\omega_n) = \hat{\Sigma}_j(i\omega_n)\delta_{ij}$. We also define the full self-energy as the block-diagonal matrix $\hat{\Sigma} = \text{diag}(\hat{\Sigma}_1, \ldots, \hat{\Sigma}_{N_{\text{sites}}})$.

Since now there are N_{sites} independent self-energies to be determined at each DMFT iteration, we need to solve N_{sites} independent Anderson impurity problems, all of them being described by the same Hamiltonian, but with independent bath parameters. The computational cost to solve the impurity problems is considerably enhanced by a factor N_{sites}, however it is straightforward to parallelize the calculation on different CPUs, as there is no communication required between different threads. Furthermore, we can exploit residual lattice symmetries (such as lattice inversion symmetry or residual translation invariance) to speed up the evaluation by avoiding repeated calculations on sites that are physically symmetric.

From the self-energy we can compute the lattice Green function

$$\hat{G}_{ij}(i\omega_n) = [(i\omega_n - \hat{H} - \hat{\Sigma}(i\omega_n))^{-1}]_{ij}, \tag{1.30}$$

whose diagonal components $\hat{G}_{jj}(i\omega_n)$ represent the local Green functions on site j. In analogy to single-site DMFT, the Weiss field of the impurity problem associated to site j can be computed as $\hat{W}_j(i\omega_n) = \hat{G}^{-1}_{jj}(i\omega_n) + \hat{\Sigma}_j(i\omega_n)$. Finally, we can find the bath parameters to start a new DMFT loop by repeating the fitting procedure outlined in the previous section for all the N_{sites} Weiss fields. Once again, this procedure can be parallelized on all the available CPUs and it can be simplified by implementing residual lattice symmetries.

This extension of DMFT, where translation invariance is not required, but we still assume locality of quantum fluctuations is known as real-space DMFT, or R-DMFT and it has been used to investigate several problems, including the effect of an external DC voltage in multicomponent Fermi systems [51], or the effect of harmonic trapping potentials in the antiferromagnetic order of interacting fermions [52]. In the present work, real-space DMFT will be useful in chapter [3] to deal with antiferromagnetic order in multicomponent Fermi systems, which breaks translational symmetry of the original lattice, differentiating the system properties on two distinct sublattices A and B. As a future perspective, we mention that real-space DMFT can be used to take into account the presence of a trapping potential in cold-atomic platforms, or to investigate the effect of tilting the optical lattice, which has recently lead to the measure of the Hall coefficient in synthetic ladders [53].

1.3.5 Observables

In this section we briefly discuss some of the subtleties related to the calculation of the most relevant physical observables in the context of DMFT. In principle, the expectation value of any single-particle operator can be computed from the converged self-energy $\hat{\Sigma}(i\omega_n)$. For example, let's consider the quantity $\langle \Psi^\dagger_{\mathbf{k}\alpha}\Psi_{\mathbf{k}\beta}\rangle$, which can be rewritten in terms of the lattice Green function as follows:

$$\begin{aligned}\langle \Psi^\dagger_{\mathbf{k}\alpha}\Psi_{\mathbf{k}\beta}\rangle &= -\lim_{\tau\to 0^-}\langle \mathcal{T}\left(\Psi_{\mathbf{k}\beta}(\tau)\Psi^\dagger_{\mathbf{k}\alpha}(0)\right)\rangle = G_{\beta\alpha}(\mathbf{k},\tau\to 0^-)\\ &= \lim_{\tau\to 0^-} T\sum_{i\omega_n} G_{\beta\alpha}(\mathbf{k},i\omega_n)e^{-i\omega_n\tau} = \lim_{\eta\to 0^+} T\sum_{i\omega_n} G_{\beta\alpha}(\mathbf{k},i\omega_n)e^{i\omega_n\eta},\end{aligned} \tag{1.31}$$

where $\mathcal{T}$ denotes the imaginary time ordered product, and T is the temperature used as a spacing for Matsubara frequencies. The sum runs over all the positive and negative integer numbers n; however in the DMFT loop we generally compute dynamical correlations only on a finite set of positive Matsubara frequencies, labeled by $n = 1, \ldots, N_{\text{Mats}}$. This is due to a remarkable symmetry property of the Green function $\hat{G}(-i\omega_n) = \hat{G}^\dagger(i\omega_n)$, which stems from the definition $\hat{G}(i\omega_n) = [i\omega_n - \hat{H}]^{-1}$:

$$\hat{G}(-i\omega_n) = [-i\omega_n - \hat{H}]^{-1} = [-i\omega_n - \hat{H}^\dagger]^{-1} = \left\{[i\omega_n - \hat{H}]^{-1}\right\}^\dagger = \hat{G}^\dagger(i\omega_n),$$

where we have used the fact that the Hamiltonian is a hermitian matrix. Due to this symmetry, dynamical correlations at negative frequencies provide redundant information, thus we can consider only $\omega_n > 0$ during the DMFT loops and use the computational resources to achieve a finer frequency resolution. However, the contribution of $\omega_n < 0$ must be included in the calculation of observables.

The other subtle point is related to the contribution of large frequencies with $|n| > N_{\text{Mats}}$. Assuming that this contribution is just negligible is a strong assumption which can lead to significant numerical errors, especially when the self-energy remains finite at large frequencies (a typical circumstance in phases with broken symmetries). This issue can be solved (at least partially) by giving an analytic estimate of the contribution of the "tails" of $\hat{G}(\mathbf{k}, i\omega_n)$. Let us assume that the large-ω_n expansion of the self-energy takes the form

$$\hat{\Sigma}(i\omega_n) \underset{n\to+\infty}{\sim} \hat{\Sigma}_0 + \mathcal{O}\left(\frac{1}{n}\right), \qquad \hat{\Sigma}(i\omega_n) \underset{n\to-\infty}{\sim} \hat{\Sigma}_0^\dagger + \mathcal{O}\left(\frac{1}{n}\right), \tag{1.32}$$

where $\hat{\Sigma}_0$ is a constant matrix. Here we have also used the fact that the self-energy inherits the same symmetry property as the Green function, i.e. $\hat{\Sigma}(-i\omega_n) = \hat{\Sigma}^\dagger(i\omega_n)$. This assumption is true for all the systems studied in the present work. The corresponding large-ω_n expansion of the Green function is

$$\hat{G}(\mathbf{k}, i\omega_n) \underset{n\to\infty}{\sim} \frac{1}{i\omega_n} + \frac{\hat{H}_{\mathbf{k}} + \hat{\Sigma}_0}{(i\omega_n)^2} + \mathcal{O}\left(\frac{1}{n^3}\right), \qquad \hat{G}(\mathbf{k}, i\omega_n) \underset{n\to-\infty}{\sim} \frac{1}{i\omega_n} + \frac{\hat{H}_{\mathbf{k}} + \Sigma_0^\dagger}{(i\omega_n)^2} + \mathcal{O}\left(\frac{1}{n^3}\right). \tag{1.33}$$

We can now define the "tail" Green function by extending the large-ω_n expansion to all the Matsubara frequencies:

$$\hat{G}^{\text{tail}}(\mathbf{k}, i\omega_n) = \begin{cases} \frac{1}{i\omega_n} + \frac{\hat{H}_{\mathbf{k}} + \hat{\Sigma}_0}{(i\omega_n)^2} & n > 0 \\ \frac{1}{i\omega_n} + \frac{\hat{H}_{\mathbf{k}} + \hat{\Sigma}_0^\dagger}{(i\omega_n)^2} & n \leq 0 \end{cases}. \tag{1.34}$$

Adding and subtracting $\hat{G}^{\text{tail}}(\mathbf{k}, i\omega_n)$ to eq. [1.31] we get

$$\langle \Psi^\dagger_{\mathbf{k}\alpha} \Psi_{\mathbf{k}\beta} \rangle = \lim_{\eta\to 0^+} T \sum_{i\omega_n} \left(G_{\beta\alpha}(\mathbf{k}, i\omega_n) - G^{\text{tail}}_{\beta\alpha}(\mathbf{k}, i\omega_n) \right) e^{i\omega_n \eta} + \lim_{\eta\to 0^+} T \sum_{i\omega_n} G^{\text{tail}}_{\beta\alpha}(\mathbf{k}, i\omega_n) e^{i\omega_n \eta} \tag{1.35}$$

and the advantage is that not only the last sum can be evaluated analytically, but also the first sum can be restricted to $-N_{\text{Mats}} < n \leq N_{\text{Mats}}$ because $\hat{G}(\mathbf{k}, i\omega_n) - \hat{G}^{\text{tail}}(\mathbf{k}, i\omega_n) = 0 + \mathcal{O}(n^{-3})$ out of that interval. The sum over all Matsubara frequencies of the tail Green function is

$$\lim_{\eta\to 0^+} T \sum_{i\omega_n} G^{\text{tail}}_{\beta\alpha}(\mathbf{k}, i\omega_n) e^{i\omega_n \eta} = \frac{\delta_{\beta\alpha}}{2} - \frac{1}{8T} \left[H_{\mathbf{k},\beta\alpha} + H^*_{\mathbf{k},\alpha\beta} + \Sigma_{0,\beta\alpha} + \Sigma^*_{0,\alpha\beta} \right] \tag{1.36}$$

where we have used the fact that

$$\begin{aligned} \lim_{\eta\to 0^+} T \sum_{i\omega_n} \frac{e^{i\omega_n \eta}}{i\omega_n} &= \lim_{\eta\to 0^+} \text{Res}\left(\frac{e^{iz\eta}}{z} f(z);\ z = 0 \right) = f(0) = \frac{1}{2} \\ \lim_{\eta\to 0^+} T \sum_{n>0} \frac{e^{i\omega_n \eta}}{(i\omega_n)^2} &= -\frac{1}{\pi^2 T} \sum_{n=1}^{\infty} \frac{1}{(2n-1)^2} = -\frac{1}{\pi^2 T} \frac{\pi^2}{8} = -\frac{1}{8T} \end{aligned} \tag{1.37}$$

where $f(z) = \left[e^{z/T} + 1\right]^{-1}$ is the Fermi function.

Splitting the sum into two sums over positive and negative Matsubara frequencies and using the properties outlined above we get

$$\begin{aligned}\langle \Psi^\dagger_{\mathbf{k}\alpha}\Psi_{\mathbf{k}\beta}\rangle = T\sum_{n=1}^{N_{\text{Mats}}}\left[G_{\beta\alpha}(\mathbf{k},i\omega_n) - \frac{\delta_{\beta\alpha}}{i\omega_n} + \frac{H_{\mathbf{k},\beta\alpha}+\Sigma_{0,\beta\alpha}}{\omega_n^2}\right] \\ +T\sum_{n=1}^{N_{\text{Mats}}}\left[G^*_{\alpha\beta}(\mathbf{k},i\omega_n) + \frac{\delta_{\alpha\beta}}{i\omega_n} + \frac{H^*_{\mathbf{k},\alpha\beta}+\Sigma^*_{0,\alpha\beta}}{\omega_n^2}\right] \\ +\frac{\delta_{\beta\alpha}}{2} - \frac{1}{8T}\left[H_{\mathbf{k},\beta\alpha}+\Sigma_{0,\beta\alpha}+H^*_{\mathbf{k},\alpha\beta}+\Sigma^*_{0,\alpha\beta}\right].\end{aligned} \tag{1.38}$$

The terms $\propto 1/\omega_n$ cancel out and finally we get

$$\boxed{\langle \Psi^\dagger_{\mathbf{k}\alpha}\Psi_{\mathbf{k}\beta}\rangle = T\sum_{n=1}^{N_{\text{Mats}}}\left[G_{\beta\alpha}(\mathbf{k},i\omega_n) + \frac{H_{\mathbf{k},\beta\alpha}+\Sigma_{0,\beta\alpha}}{\omega_n^2}\right] + \frac{\delta_{\alpha\beta}}{4} - \frac{1}{8T}\left(H_{\mathbf{k},\beta\alpha}+\Sigma_{0,\beta\alpha}\right) + \text{h.c.}} \tag{1.39}$$

The parameter $\hat{\Sigma}_0$ can be determined by fitting the high-frequency behavior of the converged self-energy with a constant matrix. Further corrections can be taken into account by repeating the calculation above expanding the self-energy to first order in $1/\omega_n$ as $\hat{\Sigma} \sim \hat{\Sigma}_0 + \hat{\Sigma}_1/i\omega_n$ and fitting the parameters $\hat{\Sigma}_0$ and $\hat{\Sigma}_1$ to the high-frequency behavior of $\hat{\Sigma}(i\omega_n)$.

In some cases we may also need to evaluate expectation values of two-particle operators, for example local correlations of the form $N_{\text{sites}}^{-1}\sum_i \langle \Psi^\dagger_{i\alpha}\Psi^\dagger_{i\beta}\Psi_{i\gamma}\Psi_{i\delta}\rangle$. In order to compute objects like this, in principle we need the four-points Green function, which is obtained by solving the Bethe-Salpeter equation using the converged self-energy [54]. This approach can be technically quite complicated, but there is a simple way to circumvent it. Since we expect that in the converged impurity problem, the impurity site mimics the local physics of the original lattice system, as long as we are interested in local correlations, we can assume that they coincide with local correlations of the impurity. The latter can be computed via exact diagonalization by simply building the corresponding operator in the chosen basis of the Hilbert space and evaluating the expectation value on the ground state manifold. A remarkable example of local correlation is the *double occupancy* in the single-band Hubbard model, which represents the fraction of doubly occupied sites on a given state and is given by the two-particle operator $N_{\text{sites}}^{-1}\sum_i n_{i\uparrow}n_{i\downarrow}$.

Chapter 2

Hubbard model with broken SU(N) symmetry and artificial gauge fields

One of the most challenging problems for the quantum simulation of electrons in materials with platforms based on cold alkaline-earth atoms, that we have introduced in the previous chapter, is the fact that electrons are electrically charged, whereas atoms are neutral. This implies that their interaction with an external electromagnetic field is completely different: electrons are point-like charges with spin, while atoms are coupled to the external field via their electric and magnetic dipole moment.

For example, when electrons on a square lattice interact with an external static magnetic field, the *minimal coupling* results in a complex phase of the hopping matrix elements, and the system is described by the Harper-Hofstadter model [55]. On the other hand, if a static magnetic field is applied to alkaline-earth atoms arranged in an optical square lattice, it would not induce complex phases in the hopping and the system would not be described by the same model.

This raises the intriguing challenge to realize a system of neutral cold atoms that are effectively coupled to an external gauge field [56], thus mimicking the presence of a static magnetic field acting on a system of electrons. So far, the realization of artificial gauge field has been achieved either via Floquet engineering (i.e. via suitable protocols of time-periodic shaking of the optical lattice) [57], or via the *synthetic dimension* approach. The latter can be realized either exploiting the "orbital" degrees of freedom via laser-induced clock transitions [58], or by effectively coupling the nuclear states via optical Raman transitions, which is the main subject of this chapter.

The discussion is organized as follows: in sec. [2.1] we provide a general overview of optical Raman transitions; in sec. [2.2] we discuss the experimental realization of a synthetic dimension with Raman transitions in ^{173}Yb; then in sec. [2.3] we introduce the most relevant observables for our investigation, the current operators; finally, sec. [2.4] is devoted to discuss important analytic results for a system of fermions with an extra synthetic dimension and coupled to a synthetic gauge field.

2.1 Optical Raman transitions

A Raman scattering process is the interaction between a system of electrically charged particles having at least three available quantum states and two photon fields in a coherent quantum state, which can be described by two classical electromagnetic fields. For the present work, the charged particles are valence electrons of an atomic species and the two classical electromagnetic fields are monochromatic waves provided by two laser beams with wave vectors $\mathbf{k}_{1,2}$ and frequencies $\omega_{1,2}$. We first consider the case of three

quantum states that, in ascending order of associated energy, are labeled by $|g_1\rangle$, $|g_2\rangle$ and $|e\rangle$ respectively. For concreteness, we can think of $|g_1\rangle$ and $|g_2\rangle$ as two states of the electronic ground state manifold, whose degeneracy has been lifted by, for example, an external magnetic field; and we can regard $|e\rangle$ as an excited electronic state. In fact there is an infinite amount of excited states available for the electrons of an atom; however for now we assume that only $|e\rangle$ is significantly populated: this is the case if the frequencies of the electromagnetic fields are nearly resonant to the atomic transitions $|g_1\rangle \leftrightarrow |e\rangle$ and $|g_2\rangle \leftrightarrow |e\rangle$. At the end of this section, we spend a few words on the case where multiple excited states are involved in the Raman transition.

2.1.1 Rotating wave approximation

We begin providing a simplified Hamiltonian description of the many-electron system within the rotating wave approximation. Setting the zero of energy to the energy level of $|g_1\rangle$ and calling $\omega_{0,1}$ and $\omega_{0,2}$ the frequencies associated to the aforementioned atomic transitions, the Hamiltonian describing the free electron dynamics is:

$$H_{\text{mat}} = \hbar\omega_{0,1}|e\rangle\langle e| + \hbar(\omega_{0,1} - \omega_{0,2})|g_2\rangle\langle g_2|, \tag{2.1}$$

where $|\alpha\rangle\langle\alpha|$ is the projector operator on the corresponding many-body state $|\alpha\rangle$. In the dipole approximation, the interaction Hamiltonian describing the coupling to the external field takes the form $H_{\text{int}} = -\mathbf{E}(\mathbf{r}, t) \cdot \hat{\mathbf{d}}$ [59], with the electric field defined by

$$\mathbf{E}(\mathbf{r}, t) = \sum_{i=1,2} E_{0i} \left(a_i e^{i\mathbf{k}_i \cdot \mathbf{r} - i\omega_i t} \mathbf{u}_i + \text{h.c.} \right), \tag{2.2}$$

where a_i is a phase factor, E_{0i} is the field amplitude and $\mathbf{u}_i$ is the Jones polarization vector of the corresponding wave; and the dipole operator defined by

$$\hat{\mathbf{d}} = \langle g_1|\hat{\mathbf{d}}|e\rangle|e\rangle\langle g_1| + \langle g_2|\hat{\mathbf{d}}|e\rangle|e\rangle\langle g_2| + \langle g_1|\hat{\mathbf{d}}|g_2\rangle|g_2\rangle\langle g_1| + \text{h.c.}, \tag{2.3}$$

where $\langle\alpha|\hat{\mathbf{d}}|\beta\rangle$ are the matrix elements of the dipole operator (we recall that, due to symmetry reasons, matrix elements of the form $\langle\alpha|\hat{\mathbf{d}}|\alpha\rangle$ vanish identically [60]).

The interaction Hamiltonian contains in total 24 terms of the form

$$\underbrace{-E_{0i} a_i \mathbf{u}_i \cdot \langle\alpha|\hat{\mathbf{d}}|\beta\rangle}_{\hbar\Omega_{i,\alpha\beta}} e^{\pm i\mathbf{k}_i \cdot \mathbf{r}} e^{\mp i\omega_i t} \quad \text{and} \quad \underbrace{-E_{0i} a_i^* \mathbf{u}_i^* \cdot \langle\alpha|\hat{\mathbf{d}}|\beta\rangle^*}_{\hbar\Omega_{i,\alpha\beta}^*} e^{\pm i\mathbf{k}_i \cdot \mathbf{r}} e^{\mp i\omega_i t},$$

where we have introduced the complex Rabi frequencies $\Omega_{i,\alpha\beta}$, which are functions of the laser polarization and intensity (the latter being proportional to E_{0i}^2). All these terms contain the full information about fast and slow dynamics of the system; but typically we are mostly interested in the slow dynamics, which occurs over relatively long timescales; the reason is that it is extremely difficult (and sometimes impossible) to experimentally detect fast oscillations characterized by very small timescales. The standard approach to integrate out the fast dynamics is known as *rotating wave approximation* (RWA), and it consists of the following steps. First of all, we rewrite H in the Dirac's interaction picture via the unitary transformation

$$H^D = e^{iH_{\text{mat}}t/\hbar} H e^{-iH_{\text{mat}}t/\hbar}. \tag{2.4}$$

The matrix H^D expresses the time dependence via several phase factors, such as $e^{i(\omega_i + \omega_{0,i})t}$, $e^{i(\omega_i - \omega_{0,i})t}$, etc. Assuming for example that the detunings $\delta\omega_i = |\omega_i - \omega_{0,i}|$ are small compared to the natural frequencies

of the transitions $\omega_{0,i}$, i.e. that the i-th laser beam is nearly resonant to the transition $|g_i\rangle \leftrightarrow |e\rangle$, we can approximate H^D retaining only terms proportional to $e^{\pm i(\omega_i-\omega_{0,i})t}$, which describe slow dynamics, and drop all the others, which account for faster oscillations. The approximated Hamiltonian H^D_{RWA}, written in the basis $\{|g_1\rangle, |g_2\rangle, |e\rangle\}$, reads

$$H^D_{\text{RWA}} = \begin{pmatrix} 0 & 0 & \hbar\Omega_{1,eg_1} e^{-i\mathbf{k}_1\cdot\mathbf{r}} e^{i(\omega_1-\omega_{0,1})t} \\ 0 & \hbar(\omega_{0,1}-\omega_{0,2}) & \hbar\Omega_{2,eg_2} e^{-i\mathbf{k}_2\cdot\mathbf{r}} e^{i(\omega_2-\omega_{0,2})t} \\ \hbar\Omega^*_{1,eg_1} e^{i\mathbf{k}_1\cdot\mathbf{r}} e^{-i(\omega_1-\omega_{0,1})t} & \hbar\Omega^*_{2,eg_2} e^{i\mathbf{k}_2\cdot\mathbf{r}} e^{-i(\omega_2-\omega_{0,2})t} & \hbar\omega_{0,1} \end{pmatrix}. \tag{2.5}$$

Finally, we transform the approximated Hamiltonian back to the Schrödinger picture via the inverse transformation

$$H_{\text{RWA}} = e^{-iH_{\text{mat}}t/\hbar} H^D_{\text{RWA}} e^{iH_{\text{mat}}t/\hbar} \tag{2.6}$$

and, using the simplified notation $\Omega_{i,eg_i} \equiv \Omega_i$, we get

$$H_{\text{RWA}} = \hbar \begin{pmatrix} 0 & 0 & \Omega_1 e^{-i\mathbf{k}_1\cdot\mathbf{r}} e^{i\omega_1 t} \\ 0 & \omega_{0,1}-\omega_{0,2} & \Omega_2 e^{-i\mathbf{k}_2\cdot\mathbf{r}} e^{i\omega_2 t} \\ \Omega^*_1 e^{i\mathbf{k}_1\cdot\mathbf{r}} e^{-i\omega_1 t} & \Omega^*_2 e^{i\mathbf{k}_2\cdot\mathbf{r}} e^{-i\omega_2 t} & \omega_{0,1} \end{pmatrix}. \tag{2.7}$$

2.1.2 Effective two-level system

Now that the time dependence of the Hamiltonian has been considerably simplified, it is possible to perform a unitary transformation that makes the Hamiltonian time independent. Formally, this amounts to describe the dynamics on a different "rotating" frame of reference, where the system is only subject to stationary processes. The general idea is to map the state $|\psi(t)\rangle$ into another state $|\psi'(t)\rangle = U(t)|\psi(t)\rangle$, where $U(t)$ is a suitable time-dependent unitary operator with $U^\dagger(t) = U^{-1}(t)$. The state $|\psi'(t)\rangle$ evolves according to the Schrödinger equation with a time independent Hamiltonian H':

$$i\hbar\partial_t|\psi'(t)\rangle = H'|\psi'(t)\rangle. \tag{2.8}$$

Using the definition of $|\psi'(t)\rangle$ given above, we can recast this equation as

$$i\hbar[\partial_t U(t)]|\psi(t)\rangle + i\hbar U(t)\partial_t|\psi(t)\rangle = H'U(t)|\psi(t)\rangle;$$

then using the Schrödinger equation in the original frame $i\hbar\partial_t|\psi(t)\rangle = H(t)|\psi(t)\rangle$ and right-multiplying by $U^\dagger(t)$, we get H' in terms of $H(t)$ and $U(t)$:

$$H' = U(t)H(t)U^\dagger(t) + i\hbar\left[\partial_t U(t)\right]U^\dagger(t). \tag{2.9}$$

A possible choice for $U(t)$ that makes H' static is the following:

$$U(t) = \begin{pmatrix} e^{-i\omega_1 t} & 0 & 0 \\ 0 & e^{-i\omega_2 t} & 0 \\ 0 & 0 & 1 \end{pmatrix} e^{i(\omega_{0,1}+\Delta)t}, \tag{2.10}$$

where Δ is the average of the detunings $\Delta = (\delta\omega_1 + \delta\omega_2)/2$, which leads to

$$H' = \hbar \begin{pmatrix} -\frac{\delta\omega_2-\delta\omega_1}{2} & 0 & \Omega_1 e^{-i\mathbf{k}_1\cdot\mathbf{r}} \\ 0 & \frac{\delta\omega_2-\delta\omega_1}{2} & \Omega_2 e^{-i\mathbf{k}_2\cdot\mathbf{r}} \\ \Omega^*_1 e^{i\mathbf{k}_1\cdot\mathbf{r}} & \Omega^*_2 e^{i\mathbf{k}_2\cdot\mathbf{r}} & -\Delta \end{pmatrix}. \tag{2.11}$$

Remarkably, in the rotating reference frame, the spacing between energy states is modified, as one can immediately observe setting for example $\Omega_i = 0$. In particular, since $U^\dagger(t)H(t)U(t)$ has the same eigenvalues of $H(t)$, but $i[\partial_t U(t)]U^\dagger(t) = \text{diag}\,(\delta\omega_1 - \Delta,\, \omega_2 - \omega_{0,1} - \Delta,\, -\omega_{0,1} - \Delta)$, the eigenvalues of $H(t)$ are shifted by different amounts by this transformation and their spacing is consequently distorted.

Expanding a generic state in the basis of the Hilbert space as $\psi_{g_1}(t)|g_1\rangle + \psi_{g_2}(t)|g_2\rangle + \psi_e(t)|e\rangle$, we can derive dynamical equations for the coefficients through the Schrödinger equation:

$$\begin{aligned} i\partial_t\psi_{g_1} &= (\delta\omega_1 - \Delta)\psi_{g_1} + \Omega_1 e^{-i\mathbf{k}_1\cdot\mathbf{r}}\psi_e \\ i\partial_t\psi_{g_2} &= (\delta\omega_2 - \Delta)\psi_{g_2} + \Omega_2 e^{-i\mathbf{k}_2\cdot\mathbf{r}}\psi_e \\ i\partial_t\psi_e &= \Omega_1^* e^{i\mathbf{k}_1\cdot\mathbf{r}}\psi_{g_1} + \Omega_2^* e^{i\mathbf{k}_2\cdot\mathbf{r}}\psi_{g_2} - \Delta\psi_e, \end{aligned} \tag{2.12}$$

where the time-dependence is implied. An effective two-body dynamics can be obtained in the limit $\Delta \gg \Omega_1,\, \Omega_2$ and $\Delta \gg \frac{\delta\omega_2 - \delta\omega_1}{2}$ through the process of *adiabatic elimination*, which amounts to eliminate the fast oscillating part of $\psi_e(t)$, keeping only the slowly oscillating component $\tilde{\psi}_e(t)$. We can now make the substitution $\psi_e(t) \to \tilde{\psi}_e(t)$ in eq. [2.12], where we can also assume that the time derivative of $\tilde{\psi}_e(t)$ is negligible with respect to the other terms, resulting in the equation:

$$\partial_t\tilde{\psi}_e = 0 \quad \to \quad \tilde{\psi}_e = \frac{\Omega_1^*}{\Delta}e^{i\mathbf{k}_1\cdot\mathbf{r}}\psi_{g_1} + \frac{\Omega_2^*}{\Delta}e^{i\mathbf{k}_1\cdot\mathbf{r}}\psi_{g_2}. \tag{2.13}$$

However, it is difficult to justify this assumption a priori: in fact this is a consequence of the full solution of eq. [2.12], as shown in ref. [61]. Summarizing, the solution takes the form $\psi_e(t) = \sum_{a=1}^{3} C_a e^{ix_a\Delta t}$ where, if $\frac{\Omega_a}{\Delta}$ and $\frac{|\delta\omega_2 - \delta\omega_1|}{2\Delta}$ are proportional to a small parameter ε, then $x_1 = -\frac{|\delta\omega_2 - \delta\omega_1|}{2\Delta} + \mathcal{O}(\varepsilon^2)$, $x_2 = \frac{|\delta\omega_2 - \delta\omega_1|}{2\Delta} + \mathcal{O}(\varepsilon^2)$ and $x_3 = 1 + \mathcal{O}(\varepsilon^2)$. Moreover, the coefficients C_a depend on the initial condition, but in general they are $\mathcal{O}(\varepsilon)$, whereas $\psi_{g_1}(t) \approx \mathcal{O}(1)$ and $\psi_{g_2}(t) \approx \mathcal{O}(1)$. Clearly, the fast oscillating term of $\psi_e(t)$ is $C_3 e^{ix_3\Delta t}$, which means that we can define the slowly oscillating component $\tilde{\psi}_e(t) = \sum_{a=1,2} C_a e^{ix_a\Delta t}$. We can recast the last row of eq. [2.12] as

$$\underbrace{-x_1 C_1 e^{ix_1\Delta t}}_{\mathcal{O}(\varepsilon^2)} - \underbrace{x_2 C_2 e^{ix_2\Delta t}}_{\mathcal{O}(\varepsilon^2)} + \underbrace{(1 - x_3)C_3 e^{ix_3\Delta t}}_{\mathcal{O}(\varepsilon^3)} = \overbrace{\frac{\Omega_1^*}{\Delta}e^{i\mathbf{k}_1\cdot\mathbf{r}}\psi_{g_1}}^{\mathcal{O}(\varepsilon)} + \overbrace{\frac{\Omega_2^*}{\Delta}e^{i\mathbf{k}_1\cdot\mathbf{r}}\psi_{g_2}}^{\mathcal{O}(\varepsilon)} - \overbrace{\tilde{\psi}_e(t)}^{\mathcal{O}(\varepsilon)}$$

and if we only consider terms of order $\mathcal{O}(\varepsilon)$, we obtain eq. [2.13], which is then justified. Substituting $\psi_e(t) \to \tilde{\psi}_e(t)$ also in the remaining equations, which again can be justified *a posteriori* from the full solution, we finally obtain a Schrödinger equation restricted to the Hilbert subspace $\{|g_1\rangle, |g_2\rangle\}$:

$$i\hbar\partial_t \begin{pmatrix} \psi_{g_1}(t) \\ \psi_{g_2}(t) \end{pmatrix} = H_{\text{eff}} \begin{pmatrix} \psi_{g_1}(t) \\ \psi_{g_2}(t) \end{pmatrix}; \qquad H_{\text{eff}} = \begin{pmatrix} \varepsilon_1 & \hbar\Omega_R e^{i\phi} e^{i(\mathbf{k}_2 - \mathbf{k}_1)\cdot\mathbf{r}} \\ \hbar\Omega_R e^{-i\phi} e^{i(\mathbf{k}_1 - \mathbf{k}_2)\cdot\mathbf{r}} & \varepsilon_2 \end{pmatrix}, \tag{2.14}$$

where we have introduced the complex effective Rabi frequency $\Omega_R e^{i\phi}$ and the level energies $\varepsilon_{1,2}$ given by:

$$\boxed{\Omega_R e^{i\phi} = \frac{\Omega_2^*\Omega_1}{\Delta},} \qquad \boxed{\varepsilon_i = \hbar\delta\omega_i - \hbar\Delta + \hbar\frac{|\Omega_i|^2}{\Delta}.} \tag{2.15}$$

The quantity $|\Omega_i|^2/\Delta$ is called *light shift* of the i-th level and it is responsible of the AC Stark effect.

It is interesting to mention that the procedure outlined above to obtain the effective two-level dynamics can be condensed and generalized in the following formula [61]:

$$H_{\text{eff}} = \lim_{z \to E_0} P_g \left[H' + V P_e \left(z - P_e H' P_e \right)^{-1} V \right] P_g, \tag{2.16}$$

where P_g and P_e are projectors operators onto the subspaces $\{|g_1\rangle, |g_2\rangle\}$ and $\{|e\rangle\}$ respectively, E_0 is the average energy of the two states $|g_1\rangle$ and $|g_2\rangle$ in H' ($E_0 = 0$ in our case) amd V is the part of H' that describes the interaction with the photon field (i.e. the off-diagonal part).

Finally, we emphasize that in the effective two level system, the transitions $|g_1\rangle \leftrightarrow |g_2\rangle$ are characterized by a phase factor which is dependent on the specific position of the atom $\mathbf{r}$. For a single atom this is just a complex constant that can be absorbed in the definition of ϕ; however for multiple atoms it is important to keep track of this factor. The induced phase shift of Raman processes in two atoms at positions $\mathbf{r}_i$ and $\mathbf{r}_j$ is given by $(\mathbf{k}_2 - \mathbf{k}_1) \cdot (\mathbf{r}_j - \mathbf{r}_i)$, which is the projection of the difference of the laser wave vectors on the direction connecting the atoms. As we will discuss in sec. [2.2], this is the key feature that allows to perform a quantum simulation of synthetic structures pierced by an effective artificial gauge field.

2.1.3 Raman transitions through multiple excited states

For the purpose of the present work, it is interesting to discuss a generalization of Raman processes to the case where there are multiple excited states nearly resonant to the two laser fields. Consider then a manifold of excited states $|e_n\rangle$, where $n = 1, \ldots, N_{\text{states}}$ having energy $\hbar(\omega_{0,1} + \delta_n)$ with respect to the reference energy of $|g_1\rangle$, where we assume that $\delta_n \ll \omega_{0,1}$, i.e. that the splittings in the manifold of excited states are small compared to the natural frequency of the transition $|g_1\rangle \leftrightarrow |e\rangle$ in absence of splitting. This scenario is typically realized when the degeneracy of a manifold of excited states is split e.g. by an external constant magnetic field via Zeeman effect. The problem is schematically represented in fig. [2.1 (a)].

The Hamiltonian within the rotating wave approximation can be simply generalized by introducing multiple Rabi couplings $\Omega_{i,n}$, which describe the amplitude of the transition $|g_i\rangle \leftrightarrow |e_n\rangle$ stimulated by the i-th laser beam:

$$H_{\text{RWA}} = \hbar \begin{pmatrix} 0 & 0 & \Omega_{1,1} e^{-i\mathbf{k}_1 \cdot \mathbf{r}} e^{i\omega_1 t} & \Omega_{1,2} e^{-i\mathbf{k}_1 \cdot \mathbf{r}} e^{i\omega_1 t} & \dots \\ 0 & \omega_{0,1} - \omega_{0,2} & \Omega_{2,1} e^{-i\mathbf{k}_2 \cdot \mathbf{r}} e^{i\omega_2 t} & \Omega_{2,2} e^{-i\mathbf{k}_2 \cdot \mathbf{r}} e^{i\omega_2 t} & \dots \\ \Omega^*_{1,1} e^{i\mathbf{k}_1 \cdot \mathbf{r}} e^{-i\omega_1 t} & \Omega^*_{2,1} e^{i\mathbf{k}_2 \cdot \mathbf{r}} e^{-i\omega_2 t} & \omega_{0,1} + \delta_1 & 0 & \dots \\ \Omega^*_{1,2} e^{i\mathbf{k}_1 \cdot \mathbf{r}} e^{-i\omega_1 t} & \Omega^*_{2,2} e^{i\mathbf{k}_2 \cdot \mathbf{r}} e^{-i\omega_2 t} & 0 & \omega_{0,1} + \delta_2 & \dots \\ \vdots & \vdots & \vdots & \vdots & \ddots \end{pmatrix}. \tag{2.17}$$

The generalized unitary transformation to the rotating frame of reference is

$$U(t) = \begin{pmatrix} e^{-i\omega_1 t} & 0 & 0 & 0 & \dots \\ 0 & e^{-i\omega_2 t} & 0 & 0 & \dots \\ 0 & 0 & 1 & 0 & \dots \\ 0 & 0 & 0 & 1 & \dots \\ \vdots & \vdots & \vdots & \vdots & \ddots \end{pmatrix} e^{i(\omega_{0,1} + \Delta)t}, \tag{2.18}$$

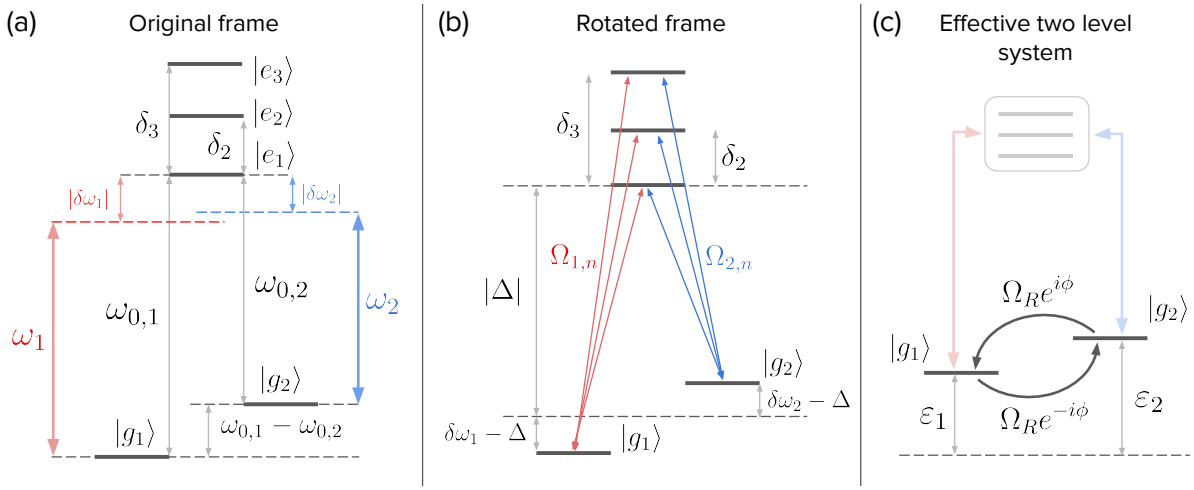

Figure 2.1: Schematic representation of the Raman transition with multiple excited states described in the text. Panel (a) shows the original problem, with the multilevel system coupled to an external electromagnetic field made of two superimposed monochromatic waves of frequencies ω_1 and ω_2 quasiresonant to the transitions $|g_1\rangle \leftrightarrow |e_n\rangle$ and $|g_2\rangle \leftrightarrow |e_n\rangle$ respectively. Panel (b) shows the system in the rotated frame after the rotating wave approximation, with a stimulated coupling to the manifold of excited states. Panel (c) shows the effective two level system obtained after adiabatic elimination of the coupling to the excited states (for graphical reasons we have omitted the spatial-dependent phase factor).

and, applying eq. [2.9], we get to the static Hamiltonian in the new frame:

$$H' = \hbar \begin{pmatrix} \delta\omega_1 - \Delta & 0 & \Omega_{1,1}e^{-i\mathbf{k}_1\cdot\mathbf{r}} & \Omega_{1,2}e^{-i\mathbf{k}_1\cdot\mathbf{r}} & \dots \\ 0 & \delta\omega_2 - \Delta & \Omega_{2,1}e^{-i\mathbf{k}_2\cdot\mathbf{r}} & \Omega_{2,2}e^{-i\mathbf{k}_2\cdot\mathbf{r}} & \dots \\ \Omega^*_{1,1}e^{i\mathbf{k}_1\cdot\mathbf{r}} & \Omega^*_{2,1}e^{i\mathbf{k}_2\cdot\mathbf{r}} & \delta_1 - \Delta & 0 & \dots \\ \Omega^*_{1,2}e^{i\mathbf{k}_1\cdot\mathbf{r}} & \Omega^*_{2,2}e^{i\mathbf{k}_2\cdot\mathbf{r}} & 0 & \delta_2 - \Delta & \dots \\ \vdots & \vdots & \vdots & \vdots & \ddots \end{pmatrix}, \tag{2.19}$$

which is depicted in fig. [2.1 (b)].

The adiabatic elimination process is done on equal grounds for all the excited states and it amounts to substitute all the coefficients ψ_{e_n} in the expansion of a generic state with their slowly varying part $\tilde{\psi}_{e,n}$ and to assume that:

$$\partial_t \tilde{\psi}_{e_n} = 0 \quad \rightarrow \quad \tilde{\psi}_{e_n} = \frac{\Omega^*_{1,n}}{\Delta - \delta_n} e^{i\mathbf{k}_1\cdot\mathbf{r}} \psi_{g_1} + \frac{\Omega^*_{2,n}}{\Delta - \delta_n} e^{i\mathbf{k}_1\cdot\mathbf{r}} \psi_{g_2}.$$

After adiabatic eliminating all the excited states, we are left with an effective Schrödinger equation for the ground states, and hence with an effective two-level Hamiltonian, formally equivalent to [2.14], with a suitable correction of the effective Rabi frequency and of the AC Stark shifts:

$$\Omega_R e^{i\phi} = \sum_n \frac{\Omega^*_{2,n}\Omega_{1,n}}{\Delta - \delta_n} \qquad \varepsilon_i = \delta\omega_i - \Delta + \sum_n \frac{|\Omega_{i,n}|^2}{\Delta - \delta_n}. \tag{2.20}$$

In conclusion, we briefly mention the interesting case of a ground state manifold having three states $|g_1\rangle$, $|g_2\rangle$ and $|g_3\rangle$ of energy 0, $\hbar(\omega_{0,1} - \omega_{0,2})$ and $2\hbar(\omega_{0,1} - \omega_{0,2})$, where $|g_1\rangle$ and $|g_2\rangle$ are coupled to an excited state $|e_1\rangle$, while $|g_2\rangle$ and $|g_3\rangle$ are coupled to a second excited state $|e_2\rangle$. Essentially, we are assuming

that matrix elements of the electric dipole operator connecting $|g_1\rangle$ with $|e_2\rangle$ vanish, as well as those connecting $|g_3\rangle$ and $|e_1\rangle$: this can happen when these transition do not respect conservation laws, such as the conservation of angular momentum, as we will discuss in the next section. As a matter of fact, we can think about this situation as a combination of two independent problems like the ones we have studied above: one involving $\{|g_1\rangle, |g_2\rangle, |e_1\rangle\}$ and the other involving $\{|g_2\rangle, |g_3\rangle, |e_2\rangle\}$, where the two problems are characterized by different detunings and different dipole matrix elements. Applying the formalism introduced above, we obtain an effective three-level dynamics where the three states are characterized by different AC light shifts and where the hopping processes connect $|g_1\rangle$ with $|g_2\rangle$ and similarly $|g_2\rangle$ with $|g_3\rangle$ with a different amplitude, but with the same space-dependent phase factor. The same qualitative picture holds in the case where $|e_1\rangle$ and $|e_2\rangle$ are manifolds.

2.2 Artificial gauge field with Raman transitions in ^{173}Yb

We have shown that optical Raman transitions provide a valuable tool to implement the quantum simulation of a lattice system coupled to an artificial gauge field with alkaline-earth like atoms [20, 62, 63]. In a nutshell, the idea is to couple two or more nuclear states exploiting Raman transitions (and hence explicitly breaking the SU(N) symmetry) and to regard this processes as tunneling events along a "synthetic dimension", which is the abstract direction of internal states. Since the effective Rabi frequency between these states has a complex phase, which depends on the specific position of the atom in the optical lattice, this mimics the effect of a static magnetic field acting perpendicular to the synthetic direction (see fig. [2.3]).

Consider for example a gas of alkaline-earth-like atoms prepared in the electronic ground state $^1S_0$ and in a single specific nuclear state $|m_1\rangle$ and let us call this state $|g_1\rangle = |^1S_0\rangle \otimes |m_1\rangle$. Using optical Raman transitions, we can couple this state to another state $|g_2\rangle = |^1S_0\rangle \otimes |m_2\rangle$ with a different nuclear state $|m_2\rangle$, a process that would be otherwise forbidden by the SU(N) symmetry of interactions. The manifold of auxiliary excited states comes from the electronic state $|e\rangle = {}^3P_1$. We emphasize that this is not an eigenstate of the atomic Hamiltonian, as its total electronic angular momentum is $J = 1$, which implies that there is a significant hyperfine coupling to the nuclear states, hence the eigenstates are labeled by the total angular momentum $F = I + J$ (nuclear + electronic) and by its component along a given axis m_F. The allowed values are given by standard sum rules, for example ^{173}Yb has $I = \frac{5}{2}$ and therefore $F = \frac{3}{2}, \frac{5}{2}, \frac{7}{2}$, with $m_F = -F, \ldots, +F$. The necessary energy splitting between the two otherwise degenerate ground states is provided by an external uniform and static magnetic field $\mathbf{B} = B\hat{z}$ via Zeeman effect: $\hbar(\omega_{0,1} - \omega_{0,2}) = \mu_B g_g (m_2 - m_1)B$, where μ_B is the Bohr magneton and g_g the nuclear Landé g-factor when the electronic state is $^1S_0$. It should be noted that this magnetic field also induces extra Zeeman splittings in the manifold of excited states.

Raman transitions are induced by two laser beams with wave vectors $\mathbf{k}_1$, $\mathbf{k}_2$ perpendicular to $\mathbf{B}$ and frequencies ω_1, ω_2 having a slight detuning $\delta\omega_1 = \delta\omega_2 = \Delta$ with respect to an arbitrary electronic transition taken as a reference. The geometry of the laser beams controls the spatial dependence of the phase field associated to the effective Rabi transitions: $\varphi(\mathbf{r}) = (\mathbf{k}_1 - \mathbf{k}_2) \cdot \mathbf{r} + \phi$, where we can set the constant term $\phi = 0$ without loss of generality.

The correct choice of polarization vectors $\mathbf{u}_1$, $\mathbf{u}_2$ is a crucial and subtle point. First of all, this choice determines the angular momentum that the photon field can exchange with the atom, as the process should obey the conservation of angular momentum. For example, let's focus on $\mathbf{u}_1$ and consider an even linear combination $\mathbf{u}_1 = (\mathbf{u}_1^+ + \mathbf{u}_1^-)/\sqrt{2}$ of two Jones polarization vectors $\mathbf{u}_1^\pm$ describing right-handed and left-handed polarization states with respect to the propagation direction $\mathbf{k}_1$. This results in a linearly

polarized wave with the electric field perpendicular to $\hat{z}$ and $\mathbf{k}_1$. Such a field can only induce $\sigma^{\pm}$ transitions, i.e. it can only change the $\hat{z}$ component of the total angular momentum by $\Delta m_F = \pm 1$. The reason is that, in the dipole approximation, where the atom is treated as a point-like electric dipole, this electric field is indistinguishable from the electric field of a wave propagating along $\hat{z}$ and being in an even superposition of the two corresponding circular polarizations, as sketched in fig. [2.2 (d)]. As another example, let's consider the linear combination $\mathbf{u}_1 = i(\mathbf{u}_1^+ - \mathbf{u}_1^-)/\sqrt{2}$ describing a linearly polarized light with the electric field parallel to $\hat{z}$: such a field can only induce π transitions, i.e. transitions between states with $\Delta m_F = 0$. In general, if the light is linearly polarized along any direction perpendicular to $\mathbf{k}_1$, it will induce both $\sigma^{\pm}$ and π transitions with different probabilities, depending on the specific angle between the polarization direction and the $\hat{z}$ axis. Secondly, the projection of the atomic dipole moment along the polarization direction affects the couplings $\Omega_{i,\alpha\beta}$ and consequently the effective Rabi frequency and the AC Stark light-shifts (see eq. [2.20]). Depending on the specific polarization and detuning chosen for the beams, it is possible to induce effective tunneling events in a subset of N different nuclear states out of the $2I+1$ available. The remaining states are cut off either by conservation of angular momentum, or by a large value of the AC light shift, such that the effective energy of that state is too high.

Let us give a concrete example focusing on the specific case of ^{173}Yb. The typical intensity of the Zeeman magnetic field is ≈ 150 G, and the induced energy splitting between two nuclear states with successive values of m is $\approx \hbar \times 31$ kHz. If the atomic cloud is initially polarized in the nuclear state with lowest energy ($m = -\frac{5}{2}$) and we choose for both beams a linear polarization perpendicular to $\mathbf{B}$, then only $\sigma^{\pm}$ electronic transitions are allowed. This implies that two-photon processes can only induce an overall change of the $\hat{z}$ component of angular momentum $\Delta m = \pm 2$, effectively coupling three states ($m = -\frac{5}{2}, -\frac{1}{2}, +\frac{3}{2}$) and cutting off the other three. This coupling is actually realized by choosing the laser frequencies in such a way that $\omega_1 - \omega_2 \approx \Delta m \times 31\,\text{kHz} \approx 62$ kHz. Furthermore, in order to minimize inelastic collisions in the excited channel, ω_1 and ω_2 are blue-detuned by ≈ 1.88 GHz with respect to the reference atomic transition $^1S_0 \to {}^3P_1(F = \frac{7}{2})$ (measured in absence of magnetic field). In principle, three out of six nuclear states are involved in the dynamics; but the AC Stark light-shift of the state $m = +\frac{3}{2}$ is much larger than the other two, which are instead comparable. This further restricts the dynamics to only two states out of six: $m = -\frac{5}{2}, -\frac{1}{2}$, as the state $m = +\frac{3}{2}$ is effectively cut-off by the large energy barrier required to populate it. In this case, the synthetic direction is very short, and in fact limited to only two sites.

The realization of a synthetic direction with three sites requires to have almost equivalent light-shifts for the three states, which can be obtained by tuning the polarization of laser light. This result has been achieved by means of linearly polarized light along a direction forming an angle of ≈ 55 degrees with respect to $\hat{z}$; however, this allows $\sigma^{\pm}$-π electronic transitions with an overall exchange of angular momentum $\Delta m = \pm 1$. As a result, none of the six nuclear states is exactly cut-off from the dynamics; but choosing $\omega_2 - \omega_1 \approx 62$ kHz actually makes these spurious $\sigma^{\pm}$-π processes off-resonant, limiting the significant population to the states $m = -\frac{5}{2}, -\frac{1}{2}, +\frac{3}{2}$. Tuning the light-shifts inevitably introduces asymmetries in the effective Rabi frequencies, providing different hopping amplitudes to different bonds in the synthetic dimension; yet a compromise between equivalent light-shifts and equivalent Rabi frequencies can be found. With the experimental setting reported above, the ratio of Rabi frequencies is $\Omega_{-\frac{1}{2},+\frac{3}{2}} \approx 1.41\,\Omega_{-\frac{5}{2},-\frac{1}{2}}$ (while $\Omega_{-\frac{5}{2},+\frac{3}{2}} = 0$ as a consequence of the beams setup); while the light-shifts are $\varepsilon_{-\frac{5}{2}} = \varepsilon_{-\frac{1}{2}}$ and $\varepsilon_{\frac{3}{2}} \approx \varepsilon_{-\frac{5}{2}} + 0.16\,\Omega_{-\frac{5}{2},-\frac{1}{2}}$.

Further increasing the number of sites N along the synthetic direction is possible in principle, but it represents a technical challenge due to the problem of light-shifts. In particular, the light-shifts associated to all of the N states should be at least comparable, if not equivalent; moreover, the light-shifts of the

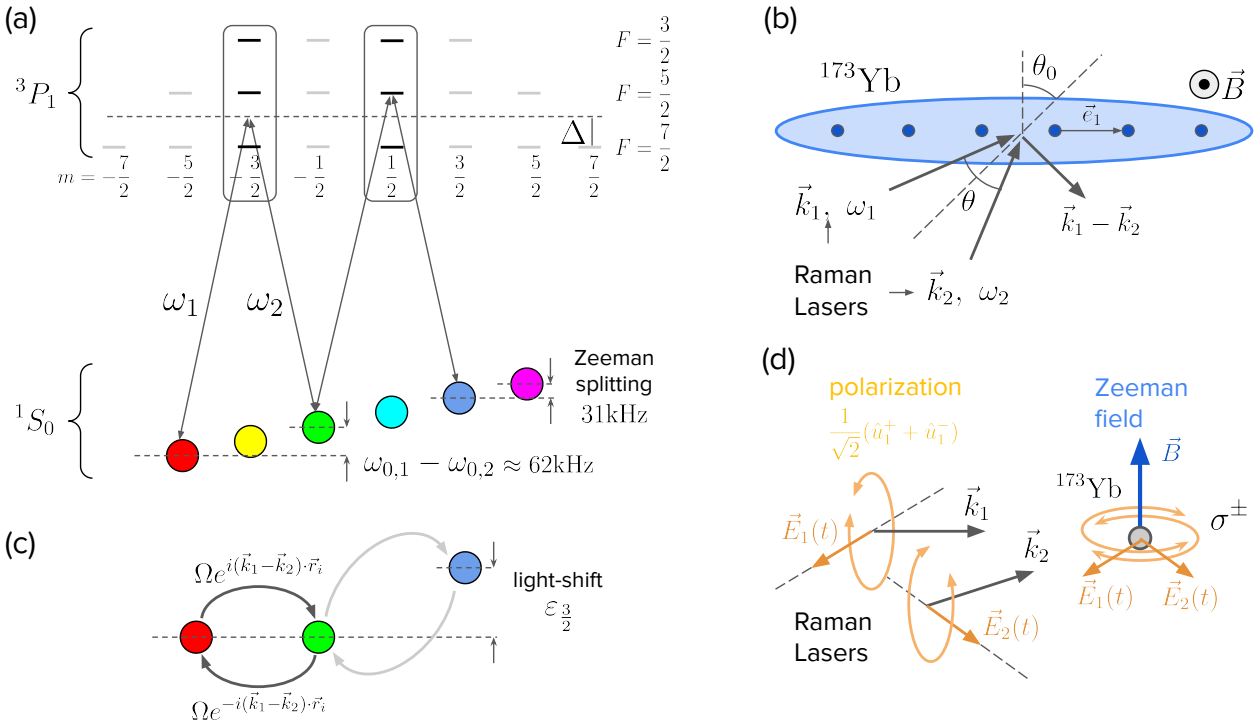

Figure 2.2: Realization of synthetic dimension and artificial gauge fields with ^{173}Yb at LENS (adapted from [20]). (a) Laser-induced $\sigma^\pm$ Raman transitions through the $^3P_1$ manifold effectively couple a subset of nuclear states: $m=-\frac{5}{2},-\frac{1}{2},+\frac{3}{2}$. (b) Geometry of Raman laser beams hitting an optical lattice loaded with ^{173}Yb in presence of a Zeeman magnetic field. (c) Sketch of the effective model: the state $m=+\frac{3}{2}$ has a large light-shift and is cut off from the dynamics. (d) Polarization of laser light that induces $\sigma^\pm$ transitions.

remaining $(2I+1)-N$ states should be large to cut these states off the dynamics, or these states should be decoupled as a result of conservation laws. Realizing this with only two laser beams requires a very difficult balance of all the properties of light; however one could in principle use more than two lasers to have more tunable degrees of freedom.

Taking into account the presence of an optical lattice and neglecting differences in the light-shifts, we can finally describe this system with the following Hamiltonian:

$$H=-t\sum_{\langle ij\rangle}\sum_{\sigma}\left(c^\dagger_{i\sigma}c_{j\sigma}+\text{h.c.}\right)+\sum_{j,\rho>\sigma}\left(\Omega_{\sigma\rho}e^{i\varphi(\mathbf{r}_j)}c^\dagger_{j\sigma}c_{j\rho}+\text{h.c.}\right)+\frac{U}{2}\sum_j n_j(n_j-1)-\mu\sum_j n_j \quad (2.21)$$

where $\Omega^*_{\sigma\rho}=\Omega_{\rho\sigma}$ and $\Omega_{\sigma\rho}=0$ if $\rho\neq\sigma\pm1$. Moreover, we have included $\hbar$ in the definition of $\Omega_{\rho\sigma}$. We have introduced two indexes σ and ρ labeling the N states involved in the dynamics and we have conventionally chosen their numerical values to run from $-\frac{N-1}{2}$ to $\frac{N+1}{2}$ at steps of 1: this choice is motivated by the fact that, when $N=2I+1$, these labels coincide with the quantum number m of the nuclear state. This model can be regarded as a system of spinless fermions moving on a $(d+1)$-dimensional geometrical structure, where d is the dimensionality of the optical lattice [64]. Every site in this structure is labeled by two indexes: $\mathbf{r}_j$, the d-dimensional vector labeling the optical lattice sites, and the "flavor" index σ, which labels the nuclear state. The SU(N) symmetry is explicitly broken by Raman processes; however the scattering lengths are not modified and the interaction part of Hamiltonian [2.21] is still SU(N) symmetric.

The resulting interaction is peculiar, as it is local with respect to the real lattice dimensions, but completely long-range in the synthetic dimension, as the occupation of two sites $(\mathbf{r}_j, \sigma)$ and $(\mathbf{r}_j, \rho)$ is penalized by an energy cost U for any $\sigma \neq \rho$. Furthermore, this model features the presence of an artificial gauge field, specifically an artificial static magnetic field perpendicular to the synthetic direction. This can be seen by computing the geometric phase acquired by a particle hopping all around a closed plaquette

$$(\mathbf{r}_i, \sigma) \to (\mathbf{r}_j, \sigma) \to (\mathbf{r}_j, \sigma + 1) \to (\mathbf{r}_i, \sigma + 1) \to (\mathbf{r}_i, \sigma),$$

where i and j denote nearest neighbors in the real directions, see for example fig. [2.3 (b)]. The result is $\varphi(\mathbf{r}_j) - \varphi(\mathbf{r}_i)$ and it represents the dimensionless artificial magnetic flux through the plaquette.

Written in this form, the Hamiltonian [2.21] is not manifestly invariant under translations along the real directions (a circumstance that complicates the numerical analysis with methods such as DMFT). However, it can still be made translation invariant by performing a unitary transformation of the fermionic operators:

$$c_{j\sigma} \to e^{i\sigma\varphi(\mathbf{r}_j)} c_{j\sigma}, \qquad c^\dagger_{j\sigma} \to e^{-i\sigma\varphi(\mathbf{r}_j)} c^\dagger_{j\sigma}, \qquad n_{j\sigma} \to n_{j\sigma}, \tag{2.22}$$

which transforms [2.21] into

$$H = -t \sum_{\langle ij \rangle} \sum_{\sigma} \left(e^{i\sigma[\varphi(\mathbf{r}_j) - \varphi(\mathbf{r}_i)]} c^\dagger_{i\sigma} c_{j\sigma} + \text{h.c.} \right) + \sum_{j,\sigma} \Omega_\sigma \left(c^\dagger_{j\sigma} c_{j\sigma+1} + \text{h.c.} \right) + \frac{U}{2} \sum_j n_j(n_j - 1) - \mu \sum_j n_j. \tag{2.23}$$

In this new gauge, the phase of Raman processes is uniform over the whole real lattice; but in turn it is the hopping along real directions that acquires a flavor-dependent phase factor, as shown in fig. [2.3 (c)]. However, the geometric phase accumulated by hopping around a plaquette, which is the physical observable, remains unchanged. The Hamiltonian [2.23] is now manifestly translation invariant, as the phase factor $\varphi(\mathbf{r}_j) - \varphi(\mathbf{r}_i) = (\mathbf{k}_1 - \mathbf{k}_2) \cdot (\mathbf{r}_j - \mathbf{r}_i)$ depends on the difference $\mathbf{r}_j - \mathbf{r}_i$; however hopping along different directions of the optical lattice can occur with different phase factors. This works only if Raman processes connect nearest neighbors along the synthetic direction: $\Omega_{\sigma\rho} = \Omega_\sigma(\delta_{\rho,\sigma+1} + \delta_{\rho,\sigma-1})$ (where we assume that Ω_σ is real without loss of generality), which is consistent with the experimental realization.

Interestingly, if the $(d+1)$-dimensional structure is bipartite, (i.e. if we can group the sites in two sublattices A and B such that every nearest neighbor of a site in A belongs to B and vice versa), the Hamiltonian [2.23] is particle-hole symmetric at $\mu = 0$. The reason is that it is invariant under the particle-hole transformation $c_{j\sigma} \to (-1)^{R_{j\sigma}} c^\dagger_{j\sigma}$, where $R_{j\sigma} = 1$ if $(\mathbf{r}_j, \sigma) \in A$ and $R_{j\sigma} = 0$ otherwise. This implies that the half-filling condition, i.e. the condition to have $N \times N_{\text{sites}}/2$ atoms on the structure, is realized setting $\mu = 0$.

2.3 Current operators

The most remarkable feature of synthetic ladders is the fact that their low-temperature equilibrium states are characterized by the presence of flavor-dependent persistent currents that are experimentally detectable. Therefore, it is important to provide proper definitions of current operators and to understand their general properties, which is the purpose of this section.

The definition of current operators stems from the continuity equation for every node of the structure, which states that the variation of local density over time equals the net current flow on the node. By

definition, a node is a site on the $(d+1)$-dimensional structure and it is labeled by a lattice vector $\mathbf{r}_i$ and a flavor index σ. The continuity equation at any node can be computed from the Heisenberg equation for the density operator $n_{i\sigma}$ at that node:

$$\frac{dn_{i\sigma}}{dt} = \frac{i}{\hbar}\left[H, n_{i\sigma}\right]. \tag{2.24}$$

Computing the commutator with [2.23], working in natural units $\hbar = k_B = 1$ and introducing a set of lattice vectors $\mathbf{e}_a$ $(a = 1, \ldots, d)$, we get

$$\frac{dn_{i\sigma}}{dt} = -\sum_{a=1}^{d}\left(I_{(\mathbf{r}_i,\sigma);\,(\mathbf{r}_i+\mathbf{e}_a,\sigma)} - I_{(\mathbf{r}_i-\mathbf{e}_a,\sigma);\,(\mathbf{r}_i,\sigma)}\right) - \left(I_{(\mathbf{r}_i,\sigma);\,(\mathbf{r}_i,\sigma+1)} - I_{(\mathbf{r}_i,\sigma-1);\,(\mathbf{r}_i,\sigma)}\right), \tag{2.25}$$

where[1]

$$I_{(\mathbf{r}_i,\sigma);\,(\mathbf{r}_j,\rho)} = -ite^{i\sigma[\varphi(\mathbf{r}_j)-\varphi(\mathbf{r}_i)]}c^{\dagger}_{i\sigma}c_{j\rho} + \text{h.c.} \tag{2.26}$$

$$I_{(\mathbf{r}_i,\sigma);\,(\mathbf{r}_i,\rho)} = i\Omega_{\sigma\rho}c^{\dagger}_{i\sigma}c_{j\rho} + \text{h.c.}. \tag{2.27}$$

As we have mentioned, eq. [2.25] is a discretized version of the continuity equation, where the right-hand side corresponds to the divergence of a current operator. The quantity $I_{(\mathbf{r}_i,\sigma);\,(\mathbf{r}_j,\rho)}$ introduced in eq. [2.26] can thus be interpreted as the current flowing along the bond connecting the two (nearest neighbor) nodes $(\mathbf{r}_i,\sigma)$ and $(\mathbf{r}_j,\rho)$. In any equilibrium or stationary state, where $d\langle n_{i\sigma}\rangle/dt = 0$ on every node, the expectation value of eq. [2.25] can be also interpreted as a Kirchhoff's current law for the circuit, and it is a useful consistency check for any numerical method.

We can now define the average current flowing along a real direction $\mathbf{e}_a$ associated to fermions of flavor σ (flavor current) and the total current flowing along the synthetic direction on the real site $\mathbf{r}_j$ (local current),

$$I_{a,\sigma} = \frac{1}{N_{\text{sites}}}\sum_i I_{(\mathbf{r}_i,\sigma);(\mathbf{r}_i+\mathbf{e}_a,\sigma)} \qquad \text{flavor current,} \tag{2.28}$$

$$I_i = \sum_\sigma I_{(\mathbf{r}_i,\sigma);(\mathbf{r}_i,\sigma+1)} \qquad \text{local current.} \tag{2.29}$$

An interesting observation is that the current operators in eqs. [2.28, 2.29] can be written as derivatives of the Hamiltonian with respect to auxiliary variables, called Peierls phases [65]. These are fictitious complex phase factors that are included in the hopping matrix elements and that are just used as derivation variables. For example, the flavor paramagnetic current operator $I_{a,\sigma}$ can be obtained by attaching a phase factor $e^{i\phi_{a,\sigma}}$ to the hopping matrix element on that specific flavor σ and direction a: $t_{a,\sigma} \to t_{a,\sigma}e^{i\phi_{a,\sigma}}$ (Peierls substitution), and then deriving with respect to $\phi_{a,\sigma}$ at $\phi_{a,\sigma} = 0$:

$$I_{a,\sigma} = \frac{1}{N_{\text{sites}}}\left.\frac{\partial H}{\partial \phi_{a,\sigma}}\right|_{\phi_{a,\sigma}=0}. \tag{2.30}$$

Similarly, the local paramagnetic current operator on a rung labeled by $\mathbf{r}_i$ can be obtained by a Peierls substitution in the Raman hopping matrix elements of that specific rung: $\Omega_{i;\,\sigma,\sigma+1} \to \Omega_{i;\,\sigma,\sigma+1}e^{i\phi_i}$, and then taking the derivative

$$I_i = \left.\frac{\partial H}{\partial \phi_i}\right|_{\phi_i=0}. \tag{2.31}$$

[1] We can write them in units of the international system setting $t \to t/\hbar$ and $\Omega_{\sigma\rho} \to \Omega_{\sigma\rho}/\hbar$.

When the system satisfies periodic boundary conditions (PBC) along the real directions, we can use the Fourier transformation in momentum space of the fermionic operators (see eq. [2.44]) to rewrite the flavor current [2.28] in a more transparent and practical fashion:

$$\boxed{I_{a,\sigma} = \frac{2t}{N_{\text{sites}}} \sum_{\mathbf{k}\in \text{BZ}} \sin\left(\mathbf{k}\cdot\mathbf{e}_a + \sigma\gamma_a\right) n_{\mathbf{k}\sigma},} \tag{2.32}$$

where $n_{\mathbf{k}\sigma} = c^\dagger_{\mathbf{k}\sigma} c_{\mathbf{k}\sigma}$ is the number operator with momentum $\mathbf{k}$ and flavor σ and

$$\gamma_a = \varphi(\mathbf{r}_i + \mathbf{e}_a) - \varphi(\mathbf{r}_i) = (\mathbf{k}_1 - \mathbf{k}_2)\cdot\mathbf{e}_a \tag{2.33}$$

represents the synthetic flux on a plaquette with one side along the direction $\mathbf{e}_a$. Under PBC, the local current [2.29] is the same on every lattice site and in momentum space it is given by

$$I_i = \sum_{\mathbf{k}\sigma} i\Omega_\sigma \left(c^\dagger_{\mathbf{k}\sigma} c_{\mathbf{k}\sigma+1} - c^\dagger_{\mathbf{k}\sigma+1} c_{\mathbf{k}\sigma} \right). \tag{2.34}$$

Finally, we define the total paramagnetic current along the real directions as the sum of all the flavor currents: $\mathbf{I} = \sum_\sigma \mathbf{I}_\sigma$. This concept is not peculiar of systems with broken SU(N) symmetry, but it is used in many contexts to measure the metallic character of a system, as we discuss in more detail in chapter [4]. Sometimes it is also called "Drude current", since it can be used to compute the Drude weight, as shown in appendix [B].

Eq. [2.32] emphasizes the connection between the flavor-current and the experimentally accessible flavor-resolved momentum distribution. The latter can be measured by absorption imaging exploiting the ${}^1S_0 \leftrightarrow {}^1P_0$ transition, after removing the Raman lasers and the optical lattice to realize a freely expanding gas. The momentum distribution of a specific flavor is obtained by removing particles with all the other flavors from the expanding cloud via suitable optical processes before performing absorption imaging [20, 62].

2.3.1 Chiral current

In the specific case of uniform Raman coupling $\Omega_\sigma \equiv \Omega$, Hamiltonian [2.23] features a point reflection symmetry about the central point of the $(d+1)$-dimensional structure, namely it is invariant under the transformation $c_{\mathbf{r}_i,\sigma} \to c_{-\mathbf{r}_i,-\sigma}$ [66]. The same symmetry is inherited by the eigenstates, therefore one can prove that the expectation values of the flavor currents satisfy $\langle \mathbf{I}_{-\sigma}\rangle = -\langle \mathbf{I}_\sigma\rangle$. An immediate consequence of this property is that, when N is odd, the expectation value of the current in the central flavor vanishes: $\langle \mathbf{I}_0\rangle = 0$. In the present work we will mostly deal with systems having $N = 2$ or $N = 3$ flavors and point reflection symmetry: these systems only have one non-trivial independent flavor current, so it is common use to encode the relevant information in the definition of *chiral current* as the difference of currents in the two outermost flavors:

$$\mathbf{I}_{\text{chir}} = \mathbf{I}_{-\frac{N-1}{2}} - \mathbf{I}_{\frac{N-1}{2}}. \tag{2.35}$$

In systems with $N > 3$, the current does not necessarily flow only along the edge flavors, hence multiple chiral currents $\mathbf{I}_{-\sigma} - \mathbf{I}_\sigma$ should be defined (more precisely, the independent currents are $N/2$ if N is even and $(N-1)/2$ if N is odd). Making use of the Peierls substitution discussed above, it is straightforward to prove that the chiral current can be written (up to a constant prefactor) as the derivative of the Hamiltonian with respect to the synthetic flux:

$$I_{\text{chir},a} = -\frac{2}{N_{\text{sites}}(N-1)} \frac{\partial H}{\partial \gamma_a}. \tag{2.36}$$

The expectation value of the chiral current operator in a thermal equilibrium state of the system at a generic temperature T can be computed as

$$\langle I_{\text{chir},a}\rangle = -\frac{2}{N_{\text{sites}}(N-1)}\sum_n \frac{e^{-\beta E_n}}{\mathcal{Z}}\langle n|\frac{\partial H}{\partial \gamma_a}|n\rangle, \tag{2.37}$$

where $|n\rangle$ is the n-th eigenstate of the Hamiltonian H, E_n is the associated energy and $\mathcal{Z} = \sum_n e^{-\beta E_n}$ is the partition function. Strictly speaking, a properly defined paramagnetic current on a state has a residual dependence on the auxiliary Peierls phase that comes from the energies $E_n(\phi)$ and the eigenstates $|n(\phi)\rangle$, which are computed starting from the Peierls-transformed Hamiltonian $H(\phi)$. However, in the following we are interested in the case where there is no external field applied, so we can take the limit $\phi \to 0$, or we can directly use the eigenstates of the original Hamiltonian $E_n(\phi = 0)$ and $|n(\phi = 0)\rangle$. As we will see, the crucial feature of fermions coupled to a synthetic gauge field is precisely the fact that they support paramagnetic persistent currents **even in absence of external driving fields**. In fact it is the synthetic field that provides the necessary driving force to support a persistent current. That being said, we can make progresses using the Hellmann-Feynman theorem:

$$\langle I_{\text{chir},a}\rangle = -\frac{2}{N_{\text{sites}}(N-1)}\sum_n \frac{e^{-\beta E_n}}{\mathcal{Z}}\frac{\partial E_n}{\partial \gamma_a} = \frac{2T}{N_{\text{sites}}(N-1)}\frac{1}{\mathcal{Z}}\frac{\partial}{\partial \gamma_a}\sum_n e^{-\beta E_n},$$

and we finally get[2]

$$\boxed{\langle I_{\text{chir},a}\rangle = \frac{2T}{N_{\text{sites}}(N-1)}\frac{\partial}{\partial \gamma_a}\log \mathcal{Z}.} \tag{2.38}$$

Therefore, the chiral current along $\hat{\mathbf{e}}_a$ is, up to a normalization constant, the derivative of the grand-canonical potential $\Omega = -\frac{1}{\beta}\log \mathcal{Z}$ with respect to the synthetic flux γ_a.

If the particles are not interacting, we can obtain a more explicit version of eq. [2.38], writing the chiral current in terms of the band structure. The partition function $\mathcal{Z}$ of non-interacting fermions with energy bands of momentum dispersion $\varepsilon_{\mathbf{k}\ell}$, where $\ell = 1, \dots, N$ is the band index, is given by

$$\mathcal{Z} = \sum_n e^{-\beta E_n} = \prod_{\mathbf{k}\in \text{BZ}}\prod_{\ell=1}^{N}\left(1 + e^{-\beta(\varepsilon_{\mathbf{k}\ell}-\mu)}\right). \tag{2.39}$$

Using eq. [2.38] and introducing the Fermi function $f(x) = 1/(e^{\beta x}+1)$, we obtain the formal expression

$$\langle I_{\text{chir},a}\rangle = -\frac{2}{N_{\text{sites}}(N-1)}\sum_{\mathbf{k}\in \text{BZ}}\sum_{\ell=1}^{N} f(\varepsilon_{\mathbf{k}\ell}-\mu)\frac{\partial \varepsilon_{\mathbf{k}\ell}}{\partial \gamma_a}. \tag{2.40}$$

In the following sections, we use this formalism to evaluate analytically the chiral current for non-interacting two-leg and three-leg ladders, while in chapter [3] we also include the interactions.

[2]Units of the international system are restored multiplying the chiral current by $k_B/\hbar$.

2.4 Non interacting ladders

2.4.1 Non interacting two-leg ladder

We begin our analysis by neglecting the atom-atom local interaction, i.e. setting $U = 0$ in eq. [2.21], and particularizing the discussion to the case of two flavors ($N = 2$) and one real dimension ($d = 1$), where analytic results can be obtained. In the following, we also identify the state $\sigma = +\frac{1}{2}$ with the symbol $\uparrow$ and $\sigma = -\frac{1}{2}$ with the symbol $\downarrow$. In this case there is only one independent element in the Raman hopping matrix: $\Omega_{\uparrow\downarrow} = \Omega_{\downarrow\uparrow} \equiv \Omega$. Therefore the resulting Hamiltonian reduces to

$$H = -t \sum_{j=1}^{N_{\text{sites}}} \sum_{\sigma=\uparrow\downarrow} \left(c^\dagger_{j\sigma} c_{j+1\sigma} + \text{h.c.} \right) + \Omega \sum_{j=1}^{N_{\text{sites}}} \left(e^{i\gamma j} c^\dagger_{j\uparrow} c_{j\downarrow} + \text{h.c.} \right) - \mu \sum_j n_j. \tag{2.41}$$

In the following we will mostly assume periodic boundary conditions (PBC) along the real direction, unless otherwise stated.

The purpose of this section is to characterize the low-temperature equilibrium state of the system described by Hamiltonian [2.41] as a function of the parameters t, Ω and γ, assuming the half-filling condition (one particle per lattice site on average), which is realized for $\mu = 0$. The unitary transformation [2.22] that enforces translation invariance reduces to

$$c_{j\sigma} \to e^{i\sigma\gamma j} c_{j\sigma}, \qquad c^\dagger_{j\sigma} \to e^{-i\sigma\gamma j} c^\dagger_{j\sigma}; \tag{2.42}$$

and the Hamiltonian written in this new gauge is

$$H = -t \sum_j \sum_{\sigma=\pm\frac{1}{2}} \left(e^{i\sigma\gamma} c^\dagger_{j\sigma} c_{j+1\sigma} + \text{h.c.} \right) + \Omega \sum_j \left(c^\dagger_{j\uparrow} c_{j\downarrow} + \text{h.c.} \right). \tag{2.43}$$

As shown in fig. [2.3], this transformation changes the phase factors of all the tunneling matrix elements, but it does not change the "magnetic" flux per plaquette of the ladder, i.e. the phase accumulated by a particle hopping all around a plaquette and coming back to the starting point, which is always γ. Being manifestly translation invariant, [2.43] can be easily rewritten in the momentum space representation by introducing the spinor Ψ_j and its Fourier transform Ψ_k:

$$\Psi_j = \begin{pmatrix} c_{j\uparrow} \\ c_{j\downarrow} \end{pmatrix} = \frac{1}{\sqrt{N_{\text{sites}}}} \sum_{k \in \text{BZ}} e^{ikj} \Psi_k, \qquad \Psi_k = \frac{1}{\sqrt{N_{\text{sites}}}} \sum_j e^{-ikj} \Psi_j; \tag{2.44}$$

where, as a consequence of the periodic structure of the real lattice, the variable k can assume N_{sites} distinct values that are equally spaced in the first Brillouin zone (BZ): $k = -\pi + \frac{2\pi n}{N_{\text{sites}}}$, where $n = 0, \ldots, N_{\text{sites}} - 1$. Moreover, with the convention adopted here, the momentum is a dimensionless quantity. Remarkably, when the number of lattice sites is large, the spacing between adjacent momentum values $\frac{2\pi}{N_{\text{sites}}}$ is very small, and the discrete sum can be replaced by an integral according to the simple prescription $\sum_{k \in \text{BZ}} \to \frac{N_{\text{sites}}}{2\pi} \int_{\text{BZ}} dk$. The resulting Hamiltonian, written in momentum space, reads

$$H = \sum_{k \in \text{BZ}} \Psi^\dagger_k \hat{H}_k \Psi_k; \qquad \hat{H}_k = \begin{pmatrix} \varepsilon(k + \frac{\gamma}{2}) & \Omega \\ \Omega & \varepsilon(k - \frac{\gamma}{2}) \end{pmatrix}, \tag{2.45}$$

where $\varepsilon(k + \sigma\gamma) = -2t \cos(k + \sigma\gamma)$.

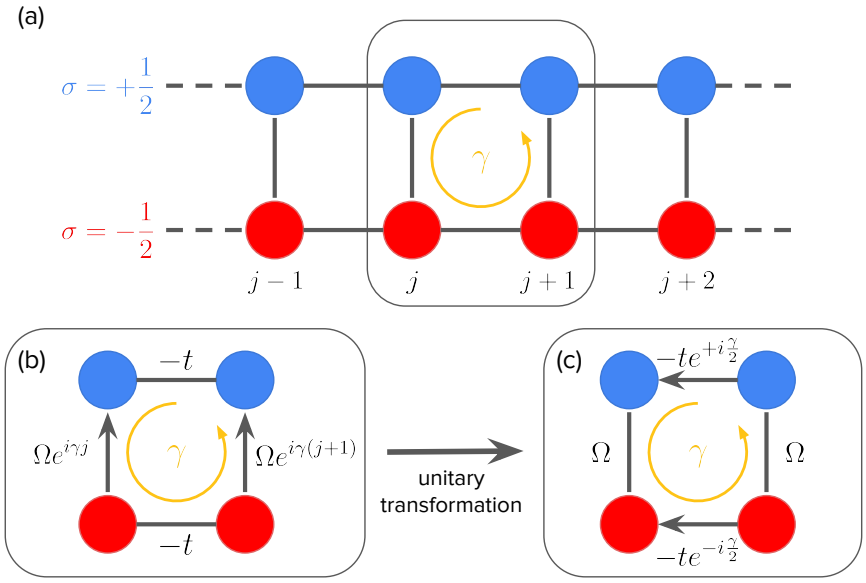

Figure 2.3: (a) Schematic representation of the two-leg ladder with one real (horizontal) and one synthetic (vertical) dimension. Each "leg" represents a fermionic flavor, i.e. a specific nuclear state and it is labeled by $\sigma = \pm\frac{1}{2}$; while each "rung" is labeled by the real site index $j = 1, \ldots, N_{\text{sites}}$. (b) Original hopping scheme with a j-dependent complex phase associated to Raman processes, as in eq. [2.41]. (c) Hopping scheme after the unitary transformation [2.42], where Raman processes have now a real amplitude, while real tunneling processes have a complex σ-dependent phase, as in eq. [2.43]. The arrows in (b) and (c) represent the hopping direction associated with the specified phase factor; hoppings in the opposite direction have the complex conjugate phase factor. Remarkably, the flux per plaquette is γ with both choices.

We can now diagonalize Hamiltonian [2.45] by means of a unitary transformation on the fermionic spinor $\Psi_k \to \Phi_k = \hat{P}_k^\dagger \Psi_k$, where $\hat{P}_k^\dagger$ is a unitary matrix ($\hat{P}_k \hat{P}_k^\dagger = \mathbb{1}$) that diagonalizes the 2×2 matrix $\hat{H}_k$: $\hat{P}_k \hat{H}_k \hat{P}_k^\dagger = \text{diag}[\varepsilon_-(k),\, \varepsilon_+(k)]$, with eigenvalues

$$\varepsilon_\pm(k) = -2t \cos\frac{\gamma}{2} \cos k \pm \Omega \sqrt{1 + \frac{4t^2}{\Omega^2} \sin^2 k \sin^2\frac{\gamma}{2}} \tag{2.46}$$

representing the dispersion relation of the band structure. It is instructive to study the Fermi points of this band structure: since by particle-hole symmetry the chemical potential is guaranteed to vanish at half filling ($\mu = 0$), then the Fermi points are solutions to the algebraic equations $\varepsilon_\pm(k) = 0$. After separating the square root from the rest, and after squaring both sides, we finally get the equation:

$$\cos^2 k = \sin^2\frac{\gamma}{2} + \left(\frac{\Omega}{2t}\right)^2 .$$

We can distinguish three cases:

- the equation does not admit any real solution if the right hand side is larger than 1, namely if

$$\sin^2\frac{\gamma}{2} + \left(\frac{\Omega}{2t}\right)^2 > 1 \quad \to \quad |\Omega| > 2t \cos\frac{\gamma}{2};$$

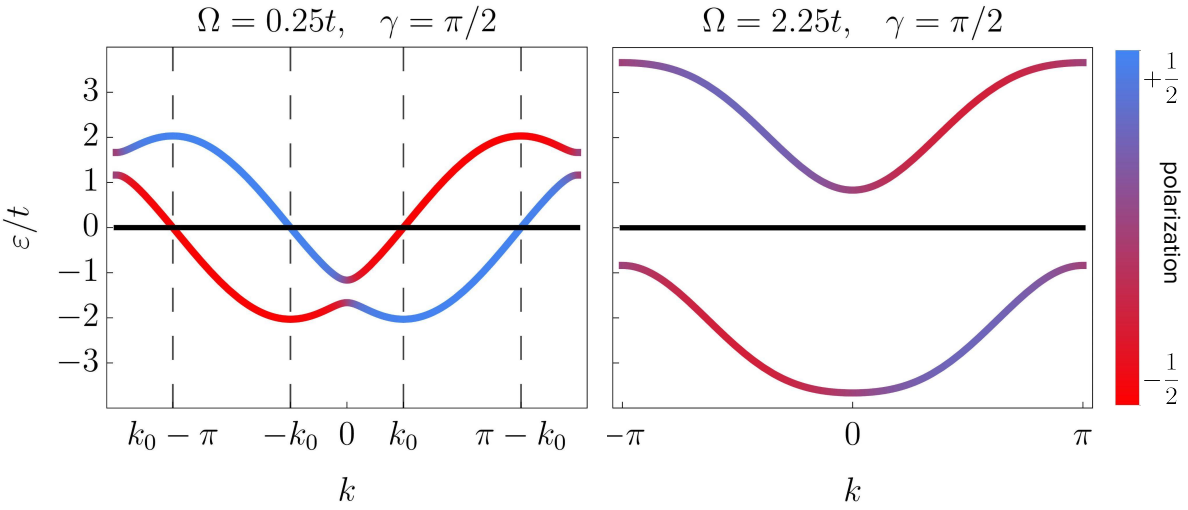

Figure 2.4: Band structure of the one dimensional two legs ladder shown in fig. [2.3]. The left panel represents the metallic phase at $\Omega < \Omega_c$, with four Fermi points located at $k = \pm k_0$ and $k = \pm(\pi - k_0)$. The right panel represents the insulating phase at $\Omega > \Omega_c$ with no Fermi points. The color scheme reflects the flavor-polarization of a state with given momentum k.

in this case there are no Fermi points, the spectrum is gapped at the Fermi level and – in analogy to the language of Solid State Physics – we can call this phase an *insulator*;

- if the right hand side is equal to 1, i.e. when $|\Omega| = 2t \cos\frac{\gamma}{2}$, the solutions to $\cos^2 k = 1$ are $k = 0, \pm\pi$; however, by direct substitution, one can see that $k = 0$ is such that only $\varepsilon_+(k) = 0$; whereas $k = \pm\pi$ are such that only $\varepsilon_-(k) = 0$. This means that the lower band touches the Fermi level at $k = \pm\pi$, while the upper band touches the Fermi level at $k = 0$.

- If the right hand side is smaller than 1, there are 4 symmetric solutions formally given by $k = \pm k_0$, and $k = \pm(\pi - k_0)$, where we have introduced the quantity

$$k_0 = \arccos\left(\sqrt{\sin^2\frac{\gamma}{2} + \left(\frac{\Omega}{2t}\right)^2}\right).$$

Again by direct substitution one can prove that $k = \pm k_0$ are the solutions of $\varepsilon_+(k) = 0$ and describe the points where the upper band crosses the Fermi level, while $k = \pm(\pi - k_0)$ are the solutions of $\varepsilon_-(k) = 0$ and describe the points where the lower band crosses the Fermi level. In analogy with the language of Solid State Physics this phase can be named a *metal*.

The band structure described above is schematically represented in fig. [2.4]. To summarize, varying t, Ω and γ, the system undergoes a quantum phase transition from a metallic state at $\Omega < \Omega_c$, where both bands are partially populated, to an insulating state at $\Omega > \Omega_c$, where only the lower band is populated. The critical value of the Raman coupling is given by $\Omega_c = 2t \cos\frac{\gamma}{2}$.

We can now use eq. [2.40] and the information about the band structure to compute the chiral current. Its behavior as a function of the physical parameters is shown in fig. [2.5]. The most salient feature is the presence of a sharp peak in correspondence of the quantum phase transition at zero temperature, followed

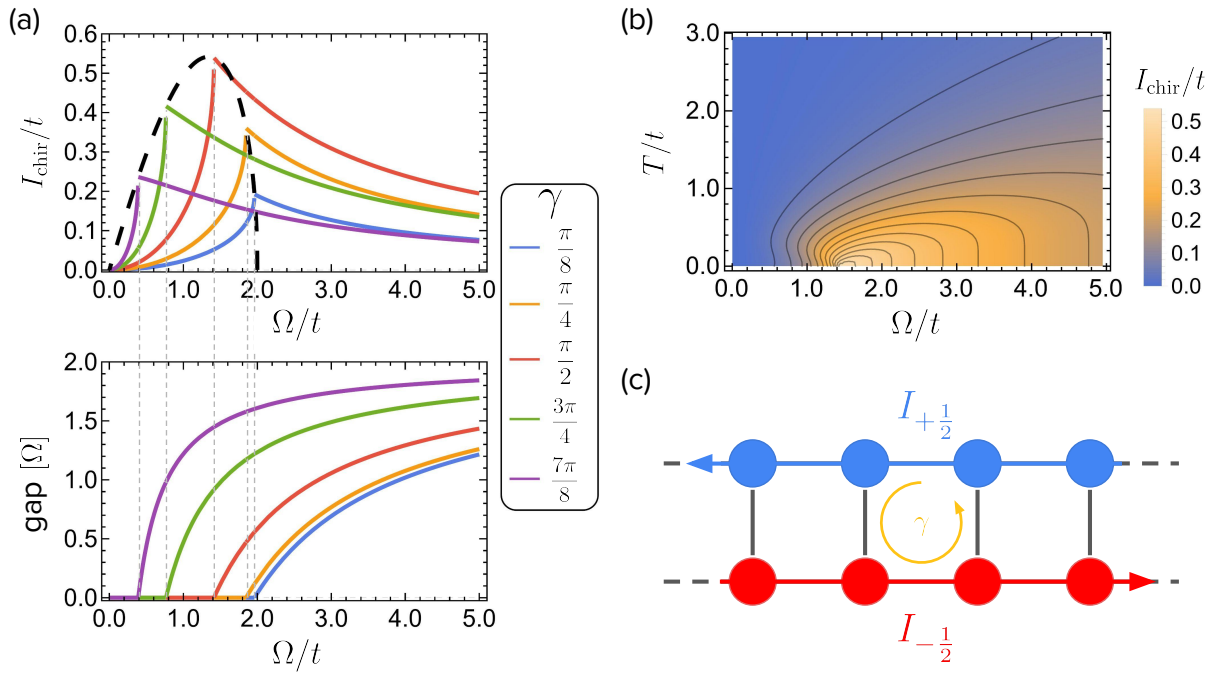

Figure 2.5: (a) Chiral current [top panel] and spectral gap [bottom panel] in the ground state of the non-interacting two-leg ladder as a function of Ω/t across the phase transition for several values of the flux γ (colored lines). The dashed line represents the location of the peak chiral current as a function of γ. (b) Color-plot of the chiral current as a function of the Raman coupling Ω/t and temperature T/t. (c) Schematic picture of the ladder showing the direction of the chiral current.

by a monotonic decrease in the insulating phase as the spectral gap increases. Another important aspect is the presence of a significantly large chiral current at finite temperatures, up to values comparable to the hopping scale t, which has enabled the experimental observation with currently available platforms [67]. However, chirality remains overall a peculiar feature of low-temperature equilibrium states, while it is completely hindered by large thermal fluctuations.

At zero temperature we can support these observations with simple analytic results. The grand canonical potential at $T = 0$ and $\mu = 0$ reduces to the internal energy, which is the energy of the many body ground state E_0. We can easily compute E_0 across the phase transition by summing the energies of all the occupied single particle states. At zero temperature, only states with energy below the chemical potential are populated, hence we get

$$E_0 = \frac{N_{\rm sites}}{2\pi}\left[\int_{-(\pi-k_0)}^{\pi-k_0} \varepsilon_-(k)dk + \int_{-k_0}^{k_0} \varepsilon_+(k)dk\right] \qquad \text{metal}$$

$$E_0 = \frac{N_{\rm sites}}{2\pi}\int_{-\pi}^{\pi} \varepsilon_-(k)dk \qquad \text{insulator} \tag{2.47}$$

These integrals can be formally evaluated by means of the incomplete elliptic integral of the second kind

$\Xi[b,m] = \int_0^b \sqrt{1 - m\sin^2 x}\, dx$, and the result is:

$$E_0 = -\frac{N_{\text{sites}}}{\pi}\left\{4t\cos\frac{\gamma}{2}\sin k_0 + |\Omega|\left[\Xi\left(\pi - k_0,\ -\frac{4t^2\sin^2\frac{\gamma}{2}}{\Omega^2}\right) - \Xi\left(k_{0a},\ -\frac{4t^2\sin^2\frac{\gamma}{2}}{\Omega^2}\right)\right]\right\} \qquad \text{metal}$$

$$E_0 = -\frac{N_{\text{sites}}}{\pi}|\Omega|\,\Xi\left(\pi,\ -\frac{4t^2\sin^2\frac{\gamma}{2}}{\Omega^2}\right). \qquad \text{insulator} \tag{2.48}$$

From eq. [2.38], the chiral current reduces to the negative derivative of the internal energy per particle: $\langle I_{\text{chir}}\rangle = -\frac{2}{N_{\text{sites}}}\frac{\partial E_0}{\partial\gamma}$. While the result is a little cumbersome for $\Omega < \Omega_c$, it is instead relatively simple and instructive in the insulating phase:

$$\boxed{\langle I_{\text{chir}}\rangle = \frac{\Omega}{\pi}\cot\frac{\gamma}{2}\left[\Xi\left(\pi, -\frac{4t^2\sin^2\frac{\gamma}{2}}{\Omega^2}\right) - F\left(\pi, -\frac{4t^2\sin^2\frac{\gamma}{2}}{\Omega^2}\right)\right], \qquad (\Omega \geq \Omega_c);} \tag{2.49}$$

where $F[b,m] = \int_0^b dx(1 - m\sin^2 x)^{-1/2}$ is the elliptic integral of the first kind. As shown in fig. [2.5 (a)], the chiral current features a sharp peak exactly at the phase transition, and the peak value can be computed by taking the limit $\Omega \to \Omega_c^+$ in eq. [2.49]:

$$I_{\text{chir}}^{\max} = \frac{\Omega_c}{\pi}\cot\frac{\gamma}{2}\left[\Xi\left(\pi, -\tan^2\frac{\gamma}{2}\right) - F\left(\pi, -\tan^2\frac{\gamma}{2}\right)\right]. \tag{2.50}$$

Searching for the maximum of this curve, we find that chirality is maximized when the synthetic flux is $\gamma = \frac{\pi}{2}$. The locus of peak currents as a function of the flux γ is shown with a dashed line in fig. [2.5 (a)]. In the deeply insulating regime, where $\Omega \gg t$, this expression can be expanded in powers of t/Ω and it yields the simple expression

$$\langle I_{\text{chir}}\rangle \approx \frac{t^2}{\Omega}\sin\gamma + \mathcal{O}\left(\frac{t^3}{\Omega^3}\right), \tag{2.51}$$

which explains the hyperbolic tails shown in fig. [2.5 (a)].

The same result can be obtained by computing the expectation value $\langle c^\dagger_{k\sigma}c_{k\rho}\rangle$ on the ground state, which is the (σ,ρ) component of the $N\times N$ dimensional matrix $\langle(\Psi_k^\dagger)^T\Psi_k^T\rangle$, where Ψ_k is the spinor introduced in eq. [2.44] and ^{T} indicates matrix transposition. The diagonal components represent the density of fermions with a given momentum k and a given flavor σ, while the off-diagonal terms are tunneling amplitudes along the synthetic direction between flavor ρ and σ. This object can be computed by moving to the basis that diagonalizes the Hamiltonian, i.e. using $\Psi_k = \hat{P}_k\Phi_k$:

$$\langle(\Psi_k^\dagger)^T\Psi_k^T\rangle = \hat{P}_k^*\langle(\Phi_k^\dagger)^T\Phi_k^T\rangle\hat{P}_k^T \tag{2.52}$$

and observing that, by construction, the matrix $\langle(\Phi_k^\dagger)^T\Phi_k^T\rangle$ must be diagonal, and the diagonal term at position (ℓ,ℓ) represents the fermionic population of the corresponding state in the ℓ-th band with momentum k, which is given by the Fermi function $f(\varepsilon_\ell(k) - \mu)$. The result is particularly simple for the specific case $T = 0$, $\Omega \gg t$, where again we can expand in powers of t/Ω to get:

$$\langle n_{k\downarrow}\rangle \approx \frac{1}{2}\left(1 + \frac{2t}{\Omega}\sin\frac{\gamma}{2}\sin k\right) + \mathcal{O}\left(\frac{t^3}{\Omega^3}\right),$$

$$\langle n_{k\uparrow}\rangle \approx \frac{1}{2}\left(1 - \frac{2t}{\Omega}\sin\frac{\gamma}{2}\sin k\right) + \mathcal{O}\left(\frac{t^3}{\Omega^3}\right),$$

$$\langle c^\dagger_{k\uparrow} c_{k\downarrow}\rangle = \langle c^\dagger_{k\downarrow} c_{k\uparrow}\rangle \approx -\frac{1}{2}\left(1 - \frac{2t^2}{\Omega^2}\sin^2\frac{\gamma}{2}\sin^2 k\right) + \mathcal{O}\left(\frac{t^3}{\Omega^3}\right). \tag{2.53}$$

We can now use eq. [2.32] to compute the flavor current and hence the chiral current, obtaining once again the result in eq. [2.51].

2.4.2 Non interacting three-leg ladder

As we have discussed in sec. [2.2], using the polarization dependence of the AC light-shifts, it is possible to tune the polarization of Raman light to include three nuclear states in the dynamics, realizing a three-leg ladder with ^{173}Yb. In the experimental realization outlined above, the light shift of the state $m = +\frac{3}{2}$ is slightly larger than the other two, and there is a difference between the Rabi frequencies connecting the central leg with the two outer legs. Nevertheless, since these discrepancies are relatively small, we can study a simplified version of the problem assuming that the three flavors are perfectly degenerate and that the tunneling amplitude along the synthetic direction is uniform [68]. This choice allows to investigate the salient qualitative features of the model by introducing a minimal amount of tunable parameters. Moreover, we limit our investigation to a filling factor of 1, where the number of atoms matches the number of sites in the optical lattice. On the one hand, this choice is motivated by the fact that, in chapter [3], we want to discuss how the chiral current is affected by the interaction-driven Mott transition, and this effect is expected to be particularly relevant for integer filling factors. On the other hand, with this choice we are keeping the same number of particles that we have considered for the two-legs ladder; so we can study how the exact same system behaves when the particles have an extra flavor degree of freedom available. From the experimental perspective, this is a straightforward extension of the two-legs ladder discussed in sec. [2.4.1], as the system preparation is the same and the only difference is the polarization direction of Raman light.

The resulting three-legs ladder is sketched in fig. [2.6 (b)] and it is described by the Hamiltonian

$$H = -t\sum_{\langle ij\rangle}\sum_{\sigma=\pm1,0}\left(e^{i\sigma\gamma}c^\dagger_{j\sigma}c_{j+1\sigma} + \text{h.c.}\right) + \Omega\sum_j\sum_{\sigma=-1,0}\left(c^\dagger_{j\sigma}c_{j\sigma+1} + \text{h.c.}\right) - \mu\sum_j n_j, \tag{2.54}$$

where now μ has to be adjusted to realize the desired filling factor, and it results in a non-trivial function of Ω/t and γ. A much simpler approach (at least for $T = 0$) is to work in the canonical ensemble, writing the Hamiltonian without the chemical potential term, finding the list of energy levels in ascending order and setting $\mu = E_F$, where E_F is the Fermi energy (N_{sites}-th element of the list). Assuming PBC along the real direction, we can switch to the momentum space representation

$$H = \sum_{k\in\text{BZ}}\Psi^\dagger_k\hat{H}_k\Psi_k, \qquad \hat{H}_k = \begin{pmatrix} \varepsilon(k+\gamma) & \Omega & 0 \\ \Omega & \varepsilon(k) & \Omega \\ 0 & \Omega & \varepsilon(k-\gamma)\end{pmatrix} \tag{2.55}$$

where $\varepsilon(k) = -2t\cos k$ and $\Psi^\dagger_k = (c^\dagger_{k,+1},\, c^\dagger_{k,0},\, c^\dagger_{k,-1})$. The dispersion relation of the energy bands can be obtained by numerically evaluating the eigenvalues of $\hat{H}_k$, and it is shown in fig. [2.6 (a)]. From the band structure, one can compute the chiral current, either using eq. [2.40], or computing the flavor resolved momentum distribution $\langle n_{k\sigma}\rangle$ and then using eq. [2.32]. The chiral current is shown as a function of Ω/t and γ in fig. [2.6 (c)]. The current flowing along the central leg ($\sigma = 0$) vanishes identically at equilibrium, as a result of the point reflection symmetry. This is not exactly true when an asymmetry between the two Raman hopping amplitudes is considered and the point reflection symmetry is broken;

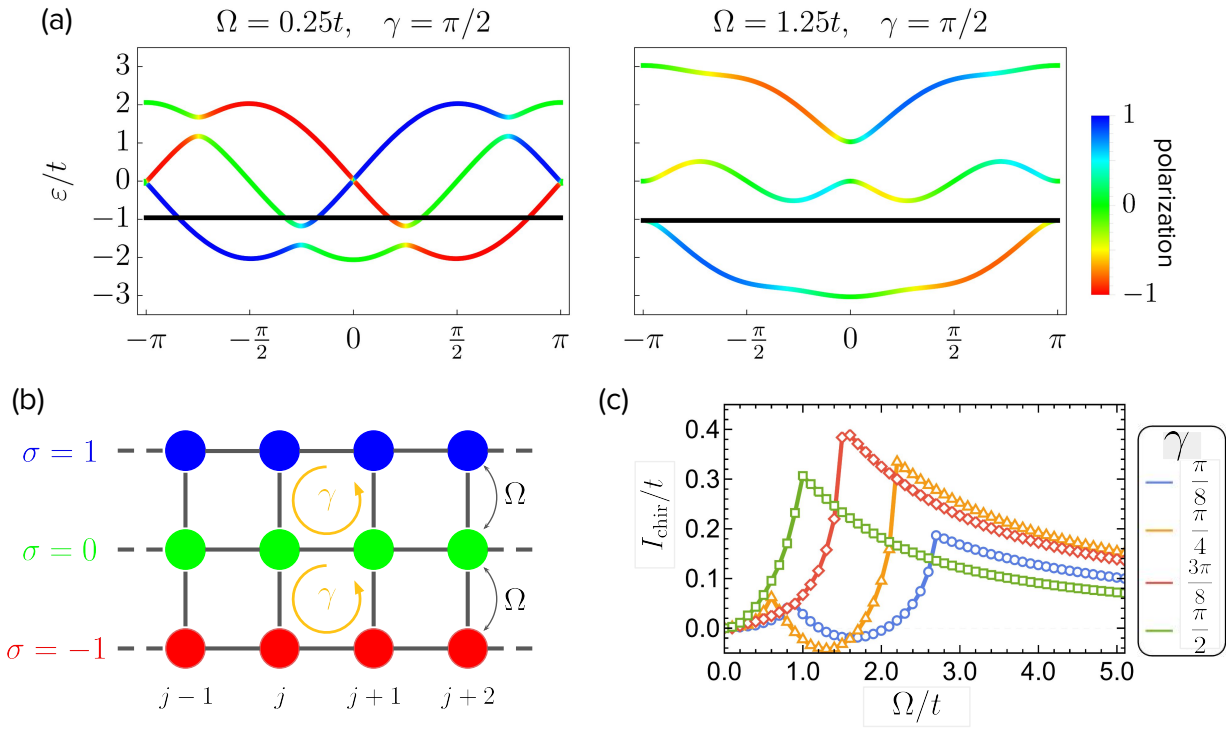

Figure 2.6: (a) Band structure of the three legs ladder in the metallic phase (left) and in the insulating phase (right). The color code reflects the flavor polarization of a given state. (b) Geometrical structure of the three legs ladder. (c) Chiral current as a function of Ω/t and γ with the sharp peak at the phase transition and a smaller peak at low fluxes and low Ω.

however $\langle I_0 \rangle$ is expected to be small as long as the hopping imbalance is small. This is confirmed looking at the experimental results in ref. [67].

The qualitative picture is for many aspects similar to the two-flavor case, with some differences that we emphasize here. First of all, as in the two-flavor case, we observe that increasing Ω above a critical value Ω_c eventually results in the opening of a spectral gap, leading to a quantum phase transition from a "metallic" phase to an "insulating" phase. In correspondence to the quantum phase transition, the chiral current features a sharp peak, followed by a hyperbolic decay $\approx t/\Omega$ in the insulating phase. This tail has a simple analytic expression that we can compute by means of perturbation theory in the limit $t \ll \Omega$. In particular, we can first compute the dispersion of the lowest energy band $\varepsilon_{\ell=1}(k)$ to second order in t/Ω, then integrate it over the Brillouin zone to get the ground state energy E_0 (in the insulating phase all the particles only populate the whole lowest band) and finally apply eq. [2.38]. Taking $t = 0$ as the unperturbed system, the zero order term is $\varepsilon^{(0)}_{\ell=1}(k) = -\sqrt{2}\Omega$, then treating t as a small perturbation, we get

$$\varepsilon_1(k) = -\Omega \left[\sqrt{2} + \frac{t}{\Omega}(1 + \cos\gamma)\cos k + \frac{t^2}{\Omega^2}\frac{\sin^2\frac{\gamma}{2}}{\sqrt{8}}\left(5 + 3\cos\gamma - (3 + 5\cos\gamma)\cos 2k\right) + \mathcal{O}\left(\frac{t^3}{\Omega^3}\right) \right].$$

Now, integrating over the Brillouin zone, all the terms with $\cos k$ and $\cos 2k$ are canceled out (which is the

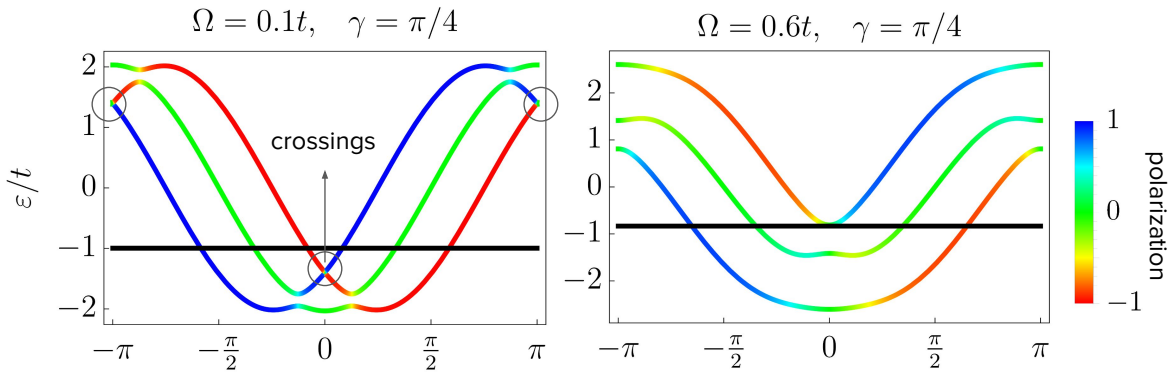

Figure 2.7: Band structure for the small flux $\gamma = \pi/4$. Deep in the metallic regime (left), the highest bands cross and all the bands are partially occupied. Increasing Ω, eventually the bands detach and one of them moves above the Fermi level (right), while the other two are still partially occupied (i.e. the phase is still a metal). The latter configuration induces a small boost in the chiral current.

reason why we have to go to second order to get a non trivial dependence of E_0 on γ), and we get

$$\frac{E_0}{N_{\text{sites}}} \approx -\Omega\sqrt{2} - \frac{t^2}{\Omega}\frac{\sin^2\frac{\gamma}{2}}{\sqrt{8}}\left(5 + 3\cos\gamma\right), \tag{2.56}$$

which finally leads to

$$I_{\text{chir}} = -\frac{1}{N_{\text{sites}}}\frac{\partial E_0}{\partial \gamma} \approx \frac{t^2}{\Omega}\frac{1 + 3\cos\gamma}{\sqrt{8}}\sin\gamma. \tag{2.57}$$

Interestingly, we observe that this function is maximized for $\gamma \approx 0.283\,\pi$.

A closer look to the metallic phase reveals the main differences with respect to the two-flavor case. From fig. [2.6 (c)] we observe that, for small values of the flux, the chiral current features a smaller peak deep in the metallic regime. We can explain this property by looking at the corresponding band structure, drawn for $\gamma = \pi/4$ in fig. [2.7], and comparing it to the same plot drawn for a larger flux $\gamma = \pi/2$ in fig. [2.6 (a)]. For every flux, at small values of Ω/t, the two highest bands cross at $k = 0$, but when Ω/t is increased, the two bands form an avoided crossing and eventually detach. If γ is sufficiently small, the detaching occurs in the metallic phase, then for some $\Omega < \Omega_c$ the highest band will be totally depopulated, while the other two will be partially occupied (right panel of fig. [2.7]). This configuration gives a small boost to the chiral character of the ground state. On the other hand, if γ is large, the detaching occurs in the insulating phase, as we observe in fig. [2.6 (a)], then none of the bands is depopulated below Ω_c and the effect disappears.

A subtle point to address when discussing a three-leg ladder is the role of topology. A thorough and complete discussion of this aspect is beyond the scope of this work; nevertheless we take a moment to discuss some literature results that we have independently verified [66]. First of all, the three-leg ladder can be regarded as a minimal version of the Harper-Hofstadter Hamiltonian with only three sites along one of the directions and open boundary conditions (OBC) on the same direction. From this observation, we are induced to think that the chiral current is the manifestation of an edge mode associated to the opening of boundary conditions on top of a topologically non trivial state. However, this statement is not precise for several reasons.

- The topologically non trivial state should be found by enforcing PBC along the synthetic direction, i.e. considering a modified version of [2.54], where we also include a term $\tilde{\Omega}\sum_j c^\dagger_{j,+1}c_{j,-1}$ + h.c. and imposing the identification of the neighbor of the top leg $\sigma_{\text{max}}+1$ with the bottom leg σ_{min}: $e^{i(\sigma_{\text{max}}+1)\gamma} = e^{i\sigma_{\text{min}}\gamma}$, where $\sigma_{\text{max}} = +1$ and $\sigma_{\text{min}} = -1$. This translates into a specific condition for the flux, which should be $\gamma = 2\pi n/3$, where n is an integer. Besides the trivial case $\gamma = 0$, where no topological order can be found, there are only two "magic" fluxes that guarantee PBC: $\gamma = 2\pi/3$ and $\gamma = 4\pi/3$; however we have shown that the chiral current is present for any generic non-trivial flux.

- The typical manifestation of a topological insulator is that, when one moves from PBC to OBC, some states appear in the middle of the former spectral gap, and those states are typically localized at the opened edges of the system. When the three-legs ladder with magic flux and synthetic PBC is opened along the synthetic edge, however, this mechanism is not manifestly present.

- The problem at the base of the previous considerations is that, for such a small number of legs, there is no synthetic bulk or synthetic edge that can be properly defined. In particular, for the case $N = 3$, even considering PBC along the synthetic direction, the system is made up by a single unit cell connected to itself, which is clearly a pathological version of the Harper-Hofstadter model.

Nevertheless, the topological nature of the insulating phase on a three-leg ladder can be investigated computing the topological invariant known as *Zak phase* [66]:

$$Z_\ell = \frac{i}{2\pi}\int_{-\pi}^{\pi} dk \langle u_{\ell k}|\partial_k|u_{\ell k}\rangle, \tag{2.58}$$

where $\ell = 1, 2, 3$ is the band index and $|u_{\ell k}\rangle$ is a single-particle momentum eigenstate of the Hamiltonian. This Zak phase measures the geometric phase accumulated moving along the Brillouin zone: it vanishes in topologically trivial states; otherwise it is a non-zero integer. In the insulating state considered here, the particles occupy the lowest band, so we are interested in Z_1. From a numerical calculation carried setting the magic flux $\gamma = 2\pi/3$, we observe that $Z_1 = 0$ if $\tilde{\Omega} = 0$ (this is the case of synthetic OBC considered in this section); while $Z_1 = 1$ if $\Omega_- < \tilde{\Omega} < \Omega_+$, where $\Omega_\pm$ are functions of Ω and t, in agreement with [66]. A spectral mode in the middle of the band-gap can be found by starting from a topological state (e.g. $\tilde{\Omega} = \Omega$) and moving to **OBC** along the **real** direction. Looking at the spatial distribution of this spectral mode, we observe that indeed it is localized along the **real** edges (not the synthetic edges). Furthermore, it turns out that this state is protected by the point reflection symmetry, i.e. it is robust against the introduction of perturbations that don't break this symmetry (a typical feature of topological edge modes). To summarize, the insulating phase in three-leg ladders with synthetic PBC is in fact a topological insulator, but the associated edge modes are disclosed opening the chain along the real edges.

In view of all these considerations, we are inclined to conclude that the chiral currents discussed in this section are not a direct manifestation of a topologically non trivial state, even though we do not exclude that this can be the case for ladders with a larger number of legs and a non pathological lattice structure along the synthetic direction.

Chapter 3

Chiral currents in strongly interacting systems

In the previous chapter we have discussed how synthetic ladders with artificial gauge fields can be experimentally realized with alkaline-earth-like atoms; then we have considered the non-interacting two-leg and three-leg ladders, computing the chiral current as a function of the effective Raman coupling with analytic methods. However, in the concrete experimental realization of synthetic ladders, not only two-body interactions are present; but they are also tunable via the depth of the optical lattice. This raises the intriguing question of how two-body interactions affect the characteristic chiral behavior of the system. Furthermore, we have seen that the presence of a metastable electronic excited state allows to realize two-orbital models with a non-trivial interaction scheme, characterized in particular by the presence of interorbital spin-exchange dynamics. It is then interesting to study the interplay between the Raman-induced chiral behavior of one of the orbitals and the spin exchange dynamics.

The purpose of this chapter is to investigate the role of interactions in the chiral behavior of synthetic ladders, both in the single-orbital and in the two-orbital case. We perform the study by applying several complementary methods and comparing the results, in particular the Hartree-Fock (static) mean-field theory, DMFT, perturbation theory in the strong coupling limit and exact numerical diagonalization. The discussion is organized as follows: in sec. [3.1] we introduce the Hartree-Fock method and we apply it to obtain semi-analytic results for the chiral currents of the interacting system; in sec. [3.2] we go beyond the static mean-field and include dynamical quantum correlations by means of DMFT; in sec. [3.3] we take into account the presence of open boundary conditions along the real direction and investigate the spatial pattern of currents by diagonalizing exactly the Hamiltonian on a small lattice; in sec. [3.4] we support the analysis finding an effective low-energy spin model valid in the strongly interacting regime; finally, in sec. [3.5] we consider the two-orbital case and discuss how the spin exchange allows a transfer of chirality from one orbital to another. We conclude with a summary of our results and a brief comment on future perspectives in sec. [3.6].

3.1 Hartree-Fock mean field method

We begin our analysis of the interacting system by applying the static mean field theory, also known as the Hartree-Fock method. Since later in this chapter we will compare this method to DMFT, here we underline the similarities and differences between the two approaches by presenting the former in a slightly unconventional way.

The strong approximation behind the static mean field theory is that the self-energy, which is in principle a complicated function of momentum $\mathbf{k}$ and Matsubara frequency $i\omega_n$, is instead static (i.e. frequency-independent): $\hat{\Sigma}(\mathbf{k}, i\omega_n) \approx \hat{\Sigma}_{\mathbf{k}}$. In turn, this means that the interacting system is treated as a set of effectively non interacting quasiparticles. To prove this statement, we can simply consider the Green function of the system and observe that, under this assumption, it is formally the Green function of a non-interacting system with a renormalized Hamiltonian $\hat{H}^{\text{eff}}_{\mathbf{k}} = \hat{H}_{\mathbf{k}} + \hat{\Sigma}_{\mathbf{k}}$:

$$\hat{G}(\mathbf{k}, i\omega_n) \approx \left[i\omega_n - \hat{H}_{\mathbf{k}} - \hat{\Sigma}_{\mathbf{k}} \right]^{-1} = \left[i\omega_n - \hat{H}^{\text{eff}}_{\mathbf{k}} \right]^{-1}.$$

In other words, the Hartree-Fock method neglects the role of quantum dynamical fluctuations and interparticle correlations, as it tries to describe the system with an equivalent system of noninteracting particles. The self-energy (and hence the effective Hamiltonian) is parametrized via a physically motivated variational ansatz, and the specific values of the parameters are determined self-consistently by minimizing the grand canonical potential of the system.[1] Furthermore, the variational parameters have the physical interpretation of thermal expectation values of single-particle operators. The choice of parameters to be included should be made *a priori* and based on physical considerations. In sec. [3.1.1] we begin by a uniform ansatz on the local inter-flavor hopping on the two-leg ladder; then in sec. [3.1.2] we also include a non-uniform behavior in the form of antiferromagnetic order; finally in sec. [3.1.3] we move to the three-leg ladder, again with a uniform ansatz.

3.1.1 Spatially uniform two-flavor systems

In order to illustrate the mean-field decoupling, we begin with the half-filled two-leg ladder in absence of spatial antiferromagnetism, where symmetry requires that $\langle n_{i\uparrow} \rangle = \langle n_{i\downarrow} \rangle = 1/2$. The only relevant variational parameters in this case are the expectation values of the spin ladder operators $s = \langle S^+_i \rangle = \langle c^\dagger_{i\uparrow} c_{i\downarrow} \rangle$ and $s^* = \langle S^-_i \rangle = \langle c^\dagger_{i\downarrow} c_{i\uparrow} \rangle$. In principle s and s^* are complex conjugate; however, without loss of generality, we can assume that they are real, hence $s = s^*$.

The interaction part of Hamiltonian [2.21] can be rewritten in the more convenient form $\frac{U}{2} n_i (n_i - 1) = U n_{i\uparrow} n_{i\downarrow}$, and then it can be *decoupled* to make it quadratic by the following Hartree-Fock prescription:

$$\begin{aligned} n_{i\uparrow} n_{i\downarrow} &\approx \langle n_{i\uparrow} \rangle n_{i\downarrow} + \langle n_{i\downarrow} \rangle n_{i\uparrow} - \langle n_{i\uparrow} \rangle \langle n_{i\downarrow} \rangle - \langle c^\dagger_{i\uparrow} c_{i\downarrow} \rangle c^\dagger_{i\downarrow} c_{i\uparrow} - \langle c^\dagger_{i\downarrow} c_{i\uparrow} \rangle c^\dagger_{i\uparrow} c_{i\downarrow} + \langle c^\dagger_{i\uparrow} c_{i\downarrow} \rangle \langle c^\dagger_{i\downarrow} c_{i\uparrow} \rangle \\ &= \frac{1}{2} n_i - s \left(c^\dagger_{i\uparrow} c_{i\downarrow} + c^\dagger_{i\downarrow} c_{i\uparrow} \right) + |s|^2 - \frac{1}{4}. \end{aligned} \tag{3.1}$$

The effective mean field Hamiltonian, written in momentum space, up to irrelevant constants that don't contain s, reads

$$H^{\text{eff}}_{\mathbf{k}} = \sum_{\mathbf{k}} \Psi^\dagger_{\mathbf{k}} \begin{pmatrix} \varepsilon\left(\mathbf{k} + \frac{\boldsymbol{\gamma}}{2}\right) + \frac{U}{2} - \mu & \Omega - Us \\ \Omega - Us & \varepsilon\left(\mathbf{k} - \frac{\boldsymbol{\gamma}}{2}\right) + \frac{U}{2} - \mu \end{pmatrix} \Psi_{\mathbf{k}} + Us^2 N_{\text{sites}}, \tag{3.2}$$

and the chemical potential that enforces half filling is now $\mu = \frac{U}{2}$. It is a widespread convention to absorb the constant $U/2$ into the definition of chemical potential, introducing the quantity $\tilde{\mu} = \mu - U/2$. We emphasize that the last term, despite being a constant, can't be neglected, as it is important to obtain the correct self-consistency equation (as we discuss below). Remarkably, the only effect of the interaction within the mean-field approximation is a renormalization of the Raman coupling, which has the effective

[1] This is the finite temperature extension of the method, which was originally formulated at $T = 0$.

value $\Omega - Us$. This amounts to assume that the self-energy is uniform and static: $\hat{\Sigma} = -Us\hat{\sigma}^x$, where $\hat{\sigma}^x$ is the first Pauli matrix.

The self-consistency condition can be obtained as follows. If the system is translation invariant along the real direction, every lattice site is indistinguishable from the others, so we can write s as the average of all the local expectation values: $s = \frac{1}{N_{\text{sites}}}\sum_i \langle c^\dagger_{i\uparrow} c_{i\downarrow}\rangle$. We can use this observation to write s in terms of the expectation value of the derivative of the Hamiltonian operator H with respect to the Raman coupling Ω:

$$2s = \frac{1}{N_{\text{sites}}}\sum_i \langle c^\dagger_{i\uparrow} c_{i\downarrow} + c^\dagger_{i\downarrow} c_{i\uparrow}\rangle = \frac{1}{N_{\text{sites}}}\left\langle \frac{\partial H}{\partial \Omega}\right\rangle = \frac{1}{N_{\text{sites}}}\frac{1}{\mathcal{Z}}\sum_n e^{-\beta E_n}\langle n|\frac{\partial H}{\partial \Omega}|n\rangle.$$

Using the Hellmann-Feynman theorem to write $\langle n|\frac{\partial H}{\partial \Omega}|n\rangle = \frac{\partial E_n}{\partial \Omega}$, observing that $\sum_n e^{-\beta E_n}\frac{\partial E_n}{\partial \Omega} = -T\frac{\partial \mathcal{Z}}{\partial \Omega}$, and using the fact that $\frac{1}{\mathcal{Z}}\frac{\partial \mathcal{Z}}{\partial \Omega} = \frac{\partial}{\partial \Omega}\log \mathcal{Z}$, we obtain the self-consistency condition

$$\boxed{s = -\frac{T}{2L}\frac{\partial}{\partial \Omega}\log \mathcal{Z}(s)} \tag{3.3}$$

Since the system is made up of effectively non interacting particles, the partition function is formally equivalent to [2.39], where the energy bands $\varepsilon_{k\ell}(s)$ are just like those given in eq. [2.46], with the mean field renormalized Raman coupling $\Omega \to \Omega - Us$. This leads to a more explicit version of eq. [3.3]:

$$s = \frac{1}{2N_{\text{sites}}}\sum_k \sum_{\ell=1,2} f(\varepsilon_{k\ell}(s) - \tilde{\mu})\frac{\partial \varepsilon_{k\ell}(s)}{\partial \Omega}. \tag{3.4}$$

As we have anticipated, the self-consistency equation [3.3] can also be regarded as a minimization of the grand canonical potential[2] $F(s) = -T\log \mathcal{Z}(s)$ with respect to the variational parameter s. This can be simply proved starting from the minimization condition $\frac{\partial F}{\partial s} = 0$, and observing that $F(s)$ depends on s via the quantity $\Omega - Us$, the only exception being the additive term $Us^2 N_{\text{sites}}$ (which comes from the internal energy), so that

$$\frac{\partial F}{\partial s} = 0 \quad \to \quad -U\frac{\partial F}{\partial \Omega} + 2UN_{\text{sites}}s = 0 \quad \to \quad s = \frac{1}{2N_{\text{sites}}}\frac{\partial F}{\partial \Omega} = -\frac{T}{2N_{\text{sites}}}\frac{\partial}{\partial \Omega}\log \mathcal{Z}, \tag{3.5}$$

which is exactly eq. [3.3]. In finding the self consistency equation via this approach, as we have emphasized, it is important to keep track of constant terms in the Hamiltonian that depend on the variational parameters, such as $Us^2 N_{\text{sites}}$ in this case.

The solution of eq. [3.3] is obtained iteratively: we start from an initial guess $s = s_0$ and evaluate the right-hand side at s_0 to get an updated value $s = s_1$, then we evaluate the right-hand site at s_1 to get $s = s_2$ and so on, until the convergence condition $|s_n - s_{n-1}| < \varepsilon$ (where ε is an arbitrary convergence threshold) is satisfied.

3.1.2 Antiferromagnetism in two-flavor systems

An important feature of low temperature Hubbard-like systems is the tendency towards the formation of an antiferromagnetic phase with long range order. On a bipartite lattice, the antiferromagnetic phase is characterized by a spontaneous breaking of the lattice translational symmetry and of the global SU(2)

[2] We denote the grand canonical potential with F instead of the more conventional Ω to avoid conflicts of notation. This is motivated by the fact that, for the half-filled system, it coincides with the Helmholtz free energy, typically denoted by F.

spin symmetry, and the system has different properties on two sublattices A and B, such that every site in sublattice A has sites of sublattice B as nearest neighbors and vice versa. All the sites within the same sublattice, however, have indistinguishable local properties. This can be included in the Hartree-Fock scheme outlined above by generalizing the ansatz on the local density:

$$\langle n_{i\uparrow}\rangle = \frac{1}{2} + (-1)^{R_i} m, \qquad \langle n_{i\downarrow}\rangle = \frac{1}{2} - (-1)^{R_i} m, \tag{3.6}$$

where $R_i = 0$ if site i belongs to sublattice A, and $R_i = 1$ if i belongs to sublattice B. The variational parameter m, which represents the order parameter, can be rewritten as $m = \frac{1}{2N_{\text{sites}}} \sum_i (-1)^{R_i} \langle n_{i\uparrow} - n_{i\downarrow}\rangle$ and therefore it is called *staggered magnetization*. The non magnetic case is simply recovered setting $m = 0$.

From a geometrical point of view, such a bipartite lattice can be regarded as a Bravais lattice with two sites per unit cell. For example, the one-dimensional lattice with spacing a can be regarded as another one-dimensional lattice with spacing $2a$ and the unit cell made up of two sites A and B at a distance a. The two dimensional bipartite square lattice of spacing a instead can be regarded as a square lattice of spacing $\sqrt{2}a$, rotated by 45 degrees with respect to the original, with a unit cell of two sites separated by a distance a, as shown in fig. [3.1 (a)]. Every lattice site can now be labeled by an index $j = 1, \ldots, \frac{N_{\text{sites}}}{2}$ running over all the unit cells and a sublattice index $\alpha = A, B$. The mean field effective Hamiltonian can be naturally rewritten in terms of the 4-component spinor $\Psi_j^\dagger = (c_{jA\uparrow}^\dagger, c_{jA\downarrow}^\dagger, c_{jB\uparrow}^\dagger, c_{jB\downarrow}^\dagger)$ and its Fourier transformed counterpart

$$\Psi_{\mathbf{k}}^\dagger = \sqrt{\frac{2}{N_{\text{sites}}}} \sum_j \Psi_j^\dagger e^{-i\mathbf{k}\cdot\mathbf{r}_j}, \tag{3.7}$$

where $\mathbf{k}$ belongs to the first Brillouin zone of the new Bravais lattice, which is often called *restricted* or *magnetic* Brillouin zone (MBZ). The MBZ is sampled uniformly with $\frac{N_{\text{sites}}}{2}$ values of $\mathbf{k}$, where N_{sites} is the total number of lattice sites (including both sublattices). For the one dimensional lattice, the MBZ is defined as $k = -\frac{\pi}{2} + \frac{2\pi n}{N_{\text{sites}}}$, with $n = 0, \ldots, \frac{N_{\text{sites}}}{2} - 1$; whereas for the square lattice it is shown in fig. [3.1 (c)].

The effective mean field Hamiltonian can be written in the momentum space representation by standard prescriptions; however the calculation can be lengthy and cumbersome, particularly in higher dimensional lattices; so it is instructive to discuss a graphical approach, which exploits a physical intuition to readily get the result. First of all, $H_{\mathbf{k}}^{\text{eff}}$ is a 4×4 Hermitian matrix, where the two diagonal 2×2 blocks describe local processes in sublattice A and B respectively, while the off-diagonal 2×2 blocks represent hopping processes. Therefore, $H_{\mathbf{k}}^{\text{eff}}$ has the following general structure (at half filling):

$$H_{\mathbf{k}}^{\text{eff}} = \begin{pmatrix} -Um & \Omega - Us & -tg_{\mathbf{k}\uparrow} & 0 \\ \Omega - Us & Um & 0 & -tg_{\mathbf{k}\downarrow} \\ -tg_{\mathbf{k}\uparrow}^* & 0 & Um & \Omega - Us \\ 0 & -tg_{\mathbf{k}\downarrow}^* & \Omega - Us & -Um \end{pmatrix} \tag{3.8}$$

The top-right off-diagonal block describes tunneling events from sublattice B to A, and it can be built according to the following graphical rules:

- every tunneling process B→A is represented by an arrow pointing in the direction of hopping; however, due to the residual translational symmetry of the new Bravais lattice, there is just a small subset of inequivalent hopping processes. The full hopping scheme can be reconstructed by periodically repeating this subset along the directions of the primitive lattice vectors. The relevant subset for the square lattice is shown in fig. [3.1 (b)].

- Next to every arrow, we write a phase factor which represents the phase accumulated by a particle of momentum $\mathbf{k}$ subject to the corresponding hopping process. This is given by the product of two factors: one coming from the synthetic flux, and the other one coming from the Fourier transform.
  - The gauge flux contribution is determined by the orientation of the arrow: if it is opposite to $\hat{x}$, the factor is $e^{i\sigma\gamma_x}$, else it is $e^{-i\sigma\gamma_x}$; if it is opposite to $\hat{y}$, the factor is $e^{i\sigma\gamma_y}$, else it is $e^{-i\sigma\gamma_y}$.
  - The momentum contribution is given by a factor $e^{i\mathbf{k}\cdot(\mathbf{r}_j-\mathbf{r}_i)}$, where $\mathbf{r}_j$ and $\mathbf{r}_i$ are the lattice vectors in the reduced Bravais lattice labeling the two unit cells that are connected by the hopping process $\mathbf{r}_j \to \mathbf{r}_i$.
- The functions $g_{\mathbf{k}\sigma}$ are given by the sum of all the previously identified phase factors with that specific $\sigma = \pm\frac{1}{2}$.

For instance, for a one-dimensional lattice we have

$$g_{k\sigma} = e^{i\sigma\gamma} + e^{-i\sigma\gamma}e^{-2ika}, \qquad \sigma = \pm\frac{1}{2};$$

while for the square lattice we have

$$g_{\mathbf{k}\sigma} = e^{i\sigma\gamma_x} + e^{-i\sigma\gamma_x}e^{-2ik_x a} + e^{-i\sigma\gamma_y}e^{-i(k_x+k_y)a} + e^{i\sigma\gamma_y}e^{i(-k_x+k_y)a}, \qquad \sigma = \pm\frac{1}{2}; \tag{3.9}$$

where we used the Bravais primitive vectors $\mathbf{e}_1 = a(\hat{x}-\hat{y})$ and $\mathbf{e}_2 = a(\hat{x}+\hat{y})$.

The four eigenvalues of the mean field Hamiltonian [3.8] are

$$\varepsilon_{\mathbf{k}\ell} = \pm\sqrt{U^2m^2 + (\Omega - Us)^2 + t^2\frac{|g_{\mathbf{k}\uparrow}|^2 + |g_{\mathbf{k}\downarrow}|^2}{2} \pm \frac{1}{2}\sqrt{t^4(|g_{\mathbf{k}\uparrow}|^2 - |g_{\mathbf{k}\downarrow}|^2)^2 + 4(\Omega - Us)^2t^2|g_{\mathbf{k}\uparrow} + g_{\mathbf{k}\downarrow}|^2}} \tag{3.10}$$

with the four possible combinations of plus and minus signs. The self consistency equation [3.3] for the parameter s is formally unchanged, the only difference being that $\varepsilon_{\mathbf{k}\ell}$ are given in eq. [3.10]; but now we also need to introduce a similar equation for m. This stems from the definition of m given above:

$$m = \frac{1}{2N_{\text{sites}}}\sum_{\mathbf{k}\in\text{MBZ}}\langle n_{\mathbf{k}A\uparrow} - n_{\mathbf{k}A\downarrow} - n_{\mathbf{k}B\uparrow} + n_{\mathbf{k}B\downarrow}\rangle = -\frac{1}{2N_{\text{sites}}U}\left\langle\frac{\partial H^{\text{eff}}}{\partial m}\right\rangle$$

where we used the identity $\sum_{j=1}^{N_{\text{sites}}/2} n_{j\alpha\sigma} = \sum_{\mathbf{k}\in\text{MBZ}} n_{\mathbf{k}\alpha\sigma}$, and we introduced the Hamiltonian operator $H^{\text{eff}} = \sum_{\mathbf{k}\in\text{MBZ}}\Psi^\dagger_{\mathbf{k}}H^{\text{eff}}_{\mathbf{k}}\Psi_{\mathbf{k}}$. We can now rewrite the right-hand side in terms of derivatives of the partition function, following the same steps that we outlined in the derivation of eq. [3.3], and the result is:

$$m = \frac{T}{2N_{\text{sites}}U}\frac{\partial}{\partial m}\log\mathcal{Z}(s,m). \tag{3.11}$$

Finally, the set of self-consistency equations to be solved for a two-flavor system with spatial antiferromagnetism is:

$$s = -\frac{1}{2N_{\text{sites}}U}\sum_{k\in\text{MBZ}}\sum_{\ell=1}^{4} f(\varepsilon_{\mathbf{k}\ell}(s,m)-\tilde{\mu})\frac{\partial\varepsilon_{\mathbf{k}\ell}}{\partial s}, \quad m = -\frac{1}{2N_{\text{sites}}U}\sum_{\mathbf{k}\in\text{MBZ}}\sum_{\ell=1}^{4} f(\varepsilon_{\mathbf{k}\ell}(s,m)-\tilde{\mu})\frac{\partial\varepsilon_{\mathbf{k}\ell}}{\partial m} \tag{3.12}$$

where we have emphasized the symmetry of the two equations by using $\frac{\partial\varepsilon_{\mathbf{k}\ell}}{\partial\Omega} = \frac{1}{U}\frac{\partial\varepsilon_{\mathbf{k}\ell}}{\partial s}$.

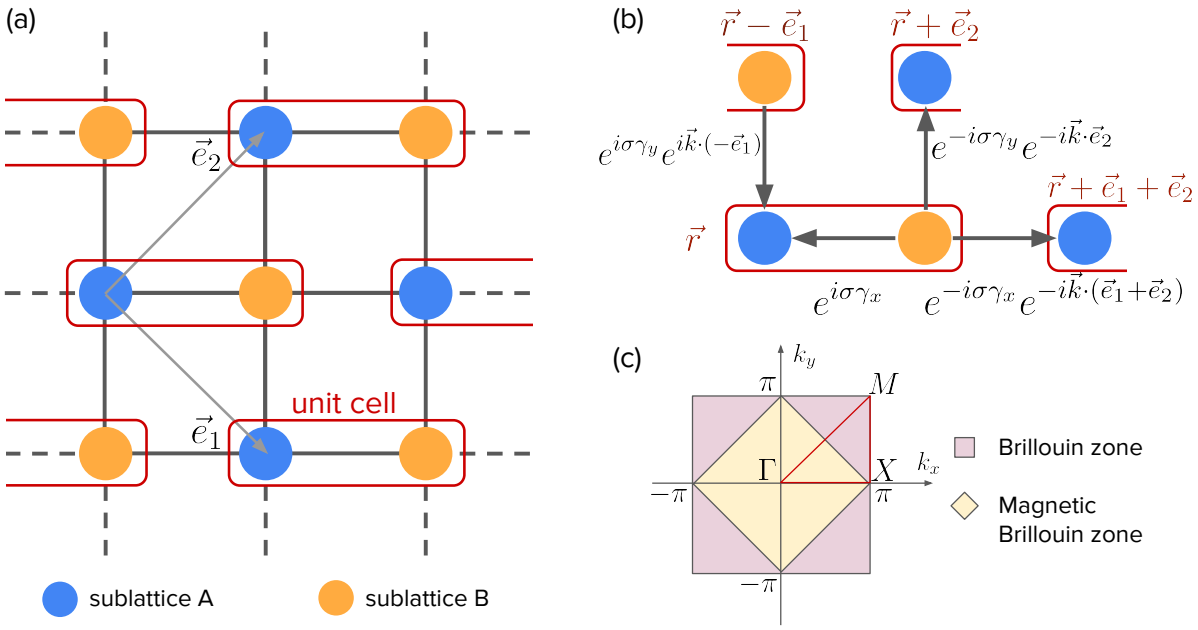

Figure 3.1: (a) Geometrical structure of a bipartite two-dimensional square lattice: the vectors $\mathbf{e}_{1,2}$ are the primitive lattice vectors and there are two sites per unit cell (belonging to sublattices A and B). (b) Representation of all the "independent" hopping processes, with the related phase factor entering the momentum space Hamiltonian. The red labels are the Bravais vectors labeling the unit cells where the sites are located. The hopping scheme for the full lattice can be obtained by periodically repeating this pattern and including the reverse hopping processes with a complex conjugate phase factor. (c) Brillouin zone and Magnetic (reduced) Brillouin zone of the square lattice, with the high symmetry path $\Gamma X M \Gamma$ highlighted in red.

After solving the self-consistency equations and finding the optimal values of s and m, any observable can be computed using the energy bands $\varepsilon_{\mathbf{k}\ell}(s,m)$ evaluated at the converged values of the variational parameters. For instance, the chiral current can be computed via a straightforward generalization of eq. [2.40]:

$$\langle I_{\text{chir},a}\rangle = -\frac{2}{N_{\text{sites}}}\sum_{\mathbf{k}\in\text{MBZ}}\sum_{\ell=1}^{4} f(\varepsilon_{\mathbf{k}\ell}(s,m)-\tilde{\mu})\frac{\partial\varepsilon_{\mathbf{k}\ell}(s,m)}{\partial\gamma_a}. \tag{3.13}$$

The converged values of s and m at $\Omega = 0.5t$ and $\gamma = \pi/2$ for several temperatures T and interaction strengths U, along with the chiral current are shown in fig. [3.2] for the two-leg ladder. We have chosen $\gamma = \pi/2$ to maximize the chiral behavior and a small value of Ω, since this is where we expect the richest physical scenario: the system is metallic at $U = 0$, and we expect that the interaction will drive the system towards an insulating phase. First of all, let's consider the behavior of s as a function of U at $T = 0$: it is always negative and its absolute value increases upon increasing U, until it rapidly saturates to $|s| \approx 0.5$ at $U = U_c \approx 4t$. Consequently, the effective Rabi coupling saturates to the value $\approx \Omega + U/2$, which is proportional to U. In this regime, antiferromagnetism is completely frustrated ($m = 0$), while for $U < U_c$ there is antiferromagnetic order with m exponentially vanishing as U goes to zero. Since for any $m \neq 0$

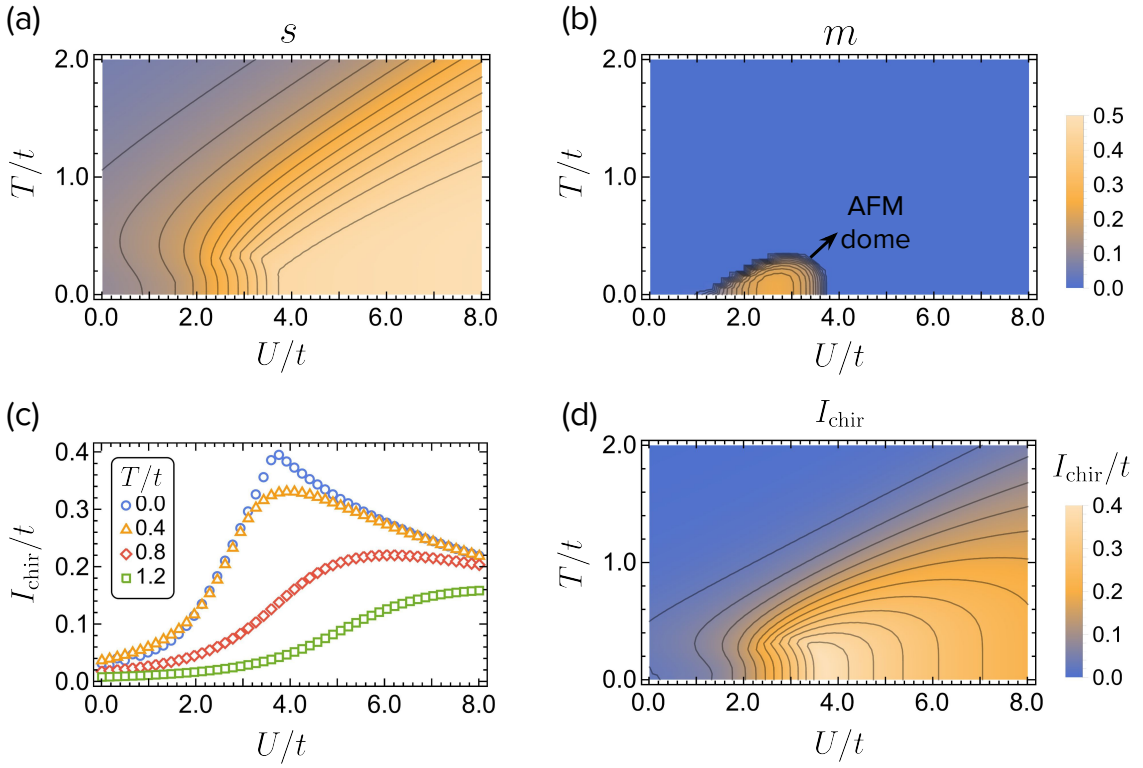

Figure 3.2: Results of the mean-field analysis for the two-flavor system in one spatial dimension at representative values of the parameters: $\Omega = 0.5t$, $\gamma = \frac{\pi}{2}$ and $N_{\text{sites}} = 500$. The converged values of s and m as functions of U and T are presented in panel (a) and (b) respectively. The chiral current across the U-driven metal-insulator phase transition is shown for some representative temperatures in panel (c) and as a color plot in panel (d). We find similar results also for the (2+1)-dimensional system.

there is a spectral gap of order $\approx Um$ opening at the Fermi level, according to the Hartree Fock method, the system at $T = 0$ is an antiferromagnetic insulator for $U < U_c$ and a band insulator similar to the non-interacting one for $U > U_c$. However, it turns out that the antiferromagnetic order is fragile with respect to thermal fluctuations, as it only survives in a small "dome" of the space of parameters (U, T) (see fig. [3.2 (b)]). In particular, it never survives at $T \gtrsim 0.3t$. The chiral current as a function of U has the same qualitative behavior as the one observed in the non interacting case as a function of Ω, with a peak at $U = U_c$ and a hyperbolic tail at $U > U_c$. This is explained by the fact that the phase at $U > U_c$ is formally equivalent to the non-interacting insulating phase with $\Omega \to \Omega + U/2$, so we have $I_{\text{chir}} \approx \frac{t^2 \sin\gamma}{\Omega + U/2}$. As a function of temperature, the chiral current is progressively lowered, and the sharp peak at $T = 0$ gets smoothed, lowered in intensity and pushed to larger values of U (see fig. [3.2 (c)]). However, it is still maximized at intermediate values of U and it slowly decays for larger U. Eventually, at large temperatures (of order $T \sim 2t$), the current effectively vanishes and the high temperature equilibrium states are non-chiral. In real experimental setups, the lowest achievable temperature is typically a few tenths of the hopping scale, so we expect that at least qualitatively this phenomenon could be experimentally observed. On the other hand, these thermal fluctuations can hinder the antiferromagnetic state, hence it can be neglected in the following.

As a final remark, we clarify that, in principle, a more general and conservative approach to the variational problem is to introduce two s parameters for the two sublattices as

$$s_A = \frac{2}{N_{\text{sites}}} \sum_{j=1}^{N_{\text{sites}}/2} \langle c^\dagger_{jA\uparrow} c_{jA\downarrow} \rangle, \qquad s_B = \frac{2}{N_{\text{sites}}} \sum_{j=1}^{N_{\text{sites}}/2} \langle c^\dagger_{jB\uparrow} c_{jB\downarrow} \rangle;$$

while here we have implicitly assumed $s_A = s_B = s$. Following the same conceptual steps that we have outlined above, we can write a set of three self-consistency equations for s_A, s_B and m. However, the numerical solution of these equations shows that, within the specified numerical tolerance, as a matter of fact $s_A = s_B$. This result justifies *a posteriori* the assumption made here, which on the other hand, allowed us to illustrate the steps of the procedure avoiding technical complications.

3.1.3 Spatially uniform three-flavor system

In the case $N > 2$ the scenario is much richer, since other mean-field parameters should be taken into account. For instance, the flavor-exchange processes are, in general, described by $N(N-1)/2$ variational parameters $s_{\sigma\rho} = \langle c^\dagger_{j\sigma} c_{j\rho} \rangle$, with $\sigma \neq \rho$ and $s_{\sigma\rho} = s_{\rho\sigma}$. For $N = 3$, we have to include three flavor exchange parameters, which reduce to two by symmetry for the Raman tunneling scheme studied in this work: $s_{-1,0} = s_{0,1} := s$ and $s_{-1,1} := \tilde{s}$. Besides flavor exchange, another parameter should be introduced when more than two flavors are available, namely the imbalance in the population of different flavors $n_\sigma = \langle c^\dagger_{j\sigma} c_{j\sigma} \rangle$. These variational parameters satisfy the constraint $\sum_\sigma n_\sigma = 1$, which means that the independent parameters are $N - 1$. For $N = 3$ we would need two parameters to describe the flavor-population imbalance, but the point reflection symmetry offers another constraint $n_{-1} = n_1$ and limits the number of independent parameters to one. We can thus write a simplified variational ansatz by means of only three parameters: δ, which measures the imbalance between the population of the outer and inner flavors ($n_0 = 1/3 - \delta$; $n_{-1} = n_1 = 1/3 + \delta/2$); s, which renormalizes the Raman matrix element ($\Omega_{\text{eff}} \to \Omega - Us$); and $\tilde{s}$, which introduces an effective hopping between the external flavors with amplitude $-U\tilde{s}$. The mean field Hamiltonian, written in the canonical ensemble, reads

$$H = \sum_{\mathbf{k}} \Psi^\dagger_{\mathbf{k}} \begin{pmatrix} \varepsilon(\mathbf{k}+\boldsymbol{\gamma}) + \frac{U\delta}{2} & \Omega - Us & -U\tilde{s} \\ \Omega - Us & \varepsilon(\mathbf{k}) - U\delta & \Omega - Us \\ -U\tilde{s} & \Omega - Us & \varepsilon(\mathbf{k}-\boldsymbol{\gamma}) + \frac{U\delta}{2} \end{pmatrix} \Psi_{\mathbf{k}} + U\left(2s^2 + \tilde{s}^2 + \frac{3}{4}\delta^2\right) N_{\text{sites}} \qquad (3.14)$$

where now the spinor has three components $\Psi^\dagger_{\mathbf{k}} = (c^\dagger_{\mathbf{k},1}, c^\dagger_{\mathbf{k},0}, c^\dagger_{\mathbf{k},-1})$.

Once again, the optimal values of the three variational parameters are obtained by minimizing the Helmholtz free energy $F(s, \tilde{s}, \delta)$. At zero temperature, the free energy reduces to the internal energy of the system $E_0(s, \tilde{s}, \delta)$, so we can avoid the problem of computing the chemical potential by working in the canonical ensemble, as sketched in sec. [2.4.2]. For a given set of parameters $\{s, \tilde{s}, \delta\}$ we can compute the internal energy by summing the N_{sites} lowest eigenvalues of H (including the constant term). Since any numerical routine for finding the minimum of a target function only requires the possibility to evaluate that function at any given point, this is enough to optimize the internal energy. The optimized parameters with the corresponding chiral current are shown in fig. [3.3] for a representative case.

We observe that the interaction induces an imbalance in the flavor-resolved density, a renormalization of the Rabi coupling $\Omega_{\text{eff}} = \Omega - Us$ and most importantly it induces an effective Rabi coupling $\tilde{\Omega}_{\text{eff}} = -U\tilde{s}$ between the unconnected flavors $\sigma = -1$ and $\sigma = +1$. Since the variational parameters are nearly constant in the insulator, where moreover we can assume $U \gg \Omega$, we conclude that the ratio between effective

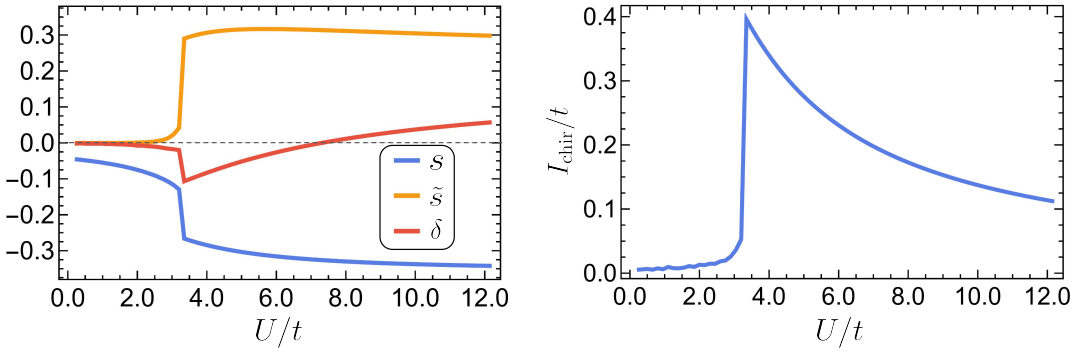

Figure 3.3: Optimized variational parameters (left) and corresponding chiral current (right) obtained by a spatially uniform mean-field analysis carried at $T = 0$ on a three-leg ladder for a representative set of parameters: $\Omega = 0.2t$, $\gamma = 3\pi/8$.

Rabi couplings is $\tilde{\Omega}_{\rm eff}/\Omega_{\rm eff} \approx \tilde{s}/s$, which is roughly ≈ -1 for the parameters used here. This suggests the intriguing idea that the interaction can drive the system to a topologically non-trivial insulator, at least at the quasiparticle level; however, a calculation of the Zak phase through eq. [2.58] reveals that this is not the case, as $Z_1 = 0$ when the effective Rabi couplings have opposite sign. Even though the interaction introduces this new process on top of the non interacting system, the qualitative behavior of the chiral current is unaltered. However, unlike the two-legs ladder, the quantitative estimate of the hyperbolic tail is not simply given by replacing $\Omega \to \Omega_{\rm eff}$ in eq. [2.57].

The role of temperature can be studied moving back to the grand canonical ensemble and numerically computing the chemical potential $\tilde{\mu}$ which satisfies the constraint on the total density $\sum_{\mathbf{k}\ell} f(\varepsilon_{\mathbf{k}\ell}(s, \tilde{s}, \delta) - \tilde{\mu}) = N_{\rm sites}$. The results (not shown) confirm the qualitative picture observed for $N = 2$: the current peak is rounded off and lowered in intensity, but the current survives up to temperatures $T \approx t$. Here we have described the mean-field method for a spatially uniform system, neglecting any form of spatial magnetic ordering. The study of magnetic orderings in three-flavor systems can be very tricky, but at the same time we expect that in this context they should be fragile with respect to experimental deviations from ideality, such as thermal fluctuations, presence of a local potential, etc.

3.2 Including dynamical correlations with DMFT

So far we have investigated the system under the assumption that we can treat the interacting particles via an effective non-interacting Hamiltonian or, alternatively, that the self-energy is a constant. This is generally a very strong assumption when studying interacting many-body systems, as in general they are subject to significant quantum fluctuations. A remarkable example is the Mott transition, where the quantum fluctuations are responsible for an interaction-driven metal-insulator phase transition. Such fluctuations are captured by the momentum and frequency dependence of the self-energy $\hat{\Sigma}(\mathbf{k}, i\omega_n)$; however, finding an approach that allows to compute the full dependence on momentum and frequency with no further assumptions is very complicated. We can take a step in this direction by means of DMFT, as described in sec. [1.3], assuming that the self-energy does not depend on momentum, while making no assumptions about the frequency dependence: $\hat{\Sigma}(\mathbf{k}, i\omega_n) \approx \hat{\Sigma}(i\omega_n)$. This assumption is generally expected to be more solid as the coordination number of the lattice increases and to be exact in the limit of infinite coordination [27].

A suitable Anderson impurity model can be constructed by choosing a spinor representation for the bath and the impurity, for example we can mimic the structure of the spinor $\Psi^\dagger_{\mathbf{k}}$ by choosing $\Psi^\dagger_\ell = (c^\dagger_{\ell,\frac{N-1}{2}}, \dots c^\dagger_{\ell,-\frac{N-1}{2}})$, so the impurity on-site energy is

$$\hat{\varepsilon}_0 = \begin{pmatrix} -\mu & \Omega \\ \Omega & -\mu \end{pmatrix} \qquad (N=2); \qquad \hat{\varepsilon}_0 = \begin{pmatrix} -\mu & \Omega & 0 \\ \Omega & -\mu & \Omega \\ 0 & \Omega & -\mu \end{pmatrix} \qquad (N=3)$$

and the interaction term mimics the local physical interaction: $\frac{U}{2} n_0(n_0-1)$, where $n_0 = \Psi^\dagger_0 \Psi_0$. The bath on-site energies and hybridization matrices $\hat{\varepsilon}_\ell$ and $\hat{V}_\ell$ should mimic the structure of $\hat{H}_{\mathbf{k}}$, so we can assume them to be real symmetric matrices. This is not the only possible choice: for example one can perform a unitary transformation $\Psi_{\mathbf{k}} \to \tilde{\Psi}_{\mathbf{k}}$ that diagonalizes $\hat{H}_{\mathbf{k}}$ on the original lattice problem and adapt the Anderson impurity model in this new basis [69]. With the latter approach we can assume $\hat{\varepsilon}_\ell$ and $\hat{V}_\ell$ to be diagonal, thus reducing the number of parameters used to fit the Weiss field and speeding up the fitting process. However, this can be tricky to generalize to multiorbital problems such as those discussed in sec. [3.5].

In the following sections we present results obtained with DMFT solving the Anderson impurity problem with exact diagonalization at $T = 0$, where we only need to evaluate the ground state (including its degeneracy). The calculation can also be extended at finite temperature using the exact diagonalization as an impurity solver: in this case we need to evaluate all the excited states having a Boltzmann weight that exceeds a given numerical threshold (again including degeneracies). This can be tricky, since at a given temperature we don't know beforehand the exact number of low-lying eigenstates that we need to compute, but it has to be determined dynamically. Moreover, in order to compute the impurity Green function, we have to repeat the Lanczos method multiple times, once per every relevant eigenstate: this can considerably slow down the computation time, especially at large temperatures. Alternatively, one could use a different impurity solver, more suitable for finite temperature calculations, for example the quantum Monte-Carlo solver based on the Hirsch-Fye algorithm [70] or its extensions [71]. This is left as a purpose for future work.

Moreover, since we expect the antiferromagnetic order to be fragile with respect to thermal fluctuations and since we are also interested in the interplay between chirality and the Mott transition, we first discuss results obtained from single-site DMFT by explicitly frustrating antiferromagnetism and we comment on spontaneous symmetry breaking at the end.

3.2.1 Chiral current

After convergence, we can compute the chiral current by evaluating $\langle c^\dagger_{\mathbf{k}\sigma} c_{\mathbf{k}\rho} \rangle$ via eq. [1.39], whose diagonal components are the flavor-resolved momentum distribution of the density $\langle n_{\mathbf{k}\sigma} \rangle$, and from the latter we get the chiral current using eq. [2.32]. The results are shown in fig. [3.4] for different lattice dimensionalities and number of flavors. In the figure we also compare these results with the Hartree-Fock method discussed in sec. [3.1.1] and with a strong coupling limit approach discussed in sec. [3.4]. We always consider a small Rabi coupling $\Omega < \Omega_c$ in order to have a metallic state at $U = 0$ and study the evolution towards an insulator as U increases.

All the curves feature a relatively smooth growth for small U, interrupted by a cusp-like maximum at a critical value U_c, where the system undergoes the U-driven metal-insulator transition, followed by a $\sim 1/U$ behavior in the insulating phase. In other words, the behavior of I_{chir} is qualitatively the same for different lattice dimensions d and number of flavors N; however, chirality is more pronounced for the

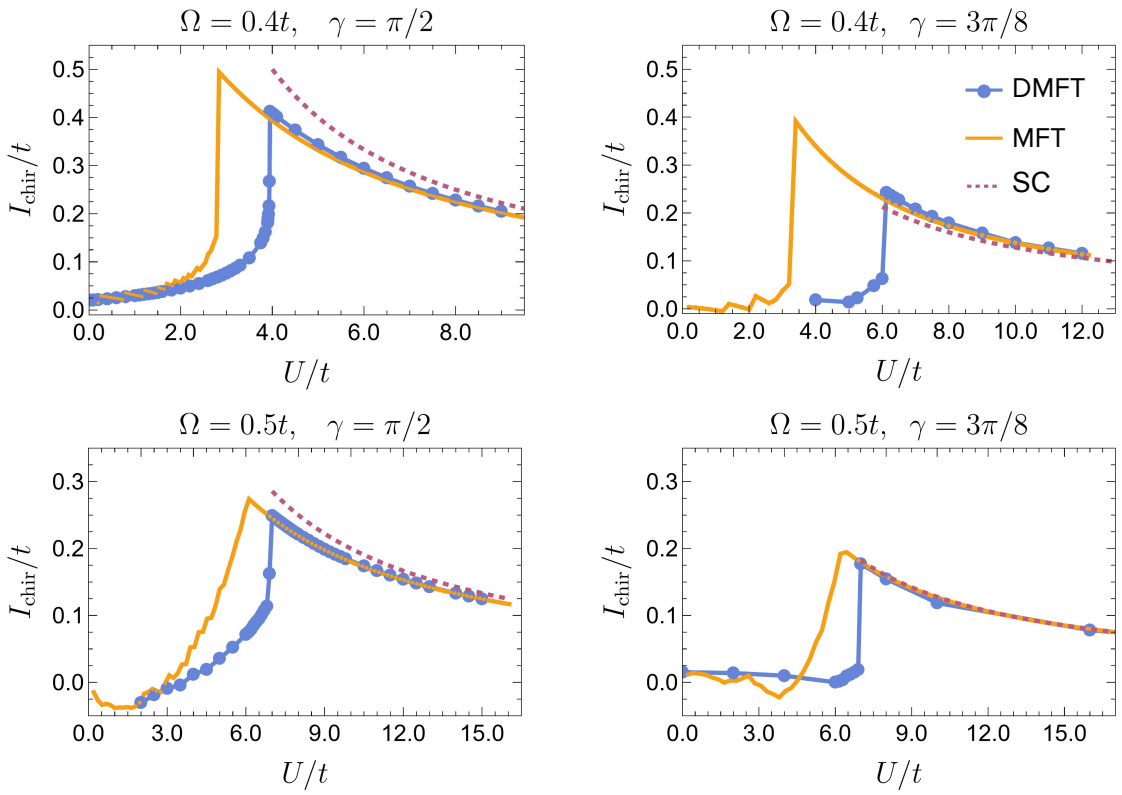

Figure 3.4: Chiral current as a function of U/t for a $(1+1)$-dimensional structure (first row) and a $(2+1)$-dimensional structure (second row); both for $N = 2$ (left column) and $N = 3$ (right column). The different colors represent results obtained with different methods: a static mean field Hartree-Fock approach (MF), dynamical mean field theory (DMFT) and the effective strong-coupling limit (SC) discussed in sec. [3.4]. All the techniques confirm the presence of a non differentiable peak in the function $I_{\rm chir}(U)$ at the transition and a $1/U$ tail in the insulating phase.

simplest case $d = 1$, $N = 2$, while it progressively becomes more fragile as the lattice coordination or the number of flavors increase. Moreover, the chiral current is typically larger in the insulating phase than in the metallic phase, and it is maximized at the metal-insulator transition, similarly to what we found in the non-interacting limit, where the transition (in that case driven by Ω) has a more conventional band character.

Surprisingly, we observe that the Hartree-Fock method captures the correct quantitative behavior both at weak coupling $U \ll t$ and at strong coupling $U \gg t$; while it is less accurate at intermediate couplings, where it underestimates U_c and overestimates the peak current.

3.2.2 Spectral properties

In order to get a more solid understanding of the role of interactions, we can look at the spectral properties. For example, we can compute the single-particle spectral function

$$A(\mathbf{k}, \omega) = -\frac{1}{\pi} \lim_{\eta \to 0^+} \sum_{\sigma=1}^{N} \mathrm{Im}[G_{\sigma\sigma}(\mathbf{k}, \omega + i\eta)], \tag{3.15}$$

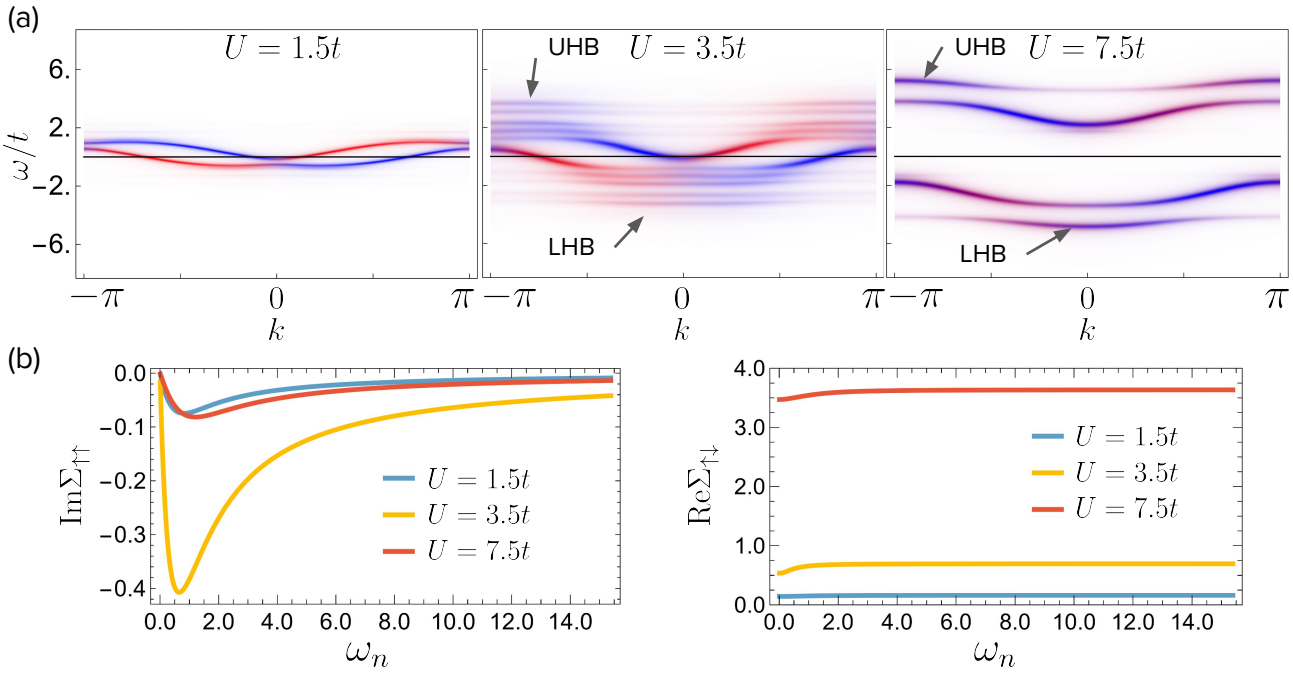

Figure 3.5: (a) Evolution of the spectral function for representative values of U in the weak, intermediate and strong coupling regimes respectively. The spectral quasiparticle peak around the Fermi level coexists with an incoherent part of the spectrum formed by a lower Hubbard band (LHB) and an upper Hubbard band (UHB). The color scheme reflects the flavor polarization of a specific state. (b) Non-vanishing components of the self energy (in units of t) as a function of Matsubara frequencies for the same representative values of U. At intermediate couplings, the diagonal part develops a non-negligible dynamical structure, while moving to weak and strong coupling it progressively reduces to a constant (left panel). The off-diagonal components are nearly constant and the value represents the effective Rabi coupling Ω_{eff} in the Hartree-Fock picture (right panel). Model parameters: $N = 2$, $\gamma = \pi/2$, $\Omega = 0.4t$.

which provides information on the whole many-body spectrum. In particular, it represents both coherent and incoherent excitations available for a single particle[3], and therefore it can be regarded as a generalized version of the band structure for an interacting system. The momentum-dependent retarded Green function can be computed from the converged self-energy evaluated at real frequencies $\hat{\Sigma}(\omega)$ through $\hat{G}(\mathbf{k}, \omega + i\eta) = [\omega + i\eta - \hat{H}_{\mathbf{k}} - \hat{\Sigma}(\omega)]^{-1}$. In turn, $\hat{\Sigma}(\omega)$ is obtained from the impurity problem by applying the Lanczos method to obtain the impurity Green function at real frequencies. Numerically, the parameter η is taken as a small arbitrary constant (of order $\eta \approx 10^{-2}$) and it provides an artificial spectral broadening, transforming singular Dirac-delta peaks into regular Lorentzian peaks with a dispersion $\propto \eta$.

The evolution of $A(\mathbf{k}, \omega)$ as a function of the interaction strength U is shown in fig. [3.5 (a)] taking a two-leg ladder as an example. While in the symmetric Hubbard model the quasiparticle peak at the Fermi level disappears continuously at the Mott transition as its spectral width goes to zero, leaving a preformed gap of order U, in SU(N)-broken systems a rather large quasiparticle peak survives just before the transition, and the insulating gap arises from a splitting of such peak into two features. As a

[3]With the word "coherent", we mean long-lived quasi-particle excitations, characterized by a large lifetime; while we use "incoherent" to denote short-lived states, where the single-particle excitation rapidly decays in the many-body state.

consequence the gap is not proportional to the Hubbard U. At the same time, analogously to the standard scenario, spectral weight moves towards high-energy features separated by an energy U already in the metallic state, which are usually referred to as *precursors* of the Hubbard bands. Upon increasing U, the band gap increases, and the central spectral features (where the band gap has opened) are continuously pushed towards the preformed Hubbard bands, until they finally merge at very large U.

We can also look at the dynamical structure of the self-energy in Matsubara frequencies $\hat{\Sigma}(i\omega_n)$, which encodes the role of dynamical quantum correlations beyond the static mean field. The relevant components for a two-leg ladder are shown in fig. [3.5 (b)] (all the other components are either vanishing or related to these by symmetry properties). First of all, we observe that the off-diagonal component is nearly constant as a function of ω_n for every representative value of U. This is consistent with the Hartree-Fock analysis and we can interpret the constant value as the effective Rabi coupling Ω_{eff}. This is particularly clear at strong coupling, where – using the specific parameters of the example shown in the figure – we have $\Sigma_{\uparrow\downarrow}(i\omega_n) \approx 4t$ and the effective Rabi coupling is $\Omega_{\text{eff}} \approx \Omega + U/2 \approx 4t$. As we will see in chapter [5], a nearly constant real part of the off-diagonal self-energy is a common feature of systems with broken symmetries. Secondly, we notice that the imaginary part of the diagonal component has a mild dynamical structure at $U \ll t$ or $U \gg t$, but it has a significant frequency dependence at intermediate couplings, especially close to the phase transition. This explains why the Hartree-Fock method, which neglects the frequency dependence, captures so well the behavior of the chiral current both for very weak and very strong interactions, while it fails to correctly predict the position of the peak. The enhanced dynamical dependence of $\hat{\Sigma}(i\omega_n)$ is typical in a correlated metal close to the Mott transition; however, in a standard Mott insulator (without symmetry breaking), the self-energy diverges at $\omega_n \to 0$ as $\approx 1/i\omega_n$. Here instead, not only the self-energy is regular in the insulating phase, but it also gets progressively less dynamical increasing U.

A quantity that reflects one of the most relevant effects of dynamical correlations at low frequency is the *quasiparticle weight*. We observe that in the limit $\omega_n \to 0$, the self-energy is typically linear in frequency, and it can be expanded as

$$\Sigma_{\sigma\sigma} = \left(1 - \frac{1}{z_\sigma}\right) i\omega_n + \mathcal{O}(\omega_n^2) \qquad \to \qquad z_\sigma = \left(1 - \left.\frac{\partial \Sigma_{\sigma\sigma}(i\omega_n)}{\partial i\omega_n}\right|_{i\omega_n \to 0}\right)^{-1}. \tag{3.16}$$

If $z_\sigma = 1$ we have a non-interacting system, while if $z_\sigma \to 0$ we have a Mott insulator, as this expansion of the self-energy breaks down due to a low-frequency divergence. Moreover, the lower z_σ, the higher the slope of $\Sigma_{\sigma\sigma}(i\omega_n)$, which suggests that the dynamical dependence is significant and that quantum correlations are important. We argue that the above picture is essentially the same for higher dimensionality and for three flavors by plotting the quasiparticle weight for $d = 2$ and $N = 3$ as a function of U, along with the corresponding fraction of doubly occupied sites $D = N_{\text{sites}}^{-1} \sum_{i,\sigma<\rho} \langle n_{i\sigma} n_{i\rho} \rangle$, in fig. [3.6]. We observe that at the phase transition, where D drops rapidly leading to a state with almost one particle per site, the quasiparticle weight is small but finite, denoting a significant degree of correlation; but in the insulating phase it jumps back to ≈ 1, supporting the general validity of the previous considerations.

In conclusion, U drives the system towards a state which can be considered a Mott state since it is stabilized by a strong suppression of doubly occupied sites, but, at the same time, is similar to a band-insulator and it can be described by static mean-field. From an intuitive point of view, the key point is that in our system with broken $SU(N)$ symmetry there is no competition between the states selected by the Hubbard U (any state with one fermion on every site) and those favored by the symmetry-breaking field, which are specific single-fermion states obtained as linear combinations of the different components. As a result, increasing U favors the stabilization of a band insulator by reducing the weight of states with more

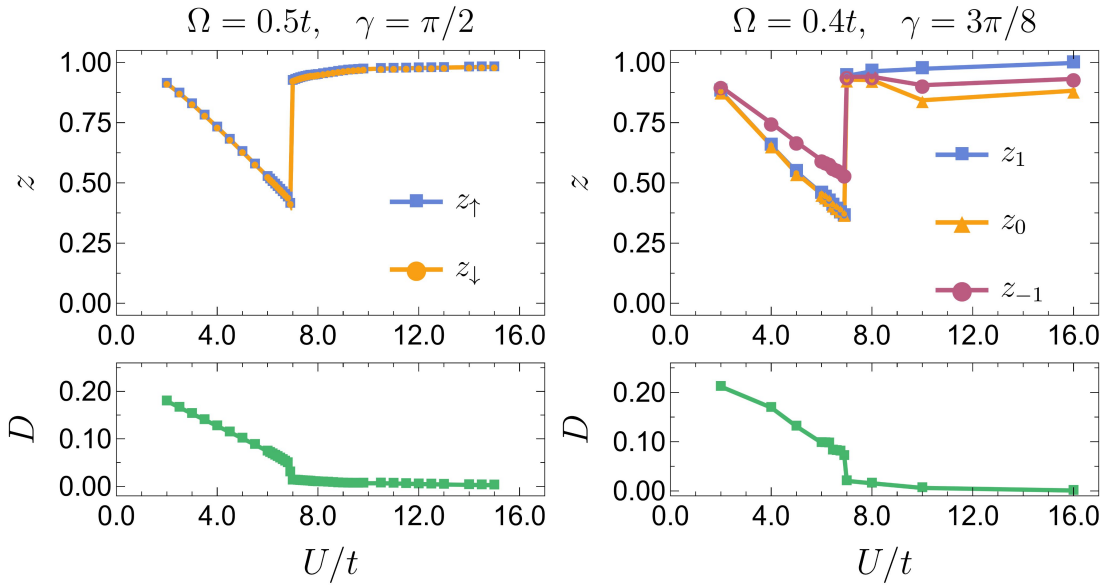

Figure 3.6: Quasiparticle weights (top panel) and double occupancies (lower panel) as a function of the Hubbard U for the two-dimensional system with $N = 2$ (left) and $N = 3$ (right). For practical reasons, the three z_σ are associated to "effective flavors", i.e. they are computed using the diagonal part of the self-energy written in a basis that diagonalizes the non-interacting lattice Hamiltonian. This explains why $z_{-1} \neq z_{+1}$, but the physical interpretation is not affected.

than one fermion per site. In other words, the Mott localization and the formation of the band insulator are not competitive effects and they can actually cooperate to stabilize the same insulating state. As a matter of fact, our interaction-driven transition is very similar to the band-insulator transition that we have found and discussed in the non-interacting system.

The picture above closely resembles the insulating phase reported in ref. [51], that the authors described as "a Mott insulator *disguised* as a conventional band insulator". This is a sort of hybrid between a Mott insulator, characterized by the suppression of local density fluctuations and by the presence of preformed Hubbard bands, and a conventional band insulator, characterized by a frequency-independent self-energy and an effective non-interacting description.

3.3 Effect of open boundary conditions

So far we have considered a virtually infinite system using a numerically large value of N_{sites} and implementing periodic boundary conditions and translational symmetry along the real directions. However, from an experimental perspective, one might argue that in a real situation the system is necessarily open at the real edges. For this reason, here we consider a system with open boundary conditions and investigate the spatial pattern of currents along the bonds. In order to obtain unbiased results, we have considered a relatively small three-legs ladder with 8 sites along the real direction and we have computed the exact numerical ground state, from which we have extracted the currents.

We summarize the results in fig. [3.7], which shows the current pattern along the three-legs ladder in two representative situations: the metallic state $U < U_c$ (left) and the insulating state $U > U_c$ (right).

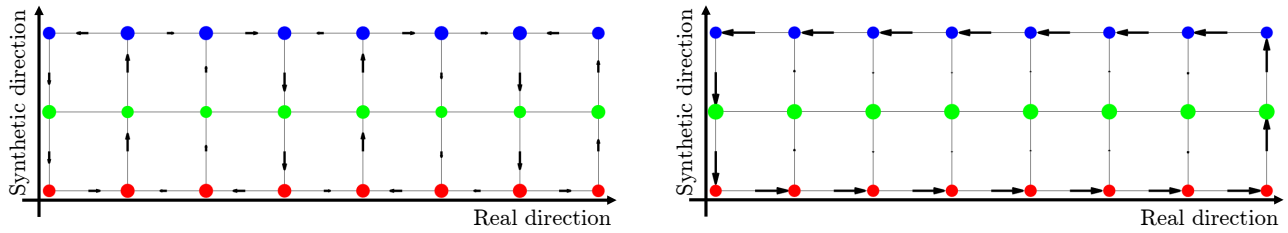

Figure 3.7: Current pattern in the metallic ($U = 2.0t$, left panel) and in the insulating ($U = 8.5t$, right panel) regimes. The color of every circle represents a flavor index, while the area is proportional to the density $\langle n_{j\sigma}\rangle$. Similarly, the length of each arrow is proportional to the corresponding current along that bond. In the former case, vertical bonds are, in general, flown by a non-zero current resulting in multiple vortexes; while in the latter case the current flows only along the edges of the ladder, resulting in a single-vortex structure, reminiscent of the Meissner effect in superconductors. Results are obtained by means of the exact diagonalization of the interacting three-legs ladder with $N_{\text{sites}} = 8$ and open boundary conditions both along the real and the synthetic direction. The model parameters are $\Omega = 0.5t$, $\gamma = 2\pi/7$.

We can appreciate that the edge current observed in the insulating phase is larger than the edge current in the metal, in agreement with our previous results. A more accurate investigation [3] shows that the exact solution features the characteristic hyperbolic behavior of the chiral current in the insulator and that there is a sharp peak at the transition point. This corroborates the idea that the qualitative behavior of the current outlined in this work can be observed experimentally.

This result is not only a check of robustness, but it also provides more information on the system. In particular, we can now spatially resolve the pattern of persistent currents in the ground state. At weak-coupling, the currents along the synthetic dimension (vertical arrows) are non-vanishing and their magnitude and sign are site-dependent, leading to a pattern of vortexes with opposite "charge" alternating in real space. This configuration has been observed in analogous bosonic systems [72, 73, 74] and is dubbed *vortex phase*. On the other hand, in the strong-coupling regime, the currents in the synthetic dimension are zero everywhere except for the two outermost sites in the physical dimension. In other words, the currents are expelled from all inner bonds and can circulate only along the outer boundary of the $(1+1)$-dimensional structure, a circumstance which is reminiscent of the Meissner effect in superconductors. Due to this similarity, the latter phase is named *Meissner phase*.

Remarkably, moving from PBC to OBC, the point-reflection symmetry discussed in sec. [2.3.1] is preserved. With spatially non uniform currents, this translates in the constraints:

$$\langle I_j\rangle = -\langle I_{-j}\rangle \quad \text{and} \quad \langle I_{(j,\sigma);(j+1,\sigma)}\rangle = -\langle I_{(-j-1,-\sigma);(-j,-\sigma)}\rangle, \tag{3.17}$$

where the sites are labeled symmetrically with respect to the geometric center of the ladder (the pivot of the symmetry). For example, with an odd number of sites, we can label the central site with $j = 0$ and those at its right (left) with $j = \pm 1, \ldots, \pm\frac{N_{\text{sites}}-1}{2}$ respectively. For an even number of sites instead we can label the site using half integers: $j = \pm\frac{1}{2}, \ldots, \pm\frac{N_{\text{sites}}-1}{2}$. We observe as a consistency check that the current pattern in fig. [3.7] reflects this symmetry. Moreover, this symmetry could be exploited to further reduce the dimension of the Hamiltonian blocks, improving the computational efficiency and allowing to further increase the number of sites. However this is left as a purpose for future optimization work on our codes. As a final consistency check, we have verified that the pattern of currents obeys the continuity equation [2.25] at every node, which at equilibrium reduces to a Kirchhoff current law, i.e. we have checked that the sum of currents flowing into a node equals the sum of currents flowing outward.

3.4 Strong coupling limit

The study of interacting particles with Hubbard-like interactions at low temperatures can be significantly simplified in the strongly coupled regime, when the Hubbard U is the dominant energy scale. In this case, configurations featuring multiple particles on the same lattice site are energetically penalized with respect to configurations where particles spread out over all the available lattice sites. The energy cost required to increase the number of multiply occupied sites is of order $\sim U$, which means that such configurations are essentially not populated by thermal fluctuations at sufficiently low temperatures $T \ll U$ or, in other words, they contribute to any equilibrium state with a vanishing statistical weight. The immediate consequence is that we can build an effective low-energy theory by restricting the original Hilbert-Fock space to the subspace of states with the lowest possible number of multiply occupied lattice sites. Moreover, if the number of particles is equivalent to the number of lattice sites, the relevant subspace is made of states with exactly one particle per site, and no multiple occupancies whatsoever. This implies that the only relevant degree of freedom is the local flavor, thus the particles can be regarded as local magnetic moments (or their multiflavor generalization) rather than fermions.

3.4.1 Generalized Schrieffer-Wolff transformation

Let's consider, for concreteness, a system of multiflavor fermions with external Raman coupling and interacting via a Hubbard like interaction, as described by Hamiltonian [2.21], which has the general structure $H = H_t + H_\Omega + H_U$, where:

$$H_t = \sum_{\langle ij \rangle} \sum_{\sigma} \left(t_\sigma c^\dagger_{i\sigma} c_{j\sigma} + \text{h.c.} \right), \qquad H_\Omega = \sum_{i,\sigma\rho} \left(\Omega_{i,\sigma\rho} c^\dagger_{i\sigma} c_{i\rho} + \text{h.c.} \right), \qquad H_U = \frac{U}{2} \sum_i n_i (n_i - 1). \tag{3.18}$$

The classical idea to build the effective low energy Hamiltonian in the strong Hubbard interaction regime is, generally speaking, to perform a suitable unitary transformation on H, known as Schrieffer-Wolff transformation, of the form $H \to e^S H e^{-S}$, where the generator of the transformation S must be determined in order to fulfill the desired constraint that, at lowest order in t_σ, the transformed Hamiltonian does not contain terms that change the number of doubly occupied sites [75]. However, this method has been recently embedded in the framework of the Floquet theory [76] and generalized to multiflavor Hubbard-like systems [77]. This modern formulation of the method allows for a more natural and flexible calculation of the effective Hamiltonian, so we will briefly revise the method in the following, with particular attention on the specific system described above (see e.g. [78] for a review on the basics of Floquet theory).

The main idea is to rephrase the problem in a "rotating" frame of reference, which is defined by the transformation of any time-dependent state $|\psi(t)\rangle$ into $|\psi_{\text{rot}}(t)\rangle = e^{iH_U t}|\psi(t)\rangle$. In the rotating frame, the Hamiltonian $H_{\text{rot}}(t)$ is time dependent and time periodic, as we deduce from the Schrödinger equation:

$$i\partial_t |\psi_{\text{rot}}(t)\rangle = H_{\text{rot}}(t)|\psi_{\text{rot}}(t)\rangle,$$

which, using the Schrödinger equation in the original frame $i\partial_t|\psi(t)\rangle = H|\psi(t)\rangle$, leads to

$$H_{\text{rot}}(t) = -H_U + e^{iH_U t} H e^{-iH_U t}. \tag{3.19}$$

The second term in eq. [3.19] can be expanded as a sum of nested commutators by means of the Baker-Campbell-Hausdorff identity and it yields

$$H_{\text{rot}}(t) = -H_U + H + it[H_U, H] + \frac{(it)^2}{2!}[H_U, [H_U, H]] + \frac{(it)^3}{3!}[H_U, [H_U, [H_U, H]]] + \dots \tag{3.20}$$

Since $[H_U, H_U] = [H_U, H_\Omega] = 0$, the only non trivial commutator is $[H_U, H_t]$, which can be evaluated as follows. First of all, let's introduce the projection operator $P_{i,n}$ which projects a state into another state with exactly n particles on site i, so for instance the operator $P_{i,n}\ c^\dagger_{i\sigma} c_{j\sigma}\ P_{j,n'}$ moves a particle with flavor σ from site j, where at the beginning there are n' particles, to site i, where in the end there are n particles. The hopping Hamiltonian can be split as a sum of such operators, in particular:

$$H_t = \sum_{n,n'=1}^{N} H_{t,nn'}, \qquad H_{t,nn'} = \sum_{\langle ij\rangle,\sigma} \left(t_\sigma P_{i,n}\ c^\dagger_{i\sigma} c_{j\sigma}\ P_{j,n'} \ +\ t^*_\sigma P_{j,n}\ c^\dagger_{j\sigma} c_{i\sigma}\ P_{i,n'} \right). \tag{3.21}$$

The main advantage of such decomposition is that the commutator of H_U and $H_{t,nn'}$ is proportional to $H_{t,nn'}$:

$$[H_U,\ H_{t,nn'}] = (n - n')U H_{t,nn'}, \tag{3.22}$$

which allows an easy evaluation of all the nested commutators in eq. [3.20]:

$$\underbrace{[H_U, \ldots, [H_U, H_{t,nn'}]]}_{p \text{ times}} = (n - n')^p U^p H_{t,nn'}.$$

The rotating frame Hamiltonian thus reads

$$H_{\text{rot}}(t) = H_\Omega + \sum_{nn'} \sum_{p=0}^{\infty} \frac{[iUt(n-n')]^p}{p!} H_{t,nn'} = H_\Omega + \sum_{nn'} e^{iUt(n-n')} H_{t,nn'} = H_\Omega + \sum_m e^{iUtm} H_{t,m}, \tag{3.23}$$

where $H_{t,m} = \sum_{n'} H_{t,n'+m,n'}$ and the label m can assume, in general, only integer values from $-(N-1)$ to $(N-1)$. This formulation represents the Fourier series of $H_{\text{rot}}(t)$, which manifestly shows its time periodicity with period $T = 2\pi/U$ and frequency U. The theoretical framework for the study of time periodic Hamiltonians is Floquet theory [78]. One of the main results of Floquet theory is that it is possible to average out the fast dynamics via a high-frequency expansion of the time periodic Hamiltonian, obtaining an effective static Hamiltonian that describes the slow dynamics of the system [76]. Since the rotation frequency U is the largest energy scale, here we can apply the high-frequency expansion and the resulting effective static Hamiltonian is:

$$H_{\text{eff}} = H_\Omega + H_{t,0} + \sum_{m\neq 0} \frac{H_{t,m} H_{t,-m}}{mU} + \mathcal{O}\left(\frac{t^2}{U^2}\right). \tag{3.24}$$

3.4.2 Two-flavor system

For a two flavor system ($N = 2$), the label m can only assume three values: 0, $+1$ and -1. The term $H_{t,0}$ includes hopping processes that leave the number of double occupancies unchanged; while $H_{t,\pm 1}$ include hopping processes that increase ($+1$) or decrease (-1) the number of double occupancies by 1. Some examples of these processes are schematically represented in fig. [3.8 (a)]. The effective Hamiltonian is

$$H_{\text{eff}} = H_\Omega + H_{t,0} + \frac{1}{U}\left(H_{t,+1} H_{t,-1} - H_{t,-1} H_{t,+1}\right) \tag{3.25}$$

and it contains all the processes that can occur at strong coupling, regardless of the filling factor, including spin interactions and double-holon dynamics. However, we are mostly interested in the particular case of

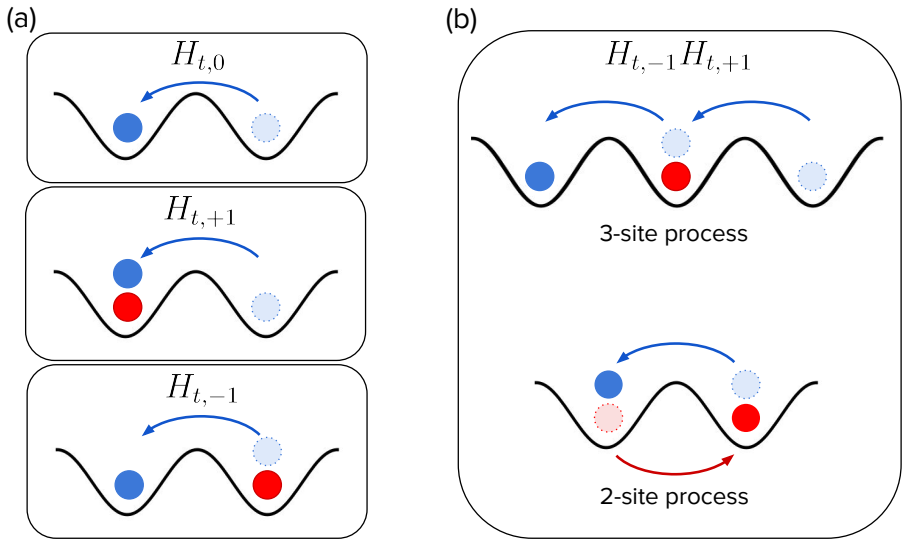

Figure 3.8: Schematic representation of the hopping processes described by $H_{t,0}$, $H_{t,\pm1}$ (a) and $H_{t,-1}H_{t,+1}$ (b). Lighter (darker) circles represent the position of particles before (after) the tunneling event, and the colors represent different flavors.

half filling, which means that we want to project H_{eff} into the subspace of the Hilbert-Fock space made of states with exactly one fermion per site. First of all, we observe that the projection of $H_{t,0}$ on this subspace vanishes, as its only effect is to move around double occupancies and empty sites (doublon-holon dynamics), which are not present in the subspace. Similarly, $H_{t,+1}H_{t,-1}$ vanishes when it is projected, as it involves processes that destroy a double occupancy and then create it back elsewhere, but the states within the subspace don't have doubly occupied sites. On the other hand, $H_{t,-1}H_{t,+1}$ describes processes where a double occupancy is created first, and then destroyed, and hence it can be successfully projected on the subspace. Expanding the latter term in a one dimensional lattice (which makes the notation more transparent while maintaining the general idea), we get

$$\begin{aligned} H_{t,-1}H_{t,+1} = \sum_{ij,\,\sigma\rho} \Big[& t_\sigma t_\rho P_{i,1} c^\dagger_{i\sigma} c_{i+1\sigma} P_{i+1,2} P_{j,2} c^\dagger_{j\rho} c_{j+1\rho} P_{j+1,1} + t_\sigma t^*_\rho P_{i,1} c^\dagger_{i\sigma} c_{i+1\sigma} P_{i+1,2} P_{j+1,2} c^\dagger_{j+1\rho} c_{j\rho} P_{j,1} \\ & + t^*_\sigma t_\rho P_{i+1,1} c^\dagger_{i+1\sigma} c_{i\sigma} P_{i,2} P_{j,2} c^\dagger_{j\rho} c_{j+1\rho} P_{j+1,1} + t^*_\sigma t^*_\rho P_{i+1,1} c^\dagger_{i+1\sigma} c_{i\sigma} P_{i,2} P_{j+1,2} c^\dagger_{j+1\rho} c_{j\rho} P_{j,1} \Big] \\ = \sum_{i,\,\sigma\rho} \Big[& t_\sigma t_\rho P_{i,1} c^\dagger_{i\sigma} c_{i+1\sigma} P_{i+1,2} c^\dagger_{i+1\rho} c_{i+2\rho} P_{i+2,1} + t_\sigma t^*_\rho P_{i,1} c^\dagger_{i\sigma} c_{i+1\sigma} P_{i+1,2} c^\dagger_{i+1\rho} c_{i\rho} P_{i,1} \\ & + t^*_\sigma t_\rho P_{i+1,1} c^\dagger_{i+1\sigma} c_{i\sigma} P_{i,2} c^\dagger_{i\rho} c_{i+1\rho} P_{i+1,1} + t^*_\sigma t^*_\rho P_{i+1,1} c^\dagger_{i+1\sigma} c_{i\sigma} P_{i,2} c^\dagger_{i\rho} c_{i-1\rho} P_{i-1,1} \Big] . \end{aligned} \tag{3.26}$$

The first and the last terms describe three-site hoppings, where a particle is transferred from a site to a next-nearest neighbor, passing through the intermediate site and "temporarily" creating a double occupancy on that site, while keeping the total number of double occupancies unchanged. These processes are not relevant in the subspace of interest, as they imply the presence of doubly occupied or empty sites, and thus can be neglected. The second and third terms, on the other hand, describe an exchange of particles between nearest neighbors, and such processes give a non trivial contribution to the effective

Hamiltonian. Examples of these two types of processes are sketched in fig. [3.8 (b)]. Using $P_{i,2} = n_{i\uparrow}n_{i\downarrow}$ and $t_\sigma = -te^{i\phi_\sigma}$, we get

$$H_{t,-1}H_{t,+1} = 2t^2 \sum_i \left[(n_{i\uparrow}n_{i+1\downarrow} + n_{i\downarrow}n_{i+1\uparrow}) - e^{i(\phi_\uparrow - \phi_\downarrow)} S_i^+ S_{i+1}^- - e^{-i(\phi_\uparrow - \phi_\downarrow)} S_i^- S_{i+1}^+ \right] =$$

$$4t^2 \sum_i \left[\frac{n_i n_{i+1}}{4} - S_i^z S_{i+1}^z - \cos(\phi_\uparrow - \phi_\downarrow) \left(S_i^x S_{i+1}^x + S_i^y S_{i+1}^y \right) - \sin(\phi_\uparrow - \phi_\downarrow) \left(S_i^x S_{i+1}^y - S_i^y S_{i+1}^x \right) \right], \quad (3.27)$$

where we have introduced the spin operators:

$$S_i^a = \frac{1}{2} \sum_{\sigma\rho} c_{i\sigma}^\dagger \sigma_{\sigma\rho}^a c_{i\rho} \qquad (a = x, y, z) \qquad \text{and} \qquad S_i^\pm = S_i^x \pm i S_i^y, \quad (3.28)$$

$\hat{\sigma}^a$ being the a-th Pauli matrix. Finally, we observe that the density-density interaction is just a constant, as every state in the subspace has a fixed local density $n_i = 1$ on every lattice site, and the charge is not really a degree of freedom, so the term $\propto \sum_i n_i n_{i+1}$ can be neglected. The specific form of H_{eff} depends on the convention used for the the phase factors of hopping matrix elements. The result is more transparent using real matrix elements for hopping along the real direction ($\phi_\uparrow = \phi_\downarrow = 0$) and choosing a site dependent phase factor for Raman processes $\Omega_{j,\uparrow\downarrow} = \Omega e^{i\gamma j}$. With this choice, the Raman matrix, written in terms of the spin operators [3.28], reads

$$H_\Omega = \Omega \sum_j e^{i\gamma j} S_j^+ + \text{h.c.} = 2\Omega \sum_j \left[\cos(\gamma j)\, S_j^x - \sin(\gamma j)\, S_j^y \right] = -\sum_j \vec{B}_j \cdot \vec{S}_j, \quad (3.29)$$

where we have introduced the site dependent magnetic field $\vec{B}_j = 2\Omega(-\cos(\gamma j),\ \sin(\gamma j),\ 0)$; and finally the effective Hamiltonian is

$$\boxed{H_{\text{eff}} = \frac{4t^2}{U} \sum_i \vec{S}_i \cdot \vec{S}_{i+1} - \sum_i \vec{B}_i \cdot \vec{S}_i.} \quad (3.30)$$

The effective strong coupling model is thus a spin-$\frac{1}{2}$ Heisenberg antiferromagnet with strength $4t^2/U \equiv 2J$ (as expected from the strong coupling limit of a Hubbard model), which is subject to an external site dependent magnetic field of constant amplitude 2Ω, lying in the xy plane and due to the Raman coupling. The angle formed between the magnetic fields acting on adjacent sites is constant and given by the synthetic gauge flux γ. Strictly speaking, this interpretation holds in the limit $U \gg T$, $U \gg t$ and $U \gg \Omega$, as U represents the frequency of the rotating frame of reference, and the effective Hamiltonian is obtained via a high-frequency expansion of the time-periodic Hamiltonian written in this frame.

Remarkably, every thermal equilibrium state of the system must satisfy a stationarity condition, which stems from the fact that the expectation value on equilibrium states of the time derivative of any operator vanishes; in particular, looking at the local spin operators, we get:

$$\frac{d\langle \vec{S}_i \rangle}{dt} = 0 \quad \rightarrow \quad \langle [\vec{S}_i, H_{\text{eff}}] \rangle = 0 \quad \rightarrow \quad -2J \langle \vec{S}_i \times \vec{S}_{i+1} + \vec{S}_i \times \vec{S}_{i-1} \rangle + \langle \vec{S}_i \times \vec{B}_i \rangle = 0, \quad (3.31)$$

where we have used the Heisenberg equation for the time evolution of spin operators and evaluated the commutator with H_{eff}. Interpreting the quantity $-2J\vec{S}_{i\pm1}$ as the magnetic field exerted by the local moment at position $i \pm 1$ on the local moment at position i, eq. [3.31] represents the balance of three torques acting on $\vec{S}_i$. Not only this equation provides us with a set of $3L$ consistency conditions that any

equilibrium state should satisfy, but it also suggests the interpretation of $-2J\vec{S}_i \times \vec{S}_{i+1}$ as a mechanical torque exerted on site i by its right nearest neighbor, which opens the door to a more transparent interpretation of the current operators.

In order to derive the effective current operators projected in the subspace of interest, we can use the definitions of leg current [2.30] and rung current [2.31] given in terms of derivatives of the Hamiltonian with respect to the auxiliary Peierls phases. The effective Hamiltonian depends on the Peierls phases only through the kinetic term $\propto H_{t,-1}H_{t,+1}$ computed in eq. [3.27]. For example, the chiral current is

$$I_{\text{chir}} = \frac{1}{N_{\text{sites}}}\left(\frac{dH_{\text{eff}}}{d\phi_\downarrow} - \frac{dH_{\text{eff}}}{d\phi_\uparrow}\right)\Big|_{\phi_\uparrow=\phi_\downarrow=0} = -\frac{1}{N_{\text{sites}}}\frac{8t^2}{U}\sum_i \left(S_i^x S_{i+1}^y - S_i^y S_{i+1}^x\right)$$

$$\boxed{I_{\text{chir}} = -\frac{1}{N_{\text{sites}}}\frac{8t^2}{U}\sum_i \left(\vec{S}_i \times \vec{S}_{i+1}\right)_z} \tag{3.32}$$

which, in light of the discussion above, can be interpreted as the z-component of the torque exerted between adjacent spins, averaged over all the lattice sites. Similarly, the effective rung current is

$$I_i = \left(\vec{S}_i \times \vec{B}_i\right)_z \tag{3.33}$$

and it can be seen as the z-component of the torque exerted by the external magnetic field on the local spin. Notice that the z-component of the mechanical equilibrium condition [3.31] is nothing but the Kirchhoff's current law at one of the nodes connected to the i-th rung.

The effective spin model outlined above provides a semiclassical picture that we can use to compute observables in some particular cases. For example, a relevant regime to compare this model with previous results is the limit $\Omega \gg J$, where the local magnetic field prevails over the Heisenberg coupling in eq. [3.30] and in the ground state all the spins are aligned to the local field (thus lying on the xy plane). The spin at site $i+1$ is oriented at an angle γ with respect to the spin at site i, which implies that the z component of the torque between the two is $\frac{1}{4}\sin\gamma$, where the factor $1/4$ is due to the fact that the spin is $1/2$. From eq. [3.32] we readily obtain $\langle I_{\text{chir}}\rangle \approx \frac{2t^2\sin\gamma}{U}$, which is plotted in fig. [3.4] and is consistent with the mean field prediction when $U \gg \Omega$. A more accurate estimate to higher orders in t/U and Ω/U can be obtained by applying perturbation theory.

Finally we briefly mention that, in the opposite regime $J \gg \Omega$, the spins form an antiferromagnet oriented along z, resulting in a vanishing torque between nearest neighbors, since two adjacent spins are antiparallel and consequently in a vanishing chiral current. This suggests that, consistently with the mean field analysis, the ground state is antiferromagnetic at intermediate U.

3.4.3 Three-flavor and multi-flavor system

This section is mainly devoted to the derivation of an effective strong coupling Hamiltonian for a three flavor system with filling factor of one particle per site; however we try to keep the discussion as general as possible with respect to the number of flavors. In the specific case of three flavors, eq. [3.24] reduces to

$$H_{\text{eff}} = H_\Omega - \frac{1}{U}H_{t,-1}H_{t,+1} - \frac{1}{2U}H_{t,-2}H_{t,+2},$$

where $H_{t,\pm 2}$ describe those processes that increase (or decrease) by one the number of triple occupancies. Once again, we have dropped terms proportional to $H_{t,+1}H_{t,-1}$ and $H_{t,+2}H_{t,-2}$, as these terms involve

processes where a double (or triple) occupancy is destroyed and then created back, and such processes are not possible in the subspace of singly occupied sites. Generally speaking, for any multi-flavor system, every term of the form $H_{t,m}H_{t,-m}$, where $m \geq 1$, is irrelevant in the manifold of singly occupied sites. Another key simplification, due to the projection process, is the fact that all the terms of the form $H_{t,-m}H_{t,m}$ vanish for $m \geq 2$. The reason is that these terms involve processes mediated by the intermediate formation of a multiple occupancy with $(m+1)$ particles on some site; however it is impossible to populate this site, which is initially singly occupied, with $(m+1)$ particles via a single hopping process, unless $m = 1$. The general form of the effective Hamiltonian for an arbitrary number of flavors is thus given by

$$H_{\text{eff}} = H_\Omega - \frac{1}{U} H_{t,-1} H_{t,+1},$$

and the problem reduces to a general evaluation of $H_{t,-1}H_{t,+1}$.

We can follow the same steps shown in eq. [3.26], neglecting terms describing three-site processes, and using the explicit expression for the projector on doubly occupied sites[4]

$$P_{i,2} = \sum_{\sigma>\rho} n_\sigma n_\rho \prod_{\tau\neq\sigma,\rho} (1 - n_\tau)$$

we get

$$H_{t,-1}H_{t,+1} = 2t^2 \sum_i \sum_{\sigma\neq\rho} \left(n_{i\sigma} n_{i+1\rho} - e^{i(\phi_\sigma - \phi_\rho)} S_{i,\sigma\rho} S_{i+1,\rho\sigma} \right), \tag{3.34}$$

where we have introduced the generalized "flavor ladder operators"

$$S_{i,\sigma\rho} = c^\dagger_{i\sigma} c_{i\rho}. \tag{3.35}$$

Using $\sum_{\sigma\neq\rho} n_{i\sigma} n_{i+1\rho} = n_i n_{i+1} - \sum_\sigma S_{i,\sigma\sigma} S_{i+1,\sigma\sigma}$ and neglecting the density-density interaction, which is just a constant, we finally get

$$H_{\text{eff}} = \Omega \sum_j \sum_{\sigma=1}^{N-1} \left(e^{i\gamma j} S_{j,\sigma,\sigma+1} + \text{h.c.} \right) + \frac{2t^2}{U} \sum_i \sum_{\sigma\rho} S_{i,\sigma\rho} S_{i+1,\rho\sigma}. \tag{3.36}$$

Here we have assumed that the Raman hopping scheme connects only adjacent flavors (σ and $\sigma+1$) with the same hopping amplitude Ω and a site dependent phase $e^{i\gamma j}$; however the generalization to an arbitrary Raman hopping scheme is straightforward, and the first term reads $\sum_{i,\sigma\rho} \Omega_{i,\sigma\rho} S_{i,\sigma\rho}$.

Similarly to the $N = 2$ case, the current operators can be computed as derivatives of H_{eff} with respect to the corresponding Peierls phases. The flavor current results

$$I_\sigma = \frac{1}{N_{\text{sites}}} \frac{\partial H_{\text{eff}}}{\partial \phi_\sigma}\bigg|_{\vec{\phi}=0} = \frac{2t^2 i}{N_{\text{sites}}} \sum_{i,\rho\neq\sigma} \left(S_{i,\sigma\rho} S_{i+1,\rho\sigma} - \text{h.c.} \right); \tag{3.37}$$

while the rung current reads

$$I_j = i\Omega \sum_j \sum_{\sigma=1}^{N-1} \left(e^{i\gamma j} S_{j,\sigma,\sigma+1} - \text{h.c.} \right). \tag{3.38}$$

So far we have described the strong coupling effective model in terms of the "flavor ladder operators" $S_{i,\sigma\rho}$, which are generators of the local $su(N)$ algebra. This is a set of N^2 operators (per lattice site); of

[4] For $N = 3$, the projector is given by $P_{i,2} = n_{+1}n_0(1-n_{-1}) + n_{+1}(1-n_0)n_{-1} + (1-n_{+1})n_0 n_{-1}$.

which only N^2-1 are independent, as they satisfy the constraint $\sum_\sigma S_{i\sigma\sigma} = \sum_\sigma n_{i\sigma} = n_i = 1$ (the local density operator n_i in fact is just the identity operator, because every site contains exactly one particle). In particular, since they act on the N-dimensional Hilbert space of local flavors, they are the fundamental irreducible representation of $su(N)$, and they obey the following fundamental commutation relation [79]:

$$[S_{i,\alpha\beta}, S_{j,\gamma\delta}] = \delta_{ij}\left(\delta_{\beta\gamma}S_{i,\alpha\delta} - \delta_{\alpha\delta}S_{i,\gamma\beta}\right). \tag{3.39}$$

However, at least for $N=3$, it is possible to rephrase eq. [3.36] in terms of just three operators (per every lattice site), which can be obtained as linear combinations of $S_{i,\sigma\rho}$ and generate an $su(2)$ subalgebra of $su(N)$, and thus can be interpreted as spin operators. In particular, for the specific case $N=3$, the spin operators are given by the following linear combinations of flavor ladder operators:

$$\Sigma_i^x = \frac{1}{\sqrt{2}}\left(S_{i,-1,0} + S_{i,0,+1} + \text{h.c.}\right), \qquad \Sigma_i^y = \frac{i}{\sqrt{2}}\left(S_{i,-1,0} + S_{i,0,+1} - \text{h.c.}\right), \qquad \Sigma_i^z = S_{i,+1,+1} - S_{i,-1,-1}; \tag{3.40}$$

and one can easily prove that they are a $su(2)$ subalgebra of $su(3)$, as they satisfy the standard commutation rule $[\Sigma_i^a, \Sigma_j^b] = i\delta_{ij}\varepsilon_{abc}\Sigma_i^c$. Moreover, since they act on a 3-dimensional space, they are a 3-dimensional irreducible representation of $su(2)$, and hence the associated spin is $S=1$ [80].

In order to rewrite any operator in terms of the spin operators [3.40], we need to express every flavor ladder operator in terms of the latter, which is not a trivial task; however this is possible by using quadratic combinations of spin operators, as we explicitly show in appendix [A]. Rewriting the effective Hamiltonian [3.36], we get

$$\boxed{H_{\text{eff}} = \frac{2t^2}{U}\sum_{\langle ij\rangle}\left[\vec{\Sigma}_i\cdot\vec{\Sigma}_j + \left(\vec{\Sigma}_i\cdot\vec{\Sigma}_j\right)^2\right] - \sum_i \vec{B}_i\cdot\vec{\Sigma}_i,} \tag{3.41}$$

up to a constant term $\propto \sum_i n_i n_{i+1}$, where the local magnetic field is $\vec{B}_j = \sqrt{2}\Omega(-\cos(\gamma j),\ \sin(\gamma j),\ 0)$. In this case, the effective strong coupling model is a spin-1 Heisenberg antiferromagnet of strength $2t^2/U$, subject to a frustration term $\propto (\vec{\Sigma}_i\cdot\vec{\Sigma}_j)^2$ having the same strength, and to an external magnetic field of constant amplitude $\sqrt{2}\Omega$, lying on the xy plane and due to the Raman processes. Similarly to the previous case, the angle between magnetic fields acting on nearest neighbor sites is the constant γ. A similar mapping for the SU(3) Heisenberg model with no Raman field has been proposed in [81], although with a slightly different choice of the $su(2)$ subalgebra. The presence of a Raman field, however, makes the choice [3.40] the most natural to provide a spin interpretation as close as possible to the $N=2$ case. In absence of an external magnetic field ($\Omega=0$), this model is known as the Lai-Sutherland model [82, 83].

Similarly we can express the chiral current operator as:

$$\boxed{I_{\text{chir}} = \frac{2t^2}{U}\sum_{\langle ij\rangle}\left(\vec{\Sigma}_i\times\vec{\Sigma}_j\right)_z + \frac{2t^2}{U}\sum_{\langle ij\rangle}\left[(\vec{\Sigma}_i\cdot\vec{\Sigma}_j)\left(\vec{\Sigma}_i\times\vec{\Sigma}_j\right)_z + \left(\vec{\Sigma}_i\times\vec{\Sigma}_j\right)_z(\vec{\Sigma}_i\cdot\vec{\Sigma}_j)\right]} \tag{3.42}$$

which once again can be regarded as the average "torque" between nearest neighbors associated to the Lai-Sutherland interaction, and the rung current operator as:

$$I_j = \left(\vec{\Sigma}_j\times\vec{B}_j\right)_z, \tag{3.43}$$

which is the torque exerted by the local magnetic field.

In the limit $\Omega \gg J$, the spins align to the local magnetic field, forming an angle γ between nearest neighbors. The expectation value of $(\vec{\Sigma}_i\times\vec{\Sigma}_{i+1})_z$ can be computed with a semiclassical approach, treating

spins as classical vectors and it is $\approx \sin\gamma$ (with no prefactors as we are dealing with spin-1 operators). The expectation value of the quartic term in eq. [3.42] is a little tricky and cannot be evaluated by a naive classical approach. The reason is that it contains quadratic combinations of local spins that can't be evaluated classically due to intrinsic quantum fluctuations of the spin operators.[5] Still, the ground state is a tensor product over the lattice sites, which leads to the expectation value

$$\langle I_{\text{chir}}\rangle \approx \frac{t^2}{2U}\left(2\sin\gamma + \sin 2\gamma\right) \qquad \Omega \gg \frac{2t^2}{U}. \tag{3.44}$$

We show this estimate, together with MFT and DMFT results in fig. [3.4].

3.5 Chirality induced by spin-exchange in multiorbital systems

In the previous sections we have discussed how Raman processes can be used to induce a chiral behavior in a single-orbital Hubbard model with N internal flavors and we have argued that chirality survives in the strongly interacting regime, where it is in fact enhanced. We can now take one step further and discuss how the chiral current behaves in a multiorbital interacting system, where we can expect an interesting phenomenology. In this section we present early encouraging results in this direction, without presumption of being exhaustive.

As we have introduced in chapter [1], it is possible to realize two-orbital Hubbard-Kanamori models with alkaline-earth-like atoms by exploiting the electronic ground and metastable states ${}^1S_0 = |g\rangle$ and ${}^3P_0 = |e\rangle$ as orbital degrees of freedom. The resulting Hamiltonian is given in eq. [1.5] and it is SU(N) symmetric; however we can once again realize a synthetic dimension by inducing Raman transitions through the auxiliary state ${}^3P_1$. If for example we choose the frequencies of the two Raman laser beams nearly resonant to the ${}^1S_0 \leftrightarrow {}^3P_1$ transition, in general they won't be resonant to ${}^3P_0 \leftrightarrow {}^3P_1$ as well. For example, in ^{173}Yb, the optical transition ${}^1S_0 \leftrightarrow {}^3P_1$ has a natural frequency of 518.7 THz (wavelength 556 nm), while ${}^3P_0 \leftrightarrow {}^3P_1$ has a much lower frequency of 20.5 THz [20]. This implies that the effective Rabi coupling between different nuclear states is only induced in those atoms that are in their ${}^1S_0$ electronic state. One could naively think that, as a direct consequence of this property, only $|g\rangle$ particles display a chiral current, whereas $|e\rangle$ particles are non-chiral. However, in the present section we show that this is not necessarily the case and in fact also $|e\rangle$ particles can develop a chiral current, provided that there is a spin-exchange interaction between the two orbitals.

We can understand this statement by means of symmetry considerations. The symmetry group of the Hamiltonian [1.5] is in general U(1)×U(1)×SU(N), generated by $N_g - N_e$ and by the ladder operators $S_{\sigma\rho}$ defined in eq. [1.7] as the sum of orbital-wise ladder operators. On the other hand, in the special case $V_{\text{ex}} = 0$, the symmetry is enhanced to U(1)×SU(N)×U(1)×SU(N), because the orbital-wise ladder operators $S_{a,\sigma\rho} = \sum_i c^\dagger_{ia\sigma} c_{ia\rho}$ separately commute with H, i.e. $[S_{a,\sigma\rho}, H] = 0$, and therefore generate two distinct U(1)×SU(N) symmetry groups. In the latter case, the introduction of Raman processes explicitly breaks one of the two copies of SU(N), in particular the one generated by "ground" ladder operators $S_{g,\sigma\rho}$, while leaving the other copy of SU(N) unbroken. We can thus expect a chiral behavior of $|g\rangle$ particles and a non-chiral behavior of $|e\rangle$ particles. In contrast to this case, when $V_{\text{ex}} \neq 0$, Raman processes involving $|g\rangle$ particles break the overall SU(N) symmetry (and there is no residual SU(N) symmetry in this case), thus potentially leading to chiral behavior of $|e\rangle$ particles. Reversing our perspective, we can use chirality of $|e\rangle$ particles as a hallmark of the presence of a spin-exchange interaction and ideally we can use the experimentally measured value of the chiral current to extrapolate the value of V_{ex}.

[5] More explicitly, quantum spin fluctuations imply that, for example, $\langle \Sigma_{ix}^2\rangle \neq \langle \Sigma_{ix}\rangle^2$.

Intuitively, this effect will be stronger in the presence of a large spin-exchange interaction, which makes ^{173}Yb a good candidate for an experimental implementation. The spin-exchange interaction is in fact a non-negligible energy scale in mixtures of ^{173}Yb atoms in the $^1S_0$ and $^3P_0$ electronic states.[6] To appreciate the order of magnitude of the different interaction terms, we can look at the experimentally measured values of scattering lengths in ^{173}Yb [20, 26]:

$$a_{gg} \approx 200a_0, \quad a_{ee} \approx 300a_0, \quad a_{eg^+} \approx 3300a_0, \quad a_{eg^-} \approx 219a_0,$$

where a_0 is the Bohr radius. From eq. [1.6] we immediately see that with these scattering lengths, the spin and direct exchange parameters are roughly equal: $V_{\text{ex}} \approx 0.9V$.

To study how a Rabi coupling in the $|g\rangle$ channel drives chirality in the $|e\rangle$ channel through the spin-exchange coupling, we can start by building a simplified model that captures the essential features described above with a minimal number of free parameters. We begin by assuming $V_{\text{ex}} = V$, which only holds for atomic species with $|a_{eg^+} - a_{eg^-}| \approx |a_{eg^+} + a_{eg^-}|$ (or equivalently $|a_{eg^-}| \ll |a_{eg^+}|$) like ^{173}Yb. Moreover, we can exclude complications due to different band structures in the two channels by assuming that the hopping scales are the same $t_g = t_e$. This is in fact perfectly reasonable, as some atomic species have the same electric polarizability in the electronic ground and excited states at specific wavelengths of the optical lattice light, called *magic wavelengths*. Electric polarizability directly affects the trapping forces impressed by laser light on the atoms, so at the magic wavelengths the two channels are subject to the same lattice potential $V_g(\mathbf{r}) = V_e(\mathbf{r})$, which results in the same hopping scale. For example, one of the magic wavelengths of ^{173}Yb is 759.34 nm [20] (the other magic wavelengths in the visible spectrum are too close to electronic transitions to be effectively used). We further assume that the local intraorbital interaction is the same for the two channels: $U_{gg} = U_{ee} \equiv U$. For an optical lattice at the magic wavelengths, where the Wannier functions of the two channels are the same: $w_g(\mathbf{r}) = w_e(\mathbf{r})$, this amounts to assume that $a_{gg} \approx a_{ee}$. This is only approximately true for ^{173}Yb, where we have $U_{ee} \approx 1.5U_{gg}$. Finally, we can start by considering only two flavor states $\sigma = \pm 1/2$ for simplicity.

In summary, all these assumptions lead to the following Hamiltonian:

$$\begin{aligned} H = &-t \sum_{\langle ij \rangle} \sum_{a=g,e} \sum_{\sigma=\uparrow\downarrow} \left(c^\dagger_{ia\sigma} c_{ja\sigma} + \text{h.c.} \right) + \Omega \sum_j \left(e^{i\varphi(\mathbf{r}_j)} c^\dagger_{jg\uparrow} c_{jg\downarrow} + \text{h.c.} \right) - \mu \sum_{ja\sigma} n_{ja\sigma} \\ &+ \frac{U}{2} \sum_{j,\, a=g,e} n_{ja}(n_{ja} - 1) + V_{\text{ex}} \sum_j (n_{jg\uparrow} n_{je\downarrow} + n_{je\uparrow} n_{jg\downarrow}) - V_{\text{ex}} \sum_j \left(c^\dagger_{jg\uparrow} c_{jg\downarrow}\, c^\dagger_{je\downarrow} c_{je\uparrow} + \text{h.c.} \right). \end{aligned} \tag{3.45}$$

In order to switch to an equivalent translation invariant Hamiltonian, we need to identify a suitable unitary transformation of the fermionic operators. If $V_{\text{ex}} = 0$, it is sufficient to apply the unitary transformation [2.22] only to fermionic operators of the $|g\rangle$ channel, while leaving $c_{je\sigma}$ and $c^\dagger_{je\sigma}$ unchanged. If instead $V_{\text{ex}} \neq 0$, this is no longer the case, as the spin-exchange term will acquire a space-dependent phase factor. In order to remove this factor, we are forced to apply the same unitary transformation to operators of the $|e\rangle$ channel as well, namely:

$$c_{ja\sigma} \to e^{i\sigma\varphi(\mathbf{r}_j)} c_{ja\sigma}, \qquad c^\dagger_{ja\sigma} \to e^{-i\sigma\varphi(\mathbf{r}_j)} c^\dagger_{ja\sigma}, \qquad n_{ja\sigma} \to n_{ja\sigma}, \qquad (a = g, e), \tag{3.46}$$

[6] This is a key ingredient in the mechanism of orbital Feshbach resonance in alkaline-earth-like atoms, that we discuss in sec. [5.3].

which leads to

$$H = -t\sum_{\langle ij\rangle}\sum_{a\,\sigma}\left(e^{i\sigma[\varphi(\mathbf{r}_j)-\varphi(\mathbf{r}_i)]}c^\dagger_{ia\sigma}c_{ja\sigma}+\text{h.c.}\right)+\Omega\sum_j\left(c^\dagger_{jg\uparrow}c_{jg\downarrow}+\text{h.c.}\right)-\mu\sum_{ja\sigma}n_{ja\sigma}$$
$$+\frac{U}{2}\sum_{j,a}n_{ja}(n_{ja}-1)+V_{\text{ex}}\sum_j(n_{jg\uparrow}n_{je\downarrow}+n_{je\uparrow}n_{jg\downarrow})-V_{\text{ex}}\sum_j\left(c^\dagger_{jg\uparrow}c_{jg\downarrow}\,c^\dagger_{je\downarrow}c_{je\uparrow}+\text{h.c.}\right). \tag{3.47}$$

In the following sections, we analyze the ground state properties of this model by using the Hartree-Fock method and DMFT. We carry the analysis as follows: first of all, we consider a representative case with a 2-dimensional optical square lattice, $t=\Omega=0.25$, $\gamma_x\equiv\varphi(\mathbf{r}_i+\hat{\mathbf{e}}_x)-\varphi(\mathbf{r}_i)=\frac{\pi}{2}$, $\gamma_y\equiv\varphi(\mathbf{r}_i+\hat{\mathbf{e}}_y)-\varphi(\mathbf{r}_i)=0$ and $U=3$, so we are in the regime $U\gg t,\Omega$. Furthermore, for simplicity we consider the case where both bands are half-filled, i.e. $N_g=N_e=N_{\text{sites}}$ (from the general discussion of sec. [1.2.2], we recall that N_g and N_e are good quantum numbers). This condition is enforced setting $\mu=(U+V_{\text{ex}})/2$, which is the condition to make Hamiltonian [3.47] invariant under a particle-hole transformation $c_{ia\sigma}\to(-1)^{R_i}c^\dagger_{ia\sigma}$. With this choice, when the two bands are perfectly decoupled ($V_{\text{ex}}=0$), the ground state is an antiferromagnetic insulator in the $|e\rangle$ channel and the hybrid Mott-band insulator described in sec. [3.2] in the $|g\rangle$ channel. Since excited particles are not coupled to Raman photons, we expect that antiferromagnetism is more robust against thermal fluctuations in the $|e\rangle$ band[7] than in the $|g\rangle$ band (where we know it is very fragile), so we take antiferromagnetic ordering into account. We then study the ground state properties as a function of the spin-exchange interaction V_{ex} expressed in units of the magnetic superexchange coupling $J=2t^2/U$.

Hartree-Fock analysis

We begin our analysis by applying the Hartree-Fock method outlined in sec. [3.1], including possible antiferromagnetic ordering in both channels. The relevant variational parameters are two copies of the previously defined m and s, corresponding to the two channels $|g\rangle$ and $|e\rangle$ respectively: $\{m_g,\,m_e,\,s_g,\,s_e\}$. Similarly, introducing two copies of the spinor: $\Psi_{\mathbf{k}g}$ and $\Psi_{\mathbf{k}e}$ and performing the mean-field decoupling, we finally get the effective Hamiltonian:

$$H=\sum_{\mathbf{k}\in\text{MBZ}}\sum_{a=g,e}\Psi^\dagger_{\mathbf{k}a}H_{\mathbf{k}a}\Psi_{\mathbf{k}a}+N_{\text{sites}}\left[U|s_g|^2+U|s_e|^2+2V_{\text{ex}}s_gs_e+Um_g^2+Um_e^2\right],$$

$$H^{\text{eff}}_{\mathbf{k}a}=\begin{pmatrix}-Um_a-V_{\text{ex}}m_{\bar a} & \Omega_a-Us_a-V_{\text{ex}}s_{\bar a} & -tg_{\mathbf{k}\uparrow} & 0\\ \Omega_a-Us_a-V_{\text{ex}}s_{\bar a} & Um_a+V_{\text{ex}}m_{\bar a} & 0 & -tg_{\mathbf{k}\downarrow}\\ -tg^*_{\mathbf{k}\uparrow} & 0 & Um_a+V_{\text{ex}}m_{\bar a} & \Omega_a-Us_a-V_{\text{ex}}s_{\bar a}\\ 0 & -tg^*_{\mathbf{k}\downarrow} & \Omega_a-Us_a-V_{\text{ex}}s_{\bar a} & -Um_a-V_{\text{ex}}m_{\bar a}\end{pmatrix} \tag{3.48}$$

where for brevity we have defined $\Omega_g=\Omega$ and $\Omega_e=0$ and $\bar a$ denotes the band index opposite to a. The self-consistency equations can be explicitly derived by a straightforward generalization of eq. [3.12]; however here we find the optimal parameter by numerically minimizing the grand canonical potential $F(s_g,s_e,m_g,m_e)$ with the constraints $-\frac{1}{2}\le s_a\le\frac{1}{2}$ and $-\frac{1}{2}\le m_a\le\frac{1}{2}$ (which stem from the definitions of s_a and m_a). At $T=0$ and global half-filling, the latter can be computed by summing the energies of the 4 lowest bands (two per every band index) and adding the constant terms containing variational parameters. Finally, the chiral current on a given band can be evaluated by adapting eq. [3.13].

[7] In fact it can be proved that in the single band Hubbard model, the critical temperature for antiferromagnetic order is proportional to the superexchange coupling: $T_c\approx t^2/U$ for $U\gg t$, which means that it decreases upon increasing the Hubbard-U.

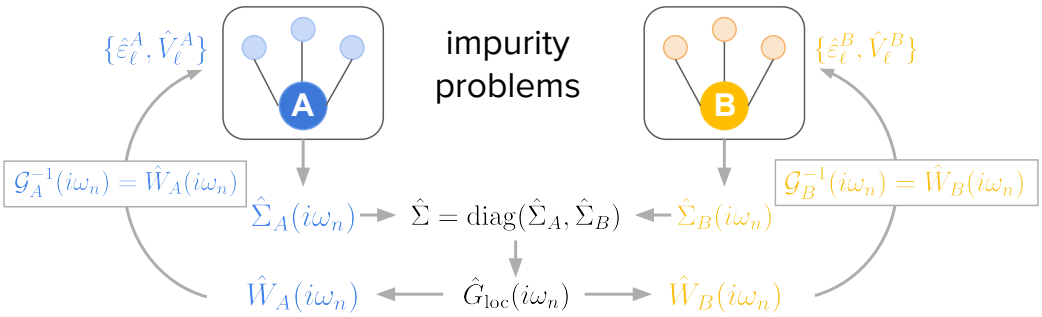

Figure 3.9: Illustration of the R-DMFT self-consistent procedure in the presence of two sublattices.

DMFT analysis

To take into account antiferromagnetism within the framework of DMFT, we implement the R-DMFT method described in sec. [1.3.4]. Antiferromagnetism breaks the translational symmetry of the original lattice, differentiating the properties of the two sublattices A and B, but it preserves a residual translational symmetry within the two sublattices, as shown in fig. [3.1 (a)]. To match the formalism introduced in sec. [1.3.4], we write the blocks of the non-interacting Hamiltonian in the antiferromagnetic spinor representation $(\hat{\Psi}^\dagger_{\mathbf{k}A}, \hat{\Psi}^\dagger_{\mathbf{k}B})$ as $\hat{H}_{\mathbf{k},ij}$, where the indexes i, j run over the two sublattices $i, j = \{A, B\}$ and $\mathbf{k}$ runs over the magnetic Brillouin zone. Every block $\hat{H}_{\mathbf{k},ij}$ has an internal structure labeled by spin and band indexes. Neglecting non-local quantum fluctuations, we assume that the self-energy is block diagonal in the antiferromagnetic spinor representation, i.e. $\hat{\Sigma}_{ij}(i\omega_n) = \hat{\Sigma}_j(i\omega_n)\delta_{ij}$. By exactly solving two independent impurity problems, we evaluate the two diagonal 2×2 blocks $\hat{\Sigma}_A(i\omega_n)$ and $\hat{\Sigma}_B(i\omega_n)$. Applying eq. [1.30] we obtain the local components of the lattice Green function on the two sublattices as:

$$\hat{G}_{jj}(i\omega_n) = \frac{2}{N_{\text{sites}}} \sum_{\mathbf{k}\in\text{MBZ}} [(i\omega_n - \hat{H}_{\mathbf{k}} - \hat{\Sigma}(i\omega_n))^{-1}]_{jj}, \tag{3.49}$$

and the corresponding Weiss fields $\hat{W}_A(i\omega_n) = \hat{G}^{-1}_{AA}(i\omega_n) + \hat{\Sigma}_A(i\omega_n)$ and $\hat{W}_B(i\omega_n) = \hat{G}^{-1}_{BB}(i\omega_n) + \hat{\Sigma}_B(i\omega_n)$. The bath parameters of the two impurity problems are adjusted to fit the corresponding Weiss fields and this procedure is repeated iteratively until convergence. This procedure is schematically illustrated in fig. [3.9].

With the converged Green function, we can compute objects like $\langle \Psi^\dagger_{\mathbf{k}\alpha} \Psi_{\mathbf{k}\beta} \rangle$ by following the prescriptions of sec. [1.3.5], where the indexes α, β include spin, band and sublattice indexes: $\alpha, \beta = \{\uparrow, \downarrow\} \otimes \{g, e\} \otimes \{A, B\}$. From this, we immediately get the orbital-wise antiferromagnetic magnetization and the parameters s_a:

$$m_a = \frac{1}{N_{\text{sites}}} \sum_{\mathbf{k}\in\text{MBZ}} \langle n_{\mathbf{k}A\uparrow a} - n_{\mathbf{k}A\downarrow a} \rangle, \qquad s_a = \frac{2}{N_{\text{sites}}} \sum_{\mathbf{k}\in\text{MBZ}} \langle c^\dagger_{\mathbf{k}A\uparrow a} c_{\mathbf{k}A\downarrow a} \rangle. \tag{3.50}$$

as well as the chiral current, which can be computed from eq. [2.36] as:

$$\mathbf{I}_{\text{chir},a} = -\frac{2}{N_{\text{sites}}} \sum_{\mathbf{k}\in\text{MBZ}} (\nabla_{\vec{\gamma}} H_{\mathbf{k};i\sigma a,j\rho a}) \langle \Psi^\dagger_{\mathbf{k},i\sigma a} \Psi_{\mathbf{k},j\rho a} \rangle. \tag{3.51}$$

Results

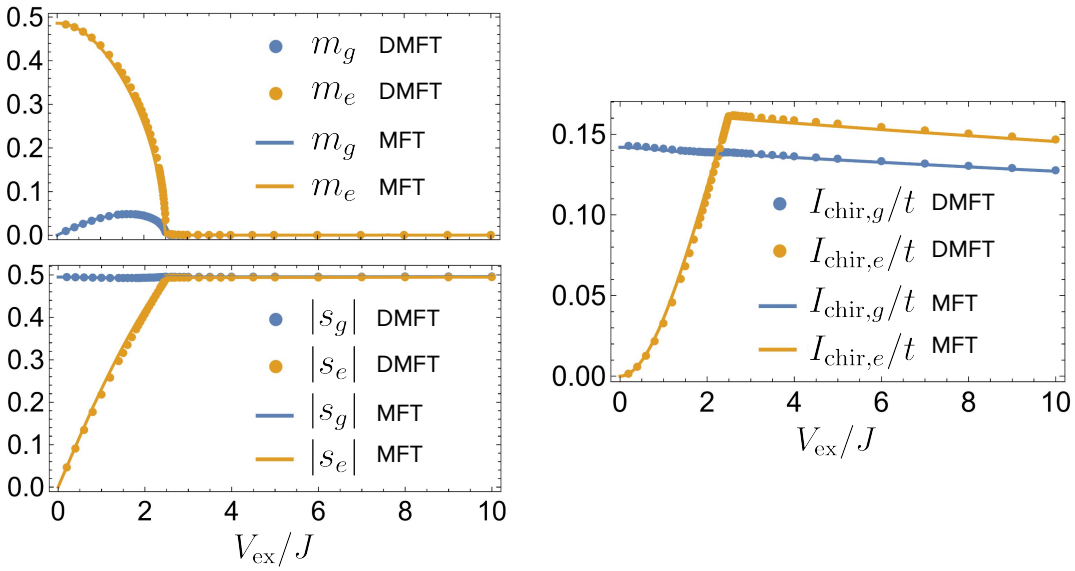

Figure 3.10: Self-consistent parameters m_a and s_a (left) and chiral currents along $\hat{\mathbf{e}}_x$ (right) in the ground state of Hamiltonian [3.45] as a function of V_{ex}/J for $t = \Omega = 0.25$, $U = 3$, $\gamma_x = \pi/2$ and $\gamma_y = 0$ on a 2-dimensional optical square lattice at global half filling.

The values of the main observables computed in the ground state are reported in fig. [3.10], where we compare the two methods. We immediately notice the good agreement between Hartree-Fock and DMFT, which suggests that the interorbital coupling does not introduce significant dynamical quantum fluctuations in this regime of parameters, simplifying the interpretation. First of all, as expected, when $V_{\text{ex}} = 0$ the two bands are decoupled: particles in the $|e\rangle$ channel are described by a Hubbard model with large U and they form an antiferromagnet with large magnetization $m_e \approx 1/2$ and no effective Rabi coupling $s_e = 0$; while particles in the $|g\rangle$ channel are coupled to Raman photons and they form a Mott-band hybrid insulator with large U, characterized by no antiferromagnetism $m_g = 0$ and large effective Rabi coupling $s_g \approx -1/2$ (hence $\Omega_g^{\text{eff}} \approx \Omega + U/2$). Consistently, $|e\rangle$ particles are non-chiral, while there is a significant chiral current in the $|g\rangle$ channel. Increasing V_{ex}, the magnetic character of $|e\rangle$ particles quickly decreases, while s_e quickly increases in module (in fact it is negative) and so does the effective Rabi coupling $\Omega_e^{\text{eff}} = -Us_e - V_{\text{ex}}s_g$. At the same time, $|g\rangle$ particles develop a very weak antiferromagnetic order, while s_g is stable and $\Omega_g^{\text{eff}} = \Omega - Us_g - V_{\text{ex}}s_e$ slightly increases. At $V_{\text{ex}} \approx 2.5J$ there is a critical point where m_g and m_e vanish together and translational symmetry over the full lattice is restored. Moreover, s_g and s_e saturate to $\approx 1/2$, and the effective Rabi couplings are given by $\Omega_g^{\text{eff}} \approx \Omega + (U + V_{\text{ex}})/2$ and $\Omega_e^{\text{eff}} \approx (U + V_{\text{ex}})/2$ respectively. For larger values of the spin-exchange, both $|g\rangle$ and $|e\rangle$ are in a hybrid Mott-band insulating phase, perfectly equivalent to the one we have described in sec. [3.2]. Consistently, the excited channel develops a chiral current which is even larger than the chiral current in the ground channel. The reason why it's larger is rather simple: since DMFT shows that quantum fluctuations are suppressed in this regime and since $s_g = e_e = 1/2$ and $m_g = m_e = 0$, the two channels can be treated as independent non-interacting two-flavor systems with effective Rabi couplings Ω_a^{eff}, and the corresponding chiral currents are given by the analytic estimate [2.51]:

$$\mathbf{I}_{\text{chir},g} \approx \frac{2t^2 \sin\gamma}{2\Omega + U + V_{\text{ex}}}\hat{\mathbf{e}}_x, \qquad \mathbf{I}_{\text{chir},e} \approx \frac{2t^2 \sin\gamma}{U + V_{\text{ex}}}\hat{\mathbf{e}}_x, \qquad (U \gg t, \Omega;\ \ V_{\text{ex}} \gg J). \tag{3.52}$$

From these relations we clearly see that $I_{\text{chir},e} > I_{\text{chir},g}$ and we see that they decrease hyperbolically with V_{ex} (this is not obvious from the plot because we should extend the calculation to larger values of spin-exchange).

In conclusion, when a Raman field is applied to one of the two bands of the multiorbital system, it induces a chiral behavior on that band; however, only in presence of a spin-exchange interaction, the chiral band drives the other one – which does not interact with Raman photons – into a chiral state characterized by an even larger chiral current. Reversing the perspective, measuring a chiral current in a band which is not coupled to Raman photons can be regarded as a hallmark of the spin-exchange interaction and it can be used – at least in principle – as a tool to experimentally measure V_{ex}.

3.6 Conclusion and outlook

In this chapter we have investigated the fate of chiral currents in presence of strong interparticle interactions, both on a single-orbital model and on a multi-orbital model. We have tackled several aspects of the problem with several complementary analytical and numerical methods such as Hartree-Fock, R-DMFT, exact diagonalization and the Schrieffer-Wolff transformation. We have clarified the following important points:

- interaction-driven insulating phases support chiral currents that are typically larger than in the metallic phases, despite a lower mobility of the particles. The chiral current is maximized at the phase transition from the metallic to the insulating state, similarly to what we have observed for the non-interacting system. The effect is not peculiar of (1+1)-dimensional synthetic ladders, but it is also observed in (2+1)-dimensional structures and it is present both in systems with $N = 2$ and $N = 3$ at integer filling. When the system has open boundaries along the real direction (as it is the case in experiments due to the harmonic confinement), in the metallic state the currents form a spatial pattern of alternating vortices and antivortices (with large currents on the internal rungs); while in the insulating state, the currents are expelled from the bulk and only flow along the edge, in a way which is reminiscent of the Meissner effect in superconductors.

- The U-driven insulator is characterized by a hybrid character between a band and a Mott insulator and by the fact that quantum dynamical fluctuations are suppressed (at least far from the phase transition). Consequently, despite the strong interaction, they can be described by means of effective non-interacting quasiparticles, a circumstance which allows to give analytical estimates of the observables. An alternative description of such insulators can be given in terms of effective spins subject to a local magnetic field with a space periodicity determined by the gauge flux and a nearest-neighbor interaction, which is the Heisenberg interaction for $N = 2$, while it is a quartic Lai-Sutherland interaction for $N = 3$. In this picture, the chiral current is the z component of the mechanical torque associated to the specific interaction between spins.

- In multiorbital systems, a chiral current can be induced in an orbital where particles are not subject to Raman processes, as a consequence of the spin-exchange interaction with another orbital subject to laser-induced Raman transitions. In principle, this phenomenon could be experimentally used as a hallmark of the presence of a spin-exchange interaction.

We conclude commenting on the perspectives for future work on this subject. First of all, it would be interesting to consider a more realistic description of the experiments, including the presence of a finite temperature and of a magneto-optical harmonic trap, and test the robustness of our results when these

complications are taken into account. By heuristic arguments, we expect that the behavior of the chiral current across the U-driven phase transition is not affected by temperature and harmonic confinement, at least qualitatively, as long as these effects are relatively small (for example if the temperature is a small fraction of the hopping and the harmonic frequency of the potential is smaller than the Hubbard-U). Nevertheless, it would be interesting to provide a more quantitative estimate and point our experimental colleagues in the right direction in the concrete research for this phenomenon. From the technical point of view, we can include the temperature by computing the low-lying excited states of the impurity problem (as discussed in sec. [3.2]), and the harmonic confinement either via a local density approximation (LDA) in the spirit of [84][8], or by performing R-DMFT. The most challenging part of both these approaches is the determination of the chemical potential that gives the correct number of particles: the LDA+DMFT or R-DMFT algorithm should be launched multiple times at several values of μ for every single point in the phase diagram, which takes a considerably long time. An important speedup is provided by the point-reflection symmetry of the system, which holds also in the presence of a harmonic trap and reduces the number of independent lattice sites by a factor 2.

The two-orbital system discloses exciting perspectives, as it is thus far an almost unexplored territory. A first step would be to expand the proof of concept outlined in this thesis to a wider range of parameters relevant for the experimental implementation with ^{173}Yb. For instance, after characterizing the two-orbital metal-insulator phase transition, we could compute the flavor currents as a function of the depth of the optical lattice, which is the experimentally tunable parameter. The path towards a more realistic and experiment-oriented calculation is even more challenging in this case, since one should also take into account the particle losses due to two-body collisions in the excited channel. A first possibility is to work in the limit $N_e \ll N_{\text{sites}}$, where two-body collisions in the $|e\rangle$ channel are infrequent and can be neglected; but for a more rigorous calculation it is necessary to include a non-hermitian term of the form $\Delta \sum_{i\sigma} c_{ie\sigma}$ in the Hamiltonian, which induces a non-unitary dynamics that is already challenging to treat at the static mean-field level, as it requires to solve the Lindblad equation [85].

Intriguing scenarios are disclosed regardless of the presence of an artificial gauge flux or of a spin exchange coupling. In a very recent work [86], the authors have considered the symmetric case $\Omega = 0$, studying the interplay between several magnetically ordered phases as a function of the average filling of the two orbitals, using tensor networks methods. In other recent works [87, 88], the authors have investigated a cold-atomic analogue of an orbital-selective Mott phase by using a single-orbital interacting three-leg ladder with only two flavors coupled by Raman processes. They have proved that the two coupled flavors localize at a smaller interaction with respect to the uncoupled one, thus realizing a flavor-selective phase, which is reminiscent of the orbital-selective Mott phase in solids (see chapter [4] for more details). The quantum simulation of an orbital-selective Mott phase can be made even more accurate by using an alkaline-earth-like gas with two orbitals and $N = 2$, with a Raman-induced flavor coupling in one of the orbitals. The study of Mott-selective two-orbital systems with cold atoms is a purpose for the near future.

[8] The idea is to assume that the chemical potential is space dependent $\mu(\mathbf{r}_i) = \mu - V(\mathbf{r}_i)$, where $V(\mathbf{r}) = \frac{1}{2}m\omega^2 r^2$ is the harmonic confinement of frequency ω and μ is the chemical potential at the center of the trap, which must to be adjusted to match the correct filling factor.

Chapter 4

Quantum simulation of Hund's physics with ultracold fermionic atoms

In sec. [1.1] we have introduced the Hubbard-Kanamori model, described by Hamiltonian [1.2], which contains all the possible electronic interaction processes stemming from the screened Coulomb repulsion in a material characterized by multiple active bands. The presence of so many independent parameters in the Hamiltonian makes the universal characterization of its spectral properties a very challenging task. The general approach to overcome this difficulty is to work case-by-case, identifying the most relevant physical processes for the specific materials under investigation, and building a simplified version of [1.2] with a reduced number of free parameters. For example, in this chapter we only take into account the competition between the Hubbard repulsion and the Hund's coupling, realizing the so-called Hund's model, which is particularly relevant for the study of transition metal oxides. We compute the ground state with an exact numerical diagonalization, complementing previous studies based on other methods and confirming the existence of a conductive state surviving to strong interactions.

A one-to-one quantum simulation of these materials with platforms of ultracold fermionic atoms is extremely challenging, due to the presence of too many orbitals and of a pair-hopping coupling, which is not reproducible with Hamiltonian [1.5]. However, the physical mechanism that stabilizes a metallic behavior in spite of large interactions is quite general and stems from the degeneracy of competing insulators. Thus we propose a different model which exhibits the same mechanism but is more reasonable to implement with alkaline-earth-like atoms, as it takes advantage of the SU(N) symmetry and of the flexibility of the optical lattice potential.

The chapter is organized as follows: in sec. [4.1] we provide an introductory background on the transition metal oxides, deriving the Hund's model; in sec. [4.2] we present the results of our exact diagonalization of the Hund's model and compare it to previous literature; in sec. [4.3] we introduce our proposal for a cold-atomic analogue of Hund's physics, discussing the phase diagram of the model; finally, sec. [4.4] is devoted to final remarks and outlook.

4.1 Hund's coupling in transition metal oxides

An isolated transition metal atom is characterized by a valence shell of 5-fold degenerate d atomic orbitals with different geometries labeled as $d_{x^2-y^2}$, d_{z^2}, d_{xy}, d_{xz} and d_{yz} with respect to three coordinate axes x, y, z. When it is embedded in a crystal environment of ligands, this degeneracy is lifted by the interaction of its electrons with other electrons of the ligands. Intuitively, this is a direct consequence of the different

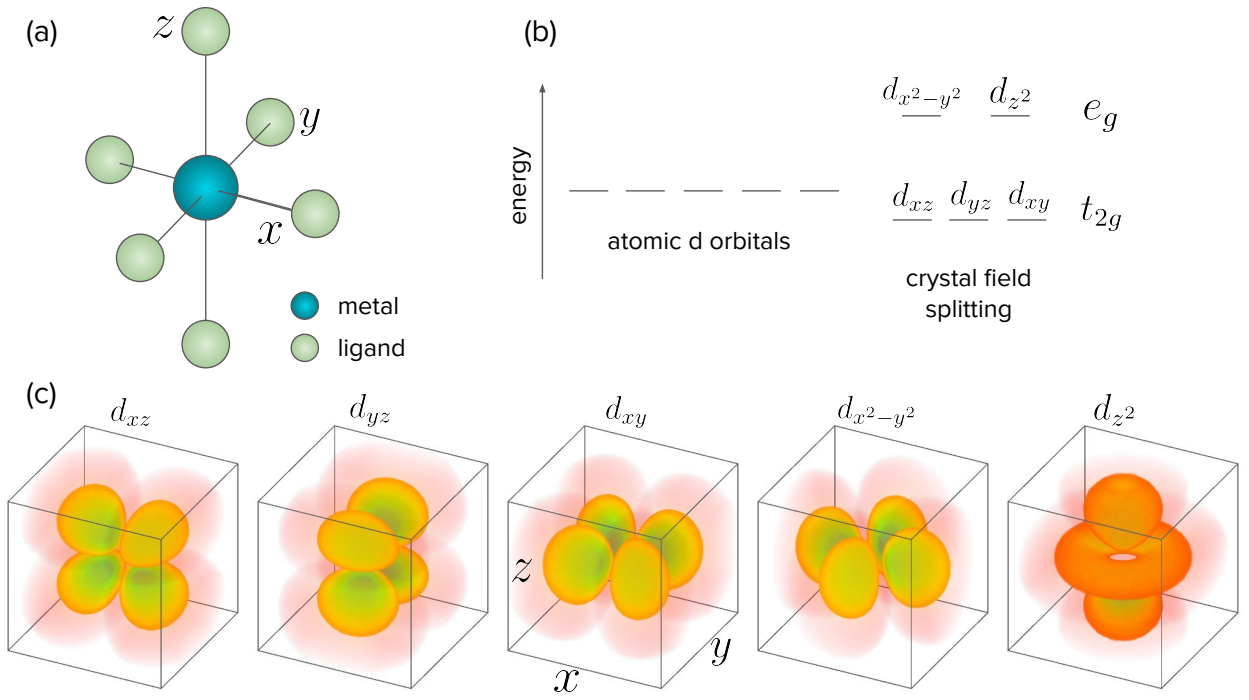

Figure 4.1: Schematic representation of crystal field splitting of atomic d orbitals of a transition metal embedded in a octahedral geometry of ligands. (a) Sketch of the octahedral geometry. (b) Splitting into t_{2g} and e_g orbitals. (c) Geometric structure of the atomic d orbitals: d_{z^2} and $d_{x^2-y^2}$ have the lobes oriented along x, y and z, resulting in a significant overlap with orbitals of the ligand.

geometry of the five d orbitals: those with a larger overlap with atomic orbitals of the ligand are subject to a greater hybridization and are involved in chemical bonds. In particular, they form pairs of bonding-antibonding molecular orbitals, where the former are lower in energy with respect to the original energy level (therefore they are fully occupied by electrons, which ensures the chemical bond and the structural stability of the coordination complex), while the latter are higher in energy. On the other hand, d orbitals that mildly overlap with the ligands approximately maintain their original energy level. The specific energetic hierarchy of split d-orbitals depends on the geometrical arrangement of ligands around the transition metal. The theory of how the degeneracy of atomic orbitals of a transition metal is lifted by the electric field provided by the environment of ligands in the crystal is known as *crystal field theory* [89, 90].

For example, a common geometry is octahedral, with six ligands surrounding the transition metal and positioned along the three perpendicular directions x, y, z used to label the five d orbitals, as shown in fig. [4.1]. In this geometry, $d_{x^2-y^2}$ and d_{z^2} have significant overlaps with atomic orbitals of the ligands, as their lobes are oriented along the coordinate axes, hence they form pairs of bonding-antibonding molecular orbitals hybridizing with all the valence atomic orbitals of the six ligands. We can ignore all the bonding orbitals because they have very low energy and are fully occupied, ensuring the chemical bonds. The manifold of antibonding orbitals is instead pushed to higher energies and the two lowest levels of this manifold, which are always degenerate in this geometry, are called e_g orbitals. The three d-orbitals d_{xy}, d_{xz} and d_{yz} instead do not overlap with orbitals of the ligands, leaving their energy essentially unchanged; in particular, they remain degenerate and are called t_{2g} orbitals. It is conventional to choose real-valued

wave functions for the t_{2g} and e_g orbitals by performing suitable linear combinations of atomic d-orbitals: the interested reader may refer to ref. [91], in particular eqs. [1.31, 1.32].

If the gap between t_{2g} and e_g orbitals is large, and the number of electrons not involved in chemical bonds with the ligands is 6 or less, they will only populate t_{2g} orbitals. In this case, the three active bands around the Fermi level originate from a spectral broadening of the three t_{2g} degenerate orbitals and we can set $N_{\text{orb}} = 3$ (instead of 5) in eq. [1.2]. Furthermore, the bands degeneracy and the hypothesis of no orbital hybridization imply $t_{ij}^{ab} \equiv t_{ij}\delta_{ab}$ and $U_a \equiv U$. A careful evaluation of the Coulomb integrals with the t_{2g} wave functions [91, 92] shows that, in this context, the five interaction parameters in eq. [1.2] can be written in terms of only three independent parameters U, U' and J; in particular: $U'' = U' - J$, $J_{\text{ph}} = J$ and $J_{\text{se}} = -J$. Another simplification is obtained by assuming that the screened Coulomb potential is spherically symmetric: this assumption introduces another constraint on the interaction parameters: $U' = U - 2J$, thus reducing the independent parameters to only U and J.

Strictly speaking, this calculation provides an approximated scheme for the local interaction in crystals of transition metal oxides. In a solid, the screened Coulomb potential is not spherically symmetric in general; moreover the Coulomb integrals should be computed using Wannier functions instead of atomic orbitals. Clearly, this is an idealization of the problem, nevertheless it captures several important features of materials formed by transition metals, while maintaining the theoretical framework quite general and not particularized to specific crystal structures.

If U and J are computed from the Coulomb integrals, then they are both positive, so we assume $U > 0$, $J > 0$ throughout this chapter. However, when the coupling of electrons to phonon modes is taken into account, the effective electronic Hamiltonian (obtained after integrating out the phonons) is similar, but with renormalized values of U and J, which in some cases can also be negative[1] [30].

To summarize, Hamiltonian [1.2] reduces to:

$$\begin{aligned} H = &\sum_{\langle ij\rangle,\, a,\, \sigma} t_{ij}\left(c^\dagger_{ia\sigma}c_{ja\sigma} + \text{h.c.}\right) - \mu\sum_{ja\sigma} n_{ja\sigma} + U\sum_{j,\,a} n_{ja\uparrow}n_{ja\downarrow} + (U-2J)\sum_{j,\,a\neq b} n_{ja\uparrow}n_{jb\downarrow} \\ &+ (U-3J)\sum_{j,\,a<b,\,\sigma} n_{ja\sigma}n_{jb\sigma} + J\sum_{j,\,a\neq b} c^\dagger_{ja\uparrow}c^\dagger_{ja\downarrow}\,c_{jb\downarrow}c_{jb\uparrow} - J\sum_{j,\,a\neq b} c^\dagger_{ja\uparrow}c_{ja\downarrow}\,c^\dagger_{jb\downarrow}c_{jb\uparrow}. \end{aligned} \tag{4.1}$$

The interaction term of [4.1] commutes with all the following operators:

$$n_j = \sum_{a\sigma} n_{ja\sigma}, \qquad \mathbf{S}_j = \frac{1}{2}\sum_{a,\sigma\rho} c^\dagger_{ja\sigma}\,\boldsymbol{\sigma}_{\sigma\rho}\,c_{ja\rho}, \qquad \mathbf{L}_j = \sum_{bc,\sigma} c^\dagger_{jb\sigma}\boldsymbol{\ell}_{bc}c_{jc\sigma} \quad (\ell^a_{bc} = -i\varepsilon_{abc})\,, \tag{4.2}$$

representing the local number of particles, the local spin and the of the local orbital angular momentum respectively. In eq. [4.2], $\boldsymbol{\sigma}$ is the vector of Pauli matrices, ℓ^a_{bc} is the a-th component of $\boldsymbol{\ell}_{bc}$ and ε_{abc} denotes the Levi-Civita antisymmetric tensor. The tensor ℓ^a_{bc} is a 3-dimensional fundamental representation of the rotation group SO(3), which implies that the orbital angular momentum of a single particle is $l = 1$. The interaction term is thus symmetric under the action of U(1)×SU(2)×SO(3), where U(1) is the charge symmetry generated by n_j, SU(2) the spin symmetry generated by $\mathbf{S}_j$ and SO(3) is the rotational symmetry generated by $\mathbf{L}_j$, which stems from the assumption of spherically symmetric interactions. This suggests that the interaction term can be rewritten more conveniently in terms of the generators of the group, and the result is

$$H = \sum_{\langle ij\rangle,\, a,\, \sigma} t_{ij}\left(c^\dagger_{ia\sigma}c_{ja\sigma} + \text{h.c.}\right) - \mu\sum_{ja\sigma} n_{ja\sigma} + \frac{U-3J}{2}\hat{n}_j(\hat{n}_j - 1) - J\left(2\mathbf{S}_j^2 + \frac{1}{2}\mathbf{L}_j^2 - \frac{5}{2}\hat{n}_j\right). \tag{4.3}$$

[1] Remarkable examples of materials displaying a negative J as a consequence of electron-phonon coupling are alkali-doped fullerides [14, 93].

Written in the form [4.3], the Hamiltonian is particularly illuminating, as it provides a lot of information without performing lengthy calculations.

First of all, let us focus on the atomic limit $t_{ij} = 0$, where all the lattice sites are decoupled and consider an arbitrary site j. At a given filling factor, n_j is just a constant and the only degrees of freedom are $\mathbf{S}_j$ and $\mathbf{L}_j$, so the Hamiltonian reduces to $-2J\mathbf{S}_j^2 - \frac{J}{2}\mathbf{L}_j^2$. The ground state is given by a configuration of n_j electrons that maximize their total spin and their total orbital angular momentum: an observation which is formulated in the first two well-known *Hund's rules*[2]. The third Hund's rule instead is not captured by this simplified model, as it would require to include the effect of electronic spin-orbit interactions.

Secondly, let's reintroduce the hopping and consider $J = 0$. In this situation, the interaction reduces to a Hubbard-like local charge repulsion, where U prevents spatial charge fluctuations. This is essentially a SU(6) Hubbard model, where 6=2·3 is the number of fermionic components (including spin and orbital degrees of freedom): therefore, we expect to observe a Mott transition as a function of U at integer filling factors. The Mott insulator will be a uniform quantum superposition of all the possible Fock states with a fixed number of particles per site which is specified by the filling factor. When a small J is included, the ground state will be adiabatically connected to the case $J = 0$, so we still expect a Mott transition, where now, in the Mott insulator, different Fock states will have different weights; in particular, we expect enhanced weights for states respecting the Hund's rules and diminished weights for states violating the rules.

Finally, if $J > U/3$, the density-density interaction becomes attractive and the electrons tend to accumulate on some of the lattice sites. However, configuration that maximize the charge disproportion are not necessarily favored, since the energy of a local configuration is lifted by the term $-2J\mathbf{S}_j^2 - \frac{J}{2}\mathbf{L}_j^2$, which penalizes a state when it violates the Hund's rules. The resulting state depends on the specific filling factor, as it is governed by a non-trivial competition (or cooperation) between the tendency towards inducing charge fluctuations and towards respecting the Hund's rules.

4.2 Interaction resilient Hund's metal

In a series of pioneer works [15, 94, 95], the authors applied DMFT to investigate how the filling factor and the Hund's coupling J affect the interaction-driven metal-insulator phase transition, unraveling a surprising scenario. For materials with half-filled t_{2g} bands, such as $SrMnO_3$ and $SrTcO_3$, the presence of a Hund's coupling favors the Mott localization by reducing the critical value U_c/t. Conversely, for materials with t_{2g} bands less than (or more than) half-filled, such as $SrVO_3$, $SrCrO_3$, $SrRuO_3$, etc.[3], in the presence of a significant Hund's coupling, the critical U_c/t is pushed to much higher values than in the case $J = 0$, stabilizing a metallic solution. This is typically a bad metal characterized by a small quasiparticle peak at the Fermi level or, equivalently, by a large effective electronic mass; nevertheless it can survive to very large values of the Hubbard-U, hence we name it "*interaction resilient metal*". Interestingly, this happens when $U - 3J \approx 0$, a condition that makes the density-density term in eq. [4.3] vanish, thus effectively decoupling the charge degrees of freedom associated to different orbitals. On the one hand, the Hund's coupling increases the critical Hubbard interaction U_c that stabilizes a Mott phase; on the other hand,

[2] Hund's rules are 3 simple rules to construct the ground state of many independent electrons on atomic orbitals avoiding lengthy calculations. 1: In the ground state, electrons tend to maximize their total spin S. 2: For a given spin, the state with lowest energy has the maximum orbital angular momentum L. 3: Given S and L, the state with lowest energy is the one with largest total angular momentum j if the valence subshell is more than half-filled, otherwise it is the state with smallest j.

[3] In compounds of the form $SrXO_3$, the transition metal X has oxidation number +4, leading to a filling factor $k-4$, where k is the group index in the periodic table, i.e. the valence number including two electrons in the closest filled s shell, which are involved in bonds with ligands as well. In general, if n_0 is the oxidation number of the transition metal, the filling factor is $k - n_0$.

it enhances the effective particle mass, reducing the mobility of carriers: this two-faced effect is usually named *Janus effect*[4]. A similar effect has been observed in the normal state of iron chalcogenides (which have been recently discovered as high-temperature superconductors [17]), where the gap between t_{2g} and e_g is sufficiently small and the population of e_g bands has to be included [96, 97].

A thorough investigation of the phase diagram for a filling factor 2 was performed in [14] by applying "rotation invariant slave bosons" (RISB) [98] in the local approximation. In ref. [99] non-local effects have been also included using dynamical cluster approximation DCA+DMFT, but the results are limited to finite temperatures. Here, we present a different approach based on the exact diagonalization method performed on a small cluster of three sites, which is the minimal number of sites that can host all the relevant insulating solutions found in [14], as we discuss later on. This method gives access to the spectral properties in an unbiased way, in particular it automatically accounts for spatial fluctuations without introducing approximations. In order to explore the physics of an interaction-resilient metal, we choose a filling factor of 2 throughout the analysis.

4.2.1 Atomic limit

For the purpose of a more quantitative analysis, it is useful to list all the local configurations that are allowed by the constraint of global antisymmetry of the electronic wave function, together with the corresponding interaction energy computed from eq. [4.3]. This is done in tab. [4.1], where every configuration, which is named *multiplet* in the following, is labeled by three quantum numbers $\{n_j, S_j, L_j\}$ and it is $(2L_j+1)(2S_j+1)$-fold degenerate.

$\{n_j, L_j, S_j\}$	E_{int}
$\{0,0,0\}$	0
$\{1,1,\frac{1}{2}\}$	0
$\{2,2,0\}$	$U-J$
$\{2,1,1\}$	$U-3J$
$\{2,0,0\}$	$U+2J$

$\{n_j, L_j, S_j\}$	E_{int}
$\{3,2,\frac{1}{2}\}$	$3U-6J$
$\{3,1,\frac{1}{2}\}$	$3U-4J$
$\{3,0,\frac{3}{2}\}$	$3U-9J$

$\{n_j, L_j, S_j\}$	E_{int}
$\{6,0,0\}$	$15U-30J$
$\{5,1,\frac{1}{2}\}$	$10U-20J$
$\{4,2,0\}$	$6U-11J$
$\{4,1,1\}$	$6U-13J$
$\{4,0,0\}$	$6U-8J$

Table 4.1: List of all the possible local atomic multiplets with the corresponding interaction energy. Adapted from the supplementary material of ref. [14].

We can characterize the nature of a given state $|\psi\rangle$ by computing its overlap with atomic multiplets, namely $p_{n,L,S} = \frac{1}{3}\sum_{j=1}^{3} |\langle\psi|P_{\{n_j,L_j,S_j\}}|\psi\rangle|^2$, where $P_{\{n_j,L_j,S_j\}}$ is the projector onto the subspace of all the Fock states having a local state $\{n, L, S\}$ on site j. The quantity $p_{n,L,S}$ is called *multiplet population* and it represents the average number of sites having n particles, orbital angular momentum L and spin S. The evolution of $p_{n,L,S}$ for the most relevant set of quantum numbers $\{n, L, S\}$, computed in the ground state as a function of J/U at large U/t, is shown in fig. [4.2].

- We observe that, if $J \ll U$, the only relevant atomic multiplet is $\{n=2,\ L=1,\ S=1\}$, which clearly indicates that the state is a Mott insulator with two particles per site. The only difference is that the preferred local configuration is the one with highest allowed spin, in agreement with the first Hund's

[4] In ancient Roman mythology, Janus was the god of duality, and he was usually represented with two faces. Metaphorically, this represents the two opposite tendencies of the Hund's coupling.

rule. Looking at tab. [4.1] we can immediately compute the approximated ground state energy in this state, which is $E_0 \approx 3(U - 3J)$.

- In the opposite regime, where $J \gg U$ (not shown), the only relevant multiplets are $n = 6$ with probability $\approx 1/3$ and $n = 0$ with probability $\approx 2/3$, denoting a tendency towards charge accumulation, which is not surprising since in this regime the attractive density-density interaction is the dominant energy scale. This regime is not considered here, since in realistic materials J is typically a fraction of the Hubbard U. The associated energy is $E_0 \approx 15U - 30J$.
- When J is significant but not huge, i.e. $U/3 \lesssim J \lesssim 3U/4$, the only relevant multiplets are $\{n = 0, L = 0, S = 0\}$ with probability $p_{0,0,0} \approx 1/3$ and $\{n = 3, L = 0, S = \frac{3}{2}\}$ with probability $p_{0,0,3/2} \approx 2/3$. This is a totally different scenario, where the ground state is characterized by two triply occupied sites and an empty site. Since spontaneous symmetry breaking is forbidden in a finite system by the analytical nature of the partition function, this is a symmetric state (i.e. a quantum superposition of all the possible combinations of two triply occupied sites and an empty site). In the occupied sites, the local spin is $\frac{3}{2}$, consistently with the first Hund's rule. The ground state energy in the corresponding atomic limit is readily computed from tab. [4.1]: $E_0 \approx 2(3U - 9J)$. Comparing the energy of this state to the energies of the previous two, we can verify that this is the ground state in the range $U/3 < J < 3U/4$.
- In the crossover region $J \approx U/3$, there are three relevant multiplets having roughly the same probability $\approx 1/3$: $\{n = 3, L = 0, S = \frac{3}{2}\}$, $\{n = 1, L = 1, S = \frac{1}{2}\}$ and $\{n = 2, L = 1, S = 1\}$. The ground state is now a quantum superposition of Fock states with one singly occupied site, one doubly occupied site with high spin and one triply occupied site with high spin. In this regime, the two more realistic solutions outlined above become degenerate: $3(U - 3J) = 2(3U - 9J) = 0$ at $J = U/3$.

4.2.2 Phase diagram based on the Drude weight

A standard approach to probe the conduction properties of the Hund's model is to compute the quasiparticle weight z, which, in absence of band-insulating phases, directly reflects on the metallic character of a state, since m/z can intuitively be regarded as the interaction-dressed electronic mass. However, here we choose a complementary approach and compute the *Drude weight*, which is the DC component of the electrical conductivity [100, 101, 102, 103]. More precisely, for a system with no disorder, the longitudinal electrical conductivity $\sigma(\omega)$, which determines the current response to an external electric field, is given by the sum of a zero-frequency singular peak $D\delta(\omega)$ (DC component) and of a regular function $\sigma_{\text{reg}}(\omega)$ (AC component). In metals and superconductors $D \neq 0$, while $D = 0$ in any insulating state [65, 104]. Computing the Drude weight is a rich and subtle topic, which deserves a dedicated dissertation: here we only consider the most important concepts relevant to our system and we address some of the subtleties in appendix [B].

In ref. [104], Kohn derived a simple formula for the Drude weight at $T = 0$, showing that it is given by the curvature of the ground state energy $E_0(\phi)$ with respect to an auxiliary Peierls phase ϕ introduced in the hopping term $t \to te^{i\phi}$ computed at its minimum $\phi = \phi_0$; for a one-dimensional ring we have

$$D = \frac{1}{N_{\text{sites}}} \frac{\partial^2 E_0}{\partial \phi^2}\bigg|_{\phi=\phi_0}. \tag{4.4}$$

This formula apparently suggests that we have to sample the ground state energy for several fluxes and then fit with a parabola to get the curvature; however this requires multiple exact diagonalizations for

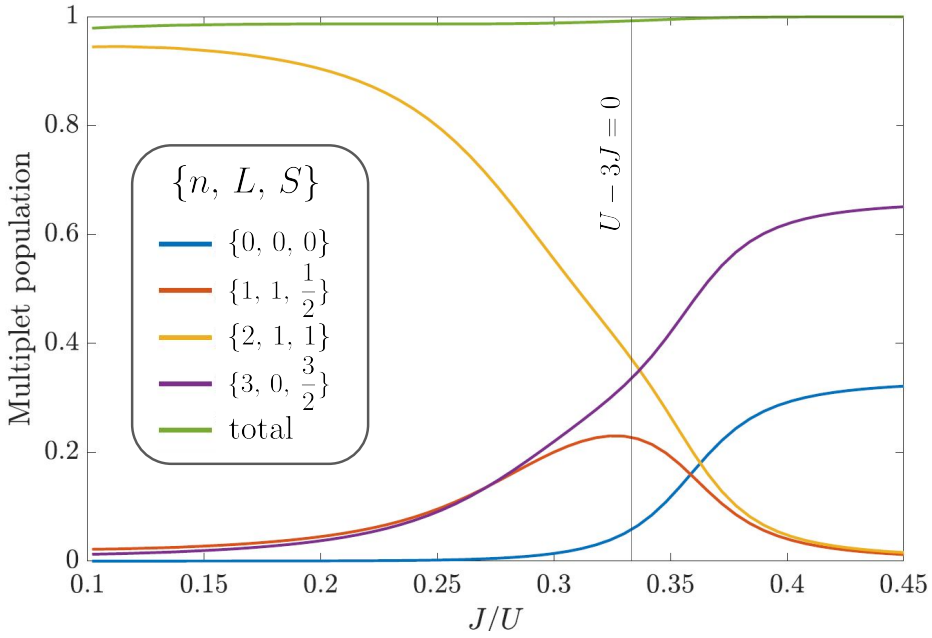

Figure 4.2: Populations of the atomic multiplets $p_{n,L,S}$ relevant to the ground state of Hamiltonian [4.1] as functions of the control parameter J/U. Calculations are perfomred in the strong coupling regime $t = 1$, $U = 22$ at filling factor 2 (6 particles on the 3-site system). The gray vertical line $J/U = 1/3$ is the point where the two distinct solutions (Mott insulator and Hund insulator) become degenerate.

every set of parameters (U, J), which is computationally demanding. Fortunately, we can considerably speed up the method by connecting the the Drude weight to the total persistent current induced on the system by the external flux via the Aharonov-Bohm effect [105]:

$$I(\phi) = \frac{1}{N_{\text{sites}}} \langle \psi(\phi) | \frac{\partial H}{\partial \phi} | \psi(\phi) \rangle \approx D(\phi - \phi_0) \qquad (\phi \approx \phi_0). \tag{4.5}$$

We stress that here $I(\phi)$ is the total current, not the paramagnetic contribution. As we argue in appendix [B], for the Hund's model on a three-site ring geometry with filling factor 2, it turns out that $\phi_0 = 0$ and that the linear dependence of $I(\phi)$ on ϕ is dramatically broken at $\phi \approx \phi_c = \pi/N_{\text{sites}}$. Therefore, we can compute D by choosing a specific flux ϕ sufficiently close to $\phi_0 = 0$ and sufficiently far from $\phi_c = \pi/3$, then computing the total current $I(\phi)$ at this flux (which requires a single exact diagonalization) and, exploiting the proportionality relation [4.5], using $D = I(\phi)/\phi$. In the results shown here, we choose $\phi = 0.1\pi/3$ for every point in the phase diagram, so if we normalize the Drude weight to the Drude weight computed at $U = J = 0$, we have $D/D|_{U=J=0} = I(\phi)/I_{U=J=0}(\phi)$. Before we move to the results, we emphasize that – as discussed in appendix [B] – the specific values of ϕ_0 and ϕ_c depend on the number of fermions, lattice sites and fermionic components. This means that the approach can be easily generalized to similar systems with the only attention of choosing ϕ in advance depending on the specific values of these parameters.

The resulting Drude weight in the plane (U, J) is shown in fig. [4.3] with a color-plot. We can clearly see the presence of two insulating solutions with $D \approx 0$: a Mott insulator for small J and large U, characterized by a uniform charge distribution and a local spin $S = 1$, and a Hund insulator at $J > U/3$, characterized by a charge disproportion between the lattice sites and a large local spin $S = 3/2$ in the occupied sites. The most interesting feature is the fact that, around the crossover line $J = U/3$, which

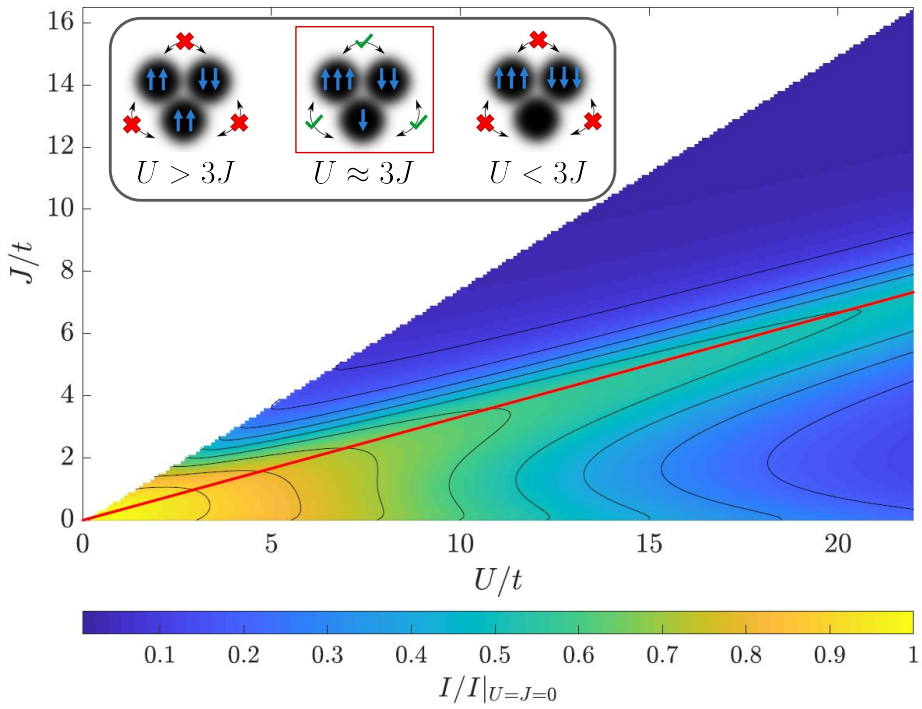

Figure 4.3: Color-plot of the Drude weight as a function of U/t and J/t in the physically realistic region $0 < J < 3U/4$. The Drude weight is computed relatively to the non-interacting case $U = J = 0$ and is given by the ratio of the respective total currents $D/D_{U=J=0} = I(\phi)/I_{U=J=0}(\phi)$ computed at $\phi = 0.1\pi/3$. The red line is the crossover line $U - 3J = 0$, where the two insulating solutions are degenerate in the atomic limit. We can clearly see an enhanced Drude weight along this line, indicating the presence of an interaction-resilient metal, consistently with [14]. The insert sketches representative Fock states having a large weight in the ground state in the three relevant regimes.

is the line where the two insulators become degenerate in the atomic limit, there is a significant Drude weight. This clearly indicates the presence of a bad metallic state surviving despite the large values of the two interaction parameters U and J, i.e. an interaction-resilient metal. This state is usually called *Hund's metal*. To understand why a conductive state can be present despite the presence of large interactions, we can look at the atomic multiplets in the crossover region. In the atomic limit we can write the ground state in this region as

$$|\psi\rangle = c_1|1,2,3\rangle + c_2|3,1,2\rangle + c_3|2,3,1\rangle + c_4|2,1,3\rangle + c_5|3,2,1\rangle + c_6|1,3,2\rangle \qquad (t = 0,\ J = \frac{U}{3}),$$

where c_j are suitable complex coefficients (all of them of comparable amplitude and significantly different from 0) and we label a Fock state on the three-site cluster with the local occupancy $|n_1, n_2, n_3\rangle$ (notice that n_j uniquely identifies a Fock state because we imply that it is the corresponding state with largest spin in tab. [4.1]). If we assume $t \ll U, J$, we can treat the hopping term as a small perturbation and apply standard perturbation theory. The first order correction to the atomic ground state energy is given by the expectation value of the hopping Hamiltonian $\langle\psi|H_{\text{hop}}|\psi\rangle$. We don't compute this object in detail, however we argue that this is non vanishing, as it includes terms that, for example, are proportional to $\langle 2,1,3|c^\dagger_{1,a\sigma}c_{2,a\sigma}|1,2,3\rangle = \pm 1$. Carefully checking that all these terms in fact don't cancel out, we obtain

a correction of order $\sim t$ to the internal energy. Conversely, in the insulating states, the first order contribution vanishes identically: $\langle\psi|H_{\text{hop}}|\psi\rangle = 0$ and we need to expand to higher orders in t. The reason is that Fock states contributing to the ground state in the atomic limit are not connected to one another by single hopping processes (for example we can't transform $|3,0,3\rangle$ into $|3,3,0\rangle$ with a single hopping process). This directly reflects on the Drude weight, which is the curvature of $E_0(\phi)$ leading to larger values in the crossover region. We sketch this simple argument in the insert of fig. [4.3].

4.2.3 Correlation functions

One of the advantages of exact diagonalization is the possibility to have easy access to all the observables of interest in an unbiased way, including those that other methods can not provide, such as non-local correlation functions. Here we analyze local and non-local correlation functions related both to the charge and to the spin degrees of freedom. In particular, we define the intraorbital and interorbital charge correlation functions:

$$C_{ij}^{\text{intra}} = \sum_{a=1}^{N_{\text{orb}}} \left(\langle n_{ia} n_{ja}\rangle - \langle n_{ia}\rangle\langle n_{ja}\rangle\right), \quad C_{ij}^{\text{inter}} = \sum_{a\neq b} \left(\langle n_{ia} n_{jb}\rangle - \langle n_{ia}\rangle\langle n_{jb}\rangle\right). \tag{4.6}$$

We also define the total charge correlation function, which is their sum $C_{ij}^{\text{tot}} = C_{ij}^{\text{intra}} + C_{ij}^{\text{inter}}$. Similar definitions hold for the spin-spin correlation functions:

$$M_{ij}^{\text{intra}} = \sum_{a=1}^{N_{\text{orb}}} \left(\langle \vec{S}_{ia}\cdot\vec{S}_{ja}\rangle - \langle \vec{S}_{ia}\rangle\cdot\langle \vec{S}_{ja}\rangle\right), \quad M_{ij}^{\text{inter}} = \sum_{a\neq b} \left(\langle \vec{S}_{ia}\cdot\vec{S}_{jb}\rangle - \langle \vec{S}_{ia}\rangle\cdot\langle \vec{S}_{jb}\rangle\right), \tag{4.7}$$

and their sum $M_{ij}^{\text{tot}} = M_{ij}^{\text{intra}} + M_{ij}^{\text{inter}}$. All these correlation functions are shown in fig. [4.4], where they are computed in the ground state for the same range of parameters used for the multiplet population of fig. [4.2].

The behavior of the on-site charge correlation function resembles the results obtained with local mean fields [106]. The total correlations are very small in the small J/U region, where the system is a Mott insulator, and they gradually increase as J/U increases and the system reaches the Hund's insulator. We notice, in particular, that charge fluctuations are not maximal in the metallic region, but they are even larger in the Hund's insulator, a circumstance which reflects the charge disproportion. The evolution as a function of J of the charge correlations is entirely due to the interorbital component, while the intraorbital contribution is totally unaffected by J and it only depends on U/t. The results for nearest-neighbor correlations follow a similar qualitative trend, with the total correlator vanishing in the Mott insulator and increasing (in absolute value) as J/U grows. Once again, the interorbital component crosses zero around the Hund's metal region, reflecting the decoupling between charge excitations in different orbitals [107]. Therefore, we find that the charge decoupling, which has been so far reported for on-site correlations, extends also to nearest-neighbor quantities, thereby strengthening its relevance. This property is at the origin of the *orbital-selective Mott transition*: when an asymmetry between the bandwidths [108] or a small crystal field splitting between t_{2g} bands [109] are included, some bands become significantly more correlated than others and they undergo Mott-localization for smaller critical values of U. In other words, for a suitable regime of parameters, some bands are Mott-localized, while others are still (poorly) conductive, hence the name "orbital-selective".

Local spin correlations are positive and they grow with J/U, reflecting the increased on-site magnetic moment. Since intraorbital spin fluctuations are constant throughout the whole explored range of J/U,

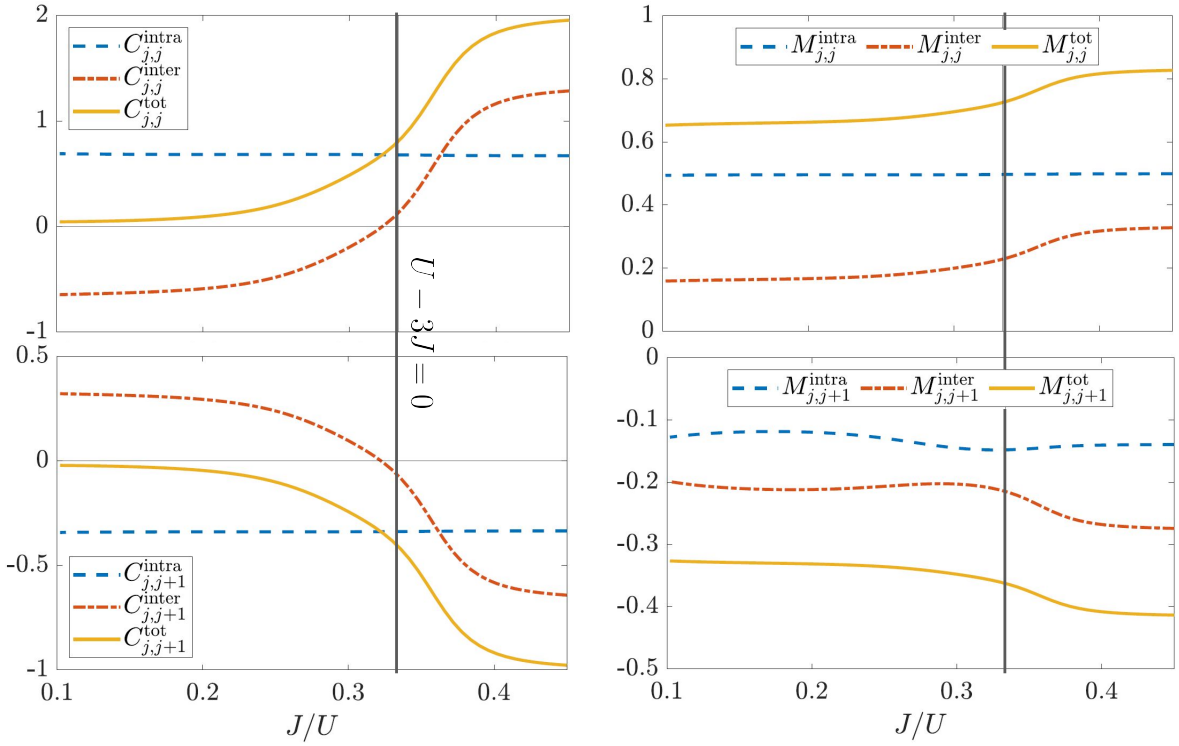

Figure 4.4: Correlation functions (averaged over the three lattice sites) in the ground state of [4.3] close to the atomic limit: $t = 1$, $U = 22$. Charge and spin correlations are shown in the left and right panels respectively. Local correlations are in the first row, while non-local in the second. In every plot, we resolve intra-orbital, inter-orbital and total correlations. The Hund's metal around $J = U/3$ is accompanied by vanishing interorbital charge correlations, both locally and non-locally (orbital decoupling).

the only contribution comes from inter-orbital spin alignment due to the Hund's coupling. The total nearest-neighbors correlator $M^{\text{tot}}_{j,j+1}$ is negative, signalling antiferromagnetic spin correlations between the large local magnetic moments. The absolute value grows with J/U without any anomaly when the Hund's metal region is reached and crossed and an antiferromagnetic ordering is found also in the Hund's insulator. In this case, intraorbital correlations are negative and they have a mild dependence on J/U which combines with the larger dependence of the interorbital terms to provide the final result.

4.2.4 Analysis of the excited states

The exact numerical diagonalization on a small cluster gives access to the full excitation spectrum of the Hamiltonian, and hence to finite temperature properties. In fig. [4.5], we plot the first 3500 out of the 18564 energy levels $E_i = \langle\psi_i|H|\psi_i\rangle$ of Hamiltonian [4.3] as a function of the control parameter J/U.[5] We identify the presence of different "bundles" of energy levels, which come together or move apart upon varying J/U, each of them corresponding to a specific class of excitations. All the states in a given bundle are degenerate in the atomic limit, but they display small splittings for finite t due to virtual hopping processes depending on the specific arrangement of the fermions in each state.

[5]The Hilbert space dimension is $18564 = \sum_{N_\uparrow,N_\downarrow} \binom{N_{\text{sites}}N_{\text{orb}}}{N_\uparrow} \cdot \binom{N_{\text{sites}}N_{\text{orb}}}{N_\downarrow} \delta_{N_\downarrow, N_{\text{particles}}-N_\uparrow}$ with $N_{\text{orb}} = 3$, $N_{\text{sites}} = 3$ and $N_{\text{particles}} = 6$.

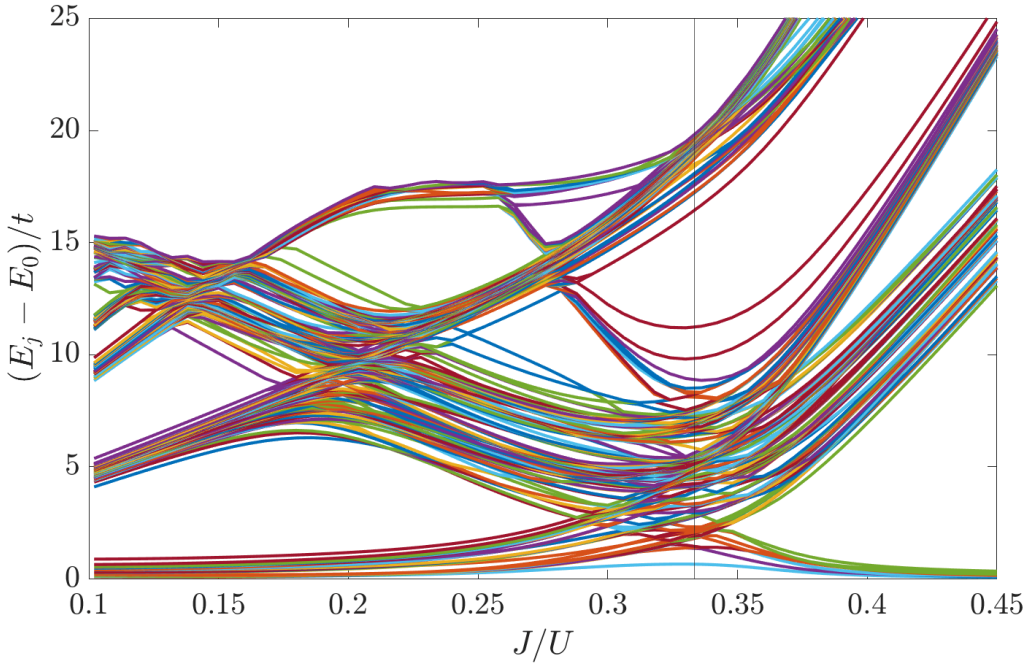

Figure 4.5: First 3500 energy levels of Hamiltonian [4.3] as a function of J/U in the regime $U \gg t$ (in particular, $U = 22$, $t = 1$). The gray vertical line at $J/U = 1/3$ represents the degeneracy condition between the Mott and Hund insulators in the atomic limit.

We can understand the nature of excitations by using this adiabatic connection to the atomic limit and counting the number of states in each bundle. As an example, we first focus on the Mott insulating state at $J/U = 0.1$, where we recognize five bundles of states.

- The lowest bundle is composed by $729 = 9^3$ energy levels, which is easily understood because each of the 3 lattice sites is characterized by a multiplet with $n_i = 2$, $S_i = 1$, and $L_i = 1$, which is $(2L_i + 1)(2S_i + 1) = 9$-fold degenerate.

- The second lowest bundle is formed by $1215 = 9^2 \cdot 5 \cdot 3$ levels. This is the number of possible states such that only *one* out of three sites features the minimal violation of Hund's rules $n_i = 2, S_i = 0, L_i = 2$. The degeneracy of this single-site configuration is 5, while the other two sites remain 9-fold degenerate, hence an overall $9^2 \cdot 5 \cdot 3$ degeneracy, where the factor 3 counts all the possible combinations of one site violating Hund's rules. The energy gap between this bundle and the lowest one is $2J$.

- With a similar reasoning, one can verify that the third lowest bundle, which includes $675 = 9 \cdot 5^2 \cdot 3$ levels, corresponds to states where *two* sites feature $n_i = 2, S_i = 0, L_i = 2$ and the energy gap to the ground state is about $4J$.

- The fourth bundle includes $243 = 9^2 \cdot 1 \cdot 3$ levels (where 1 is the degeneracy of the single-site configuration $n_i = 2$, $S_i = 0$, $L_i = 0$) and it has an energy gap $5J$. We can appreciate the linear behavior with progressively increasing slope of all these bundles close to $J/U = 0.1$ (0, 2, 4 and 5 respectively).

- Following this logic, we can now expect to encounter excitations where two sites violate the Hund's rule with $S_i = L_i = 0$; however the energetic cost of this excitation is $10J$, which is of order U for our choice $J = 0.1U$. The result is that these states are mixed with the charge excitations, i.e. states in which the Mott condition $n_i = 2$ is violated. The energy gap of charge excitations is, for small values of J/U, $U - 3J$, which depends on both U and J, and closes exactly at $J/U = 1/3$, where Hund's metallicity is found. This gap closure is clearly visible in the figure, and, indeed, it corresponds to the lowering of the energy of the charge excitation as J/U grows.

In the opposite limit, for example at $J/U = 0.45$, we identify two bundles.

- The lowest bundle is made up of $48 = 4 \cdot 4 \cdot 1 \cdot 3$ levels, where two sites have a 4-fold degeneracy due to the single-site configuration $n_i = 3$, $S_i = 3/2$, $L_i = 0$, and the remaining site is in the state $n_i = 0$, $S_i = 0$, $L_i = 0$, which is not degenerate (again, the factor 3 counts the fact that each of the three sites can be in the state $n_i = S_i = L_i = 0$).

- As opposed to the case of small Hund's coupling, here the second lowest bundle already involves *charge* excitations. In fact, it includes $1296 = 9 \cdot 4 \cdot 6 \cdot 6$ levels, where one factor 6 is the degeneracy of the single-site configuration $n_1 = 1$, $S_1 = 1/2$, $L_i = 1$, and the other factor 6 represents the number of possible permutations of site indices. Notice that the gap of this bundle is of the order of $6J - 2U$ and that this gap tends to close approaching $J/U = 1/3$ as well.

In spite of the rather complex dependence of the energy levels on the control parameter J/U, we have now a clear picture in which, approaching the limit $J/U = 1/3$, the charge gap collapses coming from both the Mott insulator and the Hund insulator, leading to the metallization.

4.3 Cold-atomic analogue of Hund's physics

The direct quantum simulation of Hund's physics by means of ultracold fermionic atoms in optical lattices is a very challenging purpose at least for two reasons. The first difficulty is related to the large number of fermionic components required, in particular one has to realize the equivalent of three stable orbital degrees of freedom (for example using metastable electronic states with moderate cross sections for inelastic scattering) and two spin degrees of freedom (for example using nuclear states), while ensuring the SU(2) spin symmetry (for example choosing electronic states that are not subject to hyperfine coupling). For alkaline-earth-like atoms, besides ${}^1S_0$ and ${}^3P_0$, we don't have any obvious candidate to simulate the third orbital. The second reason is that the Hund's coupling involves a pair hopping term in the Hamiltonian, which is not realized by alkaline-earth-like atoms (see eq. [1.5]).

We thus change our perspective and propose a different model that still captures the essential mechanism of interaction-resilient metallicity, but that, at the same time, is simpler to realize with platforms of alkaline-earth-like atoms. In particular, we consider a one dimensional single-band SU(3)-symmetric Hubbard model subject to a periodic superlattice potential that divides the system in three sublattices A, B and C, lowering the on-site energy by an amount μ on two of them (for example A and C). In this section, μ does not denote the chemical potential, but rather the on-site energy difference provided by the superlattice. The resulting Hamiltonian is

$$H = -t \sum_{j=1}^{N_{\text{sites}}} \sum_{\sigma=1}^{N} \left(c_{j\sigma}^\dagger c_{j+1,\sigma} + \text{h.c.} \right) + \frac{U}{2} \sum_{j=1}^{N_{\text{sites}}} n_j(n_j - 1) + \sum_{j=1}^{N_{\text{sites}}} \mu_j n_j, \tag{4.8}$$

where we recognize the usual SU(3) symmetric hopping and Hubbard terms and

$$\mu_j = -\mu \text{ if } j = 1 \text{ mod } 3; \qquad \mu_j = 0 \quad \text{if } j = 2 \text{ mod } 3; \qquad \mu_j = -\mu \text{ if } j = 0 \text{ mod } 3. \tag{4.9}$$

This model is for many aspects similar to the Hund's model given in eq. [4.3], where the flavor index is an analogue of the orbital degrees of freedom, while there is no analogue for the electronic spin.[6] The localizing effect provided by the Hund's coupling J is mimicked by the presence of a staggered potential. To further enhance this similarity, we work again at filling factor 2. Due to the absence of analogues to the spin, in eq. [4.8] the Hubbard U is purely interorbital; however it is the same for all the possible flavor pairs (as a consequence of the SU(3) symmetry), just like the density-density interorbital coupling is the same for every pair of orbitals in the Hund's model. An obvious difference which is worth pointing out is that in Hamiltonian [4.8] the full translational symmetry is explicitly broken by the superlattice potential (although a residual translational symmetry in every sublattice is still present); whereas the Hund's model has full translational symmetry. This broken symmetry will obviously reflect on the structure of the ground state.

Once again, we study the system by means of exact numerical diagonalization working on a three-site ring (N_{sites}), which is the minimal geometry that can host all the relevant phases. In this case, due to the absence of an effective spin degree of freedom, extending the lattice to $N_{\text{sites}} \approx 9$ is not very computationally demanding if the Hamiltonian matrix is properly written in a symmetrized basis. In fact we have checked the robustness of the following results increasing the ring size; however we haven't found any particular difference and here we just report results for $N_{\text{sites}} = 3$. We emphasize that it is also possible to implement real-space DMFT for a system like this; however this is left for future investigation.

4.3.1 Atomic limit

To begin with, we study the ground state $|\psi\rangle$ in the atomic limit by computing the relevant multiplets $p_n = \sum_j |\langle\psi|P_{n_j}|\psi\rangle|^2$, where P_{n_j} projects a state into the subspace of all the Fock states having n particles on site j. The result is shown in fig. [4.6], from which we can make the following observations.

- If $\mu < U$, we have $p_2 \approx 1$, which indicates that the system is a Mott insulator with exactly two particles per lattice site and no charge fluctuations. The energy of this state is $E_0 = 3U - 4\mu$ (when we set $t = 0$).

- If $\mu > 2U$, we have $p_3 \approx 2/3$ and $p_0 \approx 1/3$, which is a charge-ordered state with 3 particles in the low-energy sites and 0 particles in the high-energy site. This state resembles a Hund's insulator, with the difference that it is not translation invariant. In this case, the energy in the atomic limit is $E_0 = 6U - 6\mu$.

- If $U < \mu < 2U$, we have $p_1 \approx p_2 \approx p_3 \approx 1/3$, which means that in the low-energy sites there are 3 and 2 particles, while in the high-energy site there is 1 particle. Again, this state is not fully translation invariant, however it is invariant upon exchange of the low energy sites $j = 1 \leftrightarrow j = 3$ (i.e. under spatial inversion). This is a strange phase because, applying perturbation theory for small hopping t, we get $\langle\psi|H_{ij}^{\text{hop}}|\psi\rangle \neq 0$ for $i = 1$, $j = 3$ (or vice versa) and 0 otherwise. In other words, low energy sites are subject to charge fluctuations and therefore they allow charge transport from

[6] This is not mathematically rigorous, because the orbital degrees of freedom in the Hund's model transform under the action of SO(3), generated by $\mathbf{L}_j$, while here the flavors transform under the action of SU(3), generated by the ladder operators $S_{j,\sigma\rho}$ defined in eq. [1.7].

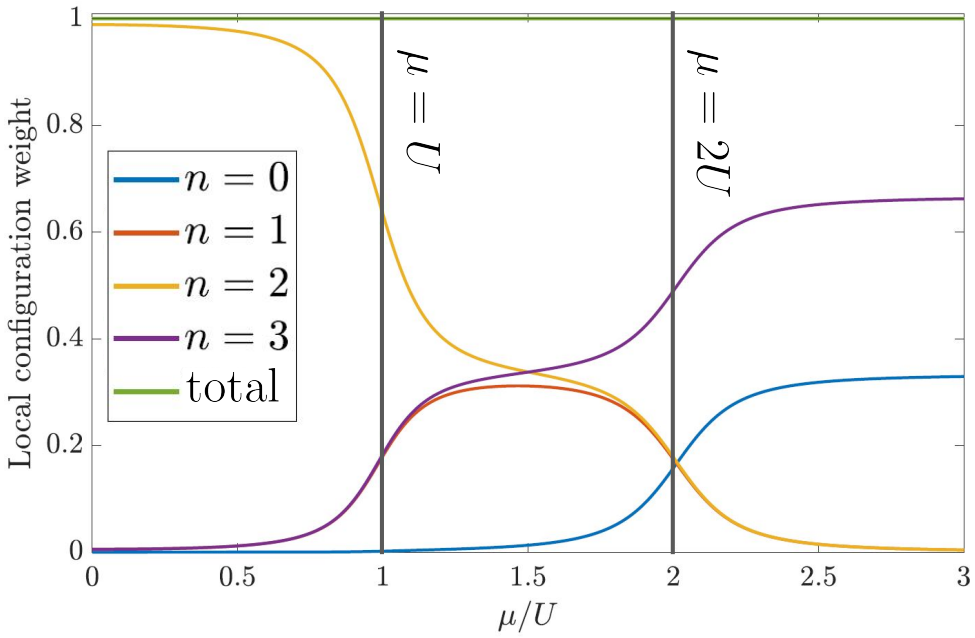

Figure 4.6: Population of the atomic multiplets p_n relevant to the ground state of Hamiltonian [4.8] as a function of the control parameter μ/U. The calculations are performed in the atomic limit $t = 1$, $U = 22$ at a filling factor of 2 (6 fermions on the 3-siste system). The gray vertical lines $\mu = U$ and $\mu = 2U$ correspond to the points where different solutions become degenerate.

one to another; but on the high-energy site the charge is frozen and transport is not allowed. We thus expect that this phase really depends on the lattice dimensionality: in $d = 1$ this is an insulator, because a particle can't move freely all around the ring, as it encounters obstacles along the way. In different lattice geometries anyway it is still possible that a particle moves from one side to the other of the sample by finding a connected path of low-energy sites, leading to a metallic state. In this intermediate regime, the ground state energy is $E_0 = 4U - 5\mu$.

- Along the two lines $\mu = U$ and $\mu = 2U$, the intermediate regime becomes degenerate with the Mott regime and the (analogue of the) Hund's regime respectively, namely $3U - 4\mu = 4U - 5\mu$ at $\mu = U$ and similarly $6U - 6\mu = 4U - 5\mu$ at $\mu = 2U$. The resulting ground state is now a quantum superposition of all the Fock states that characterize the two degenerate regimes, as we discuss below, and this reflects on the multiplets population. For $\mu = U$ we have $p_0 \approx 0$, $p_3 \approx p_1 \approx 1/6$ and $p_2 \approx 1/3$; whereas for $\mu = 2U$ we have $p_0 \approx p_1 \approx p_2 \approx 1/6$ and $p_3 \approx 1/2$.

4.3.2 Phase diagram based on the Drude weight

We are now ready to evaluate the Drude weight in the space of parameters U/t and μ/t following the prescriptions given in sec. [4.2]; there is only one subtlety which is worth pointing out first. In this specific system with $N_{\text{sites}} = 3$ and filling factor 2, the energy function $E_0(\phi)$ has a minimum located at $\phi = \phi_0 = \pi/N_{\text{sites}}$, unlike the Hund's model, where it was located at $\phi = 0$. Moreover, the critical flux where the linear proportionality $I(\phi) \approx D(\phi - \phi_0)$ breaks down is now $\phi_c = 0$ (see appendix [B] for more details). Once again, we can compute D from the persistent current $I(\phi)$ with a single exact

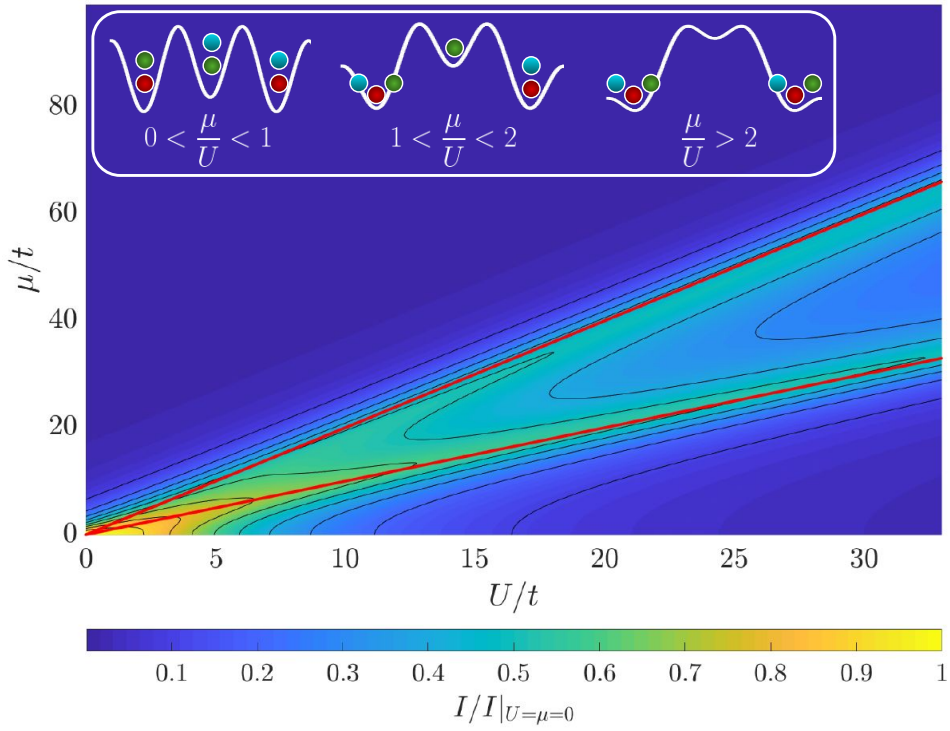

Figure 4.7: Color-plot of the Drude weight as a function of U/t and μ/t. The Drude weight is computed relatively to the non-interacting case $U = \mu = 0$ and is given by the ratio of the respective total currents $D/D_{U=\mu=0} = I(\phi)/I_{U=\mu=0}(\phi)$ at $\phi = \pi/3 - 0.1\pi/3$. The red lines are the two crossover lines $\mu = U$ and $\mu = 2U$, where two different insulating solutions become degenerate in the atomic limit. The insert sketches representative Fock states having a large weight in the ground state in the three relevant insulating regimes.

diagonalization per every point in the phase diagram at a suitably chosen ϕ via $D = I(\phi)/(\phi - \phi_0)$. The chosen flux ϕ should be close to $\phi_0 = \pi/3$ and far from $\phi_c = 0$, hence we choose $\phi = \phi_0 - 0.1\pi/3$.

We report the resulting phase diagram obtained from the Drude weight with a color plot in fig. [4.7]. We observe that, when $\mu \gg t$ and $U \gg t$, there are three insulating regions with $D \approx 0$, corresponding to the three regimes detailed above with $\mu < U$, $U < \mu < 2U$ and $\mu > 2U$ respectively. The three regions are separated by two stripes where the Drude weight is finite, yet smaller than in the trivial metallic phase $t \gg \mu, U$, and the system is a bad conductor, but not an insulator. The two stripes of interaction-resilient conductivity develop around the two lines $\mu = U$ and $\mu = 2U$ where two out of the three atomic-limit solutions are degenerate. The metallic character of these two stripes can be explained by looking at the relative weights that the Fock states have in the ground state.

For example, considering the line $\mu = U$, where the Mott and the intermediate insulators are degenerate, Fock states typical of the former (with 2 particles on every site) and of the latter (with 3 and 2 particles in the low energy sites and 1 particle in the high energy site), which transform into one another upon hopping processes, have roughly the same weights in the ground state. This means that, treating the hopping term as a small perturbation, we have a contribution of first order in t, as $\langle\psi|H_{\text{hop}}|\psi\rangle \neq 0$. This suggests that the kinetic energy is larger compared to what we find in the insulators, where first order corrections in t vanish and we have only higher order terms. We can understand this result more intuitively by considering

a specific Fock state, for example $|2_{rg}, 2_{gb}, 2_{rb}\rangle$ (insert of fig. [4.7]), where the three numbers represent the number of fermions on each site, while r, g, b are labels for the flavors (they refer to the colors used in the figure: r is red, g is green, b is blue). This state is a good representative of relevant Fock states in the Mott insulator and, for example under the action of the hopping term $c^\dagger_{1b}c_{2b}$, it transforms into $|3_{rgb}, 1_g, 2_{rb}\rangle$, a representative state of the intermediate insulating phase, which is strongly suppressed if $\mu \ll U$, but acquires a relevant weight when $\mu \approx U$. After a careful thought, we can convince ourselves that when $\mu \approx U$, every hopping term $c^\dagger_{i\sigma}c_{j\sigma}$ for all (ij, σ) transforms a relevant Fock state into another relevant Fock state, and this is precisely what guarantees a conductive behavior. In contrast, this is not the case when $\mu \ll U$, as every hopping process transforms a state of the relevant subspace $|2_-, 2_-, 2_-\rangle$ into a state orthogonal to the subspace, e.g. $|3_-, 1_-, 2_-\rangle$. A similar analysis holds for the other degeneracy line $\mu = 2U$

This picture is similar to what we have found in fig. [4.3] for the Hund's model, with the obvious difference that now we have three insulators and two distinct interaction-resilient metallic phases. Despite their differences, the two models are ruled out by the same deep mechanism: a degeneracy of insulating phases favors charge fluctuations in the ground state that are compatible with hopping processes, thus leading to a residual conductive behavior which survives to the strong interactions.

4.4 Conclusion and outlook

In this chapter, we have studied the general mechanism that stabilizes an interaction-resilient metal, i.e. a paradigm that generalizes the popular Hund's metal. In particular, we have uncovered the existence of a similar metallic phase in two rather different models of strongly correlated fermions. We have compared a three-orbital Hubbard model and a three-component SU(3) Hubbard model with a three-site patterned potential. In both models, the standard Hubbard repulsion, which tends to stabilize a Mott insulator, competes with a term of the Hamiltonian which favours a different state with inhomogeneous density distribution, namely the Hund's coupling in the first model and a non-uniform single-particle potential in the second. In both cases, the competition between the two terms leads to different insulating solutions which are separated in the respective phase diagrams by families of states which exhibit a persistent metallic character, even in the presence of strong Coulomb repulsion, hence the name "interaction-resilient metals".

The exact results on the small cluster provide information on the nearest-neighbor correlation functions of the model, which are difficult to compute with other approaches like single-site DMFT, where the self-energy is purely local. In particular, we have demonstrated that, in the Hund's metal region, the nearest-neighbor inter-orbital charge correlations vanish just like the onsite components, strengthening the relation between the Hund's metal and the effective orbital decoupling. In other words, the charge degrees of freedom of different orbitals are decoupled in the Hund's metal, hence the introduction of a crystal field splitting or of a hopping imbalance results in an asymmetric Mott localization between the bands, where localized electrons in some bands coexist with partially delocalized electrons in others. Moreover we have found that the nearest-neighbor spin correlators are always negative implying a tendency towards antiferromagnetic ordering in all the regions of the phase diagram, including the Hund's metal and the Hund's insulator. We have further supplemented previous studies with a detailed analysis of the many-body low-lying energy spectrum across the phase diagram, showing how different "bundles" of excitations characterize different states.

In sec. [4.3], we have performed a similar analysis for the SU(3) Hubbard model with a three-site energy pattern (one site out of three with a higher energy). Here, we find a richer phase diagram, characterized by two different lines along which metallic solutions survive at large interactions, in analogy

with the Hund's metal. This result is understood by inspecting the probability distribution of different local configurations in the ground state, and is connected with the similar physical scenario emerging within the Hund's model. We have therefore provided evidence that an interaction-resilient metallic state is not peculiar of the Hund's physics, where it has been widely discussed, but it is a more general feature which is present for a wide class of models featuring competing insulating states associated with different local configurations. Tuning the parameters to make the insulating states degenerate or nearly degenerate, a correlation-resistant metal exists as long as the local configurations corresponding to the two insulators are connected by hopping processes.

In this work, we have considered a minimal three-site cluster to provide unbiased results by means of exact diagonalization. For the Hund's model, the three-site cluster does not show significant differences with the scenario obtained with other methods, including DMFT, RISB, and slave-spin mean field. This agreement between different approaches represents a mutual validation of the different methods and confirms that the existence of the Hund's metal is an intrinsic feature of the multiorbital Hubbard model. Moreover, exact result for small clusters can be used to reconstruct the properties of infinite lattices using quantum cluster methods such as cluster perturbation theory [110], variational cluster approximation [111], or cluster extensions of DMFT [32, 33, 112]. The discussed results represent, in this perspective, the basic building block from which the lattice physics can be built. These approximations are particularly accurate for the strongly correlated insulating solutions, where we expect short-ranged quantum correlations [113], but they should not alter significantly the shape of the phase diagram including the region where the interaction-resilient metal is stable.

Chapter 5

Superconductivity in multiorbital systems

A phenomenon which is particularly relevant both in the study of solids and of ultracold atoms is superconductivity (or, respectively, superfluidity). In this chapter we consider superconductivity in multiorbital fermionic systems, starting from a very general theoretical question: how is the superconducting order affected by the presence of interorbital couplings? One can encounter this problem in a broad range of physical situations. For example, recently discovered high-temperature superconductors (such as the iron-based [17] and nickel-based compounds [114], alkali-doped fullerides [93, 115] and MgB_2 [116]) are characterized by several active bands around the Fermi level and by strong interorbital electronic interactions. Another example is the study of thin superconducting films, composed of few stacked layers [117]: in this case, every layer can be regarded as an independent orbital and the interlayer interaction as an effective orbital coupling. Among these, the twisted bilayer graphene, which displays remarkable superconducting properties [118], has been recently subject of a great research effort (see e.g. [119, 120, 121] and related works).

The simultaneous presence of several interactions in the Hubbard-Kanamori model makes it difficult to understand what is the role of every single term: a possible way to disentangle their role is to consider them one by one. Here we begin by studying the effect of a Josephson local pair hopping coupling on the superconducting character of the orbitals, providing an exact numerical solution of the DMFT equations on the infinite-dimensional Bethe lattice. This model is particularly instructive, as it shows the dangers of neglecting the role of quantum dynamical fluctuations when applying a static mean-field theory (even to states with spontaneously broken symmetry). This specific choice is also motivated by similar models proposed to describe a two-channel BCS-BEC crossover controlled by the orbital Feshbach resonance of ^{173}Yb [24, 122]. Even though our model does not contain all the necessary ingredients to accurately investigate the orbital Feshbach resonance, we discuss possible directions for future investigations in this regards.

This chapter is organized as follows: in sec. [5.1] we provide an overview of the standard BCS theory, discussing the BCS-BEC crossover and reviewing the concept of superfluid stiffness; in sec. [5.2] we extend the theory to a two-orbital system with a Josephson coupling, starting with a static mean-field approximation and then including the role of dynamical correlations with DMFT; in sec. [5.3] we briefly review the concept of orbital Feshbach resonance and describe how our model could be generalized to accurately describe it; finally we devote sec. [5.4] to concluding remarks.

5.1 Single channel BCS theory

We begin this chapter by giving an overview of how the well-known BCS theory can be obtained from the attractive single-band Hubbard model. This section is mainly devoted to introduce relevant notations and concepts and has no presumption of completeness. The interested reader can find more details in the original paper by Bardeen, Cooper and Schrieffer [123], in ref. [124] for BCS theory and its generalizations to a variety of phenomenology involving superconductors, or in refs. [125, 126, 127] for a quantum field theory of superconductors. Other classical resources are refs. [42, 128, 129, 130, 131].

The section is organized as follows: we begin with an overview of the attractive Hubbard model and its symmetries, then we also discuss the standard BCS theory based on a mean-field treatment of Hamiltonian [5.1]; after that, we introduce the Nambu many-body formalism relevant to perform DMFT and finally we introduce and compute the superfluid stiffness, which gives an hint on the finite-temperature behavior at large U.

5.1.1 Attractive Hubbard model and its symmetries

In this section, we consider the attractive single-orbital Hubbard model on a generic lattice:

$$H = -t\sum_{\langle ij\rangle}\sum_{\sigma}\left(c^{\dagger}_{i\sigma}c_{j,\sigma} + c^{\dagger}_{j,\sigma}c_{i,\sigma}\right) - U\sum_{i} n_{i\uparrow}n_{i\downarrow} - \mu\sum_{i\sigma} n_{i\sigma}, \tag{5.1}$$

where $U > 0$ is a local attraction. In materials, a similar attractive interaction can be provided by a coupling to vibrational modes of the crystal (phonons) and eq. [5.1] has to be regarded as an effective model for the electrons obtained after integrating out the phonons and neglecting retardation effects (see e.g. [30, 132] and references therein).

The attractive Hubbard Hamiltonian is symmetric under the action of the group $\mathrm{SU(2)_{spin}}\times\mathrm{U(1)_{charge}}$, where SU(2) is generated by the spin operators S^a ($a = x, y, z$) and U(1) by the number operator. Actually, on bipartite lattices the symmetry is more structured, as it is $\mathrm{SU(2)_{spin}}\times\mathrm{SU(2)_{pseudospin}}$, where the pseudospin algebra is generated by the operators [133]:

$$\eta^x = \frac{1}{2}\sum_j (-1)^{R_j}\left(c^{\dagger}_{j\uparrow}c^{\dagger}_{j\downarrow} + c_{j\downarrow}c_{j\uparrow}\right), \quad \eta^y = \frac{i}{2}\sum_j (-1)^{R_j}\left(-c^{\dagger}_{j\uparrow}c^{\dagger}_{j\downarrow} + c_{j\downarrow}c_{j\uparrow}\right), \quad \eta^z = \frac{1}{2}\sum_j (n_j - 1), \tag{5.2}$$

which indeed satisfy the angular momentum commutation relation $[\eta^a, \eta^b] = i\varepsilon_{abc}\eta^c$.

Under the unitary transformation $c^{\dagger}_{j\downarrow} \to (-1)^{R_j}c_{j\downarrow}$, the attractive Hubbard model is mapped into the repulsive Hubbard model (and vice versa), and the symmetry generators are swapped: $S^a \leftrightarrow \eta^a$, hence $\mathrm{SU(2)_{spin}} \leftrightarrow \mathrm{SU(2)_{pseudospin}}$. The chemical potential term is mapped into an external uniform magnetic field $\mu N \to \mu S^z$ and vice versa; however at half filling this term is not present. Furthermore, the transformation also acts on the Fock states; in particular, a given state labeled by the quantum numbers (N, S^z), representing the total number of particles and the total magnetization along z respectively, is mapped into a state with different quantum numbers according to $(N, S^z) \to (N_{\mathrm{sites}} + S^z, N - N_{\mathrm{sites}})$ [134]. The half-filled sector $(N_{\mathrm{sites}}, 0)$ remains invariant under this mapping, but a magnetized sector in the repulsive picture is mapped into a doped sector in the attractive picture and vice-versa.

Consequently, just like the ground state of the repulsive Hubbard model on a bipartite lattice is characterized by an antiferromagnetic phase that spontaneously breaks $\mathrm{SU(2)_{spin}}$, similarly in the attractive model the ground state spontaneously breaks $\mathrm{SU(2)_{pseudospin}}$. In the repulsive case, the order parameter

for antiferromagnetism is given by the expectation value of the staggered magnetization (Néel vector) $M^a = N_{\text{sites}}^{-1} \sum_i (-1)^{R_i} S_i^a$, which in the attractive model is mapped into

$$M^x \to \frac{1}{2N_{\text{sites}}} \sum_i (c_{i\uparrow}^\dagger c_{i\downarrow}^\dagger + \text{h.c.}), \quad M^y \to -\frac{i}{2N_{\text{sites}}} \sum_i (c_{i\uparrow}^\dagger c_{i\downarrow}^\dagger - \text{h.c.}), \quad M^z \to \frac{1}{2N_{\text{sites}}} \sum_i (-1)^{R_i} (n_i - 1).$$

For the staggered xy magnetization, it is more conventional to consider the mapping of ladder operators $M^\pm = M^x \pm M^y$:

$$M^+ \to \frac{1}{N_{\text{sites}}} \sum_i c_{i\uparrow}^\dagger c_{i\downarrow}^\dagger; \qquad M^- \to \frac{1}{N_{\text{sites}}} \sum_i c_{i\downarrow} c_{i\uparrow}. \tag{5.3}$$

The transformed version of $M^\pm$ are complex order parameters for superconductivity, while the transformed M^z describes a charge-density wave.

The charge-density wave and the superconducting phase are degenerate in the half-filled attractive Hubbard model, however even a small deviation from the half-filling condition favors superconductivity [135]. In this section we work at half-filling, but we neglect the presence of a charge-density wave, focusing on superconductivity instead.

5.1.2 Mean field on the attractive Hubbard model

By standard Fourier transform, eq. [5.1] can be rewritten in momentum space, where the connection to standard BCS theory becomes more transparent:

$$H = \sum_{\mathbf{k}\sigma} (\varepsilon_{\mathbf{k}} - \mu) c_{\mathbf{k}\sigma}^\dagger c_{\mathbf{k}\sigma} - \frac{U}{N_{\text{sites}}} \sum_{\mathbf{kpq}} c_{\mathbf{k+q}\uparrow}^\dagger c_{-\mathbf{k}\downarrow}^\dagger c_{-\mathbf{p+q}\downarrow} c_{\mathbf{p}\uparrow} \tag{5.4}$$

where $\varepsilon_{\mathbf{k}}$ is the dispersion relation on the given lattice. Eq. [5.4] is known as *BCS* Hamiltonian as the standard BCS theory can be obtained by a mean-field Hartree-Fock decoupling of the interaction in the superconducting channels:

$$\Delta(\mathbf{q}) = \frac{U}{N_{\text{sites}}} \sum_{\mathbf{p}} \langle c_{-\mathbf{p}+\mathbf{q}\downarrow} c_{\mathbf{p}\uparrow} \rangle, \qquad \Delta^*(\mathbf{q}) = \frac{U}{N_{\text{sites}}} \sum_{\mathbf{k}} \langle c_{\mathbf{k}+\mathbf{q}\uparrow}^\dagger c_{-\mathbf{k}\downarrow}^\dagger \rangle, \tag{5.5}$$

where $\Delta(\mathbf{q})$ is called *gap parameter*. We now assume that the gap parameter is uniform in real space, namely that the only relevant momentum mode is $\mathbf{q} = 0$: $\Delta(\mathbf{q}) = \Delta\delta_{\mathbf{q},0}$: this amounts to assume that the center of mass of a Cooper pair has a vanishing momentum. The same decoupling can be obtained by performing a similar mean-field decoupling directly from the real-space Hubbard Hamiltonian [5.1], using $\Delta = UN_{\text{sites}}^{-1} \sum_i \langle c_{i\downarrow} c_{i\uparrow} \rangle$ and $\Delta^* = UN_{\text{sites}}^{-1} \sum_i \langle c_{i\uparrow}^\dagger c_{i\downarrow}^\dagger \rangle$ as order parameters. We observe that Δ and Δ^* are, except for the prefactor U, the order parameters that we have deduced based on a mapping to the repulsive model in eq. [5.3].

Introducing a suitable spinor $\Psi_{\mathbf{k}}^\dagger = (c_{\mathbf{k}\uparrow}^\dagger, c_{-\mathbf{k}\downarrow})$, known as *Nambu spinor*, and using $\Delta = |\Delta| e^{i\varphi}$ the resulting mean field Hamiltonian reads:

$$H = \sum_{\mathbf{k}} \Psi_{\mathbf{k}}^\dagger \begin{pmatrix} \varepsilon_{\mathbf{k}} - \mu & -|\Delta| e^{i\varphi} \\ -|\Delta| e^{-i\varphi} & -(\varepsilon_{-\mathbf{k}} - \mu) \end{pmatrix} \Psi_{\mathbf{k}} + \sum_{\mathbf{k}} (\varepsilon_{\mathbf{k}} - \mu) + N_{\text{sites}} \frac{|\Delta|^2}{U}. \tag{5.6}$$

From now on, we assume to work on lattices with a symmetric momentum dispersion $\varepsilon_{-\mathbf{k}} = \varepsilon_{\mathbf{k}}$, which is fine for hypercubic lattices; however it does not necessarily hold for more sophisticated geometries.

When $\Delta \neq 0$, this Hamiltonian explicitly breaks the $\mathrm{U}(1)_{\text{charge}}$ symmetry, as it no longer commutes with the particle number $[H, N] \neq 0$. Intuitively, this mean-field model represents a Fermi sea coupled to an external reservoir of particle pairs with zero total momentum and zero total spin, and Δ represents the tunneling amplitude from the reservoir to the system (or vice versa). Since the pair susceptibility of the non interacting Fermi system diverges logarithmically with temperature, we expect this perturbation to have a significant effect in the ground state.

We can diagonalize the mean-field Hamiltonian via a unitary transformation on the Nambu spinor: $\Psi_{\mathbf{k}} \to \Phi_{\mathbf{k}} = \hat{P}_{\mathbf{k}}^{\dagger}\Psi_{\mathbf{k}}$, where $\hat{P}_{\mathbf{k}}$ is a unitary matrix (this ensures that the components of the transformed spinor $\Phi_{\mathbf{k}}$ can still be regarded as fermionic operators, as they satisfy the correct anticommutation rules). The diagonalized matrix takes the form $\hat{P}_{\mathbf{k}}^{\dagger}\hat{H}_{\mathbf{k}}P_{\mathbf{k}} = \mathrm{diag}(\lambda_k, -\lambda_k)$, where $\lambda_{\mathbf{k}} = \sqrt{(\varepsilon_{\mathbf{k}} - \mu)^2 + |\Delta|^2}$ and the corresponding transformation is in fact real and symmetric:

$$\hat{P}_{\mathbf{k}}^{\dagger} = \begin{pmatrix} -e^{-i\varphi}\cos\theta_{\mathbf{k}} & \sin\theta_{\mathbf{k}} \\ \sin\theta_{\mathbf{k}} & e^{i\varphi}\cos\theta_{\mathbf{k}} \end{pmatrix}, \quad \sin\theta_{\mathbf{k}} = \sqrt{\frac{1}{2}\left(1 - \frac{\varepsilon_{\mathbf{k}} - \mu}{\lambda_{\mathbf{k}}}\right)}, \quad \cos\theta_{\mathbf{k}} = \sqrt{\frac{1}{2}\left(1 + \frac{\varepsilon_{\mathbf{k}} - \mu}{\lambda_{\mathbf{k}}}\right)}. \tag{5.7}$$

The resulting Hamiltonian, written in terms of the components of the Nambu spinor in the new basis $\Phi_{\mathbf{k}}^{\dagger} = (\alpha_{\mathbf{k}\uparrow}^{\dagger},\, \alpha_{-\mathbf{k}\downarrow})$, reads

$$H = \sum_{\mathbf{k}\sigma} \lambda_{\mathbf{k}} \alpha_{\mathbf{k}\sigma}^{\dagger}\alpha_{\mathbf{k}\sigma} + \sum_{\mathbf{k}} (\varepsilon_{\mathbf{k}} - \mu - \lambda_{\mathbf{k}}) + N_{\text{sites}}\frac{|\Delta|^2}{U}. \tag{5.8}$$

This form allows for an intuitive physical interpretation: since $\lambda_{\mathbf{k}} \geq |\Delta|$ for any finite gap, the presence of α-quasiparticles in a state $(\mathbf{k}, \sigma)$ increases the internal energy by $+\lambda_{\mathbf{k}}$, bringing the system to an excited state; we can thus consistently name these quasiparticles *excitations*. The energetic cost of creating an excitation is at minimum $|\Delta|$, hence the name gap. Therefore, the ground state is the vacuum state of excitations $|0_\alpha\rangle$. This state can be related to the vacuum of normal electrons $|0_c\rangle$ by building a state that maps any annihilation operator $\alpha_{\mathbf{k}\sigma}$ to zero: $|0_\alpha\rangle = \prod_{\mathbf{k}} \alpha_{\mathbf{k}\uparrow}\alpha_{-\mathbf{k}\downarrow}\,|0_c\rangle$; transforming back to the original fermionic operators, we get the celebrated BCS ground state:

$$\boxed{|0_\alpha\rangle = \mathcal{N}\prod_{\mathbf{k}} \left(e^{-i\varphi}\cos\theta_{\mathbf{k}} + \sin\theta_{\mathbf{k}}\hat{c}_{\mathbf{k}\uparrow}^{\dagger}\hat{c}_{-\mathbf{k}\downarrow}^{\dagger}\right)|0_c\rangle\,,} \tag{5.9}$$

where $\mathcal{N}$ is a normalization constant. We pause here for a moment to make a few important observations.

- In the BCS ground state, the grand canonical potential is $\Omega(\Delta) = \sum_{\mathbf{k}}(\varepsilon_{\mathbf{k}} - \mu - \lambda_{\mathbf{k}}) + N_{\text{sites}}|\Delta|^2/U$. In particular, we observe that if $\Delta \neq 0$, $\lambda_{\mathbf{k}} > |\varepsilon_{\mathbf{k}}|$, which implies that – for some finite values of Δ – the BCS ground state has a lower Ω than the non-interacting Fermi sea, for which it is $\sum_{\mathbf{k}}(\varepsilon_{\mathbf{k}} - \mu)$. In other words, the presence of a pairing field (albeit small) makes the Fermi sea an unstable state. Furthermore, we observe that the internal energy depends on Δ only through $|\Delta|$ and not through the phase φ, hence there is a continuous manifold of degenerate ground states labeled by $\varphi \in [0, 2\pi[$.

- The ground state depends on the phase of the gap parameter φ, which implies that it can be written as a coherent state for the creation operator $B_{\mathbf{q}}^{\dagger} = \sum_{\mathbf{k}} \tan\theta_{\mathbf{k}}\, c_{\mathbf{k}+\mathbf{q}\uparrow}^{\dagger}c_{-\mathbf{k}\downarrow}^{\dagger}$ with a fixed phase:

$$|0_\alpha\rangle = \mathcal{N}' \exp\left\{e^{i\varphi}B_0^{\dagger}\right\}|0_c\rangle,$$

where we have absorbed some factors in the new normalization constant $\mathcal{N}'$. Consistently, although the average particle number $\langle 0_\alpha|N|0_\alpha\rangle$ corresponds to the filling factor, the BCS ground state is characterized by a fluctuating number of particles, namely $\langle 0_\alpha|N^2|0_\alpha\rangle \neq \langle 0_\alpha|N|0_\alpha\rangle^2$. This reflects the fact that $|0_\alpha\rangle$ is not symmetric under $\mathrm{U}(1)_{\text{charge}}$ generated by the number operator. At first this does not surprise, because the mean-field Hamiltonian [5.6] is not invariant under $\mathrm{U}(1)_{\text{charge}}$ either; however, in the thermodynamic limit, this is actually the ground state of the attractive Hubbard model [5.1], hence it is a state that spontaneously breaks the charge symmetry [136].

- The components of $\Phi^\dagger_{\mathbf{k}}$ can be also rewritten in terms of two fermionic creation operators as $(\beta^\dagger_{\mathbf{k}\uparrow}, \beta^\dagger_{-\mathbf{k}\downarrow})$. With this choice, the mean field Hamiltonian reads

$$H = \sum_{\mathbf{k}} (\lambda_{\mathbf{k}} \beta^\dagger_{\mathbf{k}\uparrow}\beta_{\mathbf{k}\uparrow} - \lambda_{\mathbf{k}}\beta^\dagger_{\mathbf{k}\downarrow}\beta_{\mathbf{k}\downarrow}) + \sum_{\mathbf{k}} (\varepsilon_{\mathbf{k}} - \mu) + N_{\text{sites}} \frac{|\Delta|^2}{U};$$

  in this case, adding $\uparrow$ quasiparticles increases the energy by $\lambda_{\mathbf{k}}$, while adding $\downarrow$ quasiparticles decreases the energy by $-\lambda_{\mathbf{k}}$. In this language, the ground state is obtained by fully populating the $\downarrow$ band and the advantage is that the spectral function of quasiparticles has a symmetric structure.

In the spirit of the Hartree-Fock method, the gap parameter should be determined self-consistently. The self-consistency equation at any temperature T is obtained by minimizing the grand-canonical potential $\Omega = E_0 - TS - \mu N$, where E_0 is the internal energy and S is the entropy. Since the excitations obey the Fermi statistics, we have $\langle \alpha^\dagger_{\mathbf{k}\sigma}\alpha_{\mathbf{k}\sigma}\rangle = f(\lambda_{\mathbf{k}})$, where f is the Fermi function, and the grand-canonical potential reads

$$\Omega = \sum_{\mathbf{k}} \lambda_{\mathbf{k}} f(\lambda_{\mathbf{k}}) - \sum_{\mathbf{k}} \lambda_{\mathbf{k}} + N_{\text{sites}} \frac{|\Delta|^2}{U} - T \sum_{\mathbf{k}} \left[f(\lambda_{\mathbf{k}}) \log f(\lambda_{\mathbf{k}}) + (1 - f(\lambda_{\mathbf{k}})) \log (1 - f(\lambda_{\mathbf{k}})) \right] \tag{5.10}$$

up to inessential constants. Assuming $\varphi = 0$ and replacing the momentum sum with an integral over the energy band weighted by the density of states $D(\varepsilon) = N^{-1}_{\text{sites}} \sum_{\mathbf{k}} \delta(\varepsilon - \varepsilon_{\mathbf{k}})$, the self-consistency equation reads:

$$\frac{\partial \Omega}{\partial \Delta} = 0 \quad \rightarrow \quad \boxed{\Delta = \frac{U}{2} \int d\varepsilon \, D(\varepsilon) \frac{\Delta}{\lambda(\varepsilon)} \tanh\left(\frac{\lambda(\varepsilon)}{2k_B T}\right).} \tag{5.11}$$

Simple analytical solutions (different from the unstable solution $\Delta = 0$) can be obtained under suitable conditions. The result is that the ground state as a function of U/D features a smooth crossover between two distinct regimes: the "BCS regime" at weak coupling and the "BEC regime" at strong coupling.

If Δ is large (more precisely $\Delta \gg D$, where D is the half bandwidth) and $T = 0$, we have $\lambda(\varepsilon) \approx \Delta$ and $\tanh \frac{\Delta}{2T} \to 1$, which in turn leads to $\Delta \approx U/2$. This is a consistent solution when $U \gg D$ (so that also $\Delta \gg D$). Moreover, we can formally get the critical temperature T_c at which the system gets back to a normal Fermi gas by simplifying Δ in both sides and then setting $\Delta = 0$, which leads to the implicit equation $1 = \frac{U}{2} \int d\varepsilon \frac{D(\varepsilon)}{|\varepsilon|} \tanh\left(\frac{|\varepsilon|}{2T_c}\right)$. If $T_c \gg D$, then we can expand the hyperbolic tangent as $\tanh \frac{|\varepsilon|}{2T_c} \approx \frac{|\varepsilon|}{2T_c}$, which simplifies the integral and results in $T_c \approx U/4$, then this is again consistent if $U \gg D$. This is called "BEC regime", because the coherence length of a Cooper pair is so small that the fermions are effectively bound in bosonic molecules which undergo Bose-Einstein condensation (hence the acronym BEC) at low temperature.[1] According to the mean-field picture, the superconducting order is broken when

[1] This is just an approximation, since the operator $B^\dagger_{\mathbf{q}}$ does not satisfy exact bosonic commutation relations. It turns out that only expectation values of the commutation relations are consistent with the Bose statistics in the limit $\mathbf{q} \to 0$, $U \gg D$ and for small filling factors.

the thermal fluctuations are large enough to break the bosonic molecule; but, as we will discuss in the next section, this is not correct and much lower thermal fluctuations are sufficient to break superconductivity.

Analytic results for the opposite limit $U \ll D$, known as "BCS regime", depend on the specific lattice, but in general the gap increases exponentially with U. We can give a more accurate analytic estimate for the Bethe lattice of infinite coordination, which is particularly relevant for the following sections. Setting $T = 0$ in eq. [5.11], the hyperbolic tangent is ≈ 1 and we can recast the equation as:

$$1 = \frac{U}{\pi D^2}\int_{-D}^{D} d\varepsilon \, \frac{\sqrt{D^2-\varepsilon^2}}{\sqrt{\varepsilon^2+\Delta^2}} = \frac{2U}{\pi D}\int_0^1 dx \sqrt{\frac{1-x^2}{\frac{\Delta^2}{D^2}+x^2}}.$$

In this form, the integral is difficult to expand for $\Delta/D \ll 1$ because it diverges when $\Delta = 0$ (thus we can't make a simple Taylor expansion). Fortunately, this divergence is easy to heal integrating by parts: using $\int dx \frac{1}{\sqrt{a^2+x^2}} = \log\left(x+\sqrt{a^2+x^2}\right)$, we get

$$1 = \frac{2U}{\pi D}\left[\sqrt{1-x^2}\log\left(x+\sqrt{\frac{\Delta^2}{D^2}+x^2}\right)\Bigg|_0^1 + \int_0^1 dx \frac{2x}{\sqrt{1+x^2}}\log\left(x+\sqrt{\frac{\Delta^2}{D^2}+x^2}\right)\right].$$

The first term evaluates to $-\log\frac{\Delta}{D}$ and it contains a logarithmic divergence in the limit $\Delta \to 0$; while the integral in the second term can now be expanded in powers of $\frac{\Delta}{D}$ as it is no longer singular for $\Delta \to 0$. The zero-th order expansion is obtained setting $\Delta = 0$ and using the result $\int_0^1 dx \frac{2x\log 2x}{\sqrt{1+x^2}} = 2\log 2 - 1$ we finally get

$$1 = \frac{2U}{\pi D}\left[-\log\frac{\Delta}{D} + 2\log 2 - 1 + \mathcal{O}\left(\frac{\Delta}{D}\right)\right] \quad \to \quad \boxed{\Delta \approx 4De^{-\frac{\pi D}{2U}-1},} \tag{5.12}$$

which shows that $\Delta \neq 0$ even for infinitesimal values of U, reflecting the Cooper instability of the Fermi gas. Moreover, it can be proved that the critical temperature has the same exponential behavior, hence small thermal fluctuations can significantly populate the excitation band and break superconductivity.

Here we have assumed a purely local interaction potential $V(\mathbf{r}) \propto \delta(\mathbf{r})$, which is then uniform in momentum space; however it is also interesting to mention the general case where the interaction potential has a non-trivial momentum dependence $V_{\mathbf{kp}} = \int d\mathbf{r} e^{i(\mathbf{k}-\mathbf{p})\cdot\mathbf{r}} V(\mathbf{r})$. In this case, the gap parameter depends on the "internal momentum" and it is defined as $\Delta_{\mathbf{k}}(\mathbf{q}) = \sum_{\mathbf{p}} V_{\mathbf{kp}} \langle c_{-\mathbf{p}+\mathbf{q}\downarrow} c_{\mathbf{p}\uparrow}\rangle$. Again we can assume $\mathbf{q} = 0$, but the residual momentum dependence of the gap can lead to a spatially non-uniform solution of the self-consistency equation[2], giving gaps with p-wave or d-wave symmetries that have been reported in some high-temperature superconductors [138, 139, 140, 141].

5.1.3 Many-body formalism and DMFT

A generalization of the Green's function to describe also the superconducting order is given in terms of the (imaginary-time) Nambu spinor $\Psi_{\mathbf{k}}^\dagger(\tau) = (c_{\mathbf{k}\uparrow}^\dagger(\tau),\, c_{-\mathbf{k}\downarrow}(\tau))$:

$$\hat{G}(\mathbf{k},\tau) = -\langle \mathcal{T}(\Psi_{\mathbf{k}}(\tau)\Psi_{\mathbf{k}}^\dagger(0))\rangle = -\left\langle \mathcal{T}\begin{pmatrix} c_{\mathbf{k}\uparrow}(\tau)c_{\mathbf{k}\uparrow}^\dagger(0) & c_{\mathbf{k}\uparrow}(\tau)c_{-\mathbf{k}\downarrow}(0) \\ c_{-\mathbf{k}\downarrow}^\dagger(\tau)c_{\mathbf{k}\uparrow}^\dagger(0) & c_{-\mathbf{k}\downarrow}^\dagger(\tau)c_{-\mathbf{k}\downarrow}(0)\end{pmatrix}\right\rangle, \tag{5.13}$$

[2] In this case, the self-consistency equation reads [124, 137]: $\Delta_{\mathbf{k}} = N_{\text{sites}}^{-1}\sum_{\mathbf{p}} \frac{V_{\mathbf{kp}}\Delta_{\mathbf{p}}}{\lambda_{\mathbf{p}}}\tanh\left(\frac{\lambda_{\mathbf{p}}}{2k_BT}\right)$.

(where we have used a mixed momentum-time representation). In this representation, we recognize a "normal" diagonal component (G), where a particle in state $(\mathbf{k},\sigma)$ is created at time 0 and destroyed at a later time τ (as in the standard definition) and an "anomalous" off-diagonal component (F), where two particles are destroyed in different states $(-\mathbf{k},\downarrow)$ and $(\mathbf{k},\uparrow)$ at time 0 and τ respectively:

$$G_{\sigma\sigma}(\mathbf{k},\tau) = -\langle \mathcal{T}(c_{\mathbf{k}\sigma}(\tau)c^{\dagger}_{\mathbf{k}\sigma}(0))\rangle; \qquad F(\mathbf{k},\tau) = -\langle \mathcal{T}(c_{\mathbf{k}\uparrow}(\tau)c_{-\mathbf{k}\downarrow}(0))\rangle. \tag{5.14}$$

Assuming spin symmetry and Fourier transforming to Matsubara frequencies, we get

$$\hat{G}(\mathbf{k},i\omega_n) = \begin{pmatrix} G(\mathbf{k},i\omega_n) & F(\mathbf{k},i\omega_n) \\ F^*(\mathbf{k},i\omega_n) & -G(-\mathbf{k},-i\omega_n) \end{pmatrix} \tag{5.15}$$

and the local Green function is obtained by summing over all momenta $\hat{G}_{\text{loc}}(i\omega_n) = N^{-1}_{\text{sites}}\sum_{\mathbf{k}}\hat{G}(\mathbf{k},i\omega_n)$ or, equivalently, integrating over the energies weighted by the density of states: $\hat{G}_{\text{loc}}(i\omega_n) = \int d\varepsilon\, D(\varepsilon)\hat{G}(\varepsilon,i\omega_n)$. Finally, the self-energy can be computed from the Dyson equation and it shares the same matrix structure and the same symmetry properties as the Green function:

$$\hat{\Sigma}(\mathbf{k},i\omega_n) = \hat{G}_0^{-1}(\mathbf{k},i\omega_n) - \hat{G}^{-1}(\mathbf{k},i\omega_n) = \begin{pmatrix} \Sigma(\mathbf{k},i\omega_n) & S(\mathbf{k},i\omega_n) \\ S^*(\mathbf{k},i\omega_n) & -\Sigma(-\mathbf{k},-i\omega_n) \end{pmatrix}, \tag{5.16}$$

where $\hat{G}_0^{-1}(\mathbf{k},i\omega_n) = \text{diag}[i\omega_n - \varepsilon_{\mathbf{k}},\, i\omega_n + \varepsilon_{-\mathbf{k}}]$ is the inverse non-interacting Green function. The mean-field theory outlined in the previous section is simply obtained by a constant self-energy with a vanishing normal component $\Sigma(\mathbf{k},i\omega_n) = 0$ and an anomalous part coincident with the gap $S(\mathbf{k},i\omega_n) = \Delta$.

We can particularize the general framework of DMFT to the study of superconductivity by means of the Nambu formalism. We begin by introducing a suitable Anderson impurity model, where the bath exchanges particles with an external reservoir of pairs. Following the notation of sec. [1.3.1], we introduce the set of spinors $\Psi^{\dagger}_{\ell} = (c^{\dagger}_{\ell\uparrow},\, c_{\ell\downarrow})$ on the ℓ-th site and we parameterize the bath via a set $\{\varepsilon_{\ell}, V_{\ell}, \Delta_{\ell}\}$ as:

$$\hat{\varepsilon}_0 = \begin{pmatrix} \varepsilon_0 - \mu & 0 \\ 0 & -(\varepsilon_0 - \mu) \end{pmatrix}; \qquad \hat{\varepsilon}_{\ell} = \begin{pmatrix} \varepsilon_{\ell} & -\Delta_{\ell} \\ -\Delta_{\ell} & -\varepsilon_{\ell} \end{pmatrix}; \qquad \hat{V}_{\ell} = \begin{pmatrix} V_{\ell} & 0 \\ 0 & -V_{\ell} \end{pmatrix}, \tag{5.17}$$

where $\varepsilon_0 = 0$.[3] The Weiss field $\hat{\mathcal{G}}^{-1}(i\omega_n)$ can be readily computed from eq. [1.17] and the impurity Green function in the interacting case can be obtained following the steps of sec. [1.3.2]; then the self-consistency procedure is realized applying the prescriptions of sec. [1.3.3]. The converged gap $\Delta = U\phi$ can be obtained by evaluating $\phi = N^{-1}_{\text{sites}}\sum_{\mathbf{k}}\langle c_{-\mathbf{k}\downarrow}c_{\mathbf{k}\uparrow}\rangle$ which, by virtue of eqs. [1.31] and [5.14], is given by $\phi = T\sum_{i\omega_n} F_{\text{loc}}(i\omega_n)$. A numerical evaluation which accounts for the large-ω_n tail can be obtained by applying eq. [1.39].

Solving the DMFT self-consistency equation on the infinite-dimensional Bethe lattice at $T = 0$, the order parameter is consistent with the mean-field prediction: in particular, for $U \gg D$ we have $\phi \to 1/2$ and $\Delta \to U/2$; while for $U \ll D$ we obtain $\phi \approx e^{-D/U}$. On the other hand, a finite temperature DMFT calculation, carried out in ref. [142], shows that the critical temperature at large U scales approximately like $T_c \sim 1/U$, in stark contrast with the mean-field prediction ($T_c \sim U$). The reason of this discrepancy

[3] We have included ε_0 even though it vanishes in this context because it is useful when generalizing to multiple orbitals subject to a crystal field splitting.

is ultimately the fact that the mean-field theory is not capable of accounting for quantum and spatial fluctuations of the phase field $\varphi(\mathbf{r}, \tau)$; however these fluctuations are the "soft" Goldstone mode, i.e. the low energy excitations of the system [127], at least when U is large. When the phase fluctuations are too large, the phase coherence of the order parameter is broken, which in turn determines a breakdown of the superfluid behavior.

5.1.4 Superfluid stiffness

To explain the behavior of T_c in the large-U limit (BEC regime), we can introduce the concept of superfluid stiffness [65] D_s. This quantity is central to characterize the phenomenology of superconductors, including the Meissner effect, a perfectly diamagnetic response of a superconductor to an externally applied magnetic field, as opposed to the standard weakly paramagnetic response of a Fermi gas. The external magnetic field penetrates the sample only within a distance $\approx \lambda_L$ (known as London penetration depth) from the surface, while it is screened at larger distances. The London depth is given by $\lambda_L = \sqrt{m/(\mu_0 n_s e^2)}$, where m and e are the electronic mass and charge respectively, μ_0 is the vacuum magnetic permeability and n_s is the density of carriers having this anomalous superfluid behavior[4]. The phenomenological equation that explains this effect is the London equation, which states that the current density $\mathbf{j}$ is proportional to the magnetic vector potential $\mathbf{A}$ in the Coulomb gauge $\nabla \cdot \mathbf{A} = 0$, more precisely $\mathbf{j} = -\frac{n_s e^2}{m}\mathbf{A}$. This expression is in fact quite different from the current on a conventional metal, where Ohm's law states that the current is proportional to the electric field $\mathbf{j} = \sigma \mathbf{E}$ or, in other words, to the time derivative of the vector potential $\mathbf{j} = -\sigma \partial_t \mathbf{A}$ (which holds in the specific gauge where we set the scalar potential to zero), where σ is the electrical conductivity. In general, the latter is a tensor with spatial and temporal dependence, and Ohm's law has to be generalized in the form of a convolution integral; however it can be written in much simpler terms in momentum-frequency space as $\mathbf{j}(\mathbf{q}, \omega) = i\omega \hat{\sigma}(\mathbf{q}, \omega)\mathbf{A}(\mathbf{q}, \omega)$.

Applying the machinery of *linear response theory* on a d-dimensional hypercubic lattice system, it is possible to prove that the linear response of a current density to an externally applied vector potential is $j_i(\mathbf{q}, \omega) = K_{ij}(\mathbf{q}, \omega)A_j(\mathbf{q}, \omega)$, where the linear response function is given by

$$K_{ij}(\mathbf{q}, \omega) = -e^2 \left[\chi_{ij}(\mathbf{q}, \omega) - \frac{a^2}{\hbar^2} \langle E_i^{\text{kin}} \rangle \delta_{ij} \right]. \tag{5.18}$$

Here we recognize two contributions: a *paramagnetic term* and a *diamagnetic term*. The diamagnetic term is given by the expectation value of a "component" of the kinetic energy $\langle E_i^{\text{kin}} \rangle$, which is given only by hopping processes along the direction $\hat{\mathbf{e}}_i$ (the counterpart of this term for a uniform system is proportional to the particle density). The paramagnetic term instead is given by the current-current response function χ_{ij} that, according to the Kubo formula, is given by

$$\chi_{ij}(\mathbf{q}, \omega) = \frac{1}{i\hbar} \int_0^\infty dt\, e^{i\omega t} \langle [I_i(\mathbf{q}, t), I_j(-\mathbf{q}, 0)] \rangle, \tag{5.19}$$

where $\langle \dots \rangle$ denotes the expectation value on an unperturbed equilibrium state, $I(\mathbf{q}, 0)$ is a generalization of the paramagnetic current introduced in sec. [2.3]:

$$I_j(\mathbf{q}) = \sum_{\mathbf{k}\sigma} v_{j,\mathbf{k},\mathbf{q}} c^\dagger_{\mathbf{k},\sigma} c_{\mathbf{k}+\mathbf{q},\sigma} = \sum_{\mathbf{k}} v_{j,\mathbf{k},\mathbf{q}} \Psi^\dagger_{\mathbf{k}} \mathbb{1} \Psi_{\mathbf{k}+\mathbf{q}}, \qquad v_{j,\mathbf{k},\mathbf{q}} = \frac{ita}{\hbar} \left(e^{-i(\mathbf{k}+\mathbf{q})\cdot a\hat{\mathbf{e}}_j} - e^{i\mathbf{k}\cdot a\hat{\mathbf{e}}_j} \right) \tag{5.20}$$

[4] In this section we adopt units of the international system.

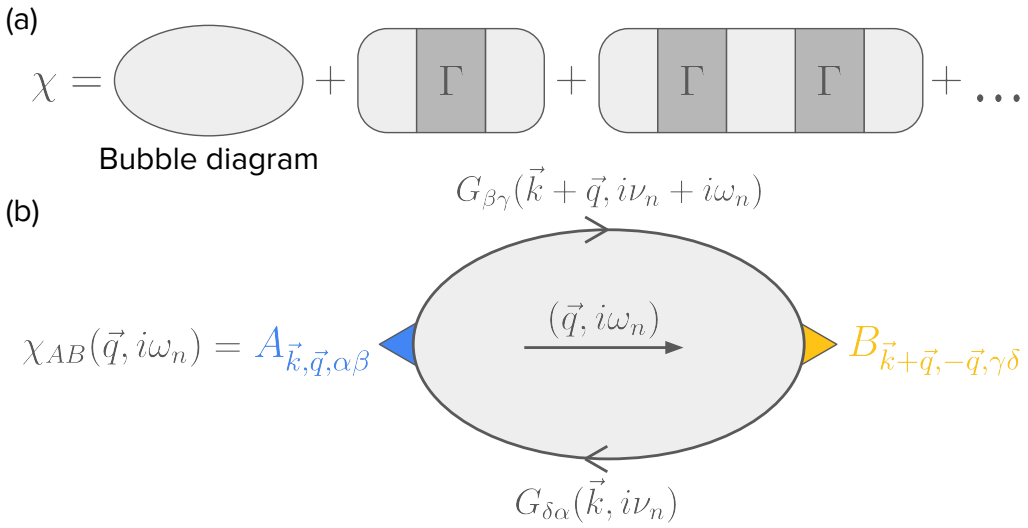

Figure 5.1: (a) Ladder expansion for a correlation function $\chi_{AB}(\mathbf{q}, i\omega_n)$ in terms of the irreducible vertex function. The operator A is defined as $A(\mathbf{q}) = \sum_{\mathbf{k},\alpha\beta} \Psi^\dagger_{\mathbf{k}\alpha} A_{\mathbf{k},\mathbf{q},\alpha\beta} \Psi_{\mathbf{k}\beta}$ and a similar definition holds for $B(-\mathbf{q})$. (b) Detail of the "bubble diagram", the only Feynman diagram that contributes in the non-interacting case or in the limit of infinite dimensionality. The summation over all the internal indexes is implied, i.e. $k_B T N^{-1}_{\text{sites}} \sum_{\mathbf{k}, i\nu_n, \alpha\beta\gamma\delta}$.

and its time evolution is given by $I_i(\mathbf{q}, t) = e^{iHt/\hbar} I_i(\mathbf{q}) e^{-iHt/\hbar}$, H being the unperturbed Hamiltonian. The coefficient $v_{i,\mathbf{k},\mathbf{q}}$ is known as *current vertex* and its explicit expression depends on the specific lattice (a is the lattice spacing). For a non interacting system, the Kubo formula [5.19] can be considerably simplified, as it can be written drawing a bubble Feynman diagram as shown in fig. [5.1], which finally yields an expression in terms of the Green function:

$$\chi_{ij}(\mathbf{q}, i\omega_n) = \frac{1}{N_{\text{sites}}} \sum_{\mathbf{k}} v_{i,\mathbf{k},\mathbf{q}} v_{j,\mathbf{k}+\mathbf{q},-\mathbf{q}} \, k_B T \sum_{i\nu_n} \text{Tr} \left[\hat{G}(\mathbf{k}, i\nu_n) \hat{G}(\mathbf{k}+\mathbf{q}, i\nu_n + i\omega_n) \right], \tag{5.21}$$

where $i\omega_n = 2\pi n k_B T$ is a bosonic Matsubara frequency, whereas $i\nu_n = (2n+1)\pi k_B T$ is a fermionic frequency. The real frequency version is simply obtained by analytic continuation $i\omega_n \to \hbar\omega + i0^+$ after performing all the internal sums. Remarkably, this expression is also exact for an interacting system in the limit of infinite dimensionality, because all the corrections to the bubble diagram involving the irreducible vertex function (which is momentum independent in this limit) vanish identically [27, 143].

In this formalism we can investigate the superfluid behavior of a system by studying the response to a divergenceless static magnetic vector potential, which in momentum space is perpendicular to its momentum: $\mathbf{q} \cdot \mathbf{A} = 0$ (for instance, if $\mathbf{q} = q\hat{\mathbf{e}}_y$, then the external field is along the x direction: $A(\mathbf{q}, 0)\hat{\mathbf{e}}_x$). For simplicity we can consider a field with a smooth spatial variation, i.e. characterized by a small momentum compared to the lattice cutoff: $qa \ll 1$. Thus we have to compute the response function $K_{xx}(q \to 0, \omega = 0)$ (where, importantly, the static limit has to be taken **before** we set $q \to 0$ [100]). If for example we find $K_{xx}(q \to 0, \omega = 0) = -D_s$ for a finite constant D_s, this is a clear hallmark of superfluidity, as this condition suggests that the current density is proportional to the vector potential itself: $j_x = -D_s A_x$, similarly to the London equation. If this is the case, the constant D_s is called *superfluid stiffness* and it is

defined as

$$\boxed{D_s = e^2 \left(\chi_{xx}(q_y \to 0, \omega = 0) - \frac{a^2}{\hbar^2} \langle E_x^{\text{kin}} \rangle \right)} \tag{5.22}$$

where implicitly we assume that all the other components of $\mathbf{q}$ are zero. Building a low energy lagrangian theory for the superconductor [144], it is possible to prove that D_s is proportional to the energy cost required to excite quantum and spatial fluctuations of the phase field, hence the name *stiffness*: it determines how "stiff" the coherent phase field in the ground state is with respect to fluctuations. Furthermore, it is related to the London penetration depth via $\lambda_L = \sqrt{1/(\mu_0 D_s)}$.

In the limit of infinite dimensionality $d \to \infty$, which is relevant for DMFT, we have to take a vanishing hopping $t \to 0$ such that $t\sqrt{2d} = \tilde{t}$ is finite ($2d$ is the lattice coordination for an hypercubic geometry). To make eq. [5.22] non-trivial in this case, we have to slightly change the definition multiplying by the dimension: $D_s \to D_s d$. Then we can write $\chi_{xx} d \approx \sum_{i=1}^{d} \chi_{ii}$ because the contribution parallel to the applied momentum becomes negligible compared to the sum of all the other $d-1$ components in the limit $d \to \infty$ and all the latter are equivalent by symmetry; and similarly $\langle E_x^{\text{kin}} \rangle d = \langle E^{\text{kin}} \rangle$. Both analytic and numeric summation over momenta are extremely unpractical when $d \to \infty$ (and they are also ill defined for a Bethe lattice), hence we should express eq. [5.22] in terms of an integral over the density of states $D(\varepsilon)$. This is straightforward for the diamagnetic term, since the momentum dependence comes through the dispersion relation $\varepsilon_{\mathbf{k}}$, hence using eq. [1.31]:

$$\langle E^{\text{kin}} \rangle = \frac{1}{N_{\text{sites}}} \sum_{\mathbf{k}} \varepsilon_{\mathbf{k}} k_B T \sum_{i\nu_n} \left[G(\varepsilon_{\mathbf{k}}, i\nu_n) - G^*(\varepsilon, i\nu_n) \right] = k_B T \int d\varepsilon \, \varepsilon D(\varepsilon) \sum_{i\nu_n} \left[G(\varepsilon, i\nu_n) - G^*(\varepsilon, i\nu_n) \right].$$

The paramagnetic term instead requires more work: we can multiply by the Dirac delta function $\delta(\varepsilon - \varepsilon_{\mathbf{k}})$ and integrate over the variable ε to get: $N_{\text{sites}}^{-1} \sum_{\mathbf{k},i} v_{i,\mathbf{k},0}^2 \delta(\varepsilon - \varepsilon_{\mathbf{k}}) = \frac{a^2}{\hbar^2} V(\varepsilon) D(\varepsilon)$, where the function $V(\varepsilon)$ can be determined by requiring that the optical conductivity satisfies the f-sum rule [145]. The latter condition leads to the simple differential equation

$$\frac{\partial}{\partial \varepsilon} [V(\varepsilon) D(\varepsilon)] = -\varepsilon D(\varepsilon) \qquad \to \qquad V(\varepsilon) = -\frac{1}{D(\varepsilon)} \int d\varepsilon \, \varepsilon D(\varepsilon). \tag{5.23}$$

The solution is $V(\varepsilon) = \frac{1}{3}(D^2 - \varepsilon^2)$ for the infinite-dimensional Bethe lattice [145, 146] and $V(\varepsilon) = \tilde{t}^2$ for the infinite-dimensional hypercubic lattice [143, 147] (whose density of states is given by a gaussian $D(\varepsilon) = \frac{1}{\tilde{t}\sqrt{2\pi}} \exp\left\{ -\frac{\varepsilon^2}{2\tilde{t}^2} \right\}$, where $\tilde{t} = t\sqrt{2d}$).

Putting it all together, we get

$$D_s = \frac{e^2 a^2}{\hbar^2} k_B T \sum_{i\nu_n} \int d\varepsilon D(\varepsilon) \left[V(\varepsilon) \operatorname{Tr}\left(\hat{G}(\varepsilon, i\nu_n)^2 \right) - 2\varepsilon G(\varepsilon, i\nu_n) \right]. \tag{5.24}$$

We can make further progresses by using the Nambu representation in eq. [5.15], which implies $\operatorname{Tr} \hat{G}^2 = G^2 + G^{*2} + 2|F|^2$ and integrating by parts the diamagnetic term, where we integrate the factor $-\varepsilon D(\varepsilon) = \partial_\varepsilon [V(\varepsilon) D(\varepsilon)]$ and differentiate $G(\varepsilon, i\nu_n)$; using $\partial_\varepsilon G = G^2 + G^{*2} - 2|F|^2$, which stems from the fact that the self-energy does not depend on ε, we finally get

$$\boxed{D_s = \frac{4e^2 a^2}{\hbar^2} k_B T \sum_{i\nu_n} \int d\varepsilon D(\varepsilon) V(\varepsilon) |F(\varepsilon, i\nu_n)|^2.} \tag{5.25}$$

We can clearly appreciate how the superfluid behavior appears only in presence of a non-trivial anomalous Green function.

Finally we can use eq. [5.25] to compute the superfluid stiffness in the context of the BCS mean-field theory. Setting $\Sigma(i\nu_n) = 0$ and $S(i\nu_n) = \Delta$, the summation over Matsubara frequencies becomes relatively simple:

$$k_B T \sum_{i\nu_n} |F(\varepsilon, i\nu_n)|^2 = k_B T \sum_{i\nu_n} \frac{1}{[(i\nu_n)^2 - \lambda^2(\varepsilon)]^2} = \frac{f'(\lambda(\varepsilon)) + f'(-\lambda(\varepsilon))}{4\lambda^2(\varepsilon)} + \frac{1 - 2f(\lambda(\varepsilon))}{4\lambda^3(\varepsilon)} \xrightarrow{T\to 0} \frac{1}{4\lambda^3(\varepsilon)}.$$

Here we have used the observation that the complex function $f(z)(z^2 - \lambda(\varepsilon)^2)^{-2}$ has two poles of second order in $z = \pm\lambda(\varepsilon)$ and we have evaluated the residues accordingly; furthermore we have used the zero temperature approximations $f(\lambda(\varepsilon)) \approx \Theta(-\lambda(\varepsilon)) = 1$ (Θ being the Heaviside step function) and $f'(\pm\lambda(\varepsilon)) \approx -\delta(\pm\lambda(\varepsilon)) = 0$ because $\lambda(\varepsilon)$ is always positive for any $\Delta \neq 0$. Writing the remaining energy integral in terms of dimensionless variables we arrive at

$$D_s = \frac{4}{3}\frac{e^2 a^2 D}{\hbar^2}\left(\frac{\Delta}{D}\right)^2 \int_0^1 dx \left[\frac{1 - x^2}{(\Delta/D)^2 + x^2}\right]^{3/2} \qquad \text{(BCS)}, \tag{5.26}$$

which can be evaluated analytically in terms of the elliptic functions introduced in sec. [2.4]:

$$D_s = \frac{4}{3}\frac{e^2 a^2 D}{\hbar^2}\frac{\Delta}{D}\left\{\left(1 + 2\frac{\Delta^2}{D^2}\right)\Xi\left[\frac{\pi}{2}, -\frac{D^2}{\Delta^2}\right] - 2\left(1 + \frac{\Delta^2}{D^2}\right)F\left[\frac{\pi}{2}, -\frac{D^2}{\Delta^2}\right]\right\}. \tag{5.27}$$

Once again it is interesting to look at the two limit situations: $U \gg D$ (or equivalently $\Delta \gg D$) and $U \ll D$ (or $\Delta \ll D$):

$$\boxed{D_s \approx \frac{4}{3}\frac{e^2 a^2 D}{\hbar^2}, \qquad U \ll D;} \qquad \boxed{D_s \approx \pi\left(\frac{ea}{\hbar}\right)^2 \frac{D^2}{2U}, \qquad U \gg D.} \tag{5.28}$$

We can make a few observations on this result. First of all, if $U \ll D$ the superfluid stiffness saturates to a constant value; however at $U = 0$ we find $D_s = 0$ because the anomalous Green function vanishes: this is not surprising, since the BCS theory has a singular behavior at $U = 0$. At larger values of U, the gap increases and the stiffness decreases monotonically, then in the strong coupling limit it is characterized by a hyperbolic tail $\propto D/U$. Consistently, the London penetration depth has a minimal value at very weak coupling, then it increases moving at strong coupling, indicating a progressively worse diamagnetic behavior. From another point of view, we can say that, at weak coupling, the phase is very coherent (or "stiff"), even in presence of large thermal fluctuations; whereas the gap is small and it closes at relatively low temperatures. In the strong coupling limit we have an opposite scenario: the gap is very large, but the stiffness is small, which means that thermal fluctuations can easily spoil the phase coherence, while the gap is only closed at much larger temperatures. The critical temperature for the superconductive phase is thus small both at weak and strong coupling, while it is maximized at intermediate values of U. At weak coupling, small thermal fluctuations close the gap, leaving a very coherent gas of weakly interacting particles that are not paired, this is a manifestation of the instability of the Fermi gas with respect to small attractive forces. At strong coupling, small thermal fluctuations are enough to destroy the phase coherence, leaving a gas of incoherent paired particles, while much higher temperatures are required to break the "molecular" pairs (see e.g. the phase diagram sketched in [148]). Remarkably, this is an effect of

the underlying lattice structure, while for a free gas the critical temperature is expected to saturate to a constant value at strong coupling [149, 150]. The superconductive phase is more robust against thermal fluctuations at intermediate couplings, where there is a compromise between a relatively large gap and a relatively large stiffness. This mechanism has been explored with DMFT at finite temperature in refs. [142, 151].

5.2 Two channel BCS theory with Josephson coupling

In this section we investigate the equilibrium properties of two s-wave superconductors described by the attractive Hubbard model, that are coupled by local pair hopping processes, where the particles are transferred in pairs from one superconductor to the other on the same lattice site (*Josephson coupling*). The system is described by the following Hamiltonian

$$H = -\sum_{a=1,2} t_a \sum_{\langle ij \rangle} \sum_{\sigma=\uparrow\downarrow} \left(c^\dagger_{ia\sigma} c_{ja\sigma} + \text{h.c.} \right) - \mu \sum_{a=1,2} \sum_i \sum_{\sigma=\uparrow\downarrow} n_{ia\sigma} - U \sum_{a=1,2} \sum_i n_{ai\uparrow} n_{ia\downarrow} \\ - J \sum_i \left(c^\dagger_{i1\uparrow} c^\dagger_{i1\downarrow} c_{i2\downarrow} c_{i2\uparrow} + \text{h.c.} \right), \tag{5.29}$$

where we assume $U > 0$ and $J > 0$. The two superconductors are characterized by the same intraorbital Hubbard attraction $U_a = U$, but the hopping amplitudes can be different in the two orbitals: in particular we assume $t_1 = t$ and $t_2 = \alpha t$, where conventionally $\alpha \in [0, 1]$. This is a specific realization of eq. [1.2], where $J_{\text{p.h.}} = -J$, $U_a = -U$, $t^{ab} = t_a \delta_{ab}$ and $U' = U'' = J_{\text{s.e.}} = 0$. We choose to work on the Bethe lattice, where we can exactly solve the model by means of DMFT; however the formalism outlined in the following can be easily generalized to other geometries. In this geometry, the non-interacting spectral functions associated to the two bands are semicircular shapes of the form [1.27] with different half-bandwidths $D_1 = D$ and $D_2 = \alpha D$ and they are centered around the same energy level. In other words, we are not accounting for a crystal field splitting between the two bands; however this might be an interesting point to address in future investigations, as we will discuss later. Finally, we work at global half filling, which is enforced by setting $\mu = 0$ to make eq. [5.29] particle-hole symmetric.

This model (or its generalized version) can be used to provide a basic description of different physical systems. The most natural application is the study of a material with two active bands around the Fermi level [152], where some microscopic mechanism (e.g. coupling with specific phonon modes) induces local intraband attraction and favors the interorbital pair hopping on top of other interaction processes. Secondly, we can use it to describe a particular Josephson junction, where two superconducting parallel 2d-layers are separated by a dielectric material, which in this description only enters as a potential barrier through which particles can hop in pairs (hence the name Josephson coupling). A caveat of this interpretation is that 2d materials have a non-interacting density of states characterized by Van Hove singularities, which are not well captured by the Bethe lattice, hence one should complement our analysis by using a more fitting lattice geometry. Finally, a suitable generalization of this model can describe a two-channel BCS-BEC crossover, that can be observed wth the orbital Feshbach resonance of alkaline-earth atoms, hence we devote sec. [5.3] to a more detailed discussion of this point.

5.2.1 Mean-field analysis

We begin by applying the Hartree-Fock method as for all the other investigations in this thesis. First of all we observe that, if $J = 0$, we are simply describing two perfectly decoupled BCS superconductors,

both described by the formalism of sec. [5.1], in particular by an orbital-wise order parameter $\phi_a = N_{\text{sites}}^{-1} \sum_{\mathbf{k}} \langle c_{ia\downarrow} c_{ia\uparrow} \rangle$. If $J > 0$, we can decouple the pair-hopping term in the two superconducting channels

$$\sum_i (c^\dagger_{i1\uparrow} c^\dagger_{i1\downarrow} c_{i2\downarrow} c_{i2\uparrow} + \text{h.c.}) \approx \left(\phi_1^* \sum_i c_{i2\downarrow} c_{i2\uparrow} + \phi_2 \sum_i c^\dagger_{i1\uparrow} c^\dagger_{i1\downarrow} - N_{\text{sites}} \phi_1^* \phi_2 \right) + \text{h.c.}, \tag{5.30}$$

which leads to the mean-field Hamiltonian (on a generic lattice)

$$H = \sum_{\mathbf{k},a=1,2} \Psi^\dagger_{\mathbf{k}a} \begin{pmatrix} \varepsilon_{\mathbf{k}a} - \mu & -\Delta_a \\ -\Delta_a^* & -(\varepsilon_{-\mathbf{k}a} - \mu) \end{pmatrix} \Psi_{\mathbf{k}a} + N_{\text{sites}} \left(U|\phi_1|^2 + U|\phi_2|^2 + J\phi_1^*\phi_2 + J\phi_2^*\phi_1 \right), \tag{5.31}$$

where $\Delta_1 = U\phi_1 + J\phi_2$ and $\Delta_2 = U\phi_2 + J\phi_1$. Following the lines of sec. [5.1], after defining $\lambda_{\mathbf{k}a} = \sqrt{(\varepsilon_{\mathbf{k}a} - \mu)^2 + |\Delta_a|^2}$, we can write an explicit expression for the grand-canonical potential:

$$\begin{aligned} \Omega = \sum_{\mathbf{k}a} \lambda_{\mathbf{k}a} f(\lambda_{\mathbf{k}a}) - \sum_{\mathbf{k}a} \lambda_{\mathbf{k}a} + N_{\text{sites}} \left(U|\phi_1|^2 + U|\phi_2|^2 + J\phi_1^*\phi_2 + J\phi_2^*\phi_1 \right) \\ -T \sum_{\mathbf{k}a} \left[f(\lambda_{\mathbf{k}a}) \log f(\lambda_{\mathbf{k}a}) + (1 - f(\lambda_{\mathbf{k}a})) \log (1 - f(\lambda_{\mathbf{k}a})) \right]. \end{aligned} \tag{5.32}$$

and derive the self consistency equations by solving $\frac{\partial \Omega}{\partial \phi_a^*} = 0$ for $a = 1, 2$. Rearranging the two equations we get the explicit form:

$$\boxed{\phi_a = \frac{\Delta_a}{2} \int d\varepsilon D_a(\varepsilon) \frac{\tanh\left(\frac{1}{2T} \sqrt{\varepsilon^2 + \Delta_a^2} \right)}{\sqrt{\varepsilon^2 + \Delta_a^2}}}, \qquad a = 1, 2, \tag{5.33}$$

which is very useful to implement the self-consistent procedure: we start by an educated guess on $\phi_{1,2}$, compute the gap parameters $\Delta_{1,2}$ and use eq. [5.33] to update $\phi_{1,2}$, then we repeat until convergence.

The converged order parameters are shown in fig. [5.2] as a function of U, J and α. First of all, we observe that both ϕ_1 and ϕ_2 are in principle complex variables with a modulus and a phase: $\phi_a = |\phi_a| e^{i\varphi_a}$; however the grand canonical potential only depends on the relative phase between the two $\varphi_2 - \varphi_1$. We thus expect a manifold of ground states, where the degenerate states are labeled by φ_1 and connected to each other by a transformation of the U(1) symmetry group generated by φ_1. Therefore we can arbitrarily set $\varphi_1 = 0$, i.e. require ϕ_1 to be real, and leave only φ_2 as a free variational parameters to be determined via the optimization process. We find that, for all the relevant regimes of parameters, $\varphi_2 = 0$, i.e. ϕ_2 is real and positive just like ϕ_1 and the two superfluids associated to the two bands (or layers) are coherent. The relative phase depends on the sign of J and we can easily guess that, if $J < 0$ (not considered here), we would get a similar solution for $|\phi_a|$ with a phase difference $\varphi_2 - \varphi_1 = \pi$, because the phase factor $e^{i(\varphi_2 - \varphi_1)} = -1$ would compensate the negative sign of J in the expression [5.32] for the grand canonical potential. Secondly, we observe that the order parameter ϕ is enhanced by the presence of a pair hopping for all the values of U, but the effect is particularly visible at weak coupling; in particular, in the limit $U \to 0$ there is a finite order parameter when $J > 0$. We can motivate this observation by a simple analytical argument: if we set $\phi_1 = \phi_2 \equiv \phi$ (which holds by symmetry if $\alpha = 1$, since we have seen that the two phase factors are the same), then $\Delta_1 = \Delta_2 = (U + J)\phi$ and eq. [5.33] reduces to the single channel equation [5.11] upon the substitution $U \to U + J$. The two superfluids are then effectively decoupled, except for the phase coherence, and they are both described by BCS theory with a renormalized interaction

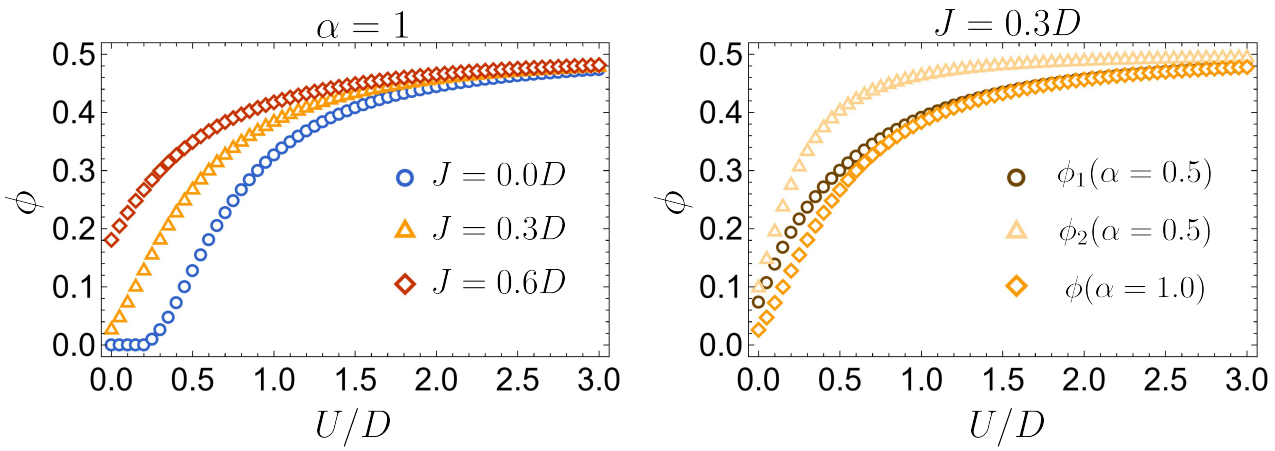

Figure 5.2: Superfluid order parameters as a function of the Hubbard-U obtained by the self-consistent Hartree-Fock method solving eq. [5.33]. The left panel shows the case with symmetric bands ($\alpha = 1$) for several values of the pair hopping. The right panel shows the result for an asymmetric case at a fixed J compared to the symmetric case.

$U + J$, which explains why ϕ is finite at $U = 0$, $J > 0$. More precisely, we have $\phi \approx 1/2$ for $U \gg D$ or $J \gg D$; while – by virtue of eq. [5.12] – we have $\phi \approx \frac{4D}{U+J} \exp\left[-\frac{\pi}{2(U+J)} - 1\right]$ for $U, J \ll D$. Finally, when we include a different bandwidth ($\alpha \neq 1$), we observe that both ϕ_1 and ϕ_2 are enhanced with respect to their original value in the symmetric case $\alpha = 1$. The effect is more pronounced for ϕ_2, which is the superfluid order parameter for the orbital with "heavier" particles (i.e. with a narrower band). We can understand this result intuitively: if $J = 0$, the superfluid with smaller hopping ($a = 2$) has a larger order parameter, because $U/D_2 > U/D_1$. Then for a finite J the other superfluid ($a = 1$) is coupled to an effective reservoir of pairs with an amplitude $\Delta_1 = U\phi_1 + J\phi_2$ proportional to ϕ_2; since now ϕ_2 is larger than in the symmetric case, the coupling is enhanced as well.

Computing the superfluid stiffness for a multiorbital system requires some attention, as in general it is not simply given by the sum of orbital-resolved contributions. The correct approach is illustrated in [28], where the "naive" method leads to a counter-intuitive and in fact wrong result for the excitonic condensate investigated by the authors. In general, not only the diamagnetic term is given by the expectation value of the total kinetic energy (including interorbital hybridization terms), but also the paramagnetic term is given by the response function of the total paramagnetic current $I_{\text{tot}}(\mathbf{q}, 0) = \sum_a I_a(\mathbf{q}, 0)$. The latter is given by $\chi_{ij} = \sum_{ab} \chi_{ij}^{ab}$, where χ_{ij}^{ab} is the response function associated to the two orbital current operators I_{ia} and I_{jb} and is proportional to the off-diagonal component of the Green function in the orbital indexes:

$$\chi_{ij}^{ab}(\mathbf{q}, i\omega_n) = a^{2d} N_{\text{sites}} \sum_{\mathbf{k}} v_{i,\mathbf{k},\mathbf{q}}^{a} v_{j,\mathbf{k}+\mathbf{q},-\mathbf{q}}^{b} \, k_B T \sum_{i\nu_n} \text{Tr}\left[\hat{G}_{ab}(\mathbf{k}, i\nu_n)\hat{G}_{ba}(\mathbf{k}+\mathbf{q}, i\nu_n + i\omega_n)\right]. \tag{5.34}$$

In our case however, there are no interorbital components of the kinetic energy, hence it is given by the sum of the orbital-wise kinetic energies $\langle E^{\text{kin}} \rangle = \sum_a \langle E_a^{\text{kin}} \rangle$; moreover the Green function is diagonal in the orbital indexes, so the paramagnetic term is given by a sum of orbital-wise contributions as well: $\chi_{ij} = \sum_a \chi_{ij}^{aa}$. We conclude that, in our specific case, we can compute the stiffness as the sum of the orbital stiffnesses $D_s = \sum_a D_s^a$. The latter can be computed by replacing Δ with Δ_a in eq. [5.27], which leads to the intuitive result that D_s saturates to a constant when $U, J \ll D$ and decreases hyperbolically with U and

J in the opposite limit, where either $U \gg D$ or $J \gg D$. The low stiffness at strong coupling suggests once again that the superfluid order is broken by small thermal fluctuations that destroy the phase coherence, while leaving the particles paired. However, as we will discuss in the next section, the strong coupling picture provided by the Hartree-Fock method is completely changed by introducing dynamical effects.

5.2.2 Including dynamical correlations with DMFT

In order to investigate the effect of dynamical quantum correlations (or fluctuations) induced by strong interactions, we have solved this model on the Bethe lattice with infinite coordination by means of DMFT; and in this section we outline some technical details and the main results concerning the ground state properties.

We begin by defining the impurity problem, which again takes the general form of eq. [1.14], where we define the spinor $\Psi_\ell^\dagger = (c_{\ell 1\uparrow}^\dagger,\, c_{\ell 1\downarrow},\, c_{\ell 2\uparrow}^\dagger,\, c_{\ell 2\downarrow})$. However, we assume that there are two independent baths, one per every orbital, i.e. that the 4×4 matrices $\hat{\varepsilon}_\ell$ and $\hat{V}_\ell$ are block diagonal in the orbital indexes. We can recast the Anderson impurity model as

$$H_{\text{AIM}} = \sum_{\ell=1}^{N_{\text{bath}}} \sum_{a=1,2} \Psi_{\ell a}^\dagger \hat{\varepsilon}_{\ell a} \Psi_{\ell a} + \sum_{\ell=1}^{N_{\text{bath}}} \sum_{a=1,2} \left(\Psi_{\ell a}^\dagger \hat{V}_{\ell a} \Psi_{0a} + \text{h.c.} \right) + \Psi_{0a}^\dagger \hat{\varepsilon}_{0a} \Psi_{0a} + H_{\text{imt}}, \tag{5.35}$$

where $\Psi_{\ell a}^\dagger = (c_{\ell a\uparrow}^\dagger,\, c_{\ell a\downarrow})$, H_{int} is the interaction part of eq. [5.29] and

$$\hat{\varepsilon}_{0a} = \begin{pmatrix} \varepsilon_{0a} - \mu & 0 \\ 0 & -(\varepsilon_{0a} - \mu) \end{pmatrix}; \qquad \hat{\varepsilon}_{\ell a} = \begin{pmatrix} \varepsilon_{\ell a} & -\Delta_{\ell a} \\ -\Delta_{\ell a} & -\varepsilon_{\ell a} \end{pmatrix}; \qquad \hat{V}_{\ell a} = \begin{pmatrix} V_{\ell a} & 0 \\ 0 & -V_{\ell a} \end{pmatrix}. \tag{5.36}$$

Here we also set $\varepsilon_{0a} = 0$ and $\mu = 0$, however the general matrices written above allow to include a crystal field splitting and/or to work out of half filling. This generalized Anderson impurity model commutes with the total orbital-wise spin-z operators $S_a^z = \sum_\ell c_{\ell a\sigma}^\dagger \hat{\sigma}_{\sigma\rho}^z c_{\ell a\rho} = N_{a\uparrow} - N_{a\downarrow}$, where $N_{a\sigma}$ denotes the total number of particles on orbital a with spin σ; hence S_a^z is a conserved quantity. This can be understood intuitively, because the particles on a given orbital are always created or destroyed in pairs with vanishing spin-z, either by exchange with an effective reservoir, or by pair hopping processes. We can exploit this symmetry to simplify the exact diagonalization, performing a sectorization based on two quantum numbers S_1^z and S_2^z.

The other important simplification is that, as we have anticipated, all the many body functions are diagonal in the orbital indexes, a circumstance which reduces the number of independent components to evaluate from 6 to 4 (two normal components $G_{aa}(i\omega_n)$ and two anomalous components $F_{aa}(i\omega_n)$, with $a = 1, 2$). In particular, this reduces the number of Lanczos runs necessary to evaluate the full impurity Green function, which is typically the bottleneck of our algorithm in terms of computational cost. Furthermore, if $\alpha = 1$ we can also exploit the orbital symmetry, i.e. symmetry upon relabeling $a = 1 \leftrightarrow a = 2$, computing the Green function for only one of the orbitals (say, $a = 1$) and simply assuming $\hat{G}_{22}(i\omega_n) = \hat{G}_{11}(i\omega_n)$, limiting the number of independent components to 2. Accordingly, the self-consistency equation can be implemented orbital-wise as

$$\hat{\mathcal{G}}_{aa}^{-1}(i\omega_n) = \hat{G}_{\text{loc},aa}^{-1}(i\omega_n) + \hat{\Sigma}_{aa}(i\omega_n) \qquad (a = 1, 2), \tag{5.37}$$

where $\hat{G}_{\text{loc},aa}(i\omega_n) = \int d\varepsilon D(\varepsilon)[i\omega_n - (\varepsilon - \mu)\hat{\sigma}^z - \hat{\Sigma}_{aa}(i\omega_n)]^{-1}$ and again, if $\alpha = 1$, we can use the orbital symmetry to limit the self-consistent procedure to only one representative orbital.

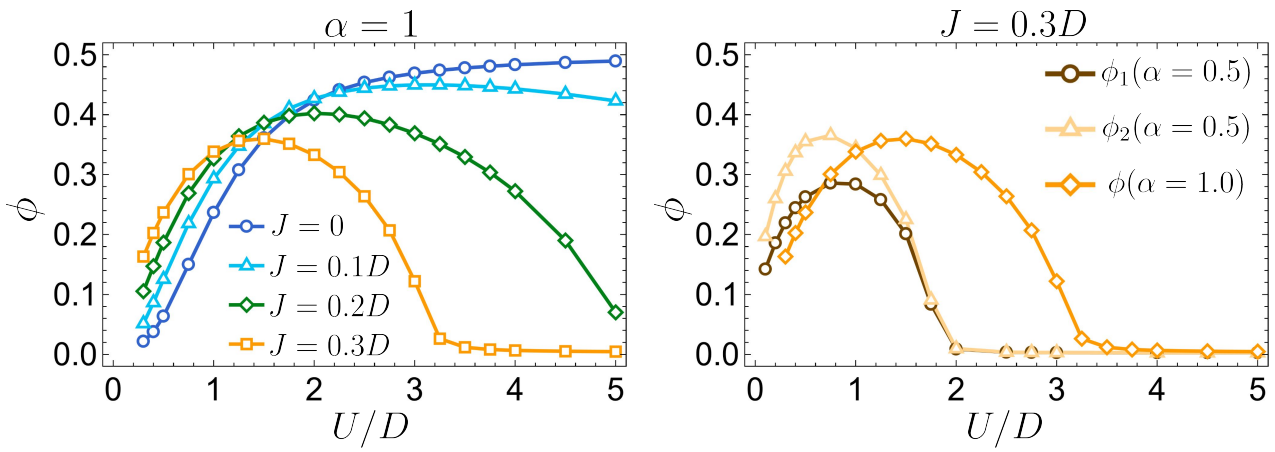

Figure 5.3: Superfluid order parameters as a function of the Hubbard-U obtained solving the DMFT self-consistent procedure. At weak coupling, the scenario is similar to the mean-field result; while at strong coupling we appreciate an increasing fragility of the superconductive order when J increases or α decreases. (Left) Case with symmetric bands ($\alpha = 1$) for several values of the pair hopping. For any finite J, the order parameter has a maximum value at a specific U_{max}, it decreases at larger U and eventually vanishes at a critical point U_c. (Right) Result for asymmetric bandwidths at a fixed J compared to the symmetric case. The superfluid order is even more fragile in this situation, since both ϕ_1 and ϕ_2 vanish at a smaller U_c with respect to the symmetric case.

We begin our discussion by commenting on the order parameter, which is shown in fig. [5.3]. Consistently with the Hartree-Fock result, we observe that ϕ_1 and ϕ_2 have the same phase factor in the regime of parameters studied here. Moreover, the weak coupling behavior for $U, J \ll D$ is perfectly consistent with the mean-field picture: the presence of a pair hopping enhances the order parameters with respect to the case of perfect orbital decoupling. Furthermore, when we include an hopping imbalance $\alpha < 1$, both ϕ_1 and ϕ_2 increase with respect to the corresponding value in the orbital-symmetric case, and the effect is more pronounced for ϕ_2, which is connected to the less mobile particles. However, at intermediate and strong couplings, the scenario is totally different with respect to the mean-field picture. In the presence of a pair hopping, no matter how small, the order parameter is no longer a monotonically increasing function of U; instead it features a maximum value at $U = U_{\text{max}}$ and then it decreases for larger values of U. Even more surprisingly, the order parameter eventually vanishes for sufficiently large values of the Hubbard interaction that exceed a critical value U_c. The situation is qualitatively similar also in presence of a hopping imbalance, where both order parameters feature a maximum value and eventually vanish together at a critical value of U. If $\alpha < 1$, the effect is even more pronounced, as both U_{max} and U_c are pushed to smaller values when α decreases and the mobility on one of the bands is gradually quenched. Rather intuitively, $\phi_2 > \phi_1$ as long as they are finite, indicating that the "heavier" particles are slightly more superfluid than the "lighter" ones. The critical value $U_c(J, \alpha)$, as well as the location of the maximum $U_{\text{max}}(J, \alpha)$ are functions of J and α: this can be visualized more explicitly from the phase diagram drawn in fig. [5.4]. The diagram clearly suggests that the system undergoes a quantum phase transition from a superconducting phase, which only survives for $U, J \ll D$ and $\alpha \gg 0$, to a non-superconducting phase that we shall further characterize below. The vanishing of the order parameters is a direct consequence of the fact that, for $U > U_c$, the anomalous Green function converges to zero: $F_a(\mathbf{k}, i\omega_n) \approx 0$, which in turn implies that also the superfluid stiffness vanishes by virtue of eq. [5.25], enforcing the idea that the

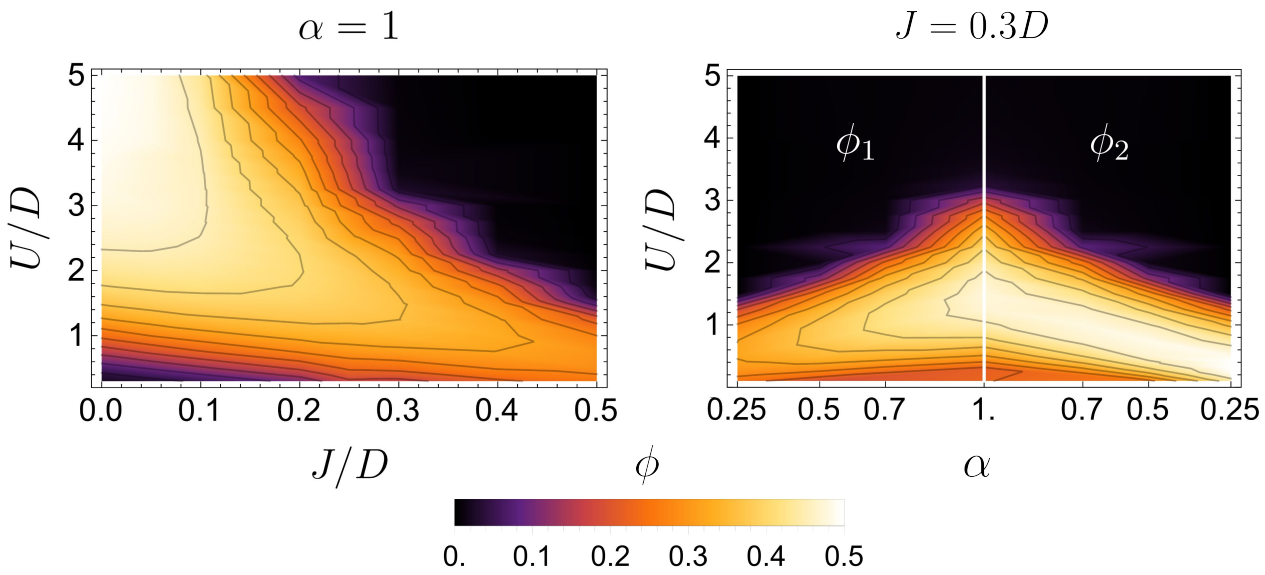

Figure 5.4: Phase diagram of the ground state of Hamiltonian [5.29] drawn with a color plot of the order parameter obtained with DMFT. We appreciate the superconductive phase (brighter) and the insulating phase of interband "resonant" pairs described in the text (darker). (Left) Phase diagram as a function of U and J for the case of symmetric bands. (Right) Phase diagram as a function of U and α at fixed J. We show two color plots, based on ϕ_1 and ϕ_2 respectively, represented in a symmetric diagram with respect to the variable α. Even though ϕ_1 and ϕ_2 are characterized by different level curves, they always vanish "simultaneously", as we can see from the mirror-symmetry of the dark region.

ground state does not break the symmetry generated by N.

The large-U phase can be investigated by comparing our solution to the *normal state*, i.e. the solution of the DMFT self-consistency equation obtained when the superconducting order is explicitly frustrated by setting $\Delta_\ell = 0$ in the impurity problem. In this case, the number of particles within one of the orbitals is still not a good quantum number, as the pair-hopping processes can transfer pairs from one orbital to the other. However, the total number of spin-up particles $N_\uparrow$ and the total number of spin-down particles $N_\downarrow$ are now conserved quantities, because the system no longer exchanges particles with an effective reservoir, hence we can base our sectorization process on these two quantum numbers. We begin by looking at the local density-density correlation functions. We can define an intraorbital component $\langle n_a^2 \rangle - \langle n_a \rangle^2$, which coincides with the orbital-resolved fraction of doubly occupied sites[5], and an interorbital component $\langle n_1 n_2 \rangle - \langle n_1 \rangle \langle n_2 \rangle$, where $n_a = N_{\text{sites}}^{-1} \sum_{i\sigma} n_{i\sigma}$ is the local density operator associated to orbital a. As we have discussed in sec. [1.3.5], we can evaluate the correlation functions directly from the impurity problem via exact diagonalization, where $n_{a\sigma}$ is the number operator associated to the impurity site, which – at convergence – is a representative of any arbitrary lattice site. The results are shown in fig. [5.5] both for the normal state and for the more general solution with a superconducting bath. We can further characterize the phase diagram by looking at the dynamical structure of the self-energy, which is shown in fig. [5.6]. Here we mostly focus on the symmetric case $\alpha = 1$, but the analysis is general.

If $J = 0$, the normal state is characterized by a Mott transition from a correlated metallic state at $U \ll D$ to the attractive-U version of a Mott insulator at $U \gg D$, i.e. a correlated electronic state where single

[5]One can prove this by writing $n_a = n_{a\uparrow} + n_{a\downarrow}$, which implies $\langle n_a^2 \rangle - \langle n_a \rangle^2 = \langle n_{a\uparrow} n_{a\downarrow} \rangle$.

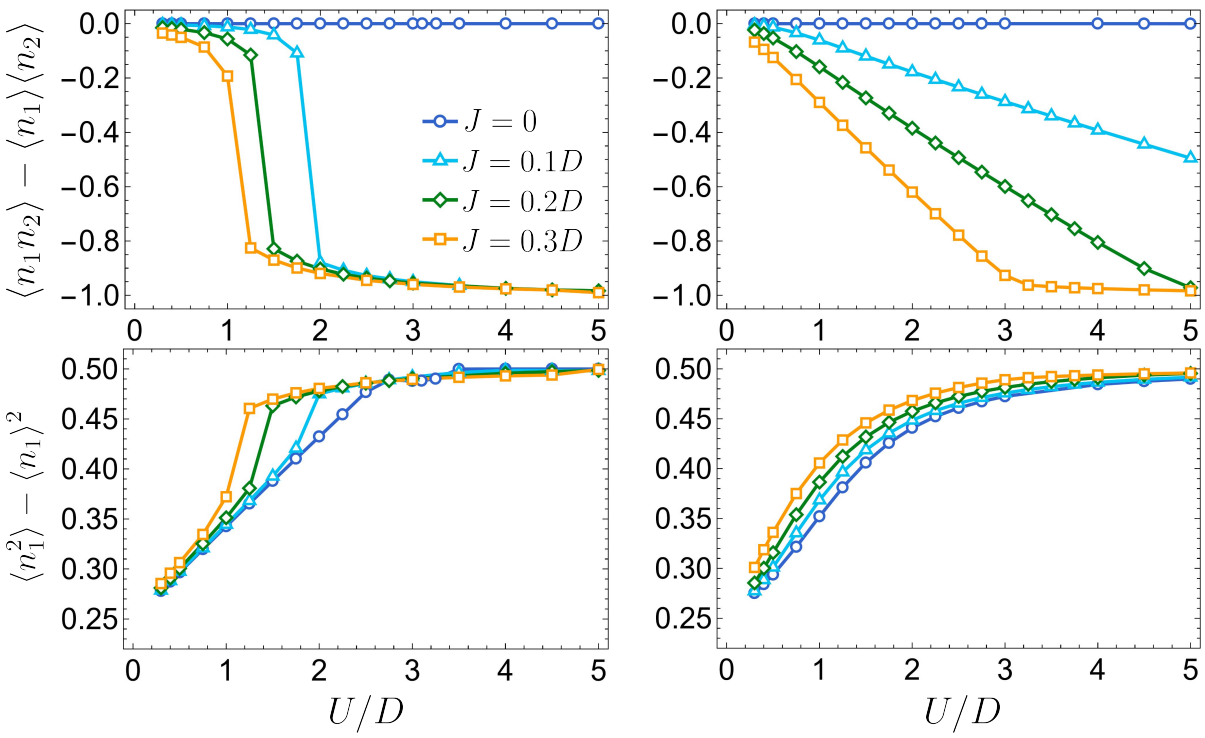

Figure 5.5: Local correlation functions computed from the converged impurity problem. The top row shows interorbital correlations, while the bottom row intraorbital correlations (or orbital-resolved double occupancies). The left column shows results for the normal state, obtained enforcing $\Delta_\ell = 0$ in the bath; while the right column shows the full solution, where superconductivity is allowed. For any $J > 0$, at sufficiently large U the former and the latter coincide.

occupations are quenched in favor of double occupancies and empty sites. Accordingly, the quasiparticle weight is finite in the metallic state and vanishes in the insulator, indicating a singularity of the self-energy at $i\omega_n \to 0$. If a superconducting order is taken into account, the system is superconductive at every U, the anomalous component of the self-energy is approximately a finite constant and the normal component is nearly vanishing, consistently with BCS theory, and this reflects on the quasiparticle weight, which is roughly $z \approx 1$ for every U. The fraction of double occupations increases with U and eventually saturates to $1/2$, describing the BCS-BEC crossover of the state [5.9]: at small U the state is a small perturbation on top of the Fermi sea, where Fock states with any number of particles acquire a small weight (the fractions of double occupancies, empty sites, singly occupied with spin up or spin down coincide); at large U the state becomes a balanced superposition of all the possible Fock states with any number of pairs and empty sites (but single occupancies are quenched).

When $J > 0$, the normal state once again features a quantum phase transition from a correlated metal to a correlated insulator characterized by the suppression of single occupancies; however the insulating phase is now characterized by a large (and negative) interorbital density-density correlation. We can expect that, for large U, the ground state is adiabatically connected to the atomic limit solution $|\psi_{D=0}\rangle$:

$$|\psi_{D=0}\rangle = \bigotimes_{i=1}^{N_{\text{sites}}} \frac{1}{\sqrt{2}} \left(c^\dagger_{i1\uparrow} c^\dagger_{i1\downarrow} + c^\dagger_{i2\uparrow} c^\dagger_{i2\downarrow} \right) |0\rangle = \bigotimes_{i=1}^{N_{\text{sites}}} \frac{1}{\sqrt{2}} \left(|\underbrace{\uparrow\downarrow}_{a=1}, \underbrace{0}_{a=2}\rangle + |\underbrace{0}_{a=1}, \underbrace{\uparrow\downarrow}_{a=2}\rangle \right), \tag{5.38}$$

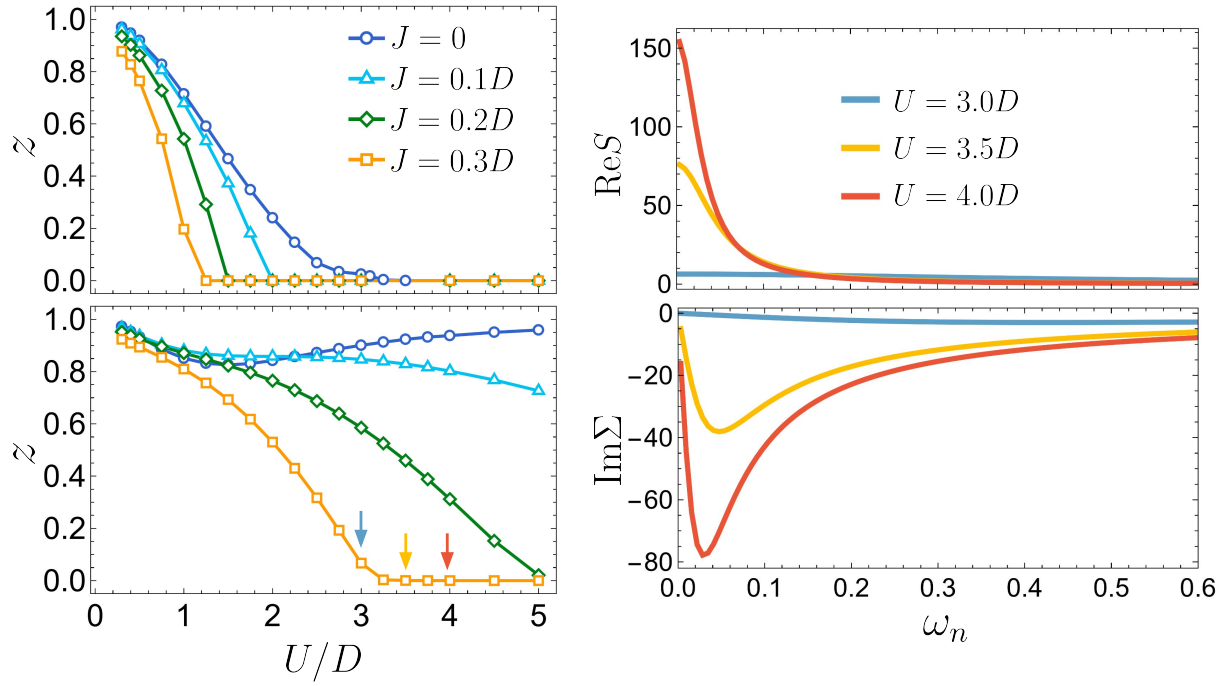

Figure 5.6: (Left) Quasiparticle weight for the normal state with enforced $\Delta_\ell = 0$ (top) and for the full solution with allowed superconductivity (bottom). (Right) Dynamical structure of the relevant components of the self-energy for a specific subset of parameters across the quantum phase transition (taken from the unconstrained solution). As U increases, both the normal and the anomalous components acquire a progressively enhanced dynamical structure at small Matsubara frequencies, indicating a strongly correlated insulator.

where $|0\rangle$ is the vacuum state. This is a state where every lattice site contains an "orbital-resonating" pair, a pair of particles which are fully delocalized between the two orbitals, being in the symmetric quantum superposition of the two possible states. Configurations with paired fermions are favored by the pair hopping, hence increasing J, the critical value of U progressively decreases and the metallic state is less resilient to the interaction. Looking at the phase transition that occurs when the symmetry is not enforced, we observe that the superconducting phase is characterized by progressively larger interorbital density-density correlations as U increases and eventually, at the critical point (and beyond), the correlation is ≈ -1. Furthermore, the quasiparticle weight progressively reduces and eventually vanishes after the critical point. This suggests that the large-U phase is the same insulator that we find enforcing the symmetry constraint, i.e. a strongly-correlated insulator with large interorbital density fluctuations due to the orbital-resonating pairs. Remarkably, the superconducting phase survives to larger values of U with respect to the symmetric metallic phase, hence we never observe a transition from a superconductor to a metal in the ground state.

The solution outlined above is spatially uniform, but this is a direct consequence of how we carried out the calculation, as we have explicitly excluded possible bipartite orders such as charge-density wave (CDW). A thorough study of spatially non-uniform solutions is a purpose for further work on the subject; however we can make a few observations here. Starting from the insulating phase at large U, we can treat the kinetic term of the Hamiltonian as a small perturbation on top of the atomic-limit ground state. We expect that the

Fock states which allow nearest-neighbor hopping will gain a larger weight over the others in the ground state. For example, if i and j are two nearest neighbors in the sublattices A and B respectively, we expect that a Fock state like $|\uparrow\downarrow, 0\rangle_i \otimes |0, \uparrow\downarrow\rangle_j$ would have larger weight with respect to $|\uparrow\downarrow, 0\rangle_i \otimes |\uparrow\downarrow, 0\rangle_j$, because the former is compatible with nearest-neighbor hopping processes, while the latter is not. This suggests the presence of an instability towards the formation of a charge-density-wave (CDW) where the average density is staggered on the two sublattices and translational symmetry is broken.[6] In particular, the two staggered densities in the two orbitals will have an opposite phase, where a lattice site featuring enhanced density for orbital $a = 1$ will have at the same time a depleted density for orbital $a = 2$ and vice versa. Guessing the fate of the superconducting phase on a bipartite lattice is much less trivial. As a matter of fact, the ground state of the attractive Hubbard model at half-filling on bipartite lattices features a degeneracy between a superconducting state and a charge-density-wave state; but this degeneracy is broken moving out of half-filling, and the superconducting order is energetically favored over the CDW. Our educated guess, based on the considerations about relative weights of different Fock states, is that at half filling the CDW would be favored by the pair hopping, while for a sufficiently doped system, superconductivity could be stabilized. A rigorous proof of this guess is left for future investigation.

We conclude the section discussing a technical subtlety that can be rather puzzling at a first glance. Looking at fig. [5.6], we can see an unexpected behavior of the self-energy across the superconductor-insulator phase transition. In particular, we observe that the normal component in the insulator becomes Fermi-liquid like, albeit with a significant dynamical structure that makes the quasiparticle weight very small, and it does not match the solution obtained in the normal state, where it diverges like $\Sigma(i\omega_n) \approx 1/i\omega_n$. At the same time, the anomalous part of the self energy survives in the insulator and it becomes frequency-dependent, with a significant low-frequency peak. Again, this is not what one would expect from a solution with conserved number of particles, where the anomalous component should vanish at every frequency. Nevertheless, it turns out that the local Green functions obtained with constrained and unconstrained symmetry coincide at $U > U_c$, hence all the relevant observables coincide as well. This puzzling behavior of the self-energy can be understood by looking at the converged Weiss field, which features a non-vanishing anomalous component $\mathcal{G}_{12}^{-1}(i\omega_n) \neq 0$, therefore the presence of an anomalous self-energy balances this effect and eventually provides a vanishing anomalous Green function. The point is that, at given J, we are starting the DMFT loop for a certain U by using the converged solution from the previous smaller value of U as an initial guess; but because DMFT is affected by the initial guess on the bath, the Weiss field typically does not change much. When we cross U_c, DMFT stabilizes an insulating symmetric phase by keeping a non vanishing anomalous Weiss field, which is similar to the initial guess and already leads to a gapped spectrum, but compensating with a diverging anomalous self-energy to eventually provide a non superconducting phase. We conclude that the specific frequency dependence of the self-energy can depend on the bath parameters used as an initial guess; however one of the components diverges at $i\omega_n \to 0$, always leading to the same local Green function and hence describing the same phase.

5.3 Pair hopping with the orbital Feshbach resonance

A Feshbach resonance is a physical phenomenon where the low energy scattering properties (for instance the s-wave scattering length) of two-body collisions are modified by strong atomic interactions, which determine a quantum superposition of the initial scattering state with a bound state. The modified value of

[6] This mechanism is equivalent to the stabilization of antiferromagnetism over the paramagnetic state in the repulsive model.

the scattering length can be controlled via an externally applied magnetic field, which makes the Feshbach resonance a tool to experimentally control the effective two-body interaction. Originally it has been studied for fermionic alkali atoms, and it has been used to investigate both theoretically [153, 154, 155] and experimentally [156] a single-channel BCS-BEC crossover [157, 158]. In this context, it is usually named *magnetic* Feshbach resonance, as it takes advantage of the strong hyperfine coupling between electronic and nuclear angular momentum in alkali atoms. More recently, it has been shown that a tunable Feshbach resonance also exists for alkaline-earth-like atoms, despite the (nearly) perfect decoupling between electronic and nuclear degrees of freedom. In this case it takes the name of *orbital* Feshbach resonance, because – as we discuss below – it is a direct consequence of the interorbital spin exchange coupling.

Let's consider, for concreteness, a gas of alkaline-earth-like atoms (for instance ^{173}Yb) prepared in a balanced mixture of $|e\uparrow\rangle$ and $|g\downarrow\rangle$ particles. The relevant scattering channel between two particles is a state with a spatially symmetric wave function and an anti-symmetric spin-orbital component, as the particles are more likely to be very close to each other and hence to collide. As a consequence of the Pauli exclusion principle, this prevents collisions of two atoms that are both in the same single-particle state, and the only scattering channel is $|o\rangle = (|e\uparrow, g\downarrow\rangle - |g\downarrow, e\uparrow\rangle)/\sqrt{2}$: this is called *open channel*[7].

Let's now focus on another two-body state: $|c\rangle = (|e\downarrow, g\uparrow\rangle - |g\uparrow, e\downarrow\rangle)/\sqrt{2}$. If the particles were perfectly non interacting (and in absence of an external magnetic field), this state would be degenerate to $|o\rangle$, but it would be inaccessible, because we have prepared the gas with no $|g\uparrow\rangle$ or $|e\downarrow\rangle$ particles, hence we call it *closed channel*. An external static magnetic field B has the effect of lifting the degeneracy between $|o\rangle$ and $|c\rangle$, pushing the latter to higher energies. This might sound surprising at first, because naively we could expect to observe the same Zeeman splitting between the single particle states $|g\uparrow\rangle$, $|g\downarrow\rangle$ and $|e\uparrow\rangle$, $|e\downarrow\rangle$, which would shift the energies of $|c\rangle$ and $|o\rangle$ by the same amount, preserving their degeneracy. However, as a consequence of the small hyperfine coupling of the $|e\rangle$ electronic state, there is a difference in the nuclear Landé g-factor for atoms in the electronic $|e\rangle = {}^3P_0$ or $|g\rangle = {}^1S_0$ states: $g_e \neq g_g$. Therefore, the Zeeman splitting between $|g\uparrow\rangle$, $|g\downarrow\rangle$ is given by $\Delta E_g = \mu_B g_g B \Delta m$, where μ_B is the Bohr magneton and Δm is the difference of nuclear angular momentum between the nuclear states labeled by $\uparrow$ and $\downarrow$; while the splitting between $|e\uparrow\rangle$, $|e\downarrow\rangle$ is $\Delta E_e = \mu_B g_e B \Delta m$. The resulting energy splitting between the open and the closed channel is $\Delta E = \mu_B (g_e - g_g) B \Delta m \neq 0$ and in particular it is experimentally tunable via the intensity of the magnetic field. This is illustrated in fig. [5.7 (a)].

We now consider the effect of interactions and, for the sake of clarity, we introduce the interaction processes one by one. To begin with, particles in the open channel experience a two-body potential $V_o(\mathbf{r})$ (where $\mathbf{r}$ is the relative coordinate) that we can realistically depict as a Van der Waals potential, weakly attractive at long distances, and strongly repulsive at short distances. Similarly, when two particles are in the closed channel, they experience a two-body potential $V_c(\mathbf{r})$ which can once again be regarded as a Van der Waals potential. Crucially, we assume that the potential $V_c(\mathbf{r})$ features a bound state at an energy $-\varepsilon_b$ measured with respect to the continuum threshold of the closed channel, i.e. to ΔE, considering the Zeeman splitting and setting the zero of energy at $V_c(\mathbf{r} \to \infty) = V_o(\mathbf{r} \to \infty) = 0$. We illustrate these potentials in fig. [5.7 (c)]. It is now clear that, when $\Delta E \approx \varepsilon_b$, the bound state of the closed channel becomes perfectly degenerate to the continuum threshold of the open channel, while if $\Delta E < \varepsilon_b$ it is energetically favored; still, if $|o\rangle$ and $|c\rangle$ are perfectly decoupled, this bound state is unavailable for two particles colliding in the open channel.

The key feature to realize a Feshbach resonance is an interaction that couples the open and the closed

[7] In the following we do not write the spatial component explicitly: it is always intended to be the spatially symmetric function $\psi(\mathbf{r}_1 - \mathbf{r}_2)$, where 1 and 2 label the particles.

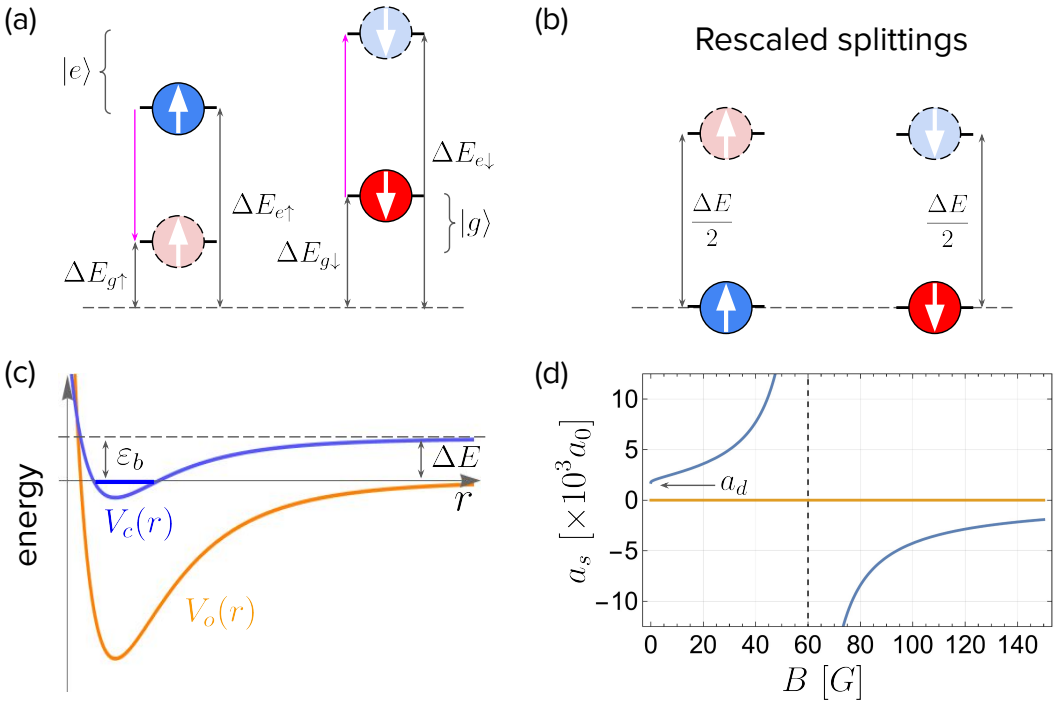

Figure 5.7: (a) Zeeman splittings $\Delta E_{a\sigma} = \mu_B g_a m_\sigma B$ of the four atomic states. Intensely colored circles with solid edge are the states forming the open channel; while faintly colored circles with dashed edge are states of the closed channel. The purple arrows represent a transition from $|o\rangle$ to $|c\rangle$, which causes an energy decrease $-(\Delta E_{e\uparrow} - \Delta E_{g\uparrow})$ and an energy increase $\Delta E_{e\downarrow} - \Delta E_{g\downarrow}$, resulting in an overall energy increase of $\Delta E = \Delta E_e - \Delta E_g$. (b) Rescaled level spacing after adding the constant term in eq. [5.47] to the Hamiltonian. (c) Two-body interaction potentials for the open and closed channels. The latter also contains the Zeeman splitting term and it features a bound state with binding energy ε_b. The resonance occurs when $\Delta E \approx \varepsilon_b$ and the bound state is degenerate to the continuum threshold of $V_o(r)$. (d) Effective scattering length of the open channel as a function of the applied magnetic field obtained from eq. [5.43] using specific numerical parameters of ^{173}Yb and $\Delta m = 1$.

channels: for alkaline-earth-like atoms this is provided by the spin exchange coupling, which destroys a pair in the open channel and recreates it in the closed channel or vice versa. Consequently, during a scattering event between two atoms in the open channel, the particles can "temporarily" form a bound state in the closed channel (Feshbach molecule), a circumstance which strongly affects the scattering properties.

A first approach to provide a mathematical description of an orbital Feshbach resonance is to apply scattering theory and make an ansatz for the two-body wave function, treating the closed channel as a bound state with a localized wave function, thus neglecting the possibility of free propagation in the closed channel [20, 24, 25, 26]. Solving the Schrödinger equation, we obtain an effective wave function for the open channel, from which we extract a renormalized scattering length that includes the effect of interactions through the closed channel. The wave function for two colliding particles, each having mass

m and momentum $\pm\mathbf{k}$ relative to the center of mass, takes the form[8]

$$\psi(\mathbf{r}) = \left(e^{i\mathbf{k}\cdot\mathbf{r}} + f_o(k)\frac{e^{ikr}}{r}\right)|o\rangle + f_c(k)\frac{e^{-\sqrt{m\Delta E/\hbar^2 - k^2}r}}{r}|c\rangle, \tag{5.39}$$

where $f_o(k)$ and $f_c(k)$ have to be determined. Assuming that the kinetic energy of the pair is well below the Zeeman splitting between the channels: $\frac{\hbar^2k^2}{m} \ll \Delta E$, the component of $\psi(\mathbf{r})$ on the closed channel is localized, as the exponential is real and decreasing with r: this reflects the fact that we do not allow free propagation in the closed channel. The interaction Hamiltonian depends on the orbital symmetry of the two-body state, as discussed in sec. [1.2], which in this context boils down to only two possibilities: $|eg^{\pm}\rangle$. The other two orbital-triplet states $|gg\rangle$ and $|ee\rangle$ are negligible if we exclude free propagation in the closed channel. The reason is that $|e\downarrow\rangle$ and $|g\uparrow\rangle$ particles always form bound molecules in this approximation, so for example there are no free $|e\downarrow\rangle$ particles to interact with $|e\uparrow\rangle$ particles via two-body collisions. Observing that $|eg^{\pm}\rangle = \frac{1}{\sqrt{2}}(|c\rangle \mp |o\rangle)$, we can recast the two-body potential in eq. [1.4] as

$$V(r) = \frac{4\pi\hbar^2}{m}\left[\frac{a_{eg^+} + a_{eg^-}}{2}(|o\rangle\langle o| + |c\rangle\langle c|) - \frac{a_{eg^+} - a_{eg^-}}{2}(|o\rangle\langle c| + |c\rangle\langle o|)\right]\frac{\delta(r)}{4\pi r^2}\frac{\partial}{\partial r}(r\cdot), \tag{5.40}$$

where we have used the Lee-Huang-Yang regularization and the fact that $\delta(\mathbf{r}) = \delta(r)/(4\pi r^2)$ when the Dirac delta is multiplied by a spherically symmetric function. The kinetic energy term includes the Zeeman splitting and it can be written as $H_0 = -\frac{\hbar^2\nabla^2}{m}|o\rangle\langle o| + (\Delta E - \frac{\hbar^2\nabla^2}{m})|c\rangle\langle c|$; however, due to the presence of a Dirac-delta potential, the Laplacian operator in spherical coordinates should be modified with an extra Dirac-delta term [159]:

$$\nabla^2\psi(r) = -k^2e^{i\mathbf{k}\cdot\mathbf{r}}|o\rangle - \frac{1}{r}\left[\frac{\partial^2}{\partial r^2} - \frac{\ell(\ell+1)}{r^2} - \frac{\delta(r)}{r}\right]\left[u_o(r)|o\rangle + u_c(r)|c\rangle\right], \tag{5.41}$$

where $u_o(r) = f_o(k)e^{ikr}$ and $u_c(r) = f_c(k)e^{-\sqrt{m\Delta E/\hbar^2 - k^2}r}$ and the Schrödinger equation should be integrated over a small spherical domain of radius ε around $r = 0$ [20]: $\lim_{\varepsilon\to 0}\int_0^\varepsilon 4\pi r^2 dr(H_0 + V(r) - E)\psi(r) = 0$. We are interested in the solution in the s-wave scattering channel $\ell = 0$ and with free propagation energy $E = \frac{\hbar^2k^2}{m}$, which leads to the two equations [24]:

$$\begin{aligned}(1 + ika_d)f_o(k) + a_{\text{ex}}f_c(k)\sqrt{\frac{m\Delta E}{\hbar^2} - k^2} + a_d = 0\\ ika_{\text{ex}}f_o(k) - \left(1 - \sqrt{\frac{m\Delta E}{\hbar^2} - k^2}\right)f_c(k) + a_{\text{ex}} = 0\end{aligned} \tag{5.42}$$

where $a_d = (a_{eg^+} + a_{eg^-})/2$ and $a_{\text{ex}} = (a_{eg^+} - a_{eg^-})/2$ are the direct and exchange scattering lengths respectively. Finally, the effective scattering length in the open channel is, by applying the standard definition of scattering theory, given by:

$$\boxed{a_s = -f_o(0) = \frac{-a_d + \sqrt{m\Delta E/\hbar^2}(a_d^2 - a_{\text{ex}}^2)}{a_d\sqrt{m\Delta E/\hbar^2} - 1}.} \tag{5.43}$$

[8] More precisely, we have recast the two-body collision problem as a single particle of momentum $\mathbf{k}$ scattering off a potential $V(r)$. This means that the wave function is not symmetric under $\mathbf{r} \to -\mathbf{r}$ and the original wave function for the two-body problem is obtained by explicitly symmetrizing: $\frac{1}{2}[\psi(\mathbf{r}) + \psi(-\mathbf{r})]$.

In absence of an external field, the effective scattering length reduces to the direct value a_d; while the resonance occurs at $\Delta E = \frac{\hbar^2}{m a_d^2}$, where a_s diverges, hence $\frac{\hbar^2}{m a_d^2}$ represents the energy of the bound state in the closed channel at resonance ε_b. In fig. [5.7 (d)] we show the dependence of a_s on the external field B for ^{173}Yb (but the qualitative behavior is the same for other species).

These theoretical predictions for the effective scattering length as a function of the applied magnetic field have been experimentally verified with ^{173}Yb in refs. [20, 25, 160]. The atomic gas is prepared in the open channel by realizing a balanced mixture of $|g\downarrow\rangle$ and $|e\uparrow\rangle$, where $\uparrow$ and $\downarrow$ can be any pair of nuclear states, and it is initially confined in a three-dimensional cigar-shaped harmonic trap. After removing the harmonic confinement and applying an external static magnetic field, the shape of the atomic cloud is measured as a function of time via imaging techniques. For comparison, the same measure is performed with a different initial state, for instance the closed channel, or a mixture of $|g\uparrow\rangle$ and $|g\downarrow\rangle$, where the orbital Feshbach resonance does not occur. In presence of an orbital Feshbach resonance, the enhanced cross-section of two-body collisions leads to a different time-evolution of the atomic cloud and this can be used to measure the scattering length. More recently, methods for the coherent manipulation of Feshbach molecules have been implemented [161], including cycles of photoassociation and photodissociation and Raman-induced exchange of the internal nuclear state of a molecule.

Similarly to well-established literature on the magnetic Feshbach resonance of alkali atoms, the system can be described by a single-channel Hamiltonian with an attractive local interaction that, in absence of an optical lattice, is given in terms of the momentum representation [5.4] with $U/N_{\text{sites}} \to g/V$, where V is the system volume and g/V has the unit of energy. The effective scattering length [5.43] determines the bare interaction g via the implicit equation:

$$\frac{m}{4\pi\hbar^2 a_s} = -\frac{1}{g} + \frac{1}{V}\sum_{\mathbf{k},\, k<\Lambda} \frac{m}{\hbar^2 k^2}, \tag{5.44}$$

where the summation over momenta is cut-off at a momentum threshold Λ, which is physically related to the range of the scattering potential r_0 via $\Lambda \sim 1/r_0$ [162, 163, 164]. Defining $\Lambda = \pi/(2r_0)$ and performing the momentum integration (for a three-dimensional gas), we can recast eq. [5.44] in the more transparent form

$$\frac{1}{g} = \frac{m}{4\pi\hbar^2}\left(\frac{1}{r_0} - \frac{1}{a_s}\right), \tag{5.45}$$

from which we observe that there is an effective attraction ($g > 0$) for $a_s < 0$ or $a_s > r_0$. In the limit of very short-range interparticle potential considered above, the effective interaction is always attractive for every value of the scattering length. This hints at the possibility to realize a single-channel BCS-BEC crossover as described by the attractive Hubbard model by means of the orbital Feshbach resonance.

The single-channel approximation outlined above, however, might not be fully accurate for orbital Feshbach resonances: the reason is that typically the Zeeman splitting between open and closed channel is rather small and comparable to the Fermi energy [24], which implies that two particles in the closed channel are not always bound in a molecule, but they can have independent scattering dynamics [165, 166]. For example, in ^{173}Yb the direct scattering length is $a_d \approx 1750 a_0$, so the Feshbach resonance occurs roughly at a Zeeman splitting $\Delta E = \frac{\hbar^2}{m a_d} \approx 2\pi\hbar \times 6.74\,\text{kHz}$; while the Fermi energy for a typical density $n \approx 5 \cdot 10^{19}\text{m}^{-3}$ is $E_F = \frac{\hbar^2}{2m}(3\pi^2 n)^{2/3} \approx 2\pi\hbar \times 2.26\,\text{kHz}$. We can see that the two energy scales are comparable, as opposed to magnetic Feshbach resonances of alkali fermions, that occur at a much larger Zeeman splitting

$\Delta E \approx 2\pi\hbar \times 100\,\text{MHz}$. This encourages us to take into account the full many-body Hamiltonian for the two channels that, in the presence of an optical lattice, is given by eq. [1.5] with an extra term given by the Zeeman splitting sketched in fig. [5.7]:

$$H_{\text{Zeeman}} = \sum_{a=g,e} \sum_{\sigma=\uparrow\downarrow} \Delta E_{a\sigma} N_{a\sigma}, \tag{5.46}$$

where $\Delta E_{a\sigma} = \mu_B g_a m_\sigma B$ and $N_{a\sigma}$ are number operators. We can recast this term in a more symmetric fashion by adding constant terms proportional to conserved quantities like N_σ, N_a or N: in particular, choosing

$$-\Delta E_{g\uparrow} N - \left(\Delta E_{e\uparrow} - \Delta E_{g\uparrow} + \frac{\Delta E}{2}\right) N_e + \frac{\Delta E}{2} N_\uparrow - (\Delta E_{g\downarrow} - \Delta E_{g\uparrow}) N_\downarrow \tag{5.47}$$

we get an Hamiltonian where the two states of the open and closed channel are respectively degenerate

$$H_{\text{Zeeman}} = \frac{\Delta E}{2} \left(N_{e\downarrow} + N_{g\uparrow}\right), \tag{5.48}$$

which is illustrated in fig. [5.7 (b)]. To see how this is related to the pair-hopping model, it is convenient to relabel the indexes as follows:

$$|g\downarrow\rangle \to |1\downarrow\rangle, \quad |e\uparrow\rangle \to |1\uparrow\rangle, \quad |g\uparrow\rangle \to |2\downarrow\rangle, \quad |e\downarrow\rangle \to |2\uparrow\rangle. \tag{5.49}$$

Assuming that the gas is loaded into an optical lattice, we can apply this mapping to Hamiltonian [1.5], including also the Zeeman term [5.48] and we get

$$\begin{aligned} H = &- \sum_{\langle ij\rangle, a\sigma} t_a \left(c^\dagger_{ia\sigma} c_{ja\sigma} + \text{h.c.}\right) - \mu \sum_{ia\sigma} n_{ia\sigma} + \frac{\Delta E}{2} \sum_{i\sigma} n_{i2\sigma} + U_{gg} \sum_i n_{i1\downarrow} n_{i2\downarrow} + U_{ee} \sum_i n_{i1\uparrow} n_{i2\uparrow} \\ &+ V \sum_{ia} n_{ia\uparrow} n_{ia\downarrow} + V \sum_i \left(n_{i1\uparrow} n_{i2\downarrow} + n_{i2\uparrow} n_{i1\downarrow}\right) - V_{\text{ex}} \sum_i \left(c^\dagger_{i1\uparrow} c^\dagger_{i1\downarrow} c_{i2\downarrow} c_{i2\uparrow} + \text{h.c.}\right). \end{aligned} \tag{5.50}$$

We can see that the spin exchange is mapped into a pair-hopping term with amplitude V_{ex}, and that the two bands are characterized by the same intraorbital Hubbard repulsion V. In the absence of an optical lattice, we can simply use the Fourier-transformed version of eq. [5.50]. For the specific case of ^{173}Yb, we can neglect U_{gg} and U_{ee} compared to the other energy scales, and we can assume $V \approx V_{\text{ex}}$, similarly to what we have done in sec. [3.5].

The resulting model is obviously quite different from what we have studied in sec. [5.2], because of the repulsive intraorbital interaction, the presence of a Zeeman splitting term and the presence of an interorbital density-density interaction involving particles with opposite spins. Nevertheless, the interesting questions are similar: does this model support a two-channel BCS-BEC crossover? In what regime of parameters? One can try to address these questions performing a mean-field decoupling of the interaction in the two intraorbital pairing channels ϕ_1 and ϕ_2. The resulting mean-field model reduces to the Hamiltonian studied in refs. [24, 167], which at $\Delta E = 0$ is essentially the mean-field model that we have studied in sec. [5.2.1], with the major difference that the gap parameters are given by $\Delta_a = V\phi_a - V_{\text{ex}}\phi_{\bar{a}}$ and the two contributions come with opposite signs.[9] From our previous discussion, we conclude that the solution to the mean-field equations should be similar to the one illustrated in fig. [5.2], with the important difference

[9] We recall that in sec. [5.2.1], the gap parameters were defined as $\Delta_a = U\phi_a + J\phi_{\bar{a}}$ where $U > 0$ and $J > 0$; while here we have $\Delta_a = V\phi_a - V_{\text{ex}}\phi_{\bar{a}}$ where $V > 0$ and $V_{\text{ex}} > 0$.

that now ϕ_1 and ϕ_2 have an opposite sign, i.e. a relative phase π; this is indeed consistent with what the authors find in [24]. However, we have shown that the pair-hopping can cause significant dynamical correlations and consequently modify the mean-field picture even at $T = 0$, a circumstance which raises the important issue of including dynamical correlations to the study of eq. [5.50]. This is also motivated by the presence of a non negligible interorbital density-density coupling $V \sum_i (n_{i1\uparrow} n_{i2\downarrow} + n_{i1\downarrow} n_{i2\uparrow})$, which is completely irrelevant within an intraorbital BCS mean-field decoupling and which is a potential source of more dynamical correlations. A thorough investigation of this problem can be performed by means of DMFT (as long as we consider the presence of an optical lattice) and it is a goal for future work.

5.4 Conclusion and outlook

In this chapter we have revised how the BCS-BEC crossover stems from a mean-field solution of the attractive Hubbard model, emphasizing the strengths and limitations of this approach. Despite being well-understood and used in research papers, it is difficult to find a pedagogical introduction to this subject; hence we have tried to bridge this gap, hopefully providing to the reader an easier access to the topic. An important drawback of the mean-field approach is the overestimation of the critical temperature in the BEC regime, which can be corrected by including dynamical correlations with DMFT. The correct behavior of $T_c \approx 1/U$ in the BEC regime can be qualitatively understood by a zero-temperature mean-field estimate of the superfluid stiffness, which is $D_s \approx 1/U$ for $U \gg D$ and saturates to a constant for $U \ll D$. This means that, while in the BCS regime thermal fluctuations at $T \approx T_c$ bring the system to the normal state by populating the band of excitations, in the BEC limit they induce large dynamical fluctuations of the phase, spoiling the phase coherence of the condensate, while leaving the fermions bound in (approximately) bosonic molecules. We have taken the opportunity to review the concept of superfluid stiffness in an organic way, from the general definition to the concrete calculation under our working assumptions.

Then, we have considered two attractive Hubbard models coupled via a local pair-hopping interaction (Josephson coupling) of amplitude J, considering the system at $T = 0$ on a Bethe lattice with infinite coordination, where the momentum-dependence of the self-energy is quenched. We have first neglected also the dynamical dependence by applying the static mean-field approximation with two superconducting amplitudes in the two orbitals. We have obtained a two-channel BCS-BEC crossover, where the two order parameters have the same phase and they increase exponentially with U and J in the limit $U, J \ll D$, then saturate to $1/2$ when either U or J are sufficiently large. Within this approximation, the interorbital coupling only enters in the self-consistent amplitudes Δ_1, Δ_2 of pair-exchange processes with the effective reservoir: for example, the first orbital exchanges pairs with amplitude $\Delta_1 = U\phi_1 + J\phi_2$ that depends on both the self-consistent order parameters.

When we include dynamical fluctuations with DMFT, this picture is confirmed only in the regime $U, J \ll D$, while it completely changes at strong coupling where, instead of entering the BEC regime, the system undergoes a quantum phase transition to a normal state with no broken symmetry. This phase is stabilized when either J or U are large: in particular, if for instance J is very small, we observe this phase at sufficiently large values of U, but as J increases, the critical U decreases considerably. From the quasiparticle weight and the intraorbital double occupancy, we find that this phase is an insulator characterized by the suppression of single occupancies; while looking at the local interorbital density correlation, we can argue that the fermionic pairs are localized in real space, but completely delocalized between the orbitals (orbital resonating pairs). This is a clear manifestation of strong quantum correlations, as the phase transition is accompanied by a divergence of the self-energy at zero frequency.

The presence of an hopping imbalance between the two orbitals enhances both the order parameters

at weak coupling, but at the same time pushes the critical value of the phase transition to smaller values compared to the balanced case; moreover, the two order parameters vanish simultaneously at the critical point. The reason is that the localization of Cooper pairs in the orbital with lower kinetic energy is favored compared to the balanced case: in the weak coupling limit this favors superconductivity in that orbital (and consequently also in the other), pushing the system towards the BCS regime; while at strong coupling this favors the formation of orbital resonating pairs.

This system can be regarded as a general paradigmatic theoretical model that explains the specific role of the local interorbital pair-hopping, witnessing the importance of including dynamical fluctuations even when the system features a phase with spontaneously broken symmetry. Suitable generalizations of this model can be used to describe a variety of physical scenarios, such as stacked bilayer superconducting materials, Josephson junctions of parallel superconducting films, phonon-driven superconductivity in multiorbital materials, etc. However, the most important application in the context of this thesis is the investigation of a two-channel BCS-BEC crossover with the orbital Feshbach resonance in alkaline-earth-like atoms. In sec. [5.3] we have discussed the orbital Feshbach resonance, presenting a well-established single channel formalism, where the system is described in terms of a single-band attractive Hubbard model, and the Hubbard-U is determined by the effective scattering length in the open collisional channel. Within this approach, the closed channel is merely considered as a bound state coupled to the open channel, but scattering states in the closed channel are neglected, as in the typical formulation of magnetic Feshbach resonances in alkali atoms. With the orbital Feshbach resonance, however, the energy of scattering states of the closed channel is much smaller, and thermal fluctuations could in principle populate these states significantly. We have proposed a many-body Hamiltonian that complements the mean-field model introduced in [24] to describe the two-channel dynamics. We have shown that the pair-hopping is a key ingredient of this description, as its amplitude is given by the spin-exchange parameter V_{ex}, which is crucial in the orbital Feshbach resonance; however we have also discussed the importance of considering other terms, in particular a Zeeman splitting and an intra- and interorbital Hubbard repulsion (with an amplitude given by the "direct" coupling V).

A concrete purpose for a future work is to investigate the ground state of Hamiltonian [5.50] by means of DMFT, to include dynamical quantum correlations on top of the mean-field results outlined in ref. [24]. In particular, we are mostly interested in studying the fate of the two-channel BCS-BEC crossover driven by the external magnetic field in presence of all these processes.

Acknowledgements

This section is devoted to personal comments and due acknowledgements to so many people to whom I will always be grateful for all their precious help, love and affection. I apologize to the reader who is not interested, but I have noticed that concluding a thesis with such personal comments is a widespread tradition, and I cannot resist.

It has been a long journey since the beginning of my Ph.D., four years ago, in the end of 2019. These years have been quite challenging sometimes, but I've had the opportunity to grow not only as a young scientist, but, most importantly, as a person. First of all, the beginning of my Ph.D. was the time when I started living on my own, after 25 years of commuting to school and university, therefore I had to face normal difficulties of a young man that has never lived alone in a new city (it was about time!). Also, the very beginning of my classes in the first year of Ph.D. has been complicated, because I could only enroll and move to Trieste two weeks after the official beginning, and I still had to defend my Master's thesis a few days later. I can't forget my first day at SISSA, as it started with an assignment about stacked bilayer graphene (a topic which I knew nothing about!) to be finished within a couple of weeks! It has been tough, but eventually we made it, and now I remember those days with great joy and pleasure.

On a more serious note, among the difficulties, I have to mention the COVID-19 pandemic, which stroke a few months after the beginning of my Ph.D. (February 2020), with the first cases in Italy reported in a small town close to the city where my family lives. After that, I was forced to live four months completely alone and in a small house with almost no sunlight passing through the windows. Nevertheless, I cannot complain too much, because it has been a hard time for so many people and, all things considered, I have been quite lucky. After those months, the situation gradually improved, even though other restrictive measures were adopted from time to time.

Besides these facts, and a few more unpleasant moments that I do not mention here, it is worth mentioning also the good times! First of all, Trieste is a rather quiet and lovely city, with a warm weather all over the year, beautiful architecture and a breath-taking panorama of the sea from the hills (and from the office as well), not to mention the friendly people and the amazing nature all around. Secondly, all my fellow Ph.D. students are amazing people, not only for their admirable proficiency and preparation, but also because they have been very kind and friendly to me since the very beginning. I've learned a lot from them and I've had a great time with all of them, so I really hope that we could keep in touch in the future, even though our careers are going their separate ways. A special mention goes to Nishan, who has been the first person that I have talked to and who now I consider a very good friend: I am so happy that we are going to defend our thesis the same day, I wish him the best of luck! Another special mention goes to Samuele, who taught me so many things and helped me a lot through the development of my code with extremely useful tips and tricks. I thank him a lot for his patience and dedication and I really hope we could work together on new research projects in the near future.

Speaking of colleagues and friends, Andrea deserves a very special mention, as well as all of my gratitude. We started working side by side at the beginning of this project as good colleagues, and I

can't count how many hours we have spent together, working and sharing our passion for Physics and for the mountains. From the professional point of view, I have learnt from Andrea the importance of carefully checking even the smallest details of a calculation, as well as precious tips and tricks for working in research. We have also shared beautiful experiences, such as the conference "Atomtronics 2022" in the beautiful town of Benasque, where we went for several hikes during the day and we worked hard on our projects at night, or our trips in Friuli and Piemonte. After all of this, I can safely admit that he is now one of my best friends and I hope I can meet him in person again very soon. By the way, I also want to greet Marianna and Giovanni (I can't wait to see how he grew up!).

Finally, I want to acknowledge Massimo, my Ph.D. supervisor, a person that I really esteem for his great scientific expertise and who taught me most of the topics that I have presented in this thesis. I truly want to thank him for letting me explore on my own a lot of topics, letting me be free to make mistakes and learn from them, while putting me under the right amount of pressure at the right moment. Also, I thank him very much for giving me precious suggestions and for valuing all of my work, especially when I underestimate it.

It is now time to acknowledge all the precious help and love that I have received from my family and friends. First of all, I want to thank all of my family: I cannot stress enough how much I love them and how lucky I am to have them close to me. Obviously, the most special thanks goes to my mom: it is impossible to list all of the things that she has done for me, but certainly she taught me the ethic of hard work through her example, and she has listened patiently to all of my never-ending streams of consciousness, encouraging and conforting me all the time. Thank you mom. I also want to thank my dad, who always helps me with his calm and with his joking personality: sometimes laughing and taking it easy is the best way to go, so thank you dad! Then I want to thank a lot my grandma, Francesca: she is a woman from another time and she is probably the greatest example of humanity, determination, kindness and hard work for me. I am so happy I can spend time with her, eating the delicious food she prepares and listening to her stories. Also, I have to acknowledge all of her encouragement and advice: thank you grandma! The same words hold for my other grandma, "Beppina", who sadly passed away, but I've had the opportunity to spend a lot o time with her. Also, a big thanks goes to my dear great-uncle Lidia, who raised me when I was a child.

A heartwarming hug goes to my beloved girlfriend, Otty, who always supports me (and tolerates me!) through the hard times, but – most importantly – makes me laugh with her funny quips. A very important acknowledgements is due to my dear friends Riccardo, Sofia and Luca for all the funny moments that we have shared together and for all their support. Also, I have to acknowledge Francesco, Nicolò and Fiammetta (group number 10) for all the fruitful discussions about the future and for all the jokes. A special thanks goes to Monica, Mario and Isabella, who supported me and helped me concretely with the move: they helped me find a house and doing the cleaning at the very beginning of my Ph.D. I also want to greet Tommaso and Beatrice for all the dinners we had together (good luck with your studies!). A final mention goes to Gabriele and Sonia, who are like parents for me and to Laura, who is like a sister: thanks for raising me as part of your family, I'll see you soon in your new house.

Appendix A

Ladder operators

In this appendix we show the explicit expression of the flavor ladder operators $S_{\sigma\rho} = c^\dagger_\sigma c_\rho$ in terms of the spin operators defined in eq. [3.40] for the three-flavor case. These relations are the building blocks to write any operator in terms of spins. In order to keep a simple notation, we omit the site index and we put the component labels x, y and z as subscripts. The relations are:

$$S_{+1,0} = \frac{1}{2\sqrt{2}} \left(\Sigma_x + i\Sigma_y + \{\Sigma_x + i\Sigma_y, \Sigma_z\}\right),$$

$$S_{0,+1} = \frac{1}{2\sqrt{2}} \left(\Sigma_x - i\Sigma_y + \{\Sigma_x - i\Sigma_y, \Sigma_z\}\right),$$

$$S_{+1,-1} = \frac{1}{2} \left(\Sigma_x + i\Sigma_y\right)^2,$$

$$S_{-1,+1} = \frac{1}{2} \left(\Sigma_x - i\Sigma_y\right)^2,$$

$$S_{0,-1} = \frac{1}{2\sqrt{2}} \left(\Sigma_x + i\Sigma_y - \{\Sigma_x + i\Sigma_y, \Sigma_z\}\right),$$

$$S_{-1,0} = \frac{1}{2\sqrt{2}} \left(\Sigma_x - i\Sigma_y - \{\Sigma_x - i\Sigma_y, \Sigma_z\}\right),$$

$$n_{+1} = S_{+1,+1} = \frac{1}{2} \left(\Sigma_z^2 + \Sigma_z\right),$$

$$n_0 = S_{0,0} = 1 - \Sigma_z^2,$$

$$n_{-1} = S_{-1,-1} = \frac{1}{2} \left(\Sigma_z^2 - \Sigma_z\right),$$

where $\{A, B\} = AB + BA$ is the anticommutator and 1 is the identity matrix. Remarkably these expressions are quadratic in the spin operators. Moreover we observe that the constraint $\sum_\sigma S_{\sigma\sigma} = 1$ is satisfied.

Appendix B

Drude weight

This appendix is devoted to provide notions about the concept of Drude weight introduced in sec. [4.2] and used in chapter [4] to realize the phase diagram of the Hund's model and of its cold-atomic analogue. First of all, we point out that this is a very rich and subtle topic, characterized by several tricky aspects which are not treated exhaustively here. In this context, we limit the discussion to those aspects that are more relevant to the present thesis.

The Drude weight D is defined as the DC component of the frequency-dependent electrical conductivity $\sigma(\omega)$, namely the coefficient in front of the Dirac-delta peak at zero frequency in absence of disorder:

$$\sigma(\omega) = D\delta(\omega) + \sigma_{\text{reg}}(\omega), \tag{B.1}$$

where $\sigma_{\text{reg}}(\omega)$ is a regular function that encodes the AC electrical conductivity. For a disordered system, the conductivity function becomes regular in $\omega = 0$ and the Dirac-delta peak is broadened: in this case the Drude weight is not well-defined and one can just use $\sigma(\omega = 0)$ as a measure of DC conductivity.

In ref. [104], Kohn applied linear response theory and derived a simple formula for the Drude weight of a many-body system at $T = 0$, showing that it is given by the curvature of the ground state energy $E_0(\phi)$ with respect to an auxiliary Peierls phase ϕ introduced in the hopping term, evaluated at the energy minimum $\phi = \phi_0$. For a one-dimensional ring lattice in suitable units it is given by:

$$\boxed{D = \frac{1}{N_{\text{sites}}} \frac{\partial^2 E_0}{\partial \phi^2}\bigg|_{\phi=\phi_0}}. \tag{B.2}$$

If the Peierls phase is physically provided by a magnetic flux threading a ring of charged particles that are minimally coupled to this field via their electric charge q, and we work in units of the international system, we have to consider a prefactor $\pi(q/\hbar)^2 a$, where a is the lattice spacing. However, the Peierls phase can also describe a physical rotation of the ring. As one would intuitively expect, in metals and superconductors $D \neq 0$, while $D = 0$ in any insulating state [65, 104].

The Drude weight is also related to the persistent current carried by the ground state of the system and induced by the Peierls phase. Consider the application of an auxiliary Peierls phase ϕ to all the hopping processes in the Hamiltonian: $t^{\alpha\alpha}_{i,i+1} \to t^{\alpha\alpha}_{i,i+1} e^{i\phi}$ for all the fermionic components α and the lattice sites i; we can define the average Drude current per bond in the ground state $|\psi(\phi)\rangle$ as

$$I(\phi) = \frac{1}{N_{\text{sites}}} \langle \psi(\phi) | \frac{\partial H}{\partial \phi} | \psi(\phi) \rangle. \tag{B.3}$$

We emphasize that this is the **total current** (paramagnetic + diamagnetic), not the paramagnetic contribution defined in sec. [2.3], where the derivative was taken at $\phi = 0$. By virtue of the Hellmann-Feynmann theorem, we can write $I(\phi) = \frac{\partial E_0}{\partial \phi}$, from which we notice that $I(\phi_0) = 0$ because $\phi = \phi_0$ is a stationary point of the energy, and we immediately get the link to the Drude weight:

$$\frac{1}{N_{\text{sites}}} \frac{\partial I}{\partial \phi}\bigg|_{\phi=\phi_0} = D \qquad \rightarrow \qquad I(\phi) \approx D(\phi - \phi_0) \quad \text{at} \quad \phi \approx \phi_0. \tag{B.4}$$

Essentially, the Drude weight determines the linear response of the total current to an externally applied Peierls flux: if $D = 0$, then the current is insensitive to the presence of a flux and the system is an insulator; else it responds to the external flux with a proportional current and it is a metal.

Here comes the first important subtlety: for interacting systems characterized by local interactions of the form $c^\dagger_{i\alpha} c^\dagger_{i\beta} c_{i\gamma} c_{i\delta}$ or on-site potentials proportional to the local density, the value of ϕ_0 is independent from the interaction parameters and it can be predicted in advance by simply looking at the corresponding non-interacting system. This stems from the invariance of the local interaction under a gauge transformation of the form $c_{j\alpha} \rightarrow e^{-i\phi j} c_{j\alpha}$ [168].

The value of ϕ_0 in the non-interacting system essentially depends on the number of particles and of available degrees of freedom. For example, let's consider the two rings studied in chapter [4], where $N_{\text{sites}} = 3$ and $N_{\text{particles}} = 6$ in both cases, with only 3 available momentum states in the Brillouin zone $k = 0, \pm\frac{2\pi}{3}$. An important difference between the two systems is that the Hund's model [4.3] has spin and orbital degeneracy, resulting in a total of $N \cdot N_{\text{orb}} = 2 \cdot 3 = 6$ degrees of freedom per every momentum index k, while its analogue [4.8] has only flavor degeneracy and 3 degrees of freedom per momentum k.

The band diagram, internal energy $E_0(\phi)$ and Drude current $I(\phi)$ for the non-interacting Hund's model are presented in fig. [B.1]. The band structure in absence of external flux $\phi = 0$ has a minimum in $k = 0$, where all the 6 electrons can be accommodated to realize the lowest energy configuration. Since the ground state comes with vanishing total momentum, the resulting Drude current is zero: $I(0) = 0$, which means that the function $E_0(\phi)$ has a minimum in $\phi_0 = 0$. Furthermore, the ground state energy, as well as the Drude current, have a periodicity of $2\pi/N_{\text{sites}}$ with respect to the flux ϕ and, most importantly, they feature a non-analytic point right in the middle of a period, at $\phi_c = \pi/N_{\text{sites}}$. In particular, $E_0(\phi)$ is non-differentiable at this point, and consistently $I(\phi)$ features a "jump" discontinuity. This is essentially the point where the ground state manifold becomes degenerate to the first excited manifold (not shown): $E_0(\phi_c) = E_1(\phi_c)$. In conclusion, the total current is proportional to the flux $I(\phi) \approx D\phi$ at $\phi \approx \phi_0 = 0$ and this is a reasonably good approximation as long as $\phi \ll \phi_c = \pi/N_{\text{sites}}$. In sec. [4.2] we have used this property to evaluate the Drude weight: we have chosen a specific value of $\phi = 0.1\pi/3$ which is much smaller than $\phi_c = \pi/3$ and reasonably close to $\phi_0 = 0$, we have computed the total current I and we have used the linearity of $I(\phi)$ to extract the Drude weight $D = I/\phi$.

For the Hund's analogue discussed in sec. [4.3], the story is completely different, as we can see from fig. [B.2]. From the band diagram computed with $\phi = 0$, it is clear that we can't accommodate the 6 particles in a momentum-symmetric configuration: 3 of them occupy the low-lying state $k = 0$, but there are 3 more particles to assign to the two degenerate single-particle states $k = \pm 2\pi/3$. We can either put 2 of them in $k = +2\pi/3$ and 1 in $k = -2\pi/3$ (or vice versa) or put all 3 of them in $k = +2\pi/3$ (or in the other state), resulting in a clear degeneracy of the many-body ground state. The momentum imbalance suggests that the zero-flux total current is non-vanishing, hence $\phi_0 \neq 0$; moreover, the zero-flux degeneracy suggests that in fact $\phi_c = 0$. To find the correct value of ϕ_0 we have to look for a specific flux that allows to create a many-body state with no total current, i.e. where the single-particle momentum states are symmetrically occupied with respect to $-\phi_0$. We stress that we are looking for a state that makes the **total** current vanish, not just the **paramagnetic** contribution: this is why we want to symmetrize momentum with respect to

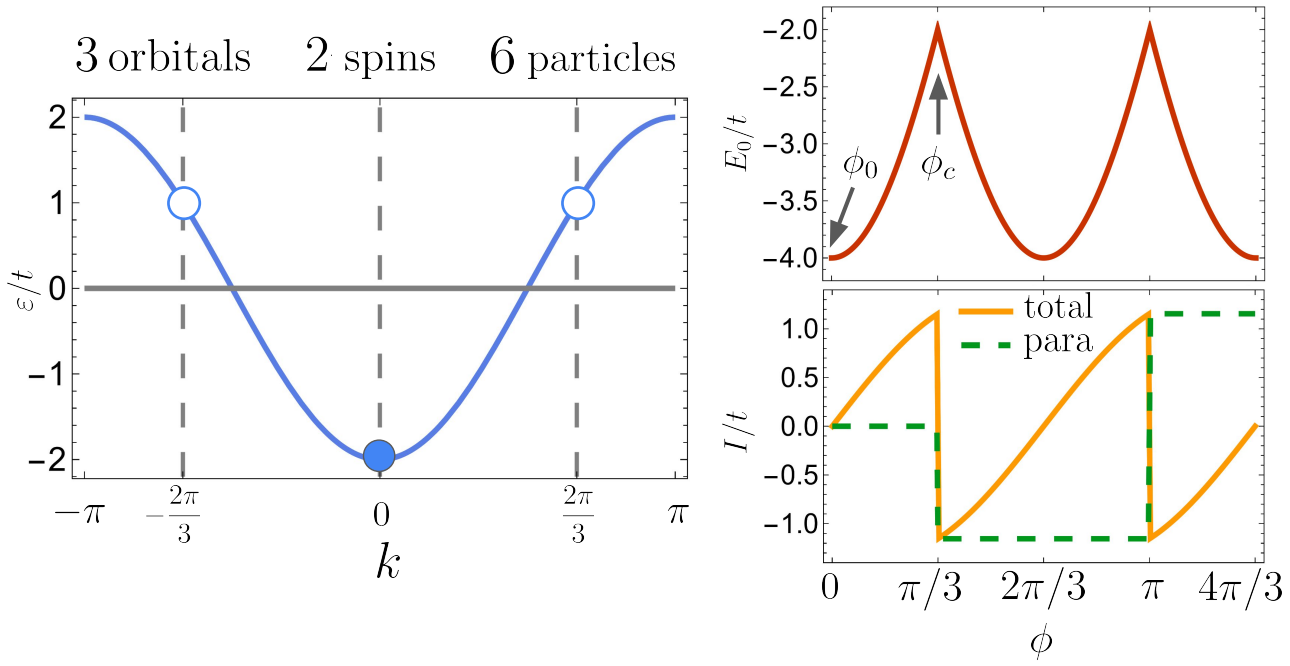

Figure B.1: (Left) Band structure of electrons on a non-interacting three-site ring threaded by an auxiliary magnetic flux ϕ with 2 spin and 3 orbital states, for a total of 6 degrees of freedom. If $\phi = 0$, the 6 electrons are all accommodated in the low-lying 6-fold degenerate single particle state at $k = 0$. (Right) Periodic behavior of the many-body ground state energy $E_0(\phi)$, total current $I(\phi)$ and paramagnetic current $I_{\text{para}}(\phi)$ as a function of ϕ. The two points ϕ_0 and ϕ_c indicate respectively the location of an energy minimum, where $I(\phi)$ can be expanded linearly, and the location of a non-analytic point, where $I(\phi)$ is discontinuous.

$-\phi_0$ rather than 0. This condition is realized at $\phi_0 = \pi/N_{\text{sites}} = \pi/3$, where 3 particles occupy $k = 0$ and the other 3 occupy $k = -2\pi/3$, two states that are in fact symmetric with respect to $-\pi/3$. Consistently, the ground state energy is minimized at ϕ_0 and the total current can be expanded as $I(\phi) \approx D(\phi - \phi_0)$. Once again, the periodicity is $2\pi/N_{\text{sites}}$. In conclusion, to evaluate the Drude weight from the current in this case, we have to choose a specific value of ϕ which is close to $\phi_0 = \pi/3$ and far from $\phi_c = 0$: in the main text we've chosen $\phi - \phi_0 = -0.1\pi/3$, evaluated the current at ϕ and computed $D = I/(\phi - \phi_0)$.

Finally, there is another subtlety related to the analytic evaluation of the Drude weight in the thermodynamic limit which is worth mentioning here. Even though in chapter [4] we have only worked with finite-size systems, it is still useful to take a look at the thermodynamic limit $N_{\text{sites}} \to +\infty$ for any future purpose. The subtle point is related to the correct order in which we have to evaluate the second derivative and the thermodynamic limit, because the two operations don't commute. The correct approach is to evaluate the energy curvature **first** and take the thermodynamic limit **afterwards** [100]. To convince ourselves about this point, let's consider the simple example of spinless fermions moving on a half-filled one-dimensional ring threaded by a flux ϕ. The energy dispersion is given by $\varepsilon_k(\phi) = -2t\cos(k + \phi)$, where t is the hopping scale. At half filling, we have $\mu = 0$ and the occupied momentum states are labeled by k such that $\varepsilon_k(\phi) < 0$, i.e. $-\pi/2 - \phi < k < \pi/2 - \phi$ (whether or not to include states at the Fermi level

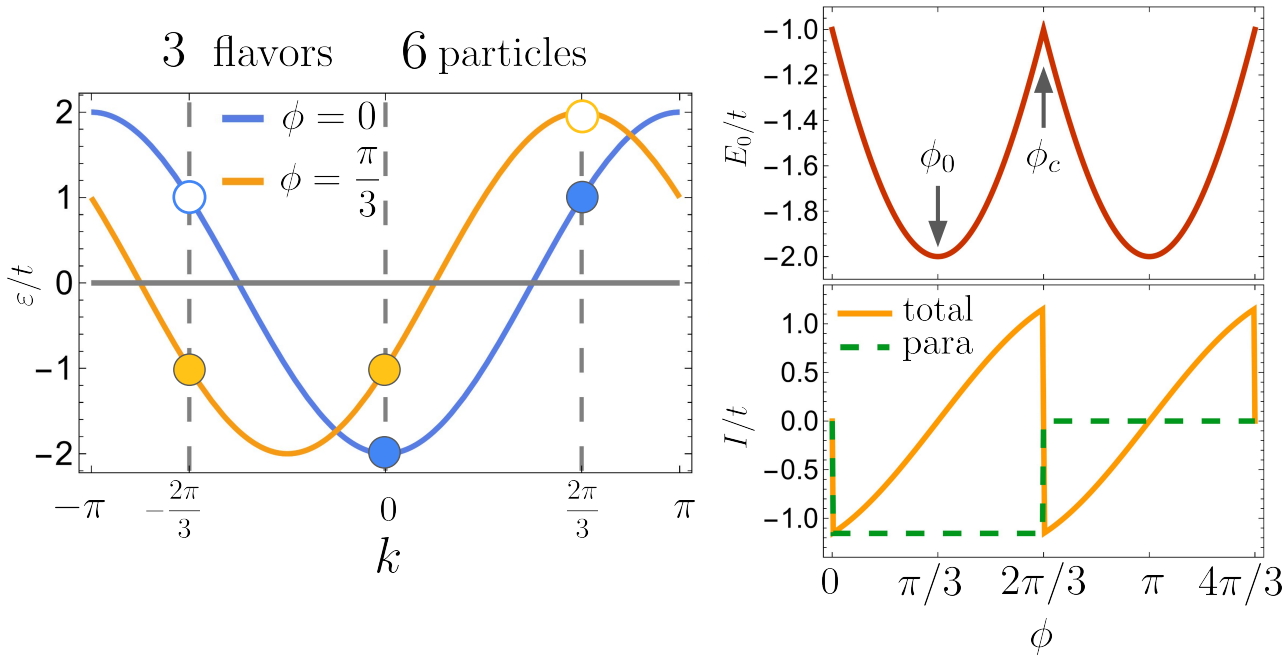

Figure B.2: (Left) Ground state of fermions with 3 flavor states on a non-interacting three-site ring threaded by an auxiliary flux ϕ at the representative values $\phi = 0$ and $\phi = \pi/3$. If $\phi = 0$, 3 particles are accommodated in the low-lying 3-fold degenerate single particle state $k = 0$, and the remaining 3 in one of the two degenerate single particle states $k = +2\pi/3$. This is one of the possible degenerate many-body states. If $\phi = \pi/3$, the particles are equally divided between the degenerate single-particle states $k = 0$ and $k = -2\pi/3$, in a symmetric configuration with respect to $-\pi/3$. This state is not degenerate. (Right) Periodic behavior of the many-body ground state energy $E_0(\phi)$, total current $I(\phi)$ and paramagnetic current $I_{\text{para}}(\phi)$ as a function of ϕ. The two points ϕ_0 and ϕ_c indicate respectively the location of an energy minimum, where $I(\phi)$ can be expanded linearly, and the location of a non-analytic point, where $I(\phi)$ is discontinuous.

will be clarified below). If we do the wrong thing and evaluate the thermodynamic limit at finite ϕ first, we get to the conclusion that $E_0(\phi)$ is a constant, and consequently that the Drude weight vanishes. In this case, the momentum states form a continuum and we can compute the internal energy per particle from the integral:

$$\frac{E_0(\phi)}{N_{\text{sites}}} = \frac{1}{2\pi}\int_{-\frac{\pi}{2}-\phi}^{\frac{\pi}{2}-\phi} -2t\cos(k+\phi)dk = \frac{1}{2\pi}\int_{-\frac{\pi}{2}}^{\frac{\pi}{2}} -2t\cos k' dk' = -\frac{2t}{\pi} \quad \text{(wrong approach)},$$

where we don't need to worry about the problem of including states at Fermi or not, because the result doesn't change. We see that $E_0(\phi)$ is constant, so we evaluate $D = 0$, which is clearly unphysical, as we expect that this system is an ideal conductor.

The correct approach is to keep N_{sites} finite and compute the energy curvature at $\phi = \phi_0$ first. For concreteness, we assume $\phi_0 = 0$, which amounts to assume that the ground state in absence of external flux is not degenerate. On a finite-size half-filled system, we encounter a degeneracy whenever there are

two single-particle states at the Fermi level with $k = \pm\pi/2$: in this case we can accommodate only one particle in these two states and we have a choice. This happens if $-\pi + n\Delta k = \pi/2$ for some integer n, where $\Delta k = 2\pi/N_{\text{sites}}$ is the spacing in the Brillouin zone, which is verified if N_{sites} is divisible by 4. We conclude that $\phi_0 = 0$ only for $N_{\text{sites}} \neq 4, 8, 12, \ldots$, otherwise we have $\phi_0 = \pi/N_{\text{sites}}$. So, assuming $\phi_0 = 0$, we can now choose a value of the flux ϕ arbitrarily close to 0 to compute the derivative. If we choose ϕ small enough, then for every N_{sites} (except $4, 8, 12$,...) the set of occupied momentum states is constant with respect to ϕ and lies in the interval $-\pi/2 < k < \pi/2$, hence we can expand the internal energy for small fluxes as:

$$E_0(\phi) \approx -2t \sum_{k \text{ occupied}} \cos(k + \phi) \qquad (\phi \approx 0), \tag{B.5}$$

hence the correct formula for the Drude weight in terms of the curvature:

$$D = \frac{1}{N_{\text{sites}}} \left.\frac{\partial^2 E_0}{\partial \phi^2}\right|_{\phi=0} = \frac{2t}{N_{\text{sites}}} \sum_{k \text{ occupied}} \cos k. \tag{B.6}$$

Evaluated the curvature for a finite system, we can now move to the thermodynamic limit by replacing the sum with an integral, and the result is

$$D = \frac{2t}{N_{\text{sites}}} \frac{N_{\text{sites}}}{2\pi} \int_{-\frac{\pi}{2}}^{\frac{\pi}{2}} \cos k \, dk \qquad \rightarrow \qquad \boxed{D = \frac{2t}{\pi}.} \tag{B.7}$$

This result states that the system is a good conductor and in particular that the DC electrical conductivity is proportional to the kinetic energy of the electrons.

The reason why the thermodynamic limit and the second derivative do not commute ultimately lies in the fact that the position of the non-analytic point ϕ_c scales as $\phi_c \approx 1/N_{\text{sites}}$ [100]. If we incorrectly take the thermodynamic limit first, then $\phi_c \to 0$ and it is no longer possible to follow adiabatically the manifold $E_0(\phi)$, as it merges with higher energy manifolds already at $\phi \approx 0$, hence we can't compute the correct curvature.

Bibliography

[1] Andrea Richaud, Matteo Ferraretto, and Massimo Capone. Interaction-resistant metals in multicomponent Fermi systems. *Phys. Rev. B*, 103:205132, May 2021.

[2] Andrea Richaud, Matteo Ferraretto, and Massimo Capone. Mimicking multiorbital systems with SU(N) atoms: Hund's physics and beyond. *Condensed Matter*, 7(1), 2022.

[3] Matteo Ferraretto, Andrea Richaud, Lorenzo Del Re, Leonardo Fallani, and Massimo Capone. Enhancement of chiral edge currents in $(d+1)$-dimensional atomic Mott-band hybrid insulators. *SciPost Phys.*, 14:048, 2023.

[4] Neil W Ashcroft and N David Mermin. *Solid state physics*. Cengage Learning, 2022.

[5] Charles Kittel and Paul McEuen. *Introduction to solid state physics*. John Wiley & Sons, 2018.

[6] Jan Kunes, Alexey V Lukoyanov, Vladimir I Anisimov, Richard T Scalettar, and Warren E Pickett. Collapse of magnetic moment drives the Mott transition in MnO. *Nature materials*, 7(3):198–202, 2008.

[7] G Stefanovich, A Pergament, and D Stefanovich. Electrical switching and Mott transition in VO_2. *Journal of Physics: Condensed Matter*, 12(41):8837, 2000.

[8] Mumtaz M Qazilbash, Markus Brehm, Byung-Gyu Chae, P-C Ho, Gregory O Andreev, Bong-Jun Kim, Sun Jin Yun, AV Balatsky, MB Maple, Fritz Keilmann, et al. Mott transition in VO_2 revealed by infrared spectroscopy and nano-imaging. *Science*, 318(5857):1750–1753, 2007.

[9] DB McWhan, TM Rice, and JP Remeika. Mott transition in Cr-doped V_2O_3. *Physical Review Letters*, 23(24):1384, 1969.

[10] Fabian HL Essler, Holger Frahm, Frank Göhmann, Andreas Klümper, and Vladimir E Korepin. *The one-dimensional Hubbard model*. Cambridge University Press, 2005.

[11] T Giamarchi. Mott transition in one dimension. *Physica B: Condensed Matter*, 230:975–980, 1997.

[12] Antoine Georges and Werner Krauth. Numerical solution of the d=∞ Hubbard model: evidence for a Mott transition. *Phys. Rev. Lett.*, 69:1240–1243, Aug 1992.

[13] Junjiro Kanamori. Electron correlation and ferromagnetism of transition metals. *Progress of Theoretical Physics*, 30(3):275–289, 1963.

[14] Aldo Isidori, Maja Berović, Laura Fanfarillo, Luca de' Medici, Michele Fabrizio, and Massimo Capone. Charge disproportionation, mixed valence, and Janus effect in multiorbital systems: A tale of two insulators. *Phys. Rev. Lett.*, 122:186401, May 2019.

[15] Luca de' Medici, Jernej Mravlje, and Antoine Georges. Janus-faced influence of Hund's rule coupling in strongly correlated materials. *Phys. Rev. Lett.*, 107:256401, Dec 2011.

[16] L. de' Medici, A. Georges, and S. Biermann. Orbital-selective Mott transition in multiband systems: slave-spin representation and dynamical mean-field theory. *Phys. Rev. B*, 72:205124, Nov 2005.

[17] Rafael M Fernandes and Andrey V Chubukov. Low-energy microscopic models for iron-based superconductors: a review. *Reports on Progress in Physics*, 80(1):014503, Nov 2016.

[18] Pablo Villar Arribi and Luca de' Medici. Hund's metal crossover and superconductivity in the 111 family of iron-based superconductors. *Phys. Rev. B*, 104:125130, Sep 2021.

[19] Sergey G. Porsev and Andrei Derevianko. Hyperfine quenching of the metastable $^3\mathrm{P}_{0,2}$ states in divalent atoms. *Phys. Rev. A*, 69:042506, Apr 2004.

[20] Lorenzo Francesco Livi. *New quantum simulations with ultracold Ytterbium gases*. Firenze University Press, 2019.

[21] Giacomo Cappellini, Jacopo Catani, and Roberto Righini. *Two-Orbital Quantum Physics in Yb Fermi Gases Exploiting the $^1S_0 \rightarrow {}^3P_0$ Clock Transition*. PhD thesis, 2016.

[22] David J Griffiths and Darrell F Schroeter. *Introduction to quantum mechanics*. Cambridge university press, 2018.

[23] A. V. Gorshkov, M. Hermele, V. Gurarie, C. Xu, P. S. Julienne, J. Ye, P. Zoller, E. Demler, M. D. Lukin, and A. M. Rey. Two-orbital SU(N) magnetism with ultracold alkaline-earth atoms. *Nature Physics*, 6:289, 2010.

[24] Ren Zhang, Yanting Cheng, Hui Zhai, and Peng Zhang. Orbital Feshbach resonance in alkali-earth atoms. *Phys. Rev. Lett.*, 115:135301, Sep 2015.

[25] M. Höfer, L. Riegger, F. Scazza, C. Hofrichter, D. R. Fernandes, M. M. Parish, J. Levinsen, I. Bloch, and S. Fölling. Observation of an orbital interaction-induced Feshbach resonance in $^{173}\mathrm{Yb}$. *Phys. Rev. Lett.*, 115:265302, Dec 2015.

[26] Francesco Scazza. *Probing SU(N)-symmetric orbital interactions with ytterbium Fermi gases in optical lattices*. PhD thesis, lmu, 2015.

[27] Antoine Georges, Gabriel Kotliar, Werner Krauth, and Marcelo J Rozenberg. Dynamical mean-field theory of strongly correlated fermion systems and the limit of infinite dimensions. *Reviews of Modern Physics*, 68(1):13, 1996.

[28] Samuele Giuli, Adriano Amaricci, and Massimo Capone. Mott-enhanced exciton condensation in a Hubbard bilayer. *Phys. Rev. B*, 108:165150, Oct 2023.

[29] Matteo Seclì, Massimo Capone, and Iacopo Carusotto. Theory of chiral edge state lasing in a two-dimensional topological system. *Phys. Rev. Res.*, 1:033148, Dec 2019.

[30] Alberto Scazzola et al. Interplay between electron-phonon interaction and electron-electron repulsion in multiorbital Hubbard models. 2022.

[31] K. Baumann, A. Valli, A. Amaricci, and M. Capone. Inducing and controlling magnetism in the honeycomb lattice through a harmonic trapping potential. *Phys. Rev. A*, 101:033611, Mar 2020.

[32] M. H. Hettler, M. Mukherjee, M. Jarrell, and H. R. Krishnamurthy. Dynamical cluster approximation: Nonlocal dynamics of correlated electron systems. *Phys. Rev. B*, 61:12739–12756, May 2000.

[33] Gabriel Kotliar, Sergej Y. Savrasov, Gunnar Pálsson, and Giulio Biroli. Cellular dynamical mean field approach to strongly correlated systems. *Phys. Rev. Lett.*, 87:186401, Oct 2001.

[34] H. Park, K. Haule, and G. Kotliar. Cluster dynamical mean field theory of the Mott transition. *Phys. Rev. Lett.*, 101:186403, Oct 2008.

[35] Thomas Maier, Mark Jarrell, Thomas Pruschke, and Matthias H. Hettler. Quantum cluster theories. *Rev. Mod. Phys.*, 77:1027–1080, Oct 2005.

[36] Olivier Parcollet, G Biroli, and G Kotliar. Cluster dynamical mean field analysis of the Mott transition. *Physical review letters*, 92(22):226402, 2004.

[37] J. K. Freericks, V. M. Turkowski, and V. Zlatić. Nonequilibrium dynamical mean-field theory. *Phys. Rev. Lett.*, 97:266408, Dec 2006.

[38] Naoto Tsuji, Takashi Oka, and Hideo Aoki. Correlated electron systems periodically driven out of equilibrium: Floquet + DMFT formalism. *Phys. Rev. B*, 78:235124, Dec 2008.

[39] Matteo Seclì et al. Topology and nonlinearity in driven-dissipative photonic lattices: Semiclassical and quantum approaches. 2021.

[40] P. W. Anderson. Localized magnetic states in metals. *Phys. Rev.*, 124:41–53, Oct 1961.

[41] Michele Fabrizio. *Kondo Effect and the Physics of the Anderson Impurity Model*, pages 313–343. Springer International Publishing, Cham, 2022.

[42] Alexander L Fetter and John Dirk Walecka. *Quantum theory of many-particle systems*. Courier Corporation, 2012.

[43] Cornelius Lanczos. An iteration method for the solution of the eigenvalue problem of linear differential and integral operators. 1950.

[44] Erik Koch. The Lanczos method. *The LDA+DMFT approach to strongly correlated materials*, 2011.

[45] Holger Fehske, Ralf Schneider, and Alexander Weisse. *Computational many-particle physics*, volume 739. Springer, 2007.

[46] A. Amaricci, L. Crippa, A. Scazzola, F. Petocchi, G. Mazza, L. de Medici, and M. Capone. Edipack: A parallel exact diagonalization package for quantum impurity problems. *Computer Physics Communications*, 273:108261, 2022.

[47] Carlos Mejuto Zaera. *Strong correlation through selected configuration interaction: From molecules to extended systems*. University of California, Berkeley, 2021.

[48] H-D Meyer and S Pal. A band-Lanczos method for computing matrix elements of a resolvent. *The Journal of chemical physics*, 91(10):6195–6204, 1989.

[49] Martin Eckstein, Marcus Kollar, Krzysztof Byczuk, and Dieter Vollhardt. Hopping on the Bethe lattice: Exact results for densities of states and dynamical mean-field theory. *Physical Review B*, 71(23):235119, 2005.

[50] Eleftherios N Economou. *Green's functions in quantum physics*, volume 7. Springer Science & Business Media, 2006.

[51] G. Mazza, A. Amaricci, M. Capone, and M. Fabrizio. Field-driven Mott gap collapse and resistive switch in correlated insulators. *Phys. Rev. Lett.*, 117:176401, Oct 2016.

[52] M Snoek, I Titvinidze, C Tőke, Krzysztof Byczuk, and Walter Hofstetter. Antiferromagnetic order of strongly interacting fermions in a trap: real-space dynamical mean-field analysis. *New Journal of Physics*, 10(9):093008, 2008.

[53] T-W Zhou, G Cappellini, D Tusi, L Franchi, J Parravicini, C Repellin, S Greschner, Massimo Inguscio, T Giamarchi, M Filippone, et al. Observation of universal Hall response in strongly interacting fermions. *Science*, 381(6656):427–430, 2023.

[54] Eva Pavarini. DMFT for linear response functions. *Lecture notes*.

[55] Douglas R Hofstadter. Energy levels and wave functions of Bloch electrons in rational and irrational magnetic fields. *Physical review B*, 14(6):2239, 1976.

[56] Nathan Goldman, G Juzeliūnas, Patrik Öhberg, and Ian B Spielman. Light-induced gauge fields for ultracold atoms. *Reports on Progress in Physics*, 77(12):126401, 2014.

[57] Monika Aidelsburger, Michael Lohse, Christian Schweizer, Marcos Atala, Julio T Barreiro, Sylvain Nascimbène, NR Cooper, Immanuel Bloch, and Nathan Goldman. Measuring the Chern number of Hofstadter bands with ultracold bosonic atoms. *Nature Physics*, 11(2):162–166, 2015.

[58] L. F. Livi, G. Cappellini, M. Diem, L. Franchi, C. Clivati, M. Frittelli, F. Levi, D. Calonico, J. Catani, M. Inguscio, and L. Fallani. Synthetic dimensions and spin-orbit coupling with an optical clock transition. *Phys. Rev. Lett.*, 117:220401, Nov 2016.

[59] Luca Salasnich. *Quantum Physics of Light and Matter: A Modern Introduction to Photons, Atoms and Many-Body Systems*. Springer, 2014.

[60] Daniel A Steck. *Quantum and atom optics*. 2007.

[61] Etienne Brion, Line Hjortshøj Pedersen, and Klaus Mølmer. Adiabatic elimination in a lambda system. *Journal of Physics A: Mathematical and Theoretical*, 40(5):1033, 2007.

[62] Marco Mancini et al. *Quantum simulation with Ytterbium atoms in synthetic dimensions*. 2016.

[63] Leonardo Fallani. Multicomponent spin mixtures of two-electron fermions. *arXiv preprint arXiv:2308.06591*, 2023.

[64] O. Boada, A. Celi, J. I. Latorre, and M. Lewenstein. Quantum simulation of an extra dimension. *Phys. Rev. Lett.*, 108:133001, Mar 2012.

[65] D. J. Scalapino, S. R. White, and S. C. Zhang. Superfluid density and the Drude weight of the Hubbard model. *Phys. Rev. Lett.*, 68:2830–2833, May 1992.

[66] Simone Barbarino, Marcello Dalmonte, Rosario Fazio, and Giuseppe E. Santoro. Topological phases in frustrated synthetic ladders with an odd number of legs. *Phys. Rev. A*, 97:013634, Jan 2018.

[67] Marco Mancini, Guido Pagano, Giacomo Cappellini, Lorenzo Livi, Marie Rider, Jacopo Catani, Carlo Sias, Peter Zoller, Massimo Inguscio, Marcello Dalmonte, et al. Observation of chiral edge states with neutral fermions in synthetic Hall ribbons. *Science*, 349(6255):1510–1513, 2015.

[68] Alessio Celi, Pietro Massignan, Julius Ruseckas, Nathan Goldman, Ian B Spielman, G Juzeliūnas, and M Lewenstein. Synthetic gauge fields in synthetic dimensions. *Physical Review Letters*, 112:043001, 2014.

[69] Lorenzo Del Re et al. Multicomponent strongly correlated fermions in optical lattices. 2016.

[70] Jorge E Hirsch and R Martin Fye. Monte Carlo method for magnetic impurities in metals. *Physical review letters*, 56(23):2521, 1986.

[71] Philipp Werner, Armin Comanac, Luca de' Medici, Matthias Troyer, and Andrew J. Millis. Continuous-time solver for quantum impurity models. *Phys. Rev. Lett.*, 97:076405, Aug 2006.

[72] Marcos Atala, Monika Aidelsburger, Michael Lohse, Julio T Barreiro, Belén Paredes, and Immanuel Bloch. Observation of chiral currents with ultracold atoms in bosonic ladders. *Nature Physics*, 10(8):588–593, 2014.

[73] R. Citro, S. De Palo, M. Di Dio, and E. Orignac. Quantum phase transitions of a two-leg bosonic ladder in an artificial gauge field. *Phys. Rev. B*, 97:174523, May 2018.

[74] M Di Dio, R Citro, S De Palo, E Orignac, and M-L Chiofalo. Meissner to vortex phase transition in a two-leg ladder in artificial gauge field. *The European Physical Journal Special Topics*, 224(3):525–531, 2015.

[75] Sergey Bravyi, David P DiVincenzo, and Daniel Loss. Schrieffer–wolff transformation for quantum many-body systems. *Annals of physics*, 326(10):2793–2826, 2011.

[76] Marin Bukov, Michael Kolodrubetz, and Anatoli Polkovnikov. Schrieffer-Wolff transformation for periodically driven systems: strongly correlated systems with artificial gauge fields. *Phys. Rev. Lett.*, 116:125301, Mar 2016.

[77] Seung-Sup B. Lee, Jan von Delft, and Andreas Weichselbaum. Generalized Schrieffer-Wolff transformation of multiflavor Hubbard models. *Phys. Rev. B*, 96:245106, Dec 2017.

[78] André Eckardt and Egidijus Anisimovas. High-frequency approximation for periodically driven quantum systems from a Floquet-space perspective. *New Journal of Physics*, 17(9):093039, sep 2015.

[79] Miguel A Cazalilla and Ana Maria Rey. Ultracold Fermi gases with emergent SU(N) symmetry. *Reports on Progress in Physics*, 77(12):124401, 2014.

[80] Jakob Schwichtenberg. *Physics from symmetry*. Springer, 2018.

[81] Elisa Ercolessi, Davide Vodola, and Costanza Benassi. SU(3) lattice gauge theories and spin chains.

[82] Bill Sutherland. Model for a multicomponent quantum system. *Phys. Rev. B*, 12:3795–3805, Nov 1975.

[83] GV Uimin. One-dimensional problem for S = 1 with modified antiferromagnetic Hamiltonian. *Soviet Journal of Experimental and Theoretical Physics Letters*, 12:225, 1970.

[84] Tung-Lam Dao, Antoine Georges, and Massimo Capone. Competing superfluid and density-wave ground-states of fermionic mixtures with mass imbalance in optical lattices. *Phys. Rev. B*, 76:104517, Sep 2007.

[85] Heinz-Peter Breuer and Francesco Petruccione. *The theory of open quantum systems*. Oxford University Press, USA, 2002.

[86] Valeriia Bilokon, Elvira Bilokon, Mari Carmen Bañuls, Agnieszka Cichy, and Andrii Sotnikov. Many-body correlations in one-dimensional optical lattices with alkaline-earth (-like) atoms. *Scientific Reports*, 13(1):9857, 2023.

[87] Lorenzo Del Re and Massimo Capone. Selective insulators and anomalous responses in three-component fermionic gases with broken SU(3) symmetry. *Phys. Rev. A*, 98:063628, Dec 2018.

[88] D Tusi, L Franchi, LF Livi, K Baumann, D Benedicto Orenes, L Del Re, RE Barfknecht, T-W Zhou, M Inguscio, G Cappellini, et al. Flavour-selective localization in interacting lattice fermions. *Nature Physics*, 18(10):1201–1205, 2022.

[89] Roger G Burns. *Mineralogical applications of crystal field theory*. Number 5. Cambridge university press, 1993.

[90] William W Porterfield. *Inorganic chemistry*. Academic press, 2013.

[91] Satoru Sugano. *Multiplets of transition-metal ions in crystals*. Elsevier, 2012.

[92] Antoine Georges, Luca de' Medici, and Jernej Mravlje. Strong correlations from Hund's coupling. *Annu. Rev. Condens. Matter Phys.*, 4(1):137–178, 2013.

[93] Massimo Capone, Michele Fabrizio, Claudio Castellani, and Erio Tosatti. Colloquium: Modeling the unconventional superconducting properties of expanded A_3C_{60} fullerides. *Rev. Mod. Phys.*, 81:943–958, Jun 2009.

[94] Luca de' Medici. Hund's coupling and its key role in tuning multiorbital correlations. *Phys. Rev. B*, 83:205112, May 2011.

[95] Jernej Mravlje, Markus Aichhorn, Takashi Miyake, Kristjan Haule, Gabriel Kotliar, and Antoine Georges. Coherence-incoherence crossover and the mass-renormalization puzzles in $\mathrm{sr_2ruo_4}$. *Phys. Rev. Lett.*, 106:096401, Mar 2011.

[96] Nicola Lanatà, Hugo U. R. Strand, Gianluca Giovannetti, Bo Hellsing, Luca de' Medici, and Massimo Capone. Orbital selectivity in Hund's metals: The iron chalcogenides. *Phys. Rev. B*, 87:045122, Jan 2013.

[97] Luca de' Medici, Gianluca Giovannetti, and Massimo Capone. Selective mott physics as a key to iron superconductors. *Phys. Rev. Lett.*, 112:177001, Apr 2014.

[98] Frank Lechermann, Antoine Georges, Gabriel Kotliar, and Olivier Parcollet. Rotationally invariant slave-boson formalism and momentum dependence of the quasiparticle weight. *Phys. Rev. B*, 76:155102, Oct 2007.

[99] Yusuke Nomura, Shiro Sakai, and Ryotaro Arita. Nonlocal correlations induced by Hund's coupling: a cluster DMFT study. *Phys. Rev. B*, 91:235107, Jun 2015.

[100] Douglas J. Scalapino, Steven R. White, and Shoucheng Zhang. Insulator, metal, or superconductor: The criteria. *Phys. Rev. B*, 47:7995–8007, Apr 1993.

[101] Raffaele Resta. Theory of longitudinal and transverse nonlinear dc conductivity. *Phys. Rev. Res.*, 4:033002, Jul 2022.

[102] Raffaele Resta. Drude weight and superconducting weight. *Journal of Physics: Condensed Matter*, 30(41):414001, 2018.

[103] Gabriele Bellomia and Raffaele Resta. Drude weight in systems with open boundary conditions. *Phys. Rev. B*, 102:205123, Nov 2020.

[104] Walter Kohn. Theory of the insulating state. *Phys. Rev.*, 133:A171–A181, Jan 1964.

[105] Murray Peshkin. The Aharonov-Bohm effect part one: Theory. *The Aharonov-Bohm Effect*, pages 1–34, 2005.

[106] L. Fanfarillo and E. Bascones. Electronic correlations in hund metals. *Phys. Rev. B*, 92:075136, Aug 2015.

[107] Luca de' Medici. Hund's coupling and its key role in tuning multiorbital correlations. *Phys. Rev. B*, 83:205112, May 2011.

[108] Akihisa Koga, Norio Kawakami, T. M. Rice, and Manfred Sigrist. Orbital-selective Mott transitions in the degenerate Hubbard model. *Phys. Rev. Lett.*, 92:216402, May 2004.

[109] Luca de' Medici, S. R. Hassan, Massimo Capone, and Xi Dai. Orbital-selective mott transition out of band degeneracy lifting. *Phys. Rev. Lett.*, 102:126401, Mar 2009.

[110] David Sénéchal, Danny Perez, and Dany Plouffe. Cluster perturbation theory for Hubbard models. *Phys. Rev. B*, 66:075129, Aug 2002.

[111] Michael Potthoff. Self-energy-functional approach: Analytical results and the Mott-Hubbard transition. *The European Physical Journal B-Condensed Matter and Complex Systems*, 36(3):335–348, 2003.

[112] Thomas Maier, Mark Jarrell, Thomas Pruschke, and Matthias H. Hettler. Quantum cluster theories. *Rev. Mod. Phys.*, 77:1027–1080, Oct 2005.

[113] Gabriele Bellomia, Carlos Mejuto-Zaera, Massimo Capone, and Adriano Amaricci. Quasilocal entanglement across the Mott-Hubbard transition. *arXiv preprint arXiv:2308.13706*, 2023.

[114] Qiangqiang Gu and Hai-Hu Wen. Superconductivity in nickel-based 112 systems. *The Innovation*, 3(1), 2022.

[115] Yusuke Nomura, Shiro Sakai, Massimo Capone, and Ryotaro Arita. Unified understanding of superconductivity and Mott transition in alkali-doped fullerides from first principles. *Science advances*, 1(7):e1500568, 2015.

[116] Jun Nagamatsu, Norimasa Nakagawa, Takahiro Muranaka, Yuji Zenitani, and Jun Akimitsu. Superconductivity at 39 K in magnesium diboride. *Nature*, 410(6824):63–64, 2001.

[117] Yu Saito, Tsutomu Nojima, and Yoshihiro Iwasa. Highly crystalline 2D superconductors. *Nature Reviews Materials*, 2(1):1–18, 2016.

[118] Matthew Yankowitz, Shaowen Chen, Hryhoriy Polshyn, Yuxuan Zhang, K Watanabe, T Taniguchi, David Graf, Andrea F Young, and Cory R Dean. Tuning superconductivity in twisted bilayer graphene. *Science*, 363(6431):1059–1064, 2019.

[119] Hoi Chun Po, Liujun Zou, Ashvin Vishwanath, and T Senthil. Origin of Mott insulating behavior and superconductivity in twisted bilayer graphene. *Physical Review X*, 8(3):031089, 2018.

[120] Fengcheng Wu, Allan H MacDonald, and Ivar Martin. Theory of phonon-mediated superconductivity in twisted bilayer graphene. *Physical review letters*, 121(25):257001, 2018.

[121] Teemu J. Peltonen, Risto Ojajärvi, and Tero T. Heikkilä. Mean-field theory for superconductivity in twisted bilayer graphene. *Phys. Rev. B*, 98:220504, Dec 2018.

[122] Haiyang Zhang, Fazal Badshah, Abdul Basit, and Guo-Qin Ge. Orbital feshbach resonance of fermi gases in an optical lattice. *Journal of Physics B: Atomic, Molecular and Optical Physics*, 51(18):185301, 2018.

[123] John Bardeen, Leon N Cooper, and John Robert Schrieffer. Theory of superconductivity. *Physical review*, 108(5):1175, 1957.

[124] Michael Tinkham. *Introduction to superconductivity*. Courier Corporation, 2004.

[125] Vitaly L Ginzburg, Vitaly Lazarevich Ginzburg, and LD Landau. *On the theory of superconductivity*. Springer, 2009.

[126] Lev Petrovich Gor'kov. Microscopic derivation of the Ginzburg-Landau equations in the theory of superconductivity. *Sov. Phys. JETP*, 9(6):1364–1367, 1959.

[127] Alexander Altland and Ben D Simons. *Condensed matter field theory*. Cambridge university press, 2010.

[128] Richard D Mattuck. *A guide to Feynman diagrams in the many-body problem*. Courier Corporation, 1992.

[129] Richard P Feynman, Albert R Hibbs, and Daniel F Styer. *Quantum mechanics and path integrals*. Courier Corporation, 2010.

[130] James F Annett. *Superconductivity, superfluids and condensates*, volume 5. Oxford University Press, 2004.

[131] Sebastian Doniach and Ernst Sondheimer. *Green's functions for solid state physicists*. World Scientific, 1998.

[132] Sijia Zhao, Zhaoyu Han, Steven A. Kivelson, and Ilya Esterlis. One-dimensional Holstein model revisited. *Phys. Rev. B*, 107:075142, Feb 2023.

[133] Atsushi Masumizu and Kiyoshi Sogo. Ward-Takahashi relations for so(4) symmetry in the Hubbard model. *Phys. Rev. B*, 72:115107, Sep 2005.

[134] A. F. Ho, M. A. Cazalilla, and T. Giamarchi. Quantum simulation of the Hubbard model: The attractive route. *Phys. Rev. A*, 79:033620, Mar 2009.

[135] Debayan Mitra, Peter T Brown, Elmer Guardado-Sanchez, Stanimir S Kondov, Trithep Devakul, David A Huse, Peter Schauß, and Waseem S Bakr. Quantum gas microscopy of an attractive Fermi–Hubbard system. *Nature Physics*, 14(2):173–177, 2018.

[136] Aron Beekman, Louk Rademaker, and Jasper van Wezel. An introduction to spontaneous symmetry breaking. *SciPost Physics Lecture Notes*, page 011, 2019.

[137] Rafael M Fernandes. Lecture notes: BCS theory of superconductivity, 2015.

[138] LJ Buchholtz and G Zwicknagl. Identification of p-wave superconductors. *Physical Review B*, 23(11):5788, 1981.

[139] Gabriel Kotliar and Jialin Liu. Superexchange mechanism and d-wave superconductivity. *Physical Review B*, 38(7):5142, 1988.

[140] Th. Maier, M. Jarrell, Th. Pruschke, and J. Keller. d-wave superconductivity in the Hubbard model. *Phys. Rev. Lett.*, 85:1524–1527, Aug 2000.

[141] P. Monthoux and G. G. Lonzarich. p-wave and d-wave superconductivity in quasi-two-dimensional metals. *Phys. Rev. B*, 59:14598–14605, Jun 1999.

[142] A. Toschi, M. Capone, and C. Castellani. Energetic balance of the superconducting transition across the bcs—bose einstein crossover in the attractive hubbard model. *Phys. Rev. B*, 72:235118, Dec 2005.

[143] Th. Pruschke, D. L. Cox, and M. Jarrell. Hubbard model at infinite dimensions: Thermodynamic and transport properties. *Phys. Rev. B*, 47:3553–3565, Feb 1993.

[144] Martin Greiter. Is electromagnetic gauge invariance spontaneously violated in superconductors? *Annals of Physics*, 319(1):217–249, 2005.

[145] A. Chattopadhyay, A. J. Millis, and S. Das Sarma. Optical spectral weights and the ferromagnetic transition temperature of colossal-magnetoresistance manganites: Relevance of double exchange to real materials. *Phys. Rev. B*, 61:10738–10749, Apr 2000.

[146] Woonki Chung and J. K. Freericks. Charge-transfer metal-insulator transitions in the spin-$\frac{1}{2}$ Falicov-Kimball model. *Phys. Rev. B*, 57:11955–11961, May 1998.

[147] E Müller-Hartmann. Correlated fermions on a lattice in high dimensions. *Zeitschrift für Physik B Condensed Matter*, 74(4):507–512, 1989.

[148] Tilman Esslinger. Fermi-Hubbard physics with atoms in an optical lattice. *Annu. Rev. Condens. Matter Phys.*, 1(1):129–152, 2010.

[149] AJ Leggett. Modern trends in the theory of condensed matter. *Modern Trends in the Theory of Condensed Matter, Proc. XVI Karpacz Winter School of Theoretical Physics, 1980*, 1980.

[150] Ph Nozières and S Schmitt-Rink. Bose condensation in an attractive fermion gas: From weak to strong coupling superconductivity. *Journal of Low Temperature Physics*, 59:195–211, 1985.

[151] A Toschi, P Barone, Massimo Capone, and C Castellani. Pairing and superconductivity from weak to strong coupling in the attractive Hubbard model. *New Journal of Physics*, 7(1):7, 2005.

[152] Giovanni Midei and Andrea Perali. Sweeping across the BCS-BEC crossover, reentrant, and hidden quantum phase transitions in two-band superconductors by tuning the valence and conduction bands. *Phys. Rev. B*, 107:184501, May 2023.

[153] Luca Salasnich, Nicola Manini, and Alberto Parola. Condensate fraction of a Fermi gas in the BCS-BEC crossover. *Phys. Rev. A*, 72:023621, Aug 2005.

[154] Wilhelm Zwerger. *The BCS-BEC crossover and the unitary Fermi gas*, volume 836. Springer Science & Business Media, 2011.

[155] Rudolf Haussmann, Walter Rantner, Stefano Cerrito, and Willhelm Zwerger. Thermodynamics of the BCS-BEC crossover. *Physical Review A*, 75(2):023610, 2007.

[156] Martin W Zwierlein, Jamil R Abo-Shaeer, Andre Schirotzek, Christian H Schunck, and Wolfgang Ketterle. Vortices and superfluidity in a strongly interacting Fermi gas. *Nature*, 435(7045):1047–1051, 2005.

[157] Stefano Giorgini, Lev P. Pitaevskii, and Sandro Stringari. Theory of ultracold atomic Fermi gases. *Rev. Mod. Phys.*, 80:1215–1274, Oct 2008.

[158] Immanuel Bloch, Jean Dalibard, and Wilhelm Zwerger. Many-body physics with ultracold gases. *Rev. Mod. Phys.*, 80:885–964, Jul 2008.

[159] AA Khelashvili and TP Nadareishvili. Singular behavior of the Laplace operator in polar spherical coordinates and some of its consequences for the radial wave function at the origin of coordinates. *Physics of Particles and Nuclei Letters*, 12:11–25, 2015.

[160] G. Pagano, M. Mancini, G. Cappellini, L. Livi, C. Sias, J. Catani, M. Inguscio, and L. Fallani. Strongly interacting gas of two-electron fermions at an orbital Feshbach resonance. *Phys. Rev. Lett.*, 115:265301, Dec 2015.

[161] G. Cappellini, L. F. Livi, L. Franchi, D. Tusi, D. Benedicto Orenes, M. Inguscio, J. Catani, and L. Fallani. Coherent manipulation of orbital Feshbach molecules of two-electron atoms. *Phys. Rev. X*, 9:011028, Feb 2019.

[162] Paivi Torma and Klaus Sengstock. *Quantum Gas Experiments: Exploring Many-Body States*, volume 3. World Scientific, 2014.

[163] E. K. Laird, Z.-Y. Shi, M. M. Parish, and J. Levinsen. Frustrated orbital Feshbach resonances in a Fermi gas. *Phys. Rev. A*, 101:022707, Feb 2020.

[164] Mohit Randeria, Ji-Min Duan, and Lih-Yir Shieh. Bound states, Cooper pairing, and Bose condensation in two dimensions. *Phys. Rev. Lett.*, 62:981–984, Feb 1989.

[165] Yi-Cai Zhang, Shanshan Ding, and Shizhong Zhang. Collective modes in a two-band superfluid of ultracold alkaline-earth-metal atoms close to an orbital feshbach resonance. *Phys. Rev. A*, 95:041603, Apr 2017.

[166] Taro Kamihori, Daichi Kagamihara, and Yoji Ohashi. Superfluid properties of an ultracold Fermi gas with an orbital Feshbach resonance in the BCS-BEC crossover region. *Phys. Rev. A*, 103:053319, May 2021.

[167] Junjun Xu, Ren Zhang, Yanting Cheng, Peng Zhang, Ran Qi, and Hui Zhai. Reaching a Fermi-superfluid state near an orbital Feshbach resonance. *Phys. Rev. A*, 94:033609, Sep 2016.

[168] Thierry Giamarchi and B. Sriram Shastry. Persistent currents in a one-dimensional ring for a disordered Hubbard model. *Phys. Rev. B*, 51:10915–10922, Apr 1995.